



materials ageing institute

Report Nr: 6125-4501-2018-00583
06/14/2021

Quantitative evaluation of the EDF local model and the EPRI-NRC xLPR models of crack initiation of the weld metals of Alloy 600 (Alloys 82 and 182)



Thierry COUVANT
HARRINGTON Craig

EDF R&D - MMC
EPRI

MAI

MATERIALS AGEING INSTITUTE

MATERIALS AGEING INSTITUTE (STAFF)

Avenue des Renardières - Ecuelles - 77818 MORET SUR LOING CEDEX - +33 (1) 60 73 60 73

10/15/2021

Quantitative evaluation of the EDF local model and the EPRI-NRC xLPR models of crack initiation of the weld metals of Alloy 600 (Alloys 82 and 182)

Thierry COUVANT
HARRINGTON Craig

EDF R&D - MMC
EPRI

| | | | |
|--|-----|--|--|
| 6125-4501-2018-00583-EN | 2.0 | | |
| Information type : Technical note | | | |
| <p>Crack initiation models are important for engineering and regulatory assessment. Although operating experience suggests that PWSCC is consistent with leak-before-break, EPRI and the U.S. NRC have jointly developed a modular-based probabilistic fracture mechanics tool, called xLPR (Extremely Low Probability of Rupture), capable of quantifying such risk. At EDF, a PWSCC code named Code_Coriolis was developed to simulate PWSCC of laboratory specimens and components.</p> <p>This study focused on the weld metals Alloys 82 and 182 to (1) provide a dataset of PWSCC initiation suitable for comparison among models, (2) use the available models to simulate observed cracking with existing codes, (3) use the results of the comparisons to identify and understand the strengths and limitations of the models and (4) make recommendations to improve the predictive capability of the models.</p> <p>Code_Coriolis and xLPR computations were performed in order to evaluate the accuracy of SCC predictions relying on EDF and EPRI/NRC models.</p> | | | |

| | | |
|------------|---|--|
| MAI | Quantitative evaluation of the EDF local model and the EPRI-NRC xLPR models of crack initiation of the weld metals of Alloy 600 (Alloys 82 and 182) | 6125-4501-2018-00583-EN Version 2.0 |
|------------|---|--|

Circuit de validation

| | | | |
|---------------------|-----------------|------------|---|
| Auteur | Thierry COUVANT | 15/10/2021 |  |
| Vérificateur | Claire RAINASSE | 15/10/2021 |  |
| Approbateur | Hing ip WONG | 15/10/2021 |  |

| | |
|---------------------|--------------|
| Code affaire | P121M |
|---------------------|--------------|

| | | |
|------------|---|--|
| MAI | Quantitative evaluation of the EDF local model and the EPRI-NRC xLPR models of crack initiation of the weld metals of Alloy 600 (Alloys 82 and 182) | 6125-4501-2018-00583-EN Version 2.0 |
|------------|---|--|

Liste de diffusion

| |
|----------------------------|
| Groupe destinataire |
| 21-MMC Chefs |
| 21-MMC Chefs groupe |
| 45-MAI Chefs |

| Pré-diff | Diff | Destinataire | Structure | E-mail |
|----------|------|----------------------|---------------|--------------------------------|
| X | X | ALBRECHT David | EDF DT | david.albrecht@edf.fr |
| | X | ANDRIEU Antoine | EDF DT | antoine.andrieu@edf.fr |
| | X | AUDEBERT Bruno | EDF R&D - FC | bruno.audebert@edf.fr |
| | X | BITSINDOU Chaveli | EDF R&D - MMC | chaveli.bitsindou@edf.fr |
| | X | BOISSON Marylou | EDF DI | marylou.boisson@edf.fr |
| | X | BONZOM Remy | EDF R&D - MMC | remy.bonzom@edf.fr |
| | X | CHOU Peter | EPRI | pchou@epri.com |
| X | X | COQUIO Nicolas | EDF DI | nicolas.coquio@edf.fr |
| | X | COUVANT Thierry | EDF R&D - MMC | thierry.couvant@edf.fr |
| | X | DE BOUVIER Odile | EDF DI | odile.debouvier@edf.fr |
| X | X | DERNIAUX Eric | EDF DI | eric.derniaux@edf.fr |
| | X | DOMINE Sebastien | EDF R&D - MMC | sebastien.domine@edf.fr |
| | X | GODARD-DESMAREST | EDF DI | sophie.godard-desmarest@edf.fr |
| X | X | HARRINGTON Craig | EPRI | charrington@epri.com |
| | X | MAI Members | Diffusion MAI | MAI |
| | X | MARTIN-CABANAS Bruna | EDF R&D - MMC | bruna.martin-cabanas@edf.fr |
| | X | MASSOUD Jean-Paul | EDF DT | jean-paul.massoud@edf.fr |
| | X | MISON Maxime | EDF DI | maxime.mison@edf.fr |
| | X | MONCHY-LEROY Carole | EDF R&D - MMC | carole.monchy-leroy@edf.fr |
| X | X | NGUYEN Bich Chau | EDF DI | bich-chau.nguyen@edf.fr |
| | X | PASUTTO Thomas | EDF R&D - MMC | thomas.pasutto@edf.fr |
| X | X | RAINASSE Claire | EDF R&D - MMC | claire.rainasse@edf.fr |
| | X | THEBAULT Yannick | EDF DI | yannick.thebault@edf.fr |
| | X | TIREAU Jonathan | EDF R&D - MMC | jonathan.tireau@edf.fr |
| | X | VARE Christophe | EDF R&D - FC | christophe.vare@edf.fr |
| | X | VERLET Romain | EDF R&D - MMC | romain.verlet@edf.fr |
| | X | VIDAL Julien | EDF R&D - MMC | julien.vidal@edf.fr |
| | X | VISSE Eric | EDF UNIE | eric.visse@edf.fr |
| | X | WONG Hing-ip | EDF R&D - MAI | hing-ip.wong@edf.fr |

| | | |
|------------|---|--|
| MAI | Quantitative evaluation of the EDF local model and the EPRI-NRC xLPR models of crack initiation of the weld metals of Alloy 600 (Alloys 82 and 182) | 6125-4501-2018-00583-EN Version 2.0 |
|------------|---|--|

AVERTISSEMENT / CAUTION

L'accès à ce document, ainsi que son utilisation, sont strictement limités aux personnes expressément habilitées par EDF.

EDF ne pourra être tenu responsable, au titre d'une action en responsabilité contractuelle, en responsabilité délictuelle ou de toute autre action, de tout dommage direct ou indirect, ou de quelque nature qu'il soit, ou de tout préjudice, notamment, de nature financière ou commerciale, résultant de l'utilisation d'une quelconque information contenue dans ce document.

Les données et informations contenues dans ce document sont fournies "en l'état" sans aucune garantie expresse ou tacite de quelque nature que ce soit.

Toute modification, reproduction, extraction d'éléments, réutilisation de tout ou partie de ce document sans autorisation préalable écrite d'EDF ainsi que toute diffusion externe à EDF du présent document ou des informations qu'il contient est strictement interdite sous peine de sanctions.

The access to this document and its use are strictly limited to the persons expressly authorized to do so by EDF.

EDF shall not be deemed liable as a consequence of any action, for any direct or indirect damage, including, among others, commercial or financial loss arising from the use of any information contained in this document.

This document and the information contained therein are provided "as are" without any warranty of any kind, either expressed or implied.

Any total or partial modification, reproduction, new use, distribution or extraction of elements of this document or its content, without the express and prior written consent of EDF is strictly forbidden. Failure to comply to the above provisions will expose to sanctions.

| | | |
|-----|---|--|
| MAI | Quantitative evaluation of the EDF local model and the EPRI-NRC xLPR models of crack initiation of the weld metals of Alloy 600 (Alloys 82 and 182) | 6125-4501-2018-00583-EN Version 2.0 |
|-----|---|--|

Synthèse

La prévision de l'amorçage est importante pour définir la maintenance industrielle mais aussi pour justifier la tenue en service des composants. Dans certains cadres réglementaires (par exemple aux USA) la prévision de fuite du circuit primaire avant rupture ne peut inclure un mécanisme de fissuration actif tel que la Corrosion Sous Contrainte (CSC). Cependant, le retour d'expérience suggère que le mécanisme de CSC pourrait être considéré dans la prévision de fuite avant rupture. Ainsi, l'EPRI et la NRC ont engagé un programme commun de développement d'un outil numérique modulaire nommé xLPR (Extremely Low Probability of Rupture) afin de prévoir, via une approche probabiliste, le risque de fissuration lorsque le mécanisme de CSC est impliqué. A EDF, le Code_Coriolis est quant à lui développé pour simuler la CSC des éprouvettes de laboratoire mais aussi des composants.

Cette étude porte sur les soudures de nickel en alliages 182 et 82. Les objectifs étaient les suivants :

1. Bâtir une base de données permettant la comparaison des prévisions des modèles de CSC du Code_Coriolis et du code xLPR.
2. Utiliser les modèles disponibles pour simuler la CSC observée sur les éprouvettes de cette base à l'aide des codes existants.
3. Comparer les prévisions des modèles par les deux codes (Code_Coriolis et xLPR), leurs avantages et leurs limites.
4. Dégager des voies d'amélioration de la prévision de la CSC.

Les simulations Code_Coriolis (version de développement TCV v2.1.5) se sont appuyées sur deux modèles d'amorçage développés à EDF :

- Le modèle des indices, totalement empirique, pour lequel une large base d'essais d'amorçage est requise pour identifier ses paramètres.
- Le modèle local, phénoménologique, qui ne nécessite pas la réalisation d'essais d'amorçages pour identifier ses paramètres. Les essais d'amorçage peuvent être utilisés pour valider le modèle ou améliorer la loi de propagation (notamment dans le régime lent).

Les paramètres actuels du modèle des indices permettent une estimation conservatrice de la cinétique de fissuration dans le cas des fissures dont la profondeur dépasse 1 mm. Les paramètres actuels contrôlant le régime lent de fissuration doivent être ajustés pour garantir le conservatisme des prévisions de fissuration basées sur le modèle local.

Les essais réalisés par PNNL confirment que le temps d'amorçage peut être extrêmement bref (inférieur à 30 h), en accord avec les prévisions du modèle local. Ces essais montrent également que des effets microstructuraux ou métallurgiques peuvent significativement affecter la cinétique de fissuration, a minima dans son régime lent d'extension. Cependant, la représentativité des soudures étudiées vis à vis des soudures des composants des REP n'est pas garantie, en particulier du fait de leur écrouissage (15%) par forgeage.

La simulation des essais PNNL suggère que les soudures fournies par Studsvik et KAPL sont, à l'état forgé, plus sensibles que la soudure EDF (non pré-écrouie avant essai) repérée RND-M-D-1054, alors que cette dernière est la plus sensible des soudures testées au laboratoire par EDF. Des caractérisations supplémentaires seraient utiles pour mieux hiérarchiser les sensibilités des différentes soudures selon leur précipitation en carbures de chrome et leur écrouissage.

Des essais et simulations complémentaires sur ces trois soudures permettraient d'améliorer les différents modèles de CSC :

- Essais d'oxydation, pour améliorer la prévision de la cinétique d'oxydation.
- Essais de rupture des joints de grains oxydés et modélisation du comportement mécanique cristallin, pour améliorer la prévision physique de l'amorçage.
- Essais de propagation sous faible facteur d'intensité de contrainte, pour mieux prévoir la vitesse lente de fissuration.

| | | |
|------------|---|--|
| MAI | Quantitative evaluation of the EDF local model and the EPRI-NRC xLPR models of crack initiation of the weld metals of Alloy 600 (Alloys 82 and 182) | 6125-4501-2018-00583-EN Version 2.0 |
|------------|---|--|

Les modèles existants pourraient être utilisés pour prévoir la CSC des pénétrations de fond de cuve. Cela offrirait des indications particulièrement utiles pour l'amélioration des modèles en cohérence avec les problématiques industrielles (influence des états de surface) ou encore la quantification des facteurs d'amélioration apportés par une mitigation (chimie de l'eau, remplacement de matériau, mise en compression de surface).

| | | |
|-----|---|--|
| MAI | Quantitative evaluation of the EDF local model and the EPRI-NRC xLPR models of crack initiation of the weld metals of Alloy 600 (Alloys 82 and 182) | 6125-4501-2018-00583-EN Version 2.0 |
|-----|---|--|

Executive Summary

Crack initiation models are important not only for engineering assessment but also for regulatory assessment. In some regulatory frameworks (e.g. in the U. S.) the evaluation of leak-before-break does not allow active degradation mechanisms such as Primary Water Stress Corrosion Cracking (PWSCC). Although operating experience suggests that PWSCC is consistent with leak-before-break, a tool for the quantitative assessment of the impact of PWSCC on leak-before-break is regarded as necessary within the regulatory framework. EPRI and the U.S. NRC have jointly developed a modular-based probabilistic fracture mechanics tool, called xLPR (Extremely Low Probability of Rupture), capable of quantifying such risk. At EDF, a PWSCC code named Code_Coriolis was developed to simulate PWSCC of laboratory specimens and components.

This study focused on the weld metals Alloys 82 and 182 to:

1. Provide a dataset of PWSCC initiation suitable for comparison among the EDF and xLPR models.
2. Use the available models to simulate observed cracking with existing codes.
3. Use the results of the comparisons to identify and understand the strengths and limitations of the models.
4. Make recommendations to improve the predictive capability of the models.

Code_Coriolis (intermediate version v2.1.5 including the latest developments to be released in the next version of the webapp) computations were performed in order to evaluate the accuracy of SCC predictions relying on two initiation models:

- The index model: a fully empirical model. A large experimental SCC database is required for the calibration of parameters.
- The local model: a phenomenological model. SCC tests are not necessary to calibrate the model. They are required for the evaluation of predictions and can be used to optimize the crack growth model.

Current parameters allow conservative predictions of cracking kinetics for cracks deeper than 1 mm, if the index model is used. Parameters of the crack growth model should be tuned to guarantee conservative predictions if using the local model.

Experiments performed by PNNL confirm that the time to initiation can be extremely short (less than 30 h), as predicted by the local model. These tests also show how microstructural or metallurgical parameters can affect initiation or the rate of cracking, at least in the slow crack growth regime. It is noted that although these observed extremely short times to initiation are considered representative of the material tested, it is possible that the material (15% cold forged) tested is not entirely representative of material in nuclear power plant components.

The simulation of PNNL tests, performed on cold worked welds, suggest that tested Studsvik and KAPL welds may have a larger susceptibility to SCC than EDF weld registered RND-M-D-1054 (not cold worked). This weld was used to calibrate the EDF SCC model upper bounds. Therefore, complementary investigations may be useful to rank the susceptibilities of these three welds, considering at least the following parameters: precipitation of chromium carbides and cold work.

Complementary tests and computations may be useful to better calibrate behaviors involved in the SCC:

- Oxidation tests, to improve the prediction of oxidation kinetics.
- Cracking tests of oxidized grain boundaries and crystal plasticity finite element modeling, to improve the prediction of initiation.
- Crack growth tests under low stress intensity factor values, to better model the slow crack growth regime.

Existing models could be used to evaluate the susceptibility to PWSCC of Bottom Mounted Instrumentation nozzles. It may offer relevant guidelines for the improvement of models in agreement

| | | |
|------------|---|--|
| MAI | Quantitative evaluation of the EDF local model and the EPRI-NRC xLPR models of crack initiation of the weld metals of Alloy 600 (Alloys 82 and 182) | 6125-4501-2018-00583-EN Version 2.0 |
|------------|---|--|

with industrial issues (surface finish effects) and factors of improvement based on mitigation (water chemistry, material replacement, peening).

| | | |
|-----|---|--|
| MAI | Quantitative evaluation of the EDF local model and the EPRI-NRC xLPR models of crack initiation of the weld metals of Alloy 600 (Alloys 82 and 182) | 6125-4501-2018-00583-EN Version 2.0 |
|-----|---|--|

Sommaire / Summary

| | |
|---|-----------|
| AVERTISSEMENT / CAUTION | 1 |
| SYNTHÈSE | 2 |
| EXECUTIVE SUMMARY | 4 |
| SOMMAIRE / SUMMARY | 6 |
| 1. BACKGROUND | 9 |
| 2. OBJECTIVE | 11 |
| 3. APPROACH | 11 |
| 4. DATABASE | 11 |
| 4.1. MATERIALS | 11 |
| 4.1.1. EDF weld Alloy 182 registered RND-M-D-1054 (AW) | 11 |
| 4.1.2. EDF weld Alloy 82 registered RND-M-D-711 (SR) | 13 |
| 4.1.3. PNNL weld Alloy 182 registered Studsvik 8001231 | 16 |
| 4.1.4. PNNL weld Alloy 182 registered KAPL 823030 | 20 |
| 4.2. SCC INITIATION TESTS | 24 |
| 4.2.1. Constant load tests on Alloy 182 registered RND-M-D-1054 | 24 |
| 4.2.2. Constant load tests on Alloy 82 registered RND-M-D-711 | 26 |
| 4.2.3. PNNL constant load tests on 15% cold forged Alloy 182 registered KAPL 823030 and 15% cold forged Alloy 182 registered Studsvik 8001231 | 27 |
| 5. SCC MODELS | 30 |
| 5.1. CRACK INITIATION | 30 |
| 5.1.1. Index model | 30 |
| 5.1.2. Local model | 31 |
| 5.1.3. xLPR initiation models | 42 |
| 5.2. CRACK PROPAGATION | 47 |
| 5.2.1. EDF Power law | 47 |
| 5.2.2. EDF sigmoid law | 48 |
| 6. SIMULATION OF SCC TESTS WITH CODE_CORIOLIS | 51 |
| 6.1. MODELING OF THE SPECIMENS | 51 |
| 6.2. MODELING OF THE LOADING | 52 |
| 6.2.1. Boundary conditions | 52 |
| 6.2.2. Stress and strain fields at the surface exposed to water | 54 |
| 6.2.3. Calculation of K | 56 |
| 6.3. ALGORITHM FOR SCC PREDICTION WITH CODE_CORIOLIS | 57 |
| 6.4. SCC PREDICTIONS RELYING ON THE INDEX INITIATION MODEL AND THE SIGMOID PROPAGATION LAW | 57 |
| 6.4.1. Results on Alloy 182 registered RND-M-D-1054 | 57 |
| 6.4.2. Results on Alloy 82 registered RND-M-D-711 | 61 |
| 6.4.3. Results on PNNL Alloy 182 registered Studsvik 8001231 | 65 |
| 6.4.4. Results on PNNL Alloy 182 registered KAPL 823030 | 69 |
| 6.5. SCC PREDICTIONS RELYING ON THE LOCAL INITIATION MODEL AND THE SIGMOID PROPAGATION LAW | 72 |
| 6.5.1. Results on Alloy 182 registered RND-M-D-1054 | 72 |
| 6.5.2. Results on Alloy 82 registered RND-M-D-711 | 77 |
| 6.5.3. Results on PNNL Alloy 182 registered Studsvik 8001231 | 80 |
| 6.5.4. Results on PNNL Alloy 182 registered KAPL 823030 | 84 |
| 6.6. COMPARISON OF CODE_CORIOLIS MODELS AND PWSCC INITIATION TEST DATA WITH xLPR INITIATION MODELS | 87 |
| 6.6.1. Results Comparison of Alloy 182 registered RND-M-D-1054 | 87 |
| 6.6.2. Results Comparison of Alloy 82 registered RND-M-D-711 | 88 |

| | | |
|-----|---|--|
| MAI | Quantitative evaluation of the EDF local model and the EPRI-NRC xLPR models of crack initiation of the weld metals of Alloy 600 (Alloys 82 and 182) | 6125-4501-2018-00583-EN Version 2.0 |
|-----|---|--|

| | | |
|------------|---|------------|
| 6.6.3. | Results Comparison of PNNL Alloy 182 registered Studsvik | 89 |
| 6.6.4. | Results Comparison of PNNL Alloy 182 registered KAPL | 90 |
| 7. | DISCUSSION | 92 |
| 7.1. | INDEX MODEL | 92 |
| 7.2. | LOCAL MODEL | 94 |
| 7.3. | xLPR INITIATION MODELS | 95 |
| 7.4. | xLPR MODEL CALIBRATION | 98 |
| 8. | CONCLUSIONS AND FUTURE WORK | 102 |
| 9. | CITED DOCUMENTS..... | 104 |
| 10. | APPENDIX 1: CGR UPPER BOUNDS VS. CRACK GROWTH DATA ON WELD REGISTERED RND-M-D-1054 | 107 |
| 11. | APPENDIX 2: CODE_CORIOLIS MAIN INPUTS/OUTPUTS | 113 |
| 11.1. | SIMULATIONS OF THE TEST ON SPECIMEN 1383-11 | 113 |
| 11.1.1. | Index initiation model with sigmoid CGR law | 113 |
| 11.1.2. | Local initiation model with sigmoid CGR law | 114 |
| 11.2. | SIMULATIONS OF THE TEST ON SPECIMEN 1383-16 | 115 |
| 11.2.1. | Index initiation model with sigmoid CGR law | 115 |
| 11.2.2. | Local initiation model with sigmoid CGR law | 116 |
| 11.3. | SIMULATIONS OF THE TEST ON SPECIMEN 1383-19 | 117 |
| 11.3.1. | Index initiation model with sigmoid CGR law | 117 |
| 11.3.2. | Local initiation model with sigmoid CGR law | 118 |
| 11.4. | SIMULATIONS OF THE TEST ON SPECIMEN 1383-20 | 119 |
| 11.4.1. | Index initiation model with sigmoid CGR law | 119 |
| 11.4.2. | Local initiation model with sigmoid CGR law | 120 |
| 11.5. | SIMULATIONS OF THE TEST ON SPECIMEN 1383-21 | 121 |
| 11.5.1. | Index initiation model with sigmoid CGR law | 121 |
| 11.5.2. | Local initiation model with sigmoid CGR law | 122 |
| 11.6. | SIMULATIONS OF THE TEST ON SPECIMEN 1383-22 | 123 |
| 11.6.1. | Index initiation model with sigmoid CGR law | 123 |
| 11.6.2. | Local initiation model with sigmoid CGR law | 124 |
| 11.7. | SIMULATIONS OF THE TEST ON SPECIMEN 1383-23 | 125 |
| 11.7.1. | Index initiation model with sigmoid CGR law | 125 |
| 11.7.2. | Local initiation model with sigmoid CGR law | 126 |
| 11.8. | SIMULATIONS OF THE TEST ON SPECIMEN 1383-26 | 127 |
| 11.8.1. | Index initiation model with sigmoid CGR law | 127 |
| 11.8.2. | Local initiation model with sigmoid CGR law | 128 |
| 11.9. | SIMULATIONS OF THE TEST ON SPECIMEN 1383-27 | 129 |
| 11.9.1. | Index initiation model with sigmoid CGR law | 129 |
| 11.9.2. | Local initiation model with sigmoid CGR law | 130 |
| 11.10. | SIMULATIONS OF THE TEST ON SPECIMEN 1383-28 | 131 |
| 11.10.1. | Index initiation model with sigmoid CGR law | 131 |
| 11.10.2. | Local initiation model with sigmoid CGR law | 132 |
| 11.11. | SIMULATIONS OF THE TEST ON SPECIMEN 1383-29 | 133 |
| 11.11.1. | Index initiation model with sigmoid CGR law | 133 |
| 11.11.2. | Local initiation model with sigmoid CGR law | 134 |
| 11.12. | SIMULATIONS OF THE TEST ON SPECIMEN 1383-CEA | 135 |
| 11.12.1. | Index initiation model with sigmoid CGR law | 135 |
| 11.12.2. | Local initiation model with sigmoid CGR law | 136 |
| 11.13. | SIMULATIONS OF THE TEST ON SPECIMEN 1588-16 | 137 |
| 11.13.1. | Index initiation model with sigmoid CGR law | 137 |
| 11.13.2. | Local initiation model with sigmoid CGR law | 138 |
| 11.14. | SIMULATIONS OF THE TEST ON SPECIMEN IN169 | 139 |
| 11.14.1. | Index initiation model with sigmoid CGR law | 139 |
| 11.14.2. | Local initiation model with sigmoid CGR law | 140 |
| 11.15. | SIMULATIONS OF THE TEST ON SPECIMEN IN170 | 141 |

| | | |
|-----|---|--|
| MAI | Quantitative evaluation of the EDF local model and the EPRI-NRC xLPR models of crack initiation of the weld metals of Alloy 600 (Alloys 82 and 182) | 6125-4501-2018-00583-EN Version 2.0 |
|-----|---|--|

| | | |
|----------|--|-----|
| 11.15.1. | <i>Index initiation model with sigmoid CGR law</i> | 141 |
| 11.15.2. | <i>Local initiation model with sigmoid CGR law</i> | 142 |
| 11.16. | SIMULATIONS OF THE TEST ON SPECIMEN IN171 | 143 |
| 11.16.1. | <i>Index initiation model with sigmoid CGR law</i> | 143 |
| 11.16.2. | <i>Local initiation model with sigmoid CGR law</i> | 144 |
| 11.17. | SIMULATIONS OF THE TEST ON SPECIMEN IN191 | 145 |
| 11.17.1. | <i>Index initiation model with sigmoid CGR law</i> | 145 |
| 11.17.2. | <i>Local initiation model with sigmoid CGR law</i> | 146 |
| 11.18. | SIMULATIONS OF THE TEST ON SPECIMEN IN192 | 147 |
| 11.18.1. | <i>Index initiation model with sigmoid CGR law</i> | 147 |
| 11.18.2. | <i>Local initiation model with sigmoid CGR law</i> | 148 |
| 11.19. | SIMULATIONS OF THE TEST ON SPECIMEN IN193 | 149 |
| 11.19.1. | <i>Index initiation model with sigmoid CGR law</i> | 149 |
| 11.19.2. | <i>Local initiation model with sigmoid CGR law</i> | 150 |
| 11.20. | SIMULATIONS OF THE TEST ON SPECIMEN IN233 | 151 |
| 11.20.1. | <i>Index initiation model with sigmoid CGR law</i> | 151 |
| 11.20.2. | <i>Local initiation model with sigmoid CGR law</i> | 152 |
| 11.21. | SIMULATIONS OF THE TEST ON SPECIMEN IN234 | 153 |
| 11.21.1. | <i>Index initiation model with sigmoid CGR law</i> | 153 |
| 11.21.2. | <i>Local initiation model with sigmoid CGR law</i> | 154 |
| 11.22. | SIMULATIONS OF THE TEST ON SPECIMEN IN235 | 155 |
| 11.22.1. | <i>Index initiation model with sigmoid CGR law</i> | 155 |
| 11.22.2. | <i>Local initiation model with sigmoid CGR law</i> | 156 |
| 11.23. | SIMULATIONS OF THE TEST ON SPECIMEN IN166 | 157 |
| 11.23.1. | <i>Index initiation model with sigmoid CGR law</i> | 157 |
| 11.23.2. | <i>Local initiation model with sigmoid CGR law</i> | 158 |
| 11.24. | SIMULATIONS OF THE TEST ON SPECIMEN IN167 | 159 |
| 11.24.1. | <i>Index initiation model with sigmoid CGR law</i> | 159 |
| 11.24.2. | <i>Local initiation model with sigmoid CGR law</i> | 160 |
| 11.25. | SIMULATIONS OF THE TEST ON SPECIMEN IN168 | 161 |
| 11.25.1. | <i>Index initiation model with sigmoid CGR law</i> | 161 |
| 11.25.2. | <i>Local initiation model with sigmoid CGR law</i> | 162 |
| 11.26. | SIMULATIONS OF THE TEST ON SPECIMEN IN194 | 163 |
| 11.26.1. | <i>Index initiation model with sigmoid CGR law</i> | 163 |
| 11.26.2. | <i>Local initiation model with sigmoid CGR law</i> | 164 |
| 11.27. | SIMULATIONS OF THE TEST ON SPECIMEN IN195 | 165 |
| 11.27.1. | <i>Index initiation model with sigmoid CGR law</i> | 165 |
| 11.27.2. | <i>Local initiation model with sigmoid CGR law</i> | 166 |
| 11.28. | SIMULATIONS OF THE TEST ON SPECIMEN IN196 | 167 |
| 11.28.1. | <i>Index initiation model with sigmoid CGR law</i> | 167 |
| 11.28.2. | <i>Local initiation model with sigmoid CGR law</i> | 168 |

| | | |
|-----|---|--|
| MAI | Quantitative evaluation of the EDF local model and the EPRI-NRC xLPR models of crack initiation of the weld metals of Alloy 600 (Alloys 82 and 182) | 6125-4501-2018-00583-EN Version 2.0 |
|-----|---|--|

1. Background

Crack initiation models are important not only for engineering assessment but also for regulatory assessment. In some regulatory frameworks (e.g. in the U. S.) the evaluation of leak-before-break does not allow active degradation mechanisms such as Primary Water Stress Corrosion Cracking (PWSCC). Although operating experience suggests that PWSCC is consistent with leak-before-break, a tool for the quantitative assessment of the impact of PWSCC on leak-before-break is regarded as necessary within the regulatory framework. EPRI and the U.S. NRC have jointly developed a modular-based probabilistic fracture mechanics tool, called xLPR (Extremely Low Probability of Rupture), capable of quantifying such risk. At EDF, a PWSCC code named Code_Coriolis was developed to simulate PWSCC of laboratory specimens and components [1, 2]. The code is available online, out of EDF, but with restricted access to EDF partners [3].

The PWSCC incubation time prior to the advent of a crack of engineering scale that conforms to fracture mechanics principles represents the main fraction of component life prior to failure and is therefore of significant interest for modeling. However, the stochastic characteristics of early crack development present significant challenges for model development and validation and have limited the role of crack initiation and short crack growth in asset management and regulatory decisions.

The xLPR code contains a 'crack initiation' module that probabilistically evaluates this crack incubation period as 'initiation'. Several non-mechanistic models of crack initiation are implemented within xLPR but are not permanent selections; a more physically-based model (module), once available, can be inserted.

Both purely empirical and physically-based modes are already available in Code_Coriolis, where initiation is systematically chained with crack growth. SCC calculations are based on a 3D finite Element Modeling (FEM) delivering local stresses and strains in the structure. Code_Coriolis is used to better fit PWSCC models, to support in-service failure analyses (Figure 1, Figure 2) [4] and to predict the life time of components. For example, Code_Coriolis was recently used to calculate factors of improvement of primary pump bolts [2].

All models have limitations. The current crack initiation models within xLPR have the following limitations:

- No explicit adoption of microstructural parameters (although heat-to-heat and within-heat variability can be modeled).
- Manufacturing defects are not addressed (however, crack-like surface-connected defects can be addressed indirectly by modeling flaws present at time = 0).
- Assumes idealized flaw shapes.

Conversely, EDF has developed a rather sophisticated, mechanistically-based crack initiation model that may benefit from further benchmarking and validation against available laboratory and field data of early crack development. Parameters of the model were calibrated for Alloy 600 [5] and Alloy 182 [6].

It is important to understand whether any particular model can be improved. This report focuses on identifying and understanding the strengths and weaknesses of the available crack initiation models, within the context of the weld metals of Alloy 600.

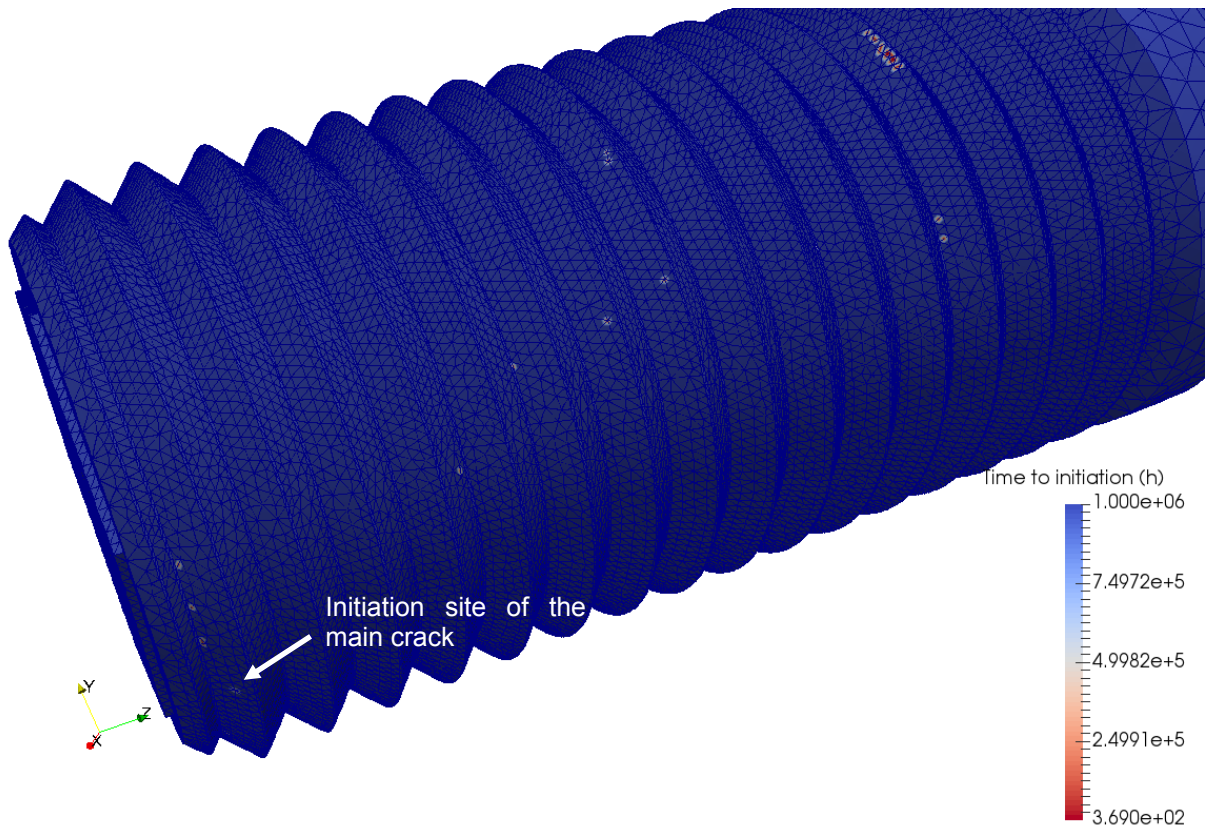


Figure 1 – Time to initiation field predicted at the surface of a primary pump stud using the local model and a sigmoid crack growth [4].

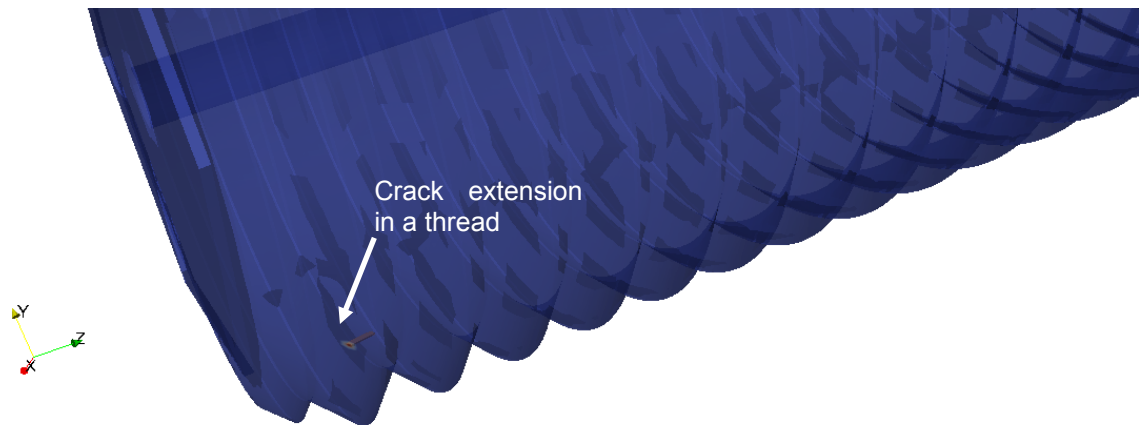


Figure 2 – Crack growth path predicted at the surface of a primary pump stud using the local model and a sigmoid crack growth [4].

2. Objective

This study focused on the weld metals Alloys 82 and 182 to:

1. Provide a dataset of PWSCC initiation suitable for comparison among the EDF and xLPR models.
2. Use the available models to simulate experiment cracking with existing codes.
3. Use the results of the comparisons to identify and understand the strengths and limitations of the models.
4. Make recommendations to improve the predictive capability of the models.

3. Approach

First, a database of SCC constant load initiation ⁽¹⁾ tests was prepared. Then existing models and fitted parameters for Alloys 182 and 82 were introduced. It is worth mentioning that EDF index initiation model was calibrated, in the past, without Code_Coriolis, on the EDF database on A182 registered RND-M-D-1054. SCC tests were simulated using EDF Code_Coriolis and U.S. xLPR code. Parameters of the models were then briefly optimized based on the simulation of the SCC tests with Code_Coriolis. Finally, the relevance of existing models and simulations with the two codes were evaluated.

Therefore:

- EDF data were used both for the historical OD calibration of the index model and the evaluation of the index and local initiation models coupled with crack growth models using a 3D simulation (Code_Coriolis).
- PNNL data were only used for evaluation.

4. Database

4.1. Materials

Notations used in the current report for the directions in the welds are given in Figure 3. The short S-direction is parallel to the direction of growth of the dendrites, the L-direction is the direction of the welding and T-direction is the transverse direction.

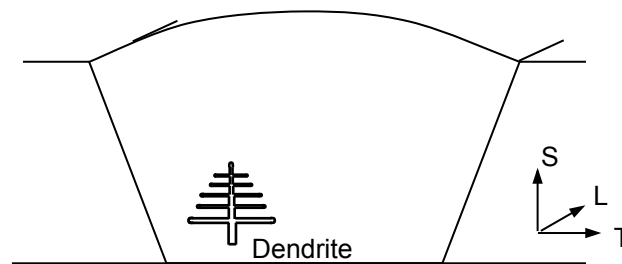


Figure 3 – Directions.

4.1.1. EDF weld Alloy 182 registered RND-M-D-1054 (AW)

Alloy 182 registered as RND-M-D-1054 is a V-shaped weld, of 600×50×30 mm³, made of 15 layers and 7 welding passes (2 mm-thick) ^[7, 8]. This material was manually welded with a Soudonel CQ5 coated electrode (diameter of 4 mm), and with Alloy 600 plates. Welding conditions were: 110 A, 28 V and 128°C between two welding passes. No stress-relief (SR) heat treatment was performed on this weld which was in as-welded (AW) conditions. The weld was fully characterized by EDF.

The weld has a dendritic microstructure with columnar-shape grains due to solidification during the welding process. A preferential <100> orientation developed along the S direction which is the axis of

⁽¹⁾ Nevertheless, tests can involve limited or large crack extension.

| | | |
|-----|---|--|
| MAI | Quantitative evaluation of the EDF local model and the EPRI-NRC xLPR models of crack initiation of the weld metals of Alloy 600 (Alloys 82 and 182) | 6125-4501-2018-00583-EN Version 2.0 |
|-----|---|--|

dendrite growth (Figure 4 and Figure 5). The weld has large equiaxed grains in the LT plane while it exhibits a columnar morphology in the S direction (reaching several millimeters long).

Mechanical properties are given in Table 1 [7, 8]. The stress-strain curves at room temperature and 350°C along the T and L axes are given in Figure 6. Chemical compositions are presented in Table 2. Tensile and chemical properties met RCC-M French requirements.

Transmission electron microscopy (TEM) and Energy Dispersive Spectroscopy (EDS) showed [20] that, along the grain boundary, Cr depletion occurs adjacent to Cr carbides. Cr content is around 7% wt at the depleted grain boundary. The thickness of the observed thin foil (lower than 100 nm) demonstrates confidence in the quantitative elemental analysis performed in the metal [9]. This result is in good agreement with previous observations [7] on Alloy 600 presenting a high density of intergranular carbides (Cr_7C_3 and $Cr_{23}C_6$). Similar tendencies (Cr level around 10% wt. at the grain boundary) were also observed by Atom Probe Tomography (APT). Authors [8] correlated the intergranular Cr-depletion to the formation of adjacent Cr-rich carbides.

Benefits of intergranular Cr carbides on resistance to SCC [10, 11, 12] may be due to:

- The local emission of dislocations from precipitates, promoting stress relaxation in adjacent grains [13].
- The decrease in grain boundary sliding induced by intergranular carbides [14, 15].
- The local increase in Cr concentration, promoting the resistance to intergranular oxide growth. However, Cr carbide formation may induce local Cr depletion.

The mean distance (d_{pcp} in nm) between intergranular precipitates ranges from 250 nm (misorientation $< 5^\circ$) to 1400 nm ($40^\circ < \text{misorientation} < 50^\circ$). Nevertheless, lower distances were noticed along Coincidence Site Lattice (CSL) boundaries, recognized to offer a good resistance to SCC. Finally, the grain boundary coverage (GBC) with chromium carbides was assigned ⁽²⁾ to $GBC(D1054) = 0.2$.

Table 1 – Tensile properties of weld registered RND-M-D-1054 [7, 8].

| EDF registration | 20 °C | | | | 350 °C | | | |
|------------------|-------------------------|-----------|-------|---------|-------------------------|-----------|-------|---------|
| | YS _{0.2} (MPa) | UTS (MPa) | El. % | E (GPa) | YS _{0.2} (MPa) | UTS (MPa) | El. % | E (GPa) |
| RND-M-D-1054 | 386 | 627 | 33 | 158 | 347 | 568 | 46 | 144 |
| RCC-M (182) | ≥ 250 | ≥ 550 | ≥ 30 | - | > 190 | - | - | - |

Table 2 – Chemical composition (%wt.) of weld registered RND-M-D-1054 [7, 8].

| EDF registration | C | S | P | Si | Mn | Ni | Cr | Mo | N | Co | Cu | Ti | Nb | Ta | Al | Fe | O |
|------------------|--------|---------|--------|-------------------|---------------|-------|-------------|--------|------|--------|--------|------|-------|----|--------|------------|---|
| RND-M-D-1054 | 0.026 | 0.003 | < 0.02 | 0.35 | 6.2 | 69.18 | 15.0 | < 0.05 | 0.03 | < 0.07 | < 0.05 | 0.05 | 2.0 | | < 0.07 | 6.9 | - |
| RCC-M (182) | ≤ 0.10 | ≤ 0.015 | ≤ 0.03 | ≤ 1 0.6 max | 5.0 to 9.5 | > 59 | 13 to 17 | - | - | ≤ 0.1 | ≤ 0.5 | ≤ 1 | > 1.8 | | - | 6 to 10 | - |

⁽²⁾ The GBC is defined as the ratio between the total length of intergranular carbides and the total length of grain boundaries, in the analyzed area.

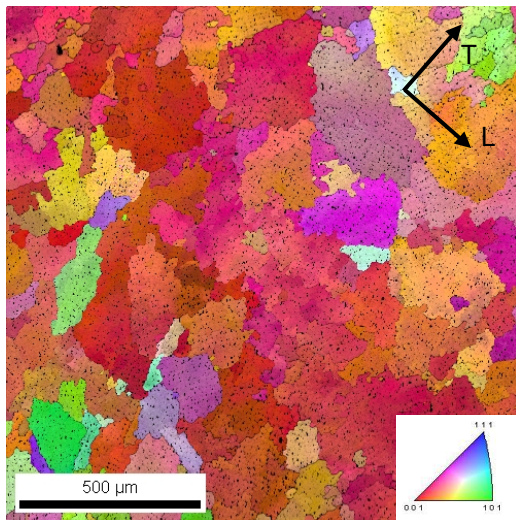


Figure 4 – Inverse Pole Figure (axis: S) on LT plane of RND-M-D-1054 weld [7, 8, 16].

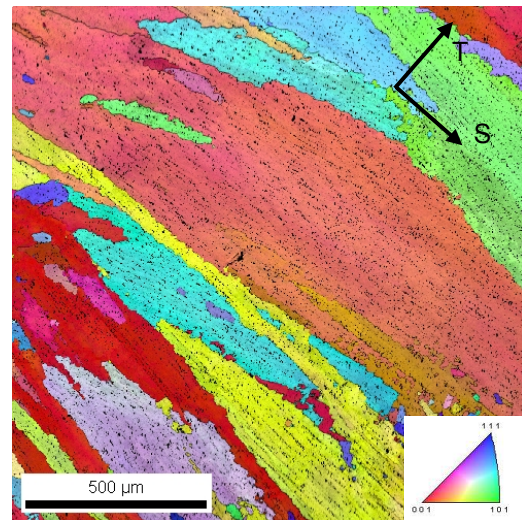


Figure 5 – Inverse Pole Figure (axis: L) on ST plane of RND-M-D-1054 weld [7, 8, 16].

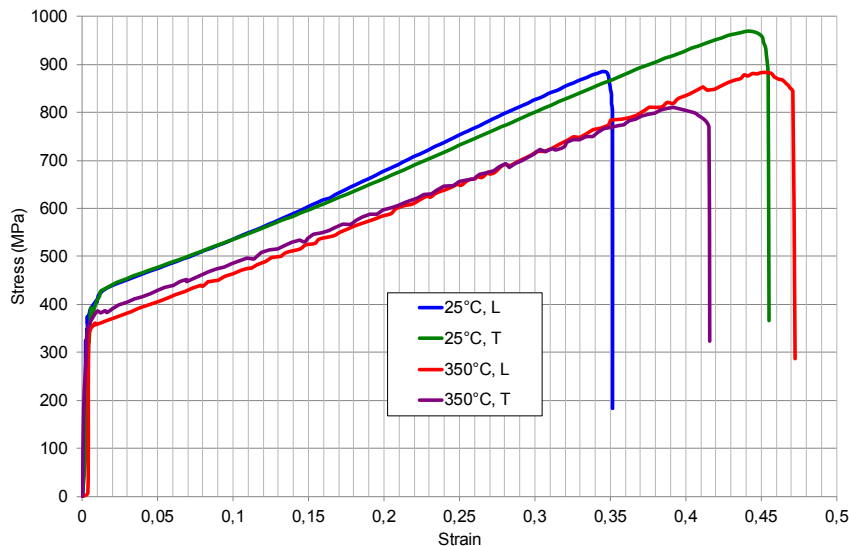


Figure 6 – Stress-strain curves for A182 registered RND-M-D-1054.

4.1.2. EDF weld Alloy 82 registered RND-M-D-711 (SR)

Alloy 82 registered RND-M-D-711 ⁽³⁾ has been welded by AREVA with an ERNiCr3 wire on Alloy 600 (warm rolled plates). The welding conditions were the following: ERNiCr3 wire, $\varnothing 1.2$ mm, TIG warm wire, 420 A, 13 V, prior heating at 200°C, maximal temperature between passes of 180°C, maximal temperature of welding of 225°C, welding rate of 15 cm.h⁻¹. The weld is composed of layers with 3 to 4 passes. The weld has been stress-relieved: heat treatment of 16h30 at 610-620°C. The weld was fully characterized by EDF. The chemical composition is in agreement with the RCC-M requirements. However, the Cr content is relatively low (18.5%), as well as the C content (0.015%), while the (Nb+Ta) content is relatively high (2.53%). It can be noticed that AREVA reported a lower (Nb+Ta): 2.015%Nb and 0.003%Ta. Stress-strain curves at room temperature and at 350°C are shown in Figure 9. The fracture toughness measured by AREVA was KCU = 19.1 daJ.cm⁻².

⁽³⁾ AREVA NP registration number: PD/ZZ665.

| | | |
|------------|---|--|
| MAI | Quantitative evaluation of the EDF local model and the EPRI-NRC xLPR models of crack initiation of the weld metals of Alloy 600 (Alloys 82 and 182) | 6125-4501-2018-00583-EN Version 2.0 |
|------------|---|--|

Table 3 – Tensile properties of weld registered RND-M-D-711 [7, 8].

| EDF registration | 20 °C | | | | 350 °C | | | |
|------------------|-------------------------|-----------|-------|---------|-------------------------|-----------|-------|---------|
| | YS _{0.2} (MPa) | UTS (MPa) | El. % | E (GPa) | YS _{0.2} (MPa) | UTS (MPa) | El. % | E (GPa) |
| RND-M-D-711 | 405 | 653 | 43 | 176 | 338 | 559 | 43.8 | 154 |
| RCC-M (82) | No requirement | | | | | | | |

Table 4 – Chemical composition (%wt.) of weld registered RND-M-D-711 [7, 8].

| EDF registration | C | S | P | Si | Mn | Ni | Cr | Mo | N | Co | Cu | Ti | Nb | Ta | Al | Fe | O |
|------------------|--------|------------|-----------|-------|---------------|------|-------------|-------|-------|-------|-------|--------|--------|----|------|------|---|
| RND-M-D-711 | 0.015 | 0.002 5 | 0.002 | 0.07 | 3.01 | Bal. | 18.5 | <0.01 | 0.014 | <0.01 | <0.01 | 0.38 | 2.53 | | 0.06 | 0.12 | - |
| RCC-M (82) | ≤ 0.10 | ≤ 0.015 | ≤ 0.03 | ≤ 0.5 | 2.5 to 3.5 | > 67 | 18 to 22 | - | - | ≤ 0.1 | ≤ 0.5 | ≤ 0.75 | 2 to 3 | | - | ≤ 3 | - |

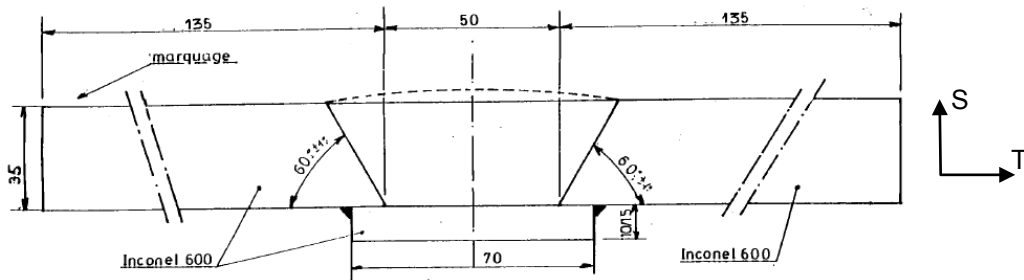


Figure 7 – Dimensions of the material registered as RND-M-D-711.



Figure 8 – Microstructure of Alloy 82 registered as RND-M-D-711.

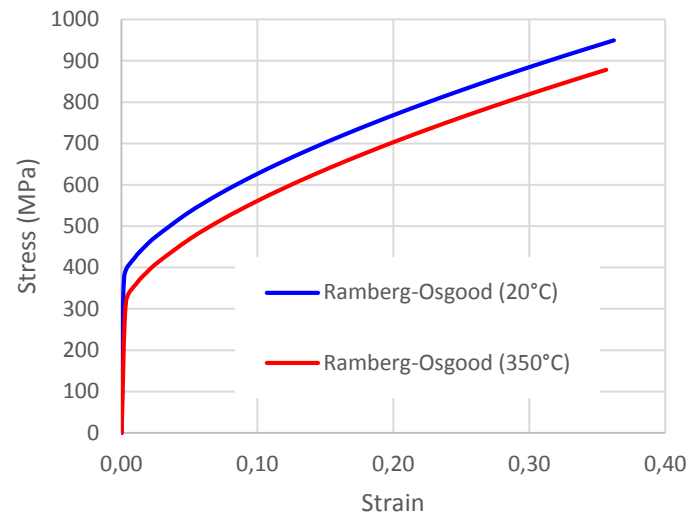


Figure 9 – Stress-strain curves at 20°C and 350°C of Alloy 82 registered as RND-M-D-711.

| | | |
|-----|---|--|
| MAI | Quantitative evaluation of the EDF local model and the EPRI-NRC xLPR models of crack initiation of the weld metals of Alloy 600 (Alloys 82 and 182) | 6125-4501-2018-00583-EN Version 2.0 |
|-----|---|--|

4.1.3. PNNL weld Alloy 182 registered Studsvik 8001231

Two pieces of A182 manufactured by ENSA for Studsvik were provided by EPRI to EDF (Figure 10). One piece was in as welded condition. The other one was 15% cold forged (CF) at PNNL. The weld is registered as 8001231 at Studsvik and RND-M-D-1691 at EDF. The chemical composition of the weld is given in Table 5.

SEM imaging performed by PNNL showed fairly linear distributions of Nb precipitates in the grain interiors, many of which were cracked by the cold forging process. Localized compositional fluctuations were observed primarily around weld pass boundaries. A TL cross section was examined at EDF (Figure 11 and Figure 12) to evaluate the grain boundary coverage with chromium carbides. A very inhomogeneous precipitation was noticed. Some grain boundaries have no carbides (GBC \approx 0), as shown in Figure 13. By contrast, some grain boundaries are fully covered with carbides (GBC \approx 1) as shown in Figure 14. Based on preliminary SEM observations with back scatter electrons their average size was estimated to 100 nm. In Code_Coriolis computations, waiting for a more accurate GBC evaluation, it was assumed that GBC = 0.2.

The mechanical properties are given in Table 6 and the stress-strain curve is shown in Figure 15. The yield strengths at room temperature of the as-welded (AW) and 15% CF materials are 390 MPa and 550 MPa, respectively.

Table 5 – Chemical composition (%wt.) of weld registered RND-M-D-1691 [18].

| EDF registration | C | S | P | Si | Mn | Ni | Cr | Co | Cu | Ti | Nb | Ta | Fe |
|------------------|-------------|--------------|-------------|------------------------|---------------|--------|-------------|------------|------------|----------|---------|----|------------|
| RND-M-D-1691 | 0.043 | 0.003 | 0.010 | 0.26 | 7.1 | 70.3 | 13.9 | - | 0.04 | 0.01 | 1.47 | | 6.6 |
| RCC-M (182) | ≤ 0.10 | ≤ 0.015 | ≤ 0.03 | ≤ 1 0.6 max | 5.0 to 9.5 | > 59 | 13 to 17 | ≤ 0.1 | ≤ 0.5 | ≤ 1 | > 1.8 | | 6 to 10 |

Table 6 – Tensile properties of weld registered RND-M-D-1691 [17].

| EDF registration | 20°C | | | | | 360°C | | | |
|---------------------|-------------------------|------------|-----------|---------|---------|-------------------------|-----------|-------|---------|
| | YS _{0.2} (MPa) | UTS (Mpa) | El. % | E (GPa) | HV | YS _{0.2} (Mpa) | UTS (Mpa) | El. % | E (Gpa) |
| AW RND-M-D-1691 | - | - | - | - | - | 390 | - | - | - |
| 15% CF RND-M-D-1691 | - | - | - | - | 240-345 | 550 | 860 | 26 | 78 |
| RCC-M (182) | ≥ 250 | ≥ 550 | ≥ 30 | - | | > 190 | - | - | - |

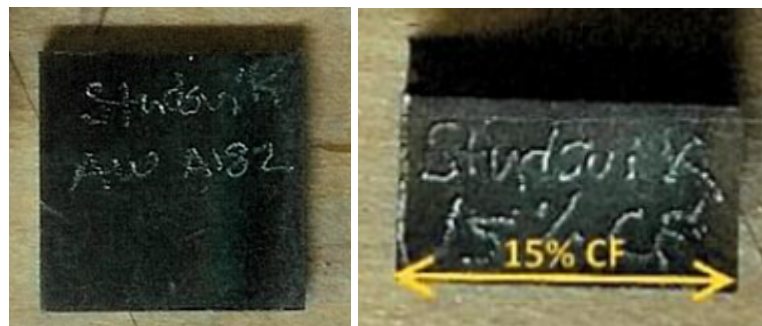


Figure 10 – Pieces of Studsvik 8001231 weld provided by EPRI.

| | | |
|------------|---|--|
| MAI | Quantitative evaluation of the EDF local model and the EPRI-NRC xLPR models of crack initiation of the weld metals of Alloy 600 (Alloys 82 and 182) | 6125-4501-2018-00583-EN Version 2.0 |
|------------|---|--|



Figure 11 – Cross section of the Studsvik 8001231 weld provided by EPRI.

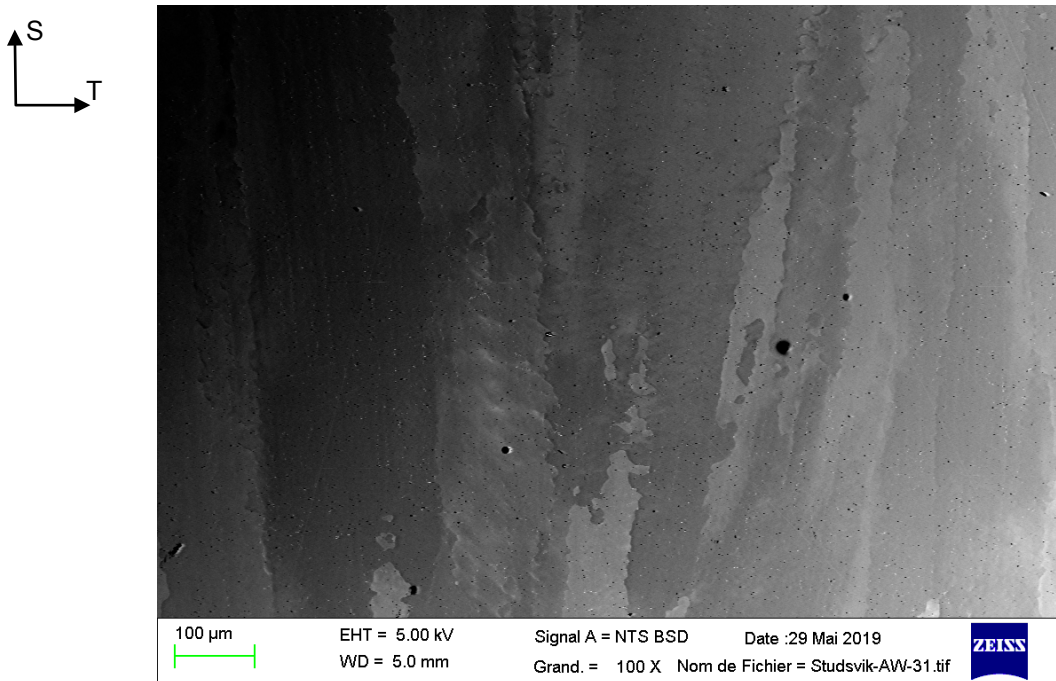


Figure 12 – Microstructure of Alloy 182 registered as RND-M-D-1691 (Studsvik 8001231).

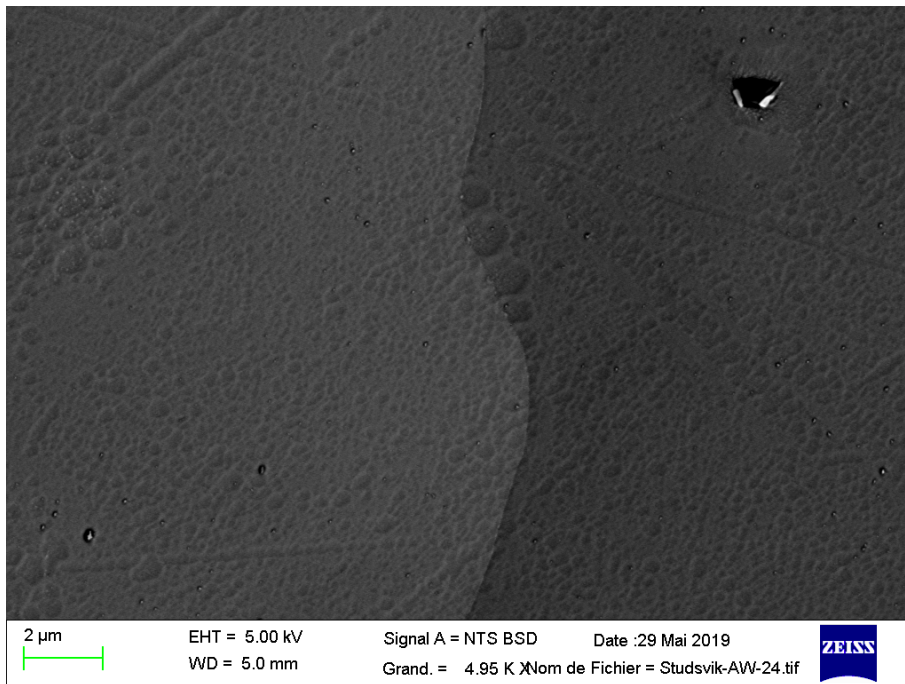


Figure 13 – Absence of intergranular precipitation in Alloy 182 registered as RND-M-D-1691 (Studsvik 8001231). GBC ≈ 0.

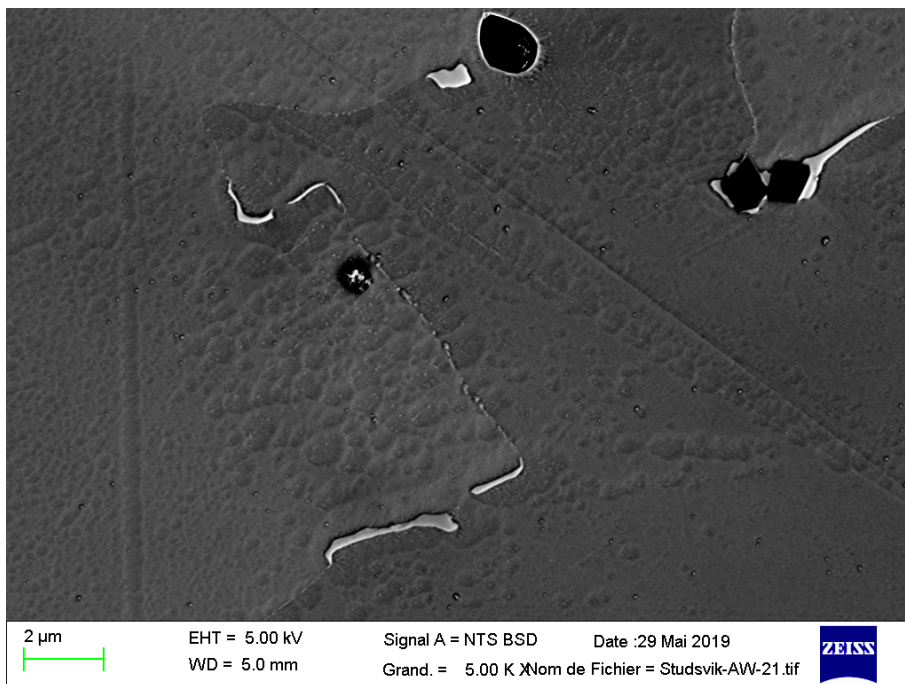


Figure 14 – Intergranular precipitation in Alloy 182 registered as RND-M-D-1691 (Studsvik 8001231). GBC ≈ 1.

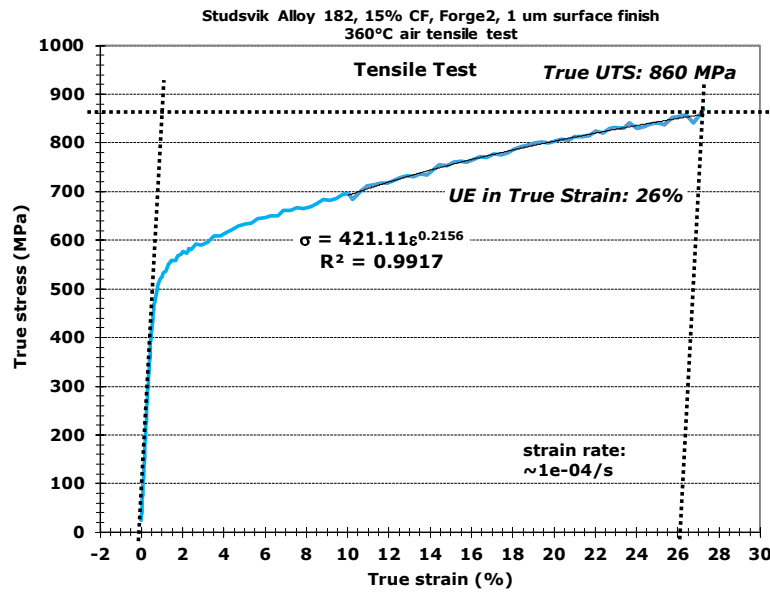


Figure 15 – Stress-strain curve at 360°C of 15% cold forged Alloy 182 registered as RND-M-D-1691 (Studsvik 8001231) [18].

| | | |
|-----|---|--|
| MAI | Quantitative evaluation of the EDF local model and the EPRI-NRC xLPR models of crack initiation of the weld metals of Alloy 600 (Alloys 82 and 182) | 6125-4501-2018-00583-EN Version 2.0 |
|-----|---|--|

4.1.4. PNNL weld Alloy 182 registered KAPL 823030

Two pieces of A182, manufactured by KAPL as a U-groove mockup in an A600 plate, were provided by EPRI to EDF (Figure 16). One piece was in as welded condition. The other one was 15% cold forged at PNNL. The weld is registered as 823030 at KAPL and RND-M-D-1690 at EDF. The chemical composition of the weld is given in Table 7.

PNNL SEM imaging showed fairly linear distributions of Nb precipitates in the grain interiors. A TL cross section was examined at EDF (Figure 17 and Figure 18) to evaluate the grain boundary coverage with chromium carbides. A poor precipitation was globally noticed. Some grain boundaries have no carbides (GBC ≈ 0), as shown in Figure 19, but some small carbides are present on other grain boundaries (GBC ≈ 0.05) as shown in Figure 20. Based on preliminary SEM observations with back scatter electrons their size was estimated lower than 100 nm. In a first approach, waiting for more accurate quantifications, the GBC was assigned to 0.05 in Code_Coriolis simulations.

The mechanical properties are given in Table 8 and the stress-strain curve is shown in Figure 21. The yield strengths of the AW and 15% CF materials are 405 MPa and 585 MPa, respectively.

Table 7 – Chemical composition (%wt.) of weld registered RND-M-D-1690 [18].

| EDF registration | C | S | P | Si | Mn | Ni | Cr | Co | Cu | Ti | Nb | Ta | Fe |
|------------------|-------------|--------------|-------------|----------|------------|--------|----------|------------|------------|----------|---------|----|---------|
| RND-M-D-1690 | 0.045 | 0.005 | 0.010 | 0.3 | 6.1 | 67.2 | 14.8 | - | 0.02 | 0.02 | 1.47 | | 9.9 |
| RCC-M (182) | ≤ 0.10 | ≤ 0.015 | ≤ 0.03 | ≤ 1 | 5.0 to 9.5 | > 59 | 13 to 17 | ≤ 0.1 | ≤ 0.5 | ≤ 1 | > 1.8 | | 6 to 10 |

Table 8 – Tensile properties of weld registered RND-M-D-1690 [17].

| EDF registration | 20°C | | | | | 360°C | | | |
|---------------------|-------------------------|------------|-----------|---------|---------|-------------------------|-----------|-------|---------|
| | YS _{0.2} (MPa) | UTS (MPa) | El. % | E (GPa) | HV | YS _{0.2} (MPa) | UTS (MPa) | El. % | E (GPa) |
| RND-M-D-1690 | - | - | - | - | - | 395-420 | - | - | - |
| 15% CF RND-M-D-1690 | - | - | - | - | 250-350 | 580-590 | 890 | 18 | 106 |
| RCC-M (182) | ≥ 250 | ≥ 550 | ≥ 30 | - | - | > 190 | - | - | - |

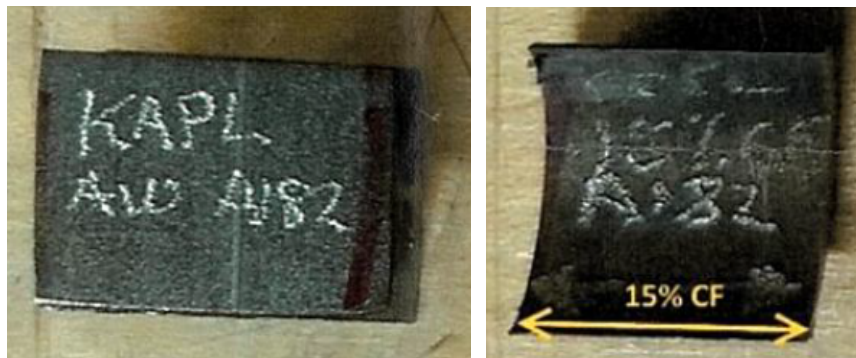


Figure 16 – Pieces of KAPL weld provided by EPRI.

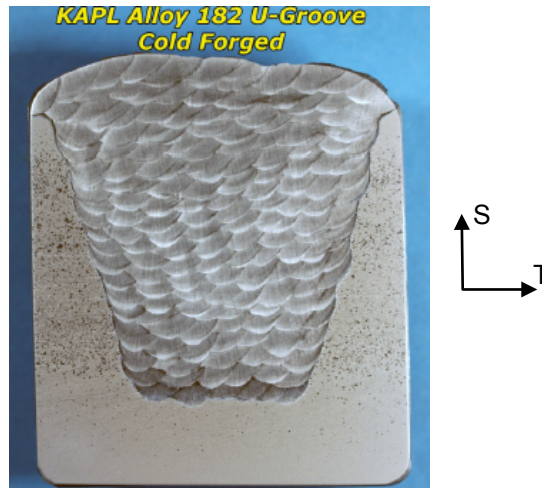


Figure 17 – Cross section of the KAPL weld provided by EPRI.

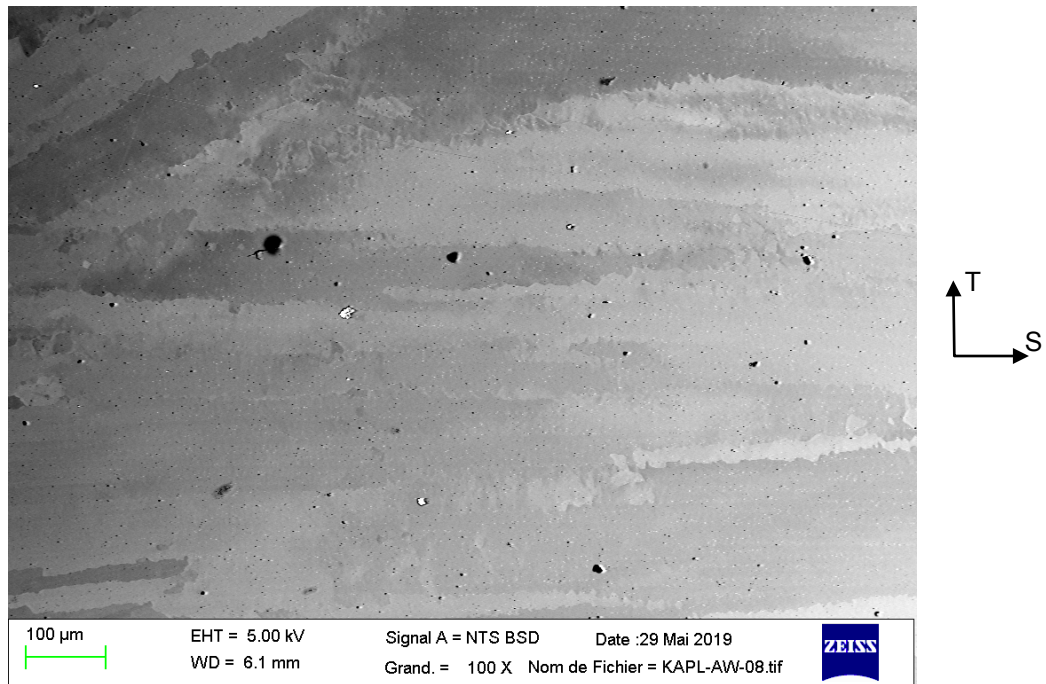
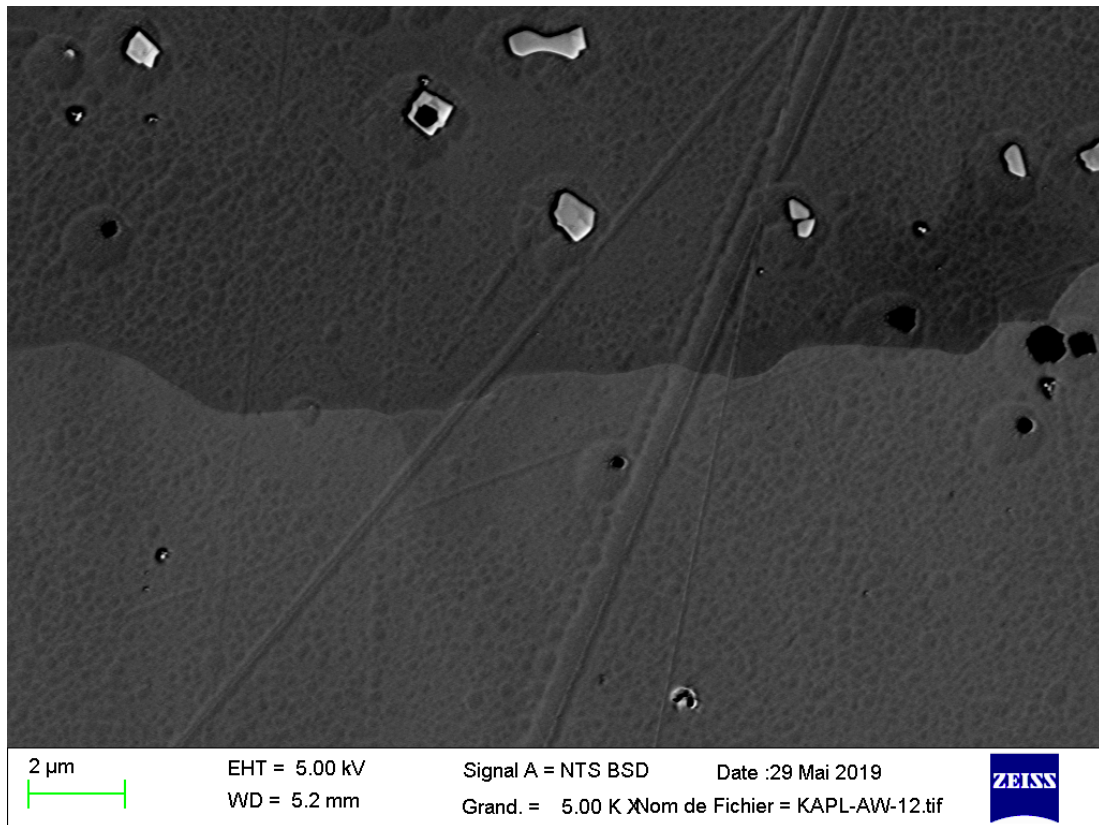
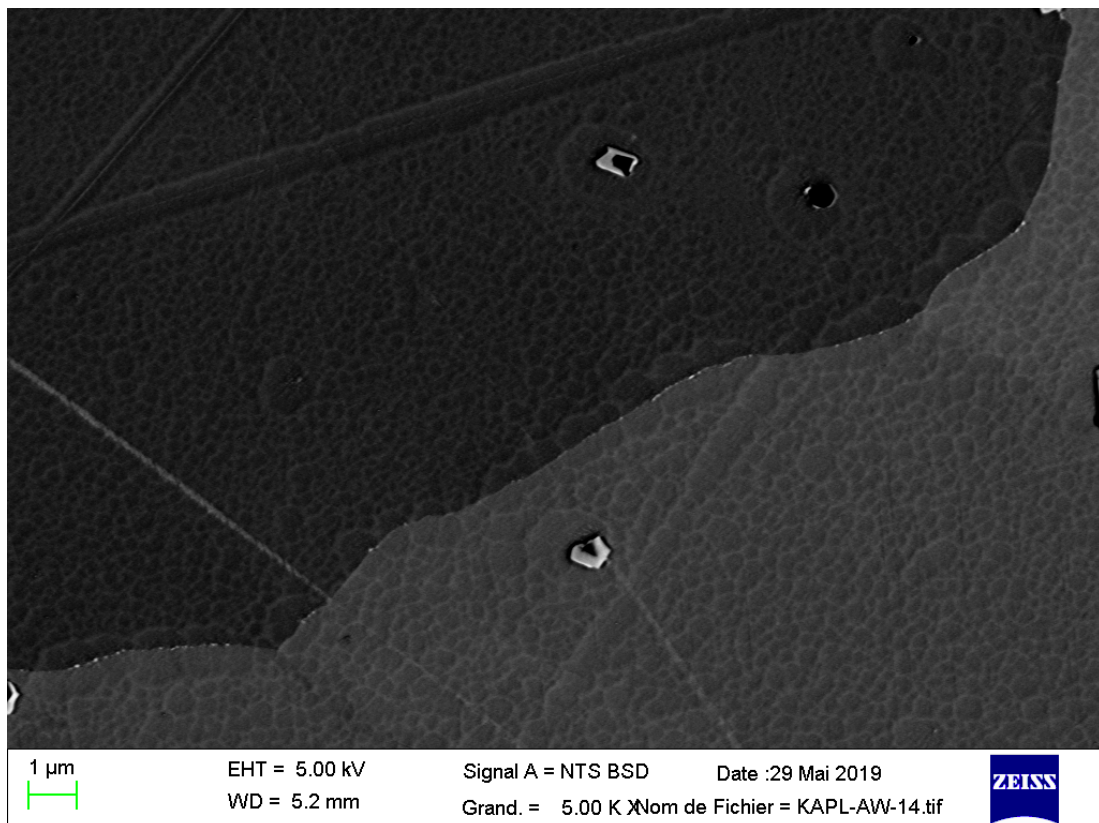


Figure 18 – Microstructure of Alloy 182 registered as RND-M-D-1690.

Figure 19 – Absence of intergranular precipitation in Alloy 182 registered as RND-M-D-1690. GBC \approx 0.Figure 20 – Intergranular precipitation in Alloy 182 registered as RND-M-D-1690. GBC \approx 0.05.

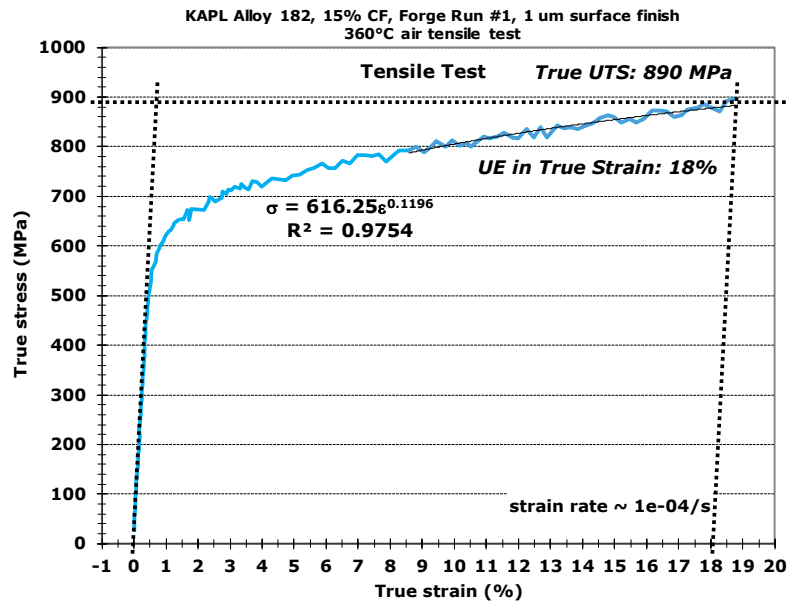


Figure 21 – Stress-strain curve at 360°C of 15% cold forged Alloy 182 registered as RND-M-D-1690 [18].

| | | |
|-----|---|--|
| MAI | Quantitative evaluation of the EDF local model and the EPRI-NRC xLPR models of crack initiation of the weld metals of Alloy 600 (Alloys 82 and 182) | 6125-4501-2018-00583-EN Version 2.0 |
|-----|---|--|

4.2. SCC initiation tests

Only constant load tests on tensile specimens were considered, to guarantee a good control on applied stress. The tests described below were dedicated to initiation. Nevertheless, they can involve limited or large crack extension. It was useful for the evaluation of the simulation chaining initiation with crack growth.

4.2.1. Constant load tests on Alloy 182 registered RND-M-D-1054

TL2-type axial tensile specimens ($\varnothing 4$ mm, gauge length of 85.6 mm) were cut along the longitudinal (L) orientation of the weld (Figure 22). PWSCC tests were conducted between 325°C and 360°C. Specimens were ultrasonically rinsed in ethanol and then in distilled water before testing. Tests were carried out in static Hastelloy (C-276) autoclaves. The specimens were insulated from the autoclave by oxidized Zircaloy to avoid galvanic coupling. Experiments were conducted under open circuit conditions. The environment was primary water (1000 ppm B as boric acid, 2 ppm Li as lithium hydroxide) at 360°C. The solution was previously de-aerated by evaporating 20% of the initial volume at 125°C, then hydrogen overpressure was introduced (30 ml.kg^{-1}) and controlled using a Pd-Ag probe. Dissolved hydrogen and temperature were recorded during testing. The chemistry was analyzed and validated before each test (B, Li, Cl^- , SO_4^{2-} , F^-). Pre-oxidation (5-7 days) in a primary water test environment was performed. The constant loads were adjusted with dead weights (no active loading, one specimen per load line, one load line per autoclave). Since the force was imposed (not the displacement), no relaxation occurred during testing. No DCPD monitoring was performed.

After completion of a test, the specimen was sectioned longitudinally for optical observation on cross section and maximum crack depth evaluation (Figure 23, Figure 24). In addition, the fracture surfaces of broken specimens were inspected by scanning electron microscopy (SEM). The maximum crack depth was measured on fracture surfaces when specimens were broken and on cross-sections when tests were arbitrary stopped. Examinations on cross-sections were performed all along the gauge length.

Results are reported in Table 9. Thirteen constant load tests were completed. Only one specimen failed (#1588-16). No defects and no IGSCC initiation were observed for 3 specimens. Shallow intergranular defects (depth lower than 150 μm) were noticed on 6 specimens. IGSCC deeper than 150 μm was observed in 4 cases, including specimens 1383-11 and 1383-CEA tested at 350 MPa, very close to yield stress (347 MPa). As shown in Figure 25, results (restricted to cracks deeper than 100 μm) are globally in good agreement with the activation energy of 185 kJ.mol^{-1} .

Finally, an overview of testing conditions covered by the database on this weld is shown in Figure 26 and Figure 27, where applied stress / yield stress ratio is plotted versus temperature and testing time. A wide range of stress ratio is covered, from 1 to 2, even if most of tests were done within the range 1 – 1.5. Wide ranges of temperatures (330-360°C) and testing times (120-23771 hours) are also covered. Such a spread of testing conditions is particularly convenient for modeling.

Table 9 – Results of constant load tests on AW weld registered RND-M-D-1054 [7].

| Specimens | T (°C) | σ at T (MPa) | σ / Y_s | Durations (h) | Max. IG crack depth (μm) |
|-----------|--------|---------------------|----------------|---------------|---------------------------------------|
| 1383-20 | 360 | 392 | 1.13 | 722 | 0 |
| 1383-23 | 360 | 400 | 1.15 | 8626 | 0 |
| 1383-22 | 330 | 400 | 1.15 | 13456 | 0 |
| 1383-26 | 325 | 521 | 1.51 | 214 | 5 |
| 1383-27 | 360 | 453 | 1.31 | 190 | 12 |
| 1383-19 | 330 | 450 | 1.30 | 5335 | 40 |
| 1383-16 | 360 | 380 | 1.10 | 12933 | 40 |
| 1383-29 | 360 | 448 | 1.29 | 5200 | 50 |
| 1588-16 | 360 | 700 | 2.02 | 120 | 1200 |
| 1383-21 | 330 | 660 | 1.90 | 737 | 1129 |
| 1383-28 | 360 | 590 | 1.30 | 1000 | 120 |
| 1383-11 | 360 | 350 | 1.01 | 13365 | 1060 |
| 1383-CEA | 350 | 350 | 1.01 | 23771 | 1060 |

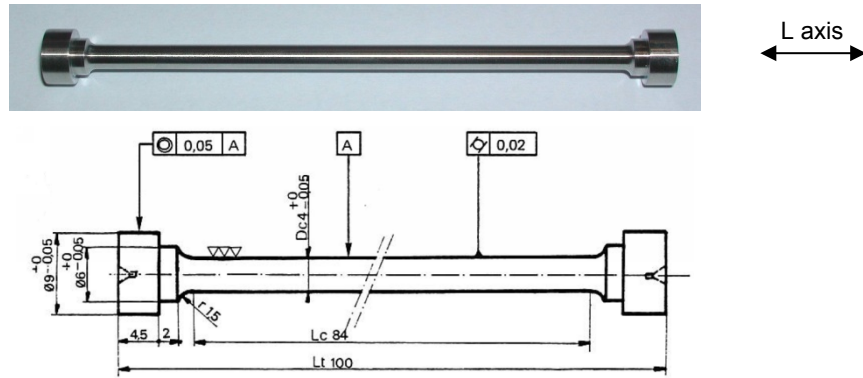


Figure 22 – TL2-type specimen.

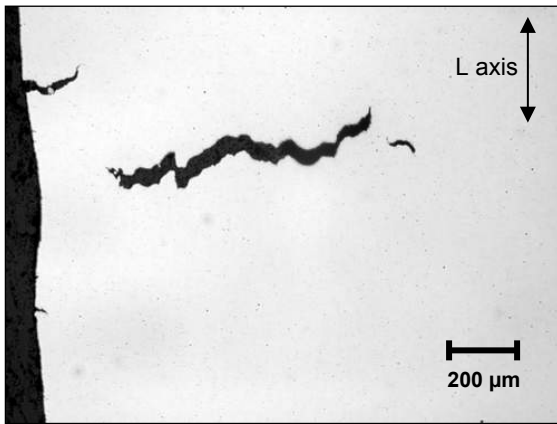


Figure 23 – SCC observed after 13365 h at 360°C, under 350 MPa. Weld registered RND-M-D-1054, specimen 1383-11 [7].

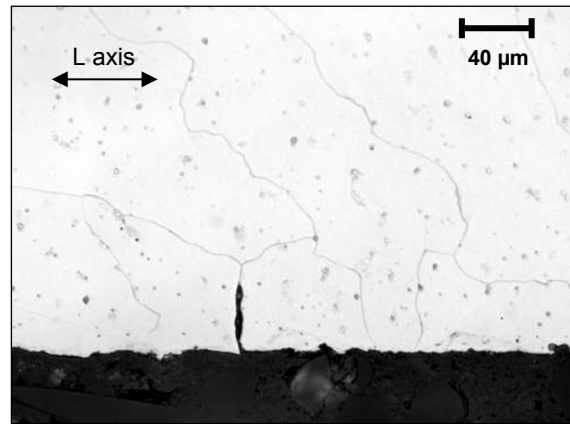


Figure 24 – SCC observed after 12300 h at 360°C, under 380 MPa. Weld registered RND-M-D-1054, specimen 1383-16 [7].

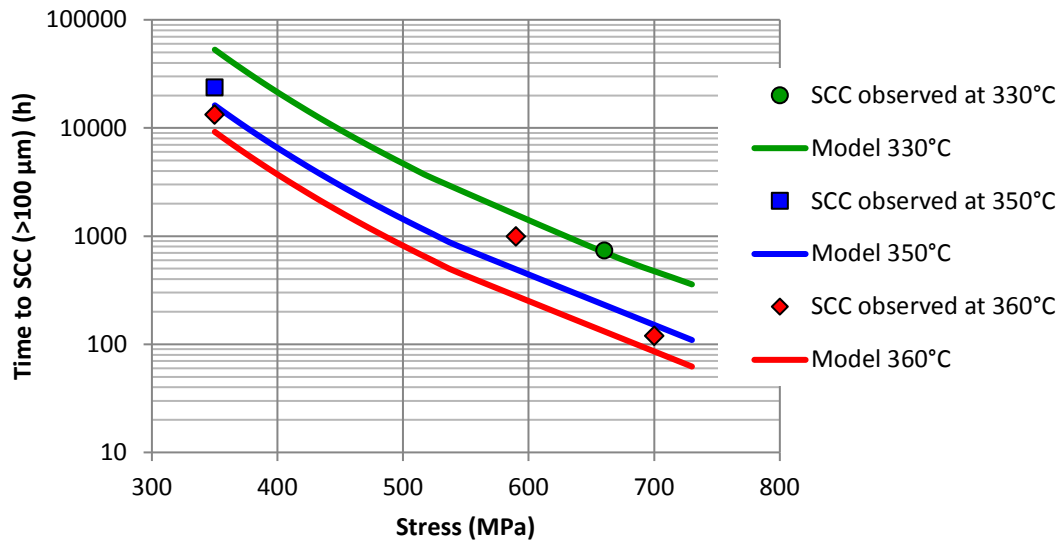


Figure 25 – Index model predictions at 330, 350 and 360°C versus experimental results restricted to SCC depth deeper than 100 µm. Weld registered RND-M-D-1054.

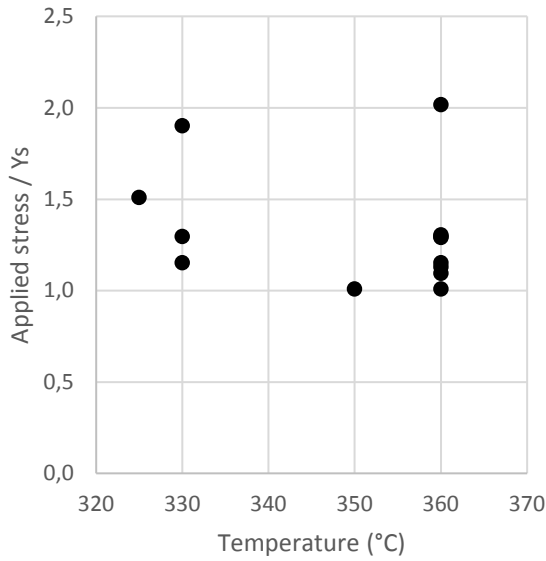


Figure 26 – Testing matrix overview: applied stress/yield stress versus temperature.

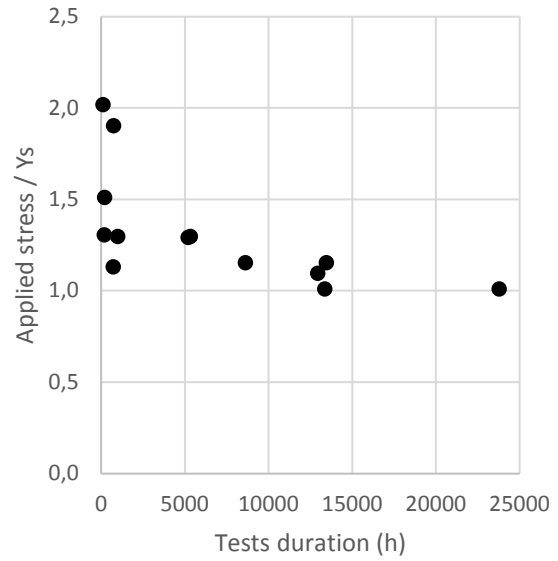


Figure 27 – Testing matrix overview: applied stress/yield stress versus testing time.

4.2.2. Constant load tests on Alloy 82 registered RND-M-D-711

The following tests were conducted on TRC-type specimens (gauge length of 25 mm) cut along the transverse (T) direction (Figure 28).

A constant load test has been done at 325°C on as-welded Alloy 82 referred RND-M-D-711 on the TRC-type specimen registered D711-BS4. After 1677 h under 545 MPa, no initiation of SCC was observed on cross sections.

Four constant load tests were carried out on specimens on the same load line. Specimens had been cut in stress relieved weld RND-M-D-711, along T axis, with four different diameters. 27570 h have been cumulated (3 successive tests) in hydrogenated (30 ml.kg⁻¹ H₂O) primary water at 360°C (Table 10). Alloy 82 tested in this study exhibited a great resistance to SCC at 360°C, up to 406 MPa: no initiation site observed (scanning electron microscopy) at the surface and on cross sections (optical microscopy).

Table 10 – Constant load tests in hydrogenated (30 ml.kg⁻¹ water) primary water performed on Alloy 82 registered as RND-M-D-711.

| Specimen | Diameter (mm) | Temperature (°C) | Stress at temperature (MPa) | σ / Y_s | Duration (h) | Max. SCC depth (µm) |
|----------|---------------|------------------|-----------------------------|----------------|--------------|---------------------|
| 1383-01T | 4.02 | 360 | 406 | 1.20 | 27570 | 0 |
| 1383-02T | 4.56 | 360 | 316 | 0.94 | 27570 | 0 |
| 1383-03T | 4.44 | 360 | 333 | 0.99 | 27570 | 0 |
| 1383-04T | 4.18 | 360 | 376 | 1.11 | 27570 | 0 |
| D711-BS4 | 4.00 | 325 | 545 | 1.61 | 1677 | 0 |

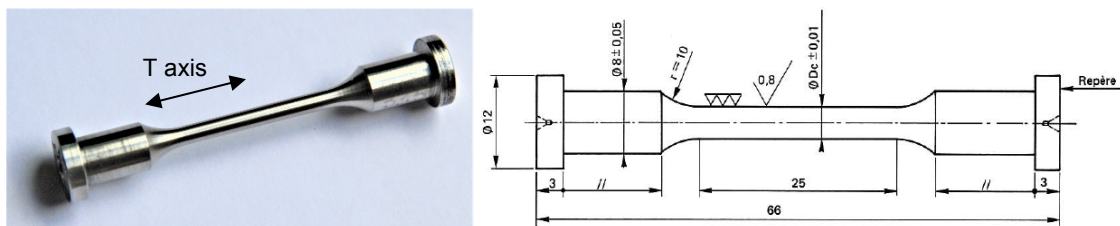


Figure 28 – TRC-type specimen (dimensions in mm).

4.2.3. PNNL constant load tests on 15% cold forged Alloy 182 registered KAPL 823030 and 15% cold forged Alloy 182 registered Studsvik 8001231

Axial tensile specimens tested by PNNL ($\varnothing 2.75$ -4.5 mm, gauge length of 4.0 mm) were cut along the width of the weld (T axis), which was aligned with the forging direction (Figure 29 and Figure 30) [17]. Gauge diameter was determined specifically for each material, depending on material strength. Specimens were polished to either a colloidal silica or 1 μm finish. The test environment was primary water (1000 ppm B as boric acid, 2 ppm Li as lithium hydroxide) with 25 ml.kg^{-1} H_2 at 360°C. Temperature, conductivity, pressure, servo load, and servo position were all measured and recorded every 60 s throughout the tests. The constant load was adjusted using a servo. Specimens were actively monitored using a direct current potential drop (DCPD) system for the onset of initiation, as defined when the slope of the strain-time curve significantly changes. With this approach, initiation is defined as the time to reach the slow to fast crack growth transition.

Tests were stopped upon initiation detection, and specimens were removed. SEM montage imaging was then performed to document the full gauge surface area and identify primary and secondary cracks. Test results for the 15% cold forged (CF) weld KAPL 823030 are summarized in Table 11. Similarly, test results for the 15% CF weld Studsvik 8001231 are summarized in Table 12.

Table 11 – Constant load tests in hydrogenated (30 ml.kg^{-1} water) primary water performed on 15% CF Alloy 182 registered as KAPL 823030 (RND-M-D-1690).

| Specimen | Temperature (°C) | Stress (MPa) | Duration (h) | Max. SCC depth (μm) |
|----------|------------------|--------------|--------------|----------------------------------|
| IN166 | 360 | 563 | 30 | > 150 (DCPD) |
| IN167 | 360 | 552 | 30 | > 150 (DCPD) |
| IN168 | 360 | 547 | 113 | > 150 (DCPD) |
| IN194 | 360 | 581 | 1635 | > 150 (DCPD) |
| IN195 | 360 | 575 | 1625 | > 150 (DCPD) |
| IN196 | 360 | 567 | 1642 | > 150 (DCPD) |

Table 12 – Constant load tests in hydrogenated (30 ml.kg^{-1} water) primary water performed on 15% CF Alloy 182 registered as Studsvik 8001231 (RND-M-D-1691).

| Specimen | Temperature (°C) | Stress (MPa) | Duration (h) | Max. SCC depth (μm) |
|----------|------------------|--------------|--------------|----------------------------------|
| IN169 | 360 | 541 | >5126 | Unknown (no DCPD detection) |
| IN170 | 360 | 536 | 30 | > 150 (DCPD) |
| IN171 | 360 | 534 | 2957 | > 150 (DCPD) |
| IN191 | 360 | 553 | 83 | > 150 (DCPD) |
| IN192 | 360 | 559 | 41 | > 150 (DCPD) |
| IN193 | 360 | 555 | 41 | > 150 (DCPD) |
| IN233 | 360 | 532 | 30 | > 150 (DCPD) |
| IN234 | 360 | 529 | 725 | > 150 (DCPD) |
| IN235 | 360 | 532 | 910 | > 150 (DCPD) |



Figure 29 – PNNL-type specimen.

| | | |
|-----|---|--|
| MAI | Quantitative evaluation of the EDF local model and the EPRI-NRC xLPR models of crack initiation of the weld metals of Alloy 600 (Alloys 82 and 182) | 6125-4501-2018-00583-EN Version 2.0 |
|-----|---|--|

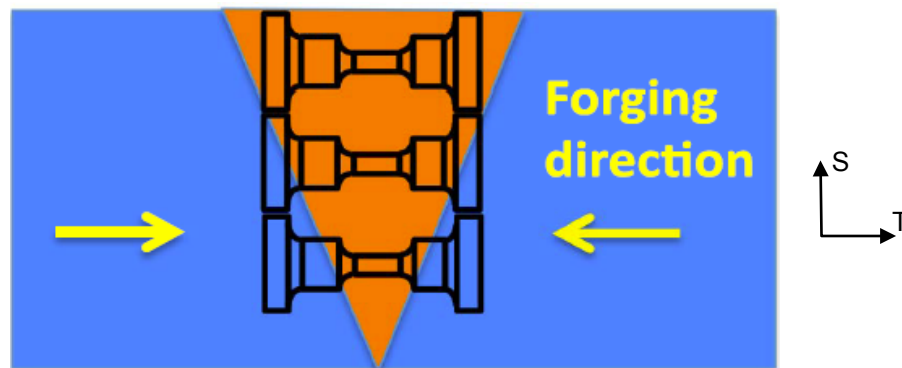


Figure 30 – Schematic showing forging and tensile specimen orientations.

4.3. Comparison of EDF and PNNL Materials and SCC Tests

The SCC data obtained by both EDF and PNNL are used for comparison against the models in the remainder of this report. There are notable differences in the two datasets that may affect these comparisons and may consequently produce different results. The key features of the materials, specimens, and testing details are summarized in Table 13 for the four welds previously described in this section. There are 5 main factors that likely contribute to any major differences in results:

1. **Thermo-mechanical Processing.** The materials tested at the two laboratories represent three different thermo-mechanical processing conditions: as-welded (EDF weld RND-M-D-1054), stress relieved (EDF weld RND-M-D-711), and 15% cold forged (PNNL welds Studsvik 8001231 and KAPL 823030). Additional testing at PNNL has shown a positive correlation between the extent of cold working and PWSCC initiation susceptibility (i.e., shorter initiation times), as well as greater variability in initiation times. Cold working increases the yield strength of the material, and it also induces strains that may be detrimental beyond the simple yield strength increase. Conversely, stress relief heat treatments are understood to be at least somewhat beneficial for reducing crack growth rates, and it is reasonable to predict that they would be beneficial for extending initiation times as well.
2. **Specimen Geometry.** While EDF and PNNL both used tensile specimens, the EDF gauge diameters were at the upper end of the range used by PNNL. Additionally, the gauge lengths were different by a factor of ~20. While the effect of specimen size is not well understood, it may have an effect on PWSCC behavior. Additionally, the specimens obtained from EDF weld RND-M-D-1054 were aligned along the L orientation and the PNNL specimens were aligned along the T orientation. The axes of all specimens were normal to the dendrite growth direction, but there may be other orientation effects at play.
3. **Environmental Conditions.** The EDF tests were run with 30 ml.kg⁻¹ dissolved hydrogen, which is in the nickel metal stable regime at all temperatures tested (from 330°C to 360°C). The PNNL tests were run at 25 ml.kg⁻¹ dissolved hydrogen at 360°C, which is at the Ni/NiO transition and corresponds to the region of greatest PWSCC susceptibility in these materials^[19].
4. **Loading Conditions.** The EDF test system employs passive loading through a dead weight, and specimens were loaded to 93-200% of their at-temperature yield strength. The PNNL test system, on the other hand, utilizes active loading through a servo-electric motor, and all specimens were loaded to 100% of their at-temperature yield strength.
5. **Initiation Detection Method.** At EDF, the tests on A82 were interrupted at predetermined intervals to check for initiation. Tests on A182 were performed in a single sequence and stopped for examinations on cross-sections to determine the maximal crack depth. Therefore, the test interruption time was a mix of initiation time and additional time for crack growth, for specimens in which cracking initiated. PNNL used online DCPD detection, from which the initiation time could be precisely estimated in real time, even if the test was continued to allow additional time for crack growth. In such a situation, there is no possibility to validate the accuracy of the estimation. Final crack depths are not observed.

| | | |
|------------|---|--|
| MAI | Quantitative evaluation of the EDF local model and the EPRI-NRC xLPR models of crack initiation of the weld metals of Alloy 600 (Alloys 82 and 182) | 6125-4501-2018-00583-EN Version 2.0 |
|------------|---|--|

Table 13 – Comparison of EDF and PNNL Specimens and Testing Conditions

| | EDF A182: RND-M-D-1054 | EDF A82: RND-M-D-711 | PNNL A182: Studsvik 8001231 RND-M-D-1691 | PNNL A182: KAPL 823030 RND-M-D-1690 |
|--|---|--|---|--|
| Weld Details | V-groove with A600 15 layers, 7 passes As-welded | V-groove with A600 3-4 passes Stress relieved at 610- 620°C for 16.5 h | Buildup ~23 layers 15% cold forged | U-groove with A600 ~19 layers 15% cold forged |
| Material / Microstructure | Alloy 182 (15% Cr) 7 wt% Cr at GB GBC = 0.2 | Alloy 82 (18.5% Cr) | Alloy 182 Sufficiently high strain to obscure GBs Cracked Nb precipitates | Alloy 182 GBC = 0-0.05 |
| Mechanical Properties at 350°C (EDF) / 360°C (PNNL) | YS: 347 MPa UTS: 568 MPa Elong: 46% E: 144 GPa | YS: 338 MPa UTS: 559 MPa Elong: 43.8% E: 154 GPa | YS: 550 MPa (390 MPa as-welded) Hardness: 240-345 HV | YS: 580-590 MPa (395-420 MPa as-welded) Hardness: 250-350 HV |
| Specimen Type | Tensile specimens L orientation (along weld length) 4 mm diam, 85.6 mm gauge length | Tensile specimens T orientation (along weld thickness) 4.00-4.56 mm diam, 25 mm gauge length | Tensile specimens T orientation (along weld thickness) 2.75-4.5 mm diam, 4 mm gauge length Colloidal silica or 1 µm surface finish | |
| Environment | 325-360°C 1000 ppm B, 2 ppm Li 30 cc/kg H ₂ | | 360°C 1000 ppm B, 2 ppm Li 25 cc/kg H ₂ | |
| Testing Methodology | 5-7 day preoxidation in primary water Passive loading (dead weight) 101-202% YS Test (single sequence) stopped on arbitrary decision 120-23,771 h | Passive loading (dead weight) 93-161% YS Test (in 3 successive sequences) interrupted on arbitrary decision 1,677-27,570 h | Active loading (servo-electric motor) 100% YS Online DCPD detection 30-5,126 h | |

5. SCC models

5.1. Crack initiation

5.1.1. Index model

The empirical index model predicts the time to initiation t_i on Alloy 182. The model depends on the intrinsic susceptibility to PWSCC of the weld (material index $init6$), the temperature of the primary water (temperature index i_T) and the macroscopic stress (stress index i_σ).

$$t_i = \frac{init5}{init6 \times i_\sigma \times i_T} \quad \text{Equation 1}$$

The temperature index i_T was defined as:

$$i_T = init3 \times \exp\left(\frac{-init4}{R \times T}\right) \quad \text{Equation 2}$$

where $R = 8.314 \text{ J.mol}^{-1}.\text{K}^{-1}$, T is the temperature in K and $init4$ is the activation energy in J . In agreement with [20] it was assumed that $init4 = 185 \text{ kJ.mol}^{-1}$. The stress index i_σ was expressed as given in Equation 3:

$$i_\sigma = init1 \times \sigma^{init2} \quad \text{Equation 3}$$

where σ is the applied stress for engineering SCC initiation, depending on the temperature, and $init2$ is a constant. Parameters calibrated for EDF welds registered RND-M-D-1054 and RND-M-D-711 are given in Table 14 [7]. For this calibration, initiation was assumed to be the time to reach a crack deeper than $100 \mu\text{m}$. As shown in Figure 25 and Figure 31, predictions relying on the calibrated parameters are conservative. However, it is important to notice that the material index proposed for Alloy 82 is an upper bound, since no initiation was observed after testing.

Indices of the model have been calibrated based on the available database: more than 92,000 h cumulated under constant load. The time-to-initiation stress dependency is in good agreement with results previously published [3, 6]. Under 350 MPa, at 290°C, the predicted time to initiation in the susceptible weld registered RND-M-D-1054 is of 730,000 h (83 years).

Table 14 – Calibrated parameters.

| Material | Registration | Init1 | init2 | Init3 | init4 (kJ.mol ⁻¹) | Init5 | init6 | Init_depth (mm) |
|----------|--------------|-------|-------|-------|-------------------------------|-------|------------------|-----------------|
| A182 | RND-M-D-1054 | 1 | 6.8 | 1 | 185 | 1 | 10 ⁻⁶ | 0.005 |
| A82 | RND-M-D-711 | 1 | 6.8 | 1 | 185 | 1 | 10 ⁻⁷ | 0.005 |

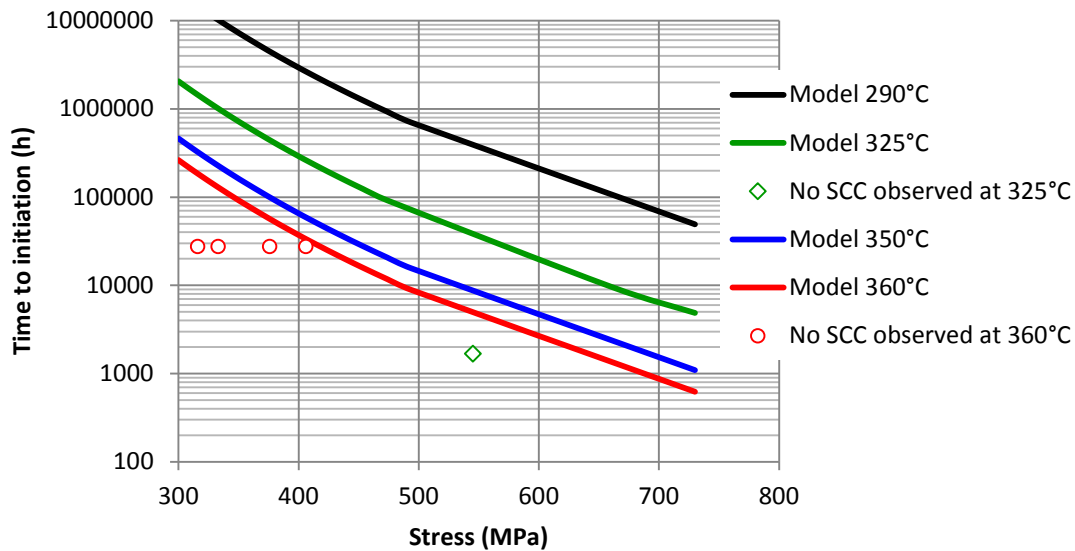


Figure 31 – Model prediction versus experiment on A82 weld registered RND-M-D-711.

5.1.2. Local model

5.1.2.1. Assumptions

The proposed model relies on a cracking scenario and local parameters. While no crack is present (incubation, initiation), ‘local’ refers to grain boundaries (GB), where the degradation happens. As soon as cracking occurred, ‘local’ refers to the intergranular crack tip. The modeled scenario is the following:

- **Incubation:** time to reach a critical oxidation depth. It is assumed that exposure to primary water allows oxidation of emerging GBs and that oxidation strongly decreases the stress necessary to fail them as soon as the critical oxidation depth is reached. Regarding nickel alloys 600 and 182, the intergranular oxidation rate mainly depends on temperature, grain boundary coverage with chromium carbides and dissolved hydrogen in primary water [21, 22, 23]. However, additional dependencies may be considered in the future, such as plastic strain, stress, hydrogen (in the metal).
- **Initiation:** probability to reach the critical stress to fail a sufficiently oxidized grain boundary.

5.1.2.2. Incubation

Incubation is assumed to be driven by the intergranular oxidation rate. The intergranular oxidation rate is supposed to be the combination of the oxidation rate of three phases:

- A ‘nom’ chromium-nominal phase (average level of the material, typically 16% in the following).
- A ‘carb’ chromium-rich phase (chromium carbides). This phase is usually quantified by the grain boundary coverage (GBC) with chromium carbides.
- A ‘depl’ chromium-depleted phase (due to chromium carbide precipitation [24]).

In a first approach, for each phase *nom*, *depl* and *carb*, the maximal oxidation depth p (in nm) is assumed to have a logarithmic dependency to the time t (in h) of exposure to primary water (Equation 4 to Equation 6).

$$p_{nom} = x_{nom} + b_{nom} \times \ln(1 + C_{nom} \times t) \times g(\Delta EcP) \times \exp\left(\frac{-oxQ}{R \times T}\right) \quad \text{Equation 4}$$

| | | |
|-----|---|--|
| MAI | Quantitative evaluation of the EDF local model and the EPRI-NRC xLPR models of crack initiation of the weld metals of Alloy 600 (Alloys 82 and 182) | 6125-4501-2018-00583-EN Version 2.0 |
|-----|---|--|

$$p_{carb} = x_{ocarb} + b_{carb} \times \ln(1 + C_{carb} \times t) \times g(\Delta EcP) \times \exp\left(\frac{-oxQ}{R \times T}\right) \quad \text{Equation 5}$$

$$p_{depl} = x_{odepl} + b_{depl} \times \ln(1 + C_{depl} \times t) \times g(\Delta EcP) \times \exp\left(\frac{-oxQ}{R \times T}\right) \quad \text{Equation 6}$$

In addition, p depends (Equation 7) on dissolved hydrogen DH content in primary water (in ml.kg⁻¹ water), via $f(\Delta EcP)$, with ΔEcP (in mV), the potential difference of the electrochemical potential of the alloy, EcP , and the potential of the Ni/NiO transition, $EcP_{Ni/NiO}$ (Equation 8) [25,26]. Last, p depends on temperature, via the activation energy oxQ (in J.mol⁻¹).

$$g(\Delta EcP) = oxg_1 + oxg_2 \times \exp(-oxg_3 \times \Delta EcP) \quad \text{Equation 7}$$

$$\text{with} \quad \Delta EcP = 1000 \times \frac{R \times T}{2 \times F} \times \ln\left(\frac{DH}{DH_{Ni/NiO}}\right) \quad \text{Equation 8}$$

where oxg_1 , oxg_2 and oxg_3 are constant. $F = 96500$ C.mol⁻¹, T is the temperature (in K), DH and $DH_{Ni/NiO}$ are respectively the hydrogen concentrations (in ml.kg⁻¹) during testing and at the Ni/NiO equilibrium (at a given T).

The oxidation rate of a GB is calculated as follows:

1. Random sampling of the 3 phases satisfying given GB properties: GBC, mean radius (rC) of chromium carbides, mean length (zCr) of chromium depletion associated to each chromium carbide.
2. Discretization (1 nm in the current paper) of the total GB length (1 mm).
3. Incremental calculation of the time to oxidize the discretized GB with the following rules:
 - a. The time to oxidize a GB portion composed of a given phase is estimated thanks to oxidation kinetics of the same phase.
 - b. When a new phase is reached by the oxidation front at a depth p (transition from phase i to phase j), the new oxidation rate is the oxidation rate of phase j for the depth p , assuming that formed oxides are similar whatever the phase where they grow. In other words, a transition in oxidation rate corresponds to the shift in time at the depth p of the new oxidation law to reach the time and depth of the transition.
 - c. A direct transition between kinetics is assumed as soon as the oxide front meets a new phase.

Figure 32 illustrates the simulated oxidation process (320°C, 30 ml.kg⁻¹): kinetics of oxidation following nominal Cr phase, Cr carbide phase and Cr depleted phase are given in blue, green and red on the left. The random grain boundary, including one Cr carbide and two associated depleted areas is shown on the right. The simulated oxidation rate along the grain boundary is the dark curve: it matches first with the oxide growth rate of the nominal Cr phase. Then, a short increase in oxidation rate is experienced when the oxidation reaches the chromium-depleted zone, until the oxide front reaches the Cr carbide. This last transition is followed by a large decrease in oxidation rate.

As shown in [20], at a given temperature (320°C-325°C), the maximum intergranular oxidation depth decreases when ΔEcP increases (when the dissolved hydrogen content increases from 3 ml.kg⁻¹ to 60 ml/kg). In other words, intergranular oxidation is enhanced when NiO stability increases. In addition, the increase in temperature, for a given ΔEcP , is accompanied by a significant increase in intergranular oxidation.

Assumed typical extension of the Cr-depletion (zCr) observed in the D1054 weld was of 30 nm, while the typical carbide length ($2 \times rC$) was of 60 nm. Based on these values, random representative boundaries were simulated to simulate 100 GBs of the D1054 weld (poor resistance to SCC).

Parameters of the oxidation law (Table 15) were calibrated on different A182 thanks to TEM and SEM/Tomography examinations [20]. Indeed, these observations provided the required input parameters

(grain boundary length, GBC, maximum oxidation depth, environmental conditions...). Figure 33 shows how intergranular oxidation rates in Alloy 182 change when temperature and DH change. Figure 34 compares observed intergranular oxidation depths with predicted ones. Current fitted parameters overestimate short oxidation depths (< 250 nm) and underestimate deep oxidation depths (780 nm). In a first approach, parameters fitted on A182 are used for A82.

Calculations were performed considering a sampling of 100 GBs, for two representative GBCs. As shown in Figure 35, at 320°C, for a dissolved hydrogen content (DH) of 30 ml.kg⁻¹, for a poor GBC (0.2), most of the GBs experience oxide penetrations deeper than 500 nm after 10⁵ h (≈11 years), and a lot of them already reached this oxide penetration after a few thousands of hours. By contrast, for a good GBC (0.5), only one GB experienced an oxide penetration of 500 nm after 20,000 h and oxide penetrations are mainly lower than 500 nm after 10⁵ h. When DH is increased to 50 ml.kg⁻¹, at 320°C, for GBC = 0.5, only few GBs have an oxidation depth of 500 nm after 10⁵ h. As a consequence, longer times to initiation are expected in such conditions. Decreasing the temperature down to 290°C, for GBC = 0.2 and DH = 30 ml.kg⁻¹, the maximum oxidation depth is strongly decreased (mainly lower than 300 nm after 10⁵ h), promoting the resistance to SCC initiation.

Assuming that oxidized GBs are submitted to an applied stress higher than the critical stress to failure, the probability to initiate SCC is expected to be higher in the material having a poor GBC than in the material having a good GBC, to be increased by an increase in temperature and a decrease in dissolved hydrogen (within the range 3-60 ml.kg⁻¹).

Table 15 – Parameters of the oxidation rate model for Alloys 182/82.

| x0nom (nm) | bnom | cnom | x0depl (nm) | bdepl | Cdepl | x0carb (nm) | bcarb | Ccarb | oxQ (J/mol) | oxg1 | oxg2 | oxg3 |
|------------|-----------------------|------|-------------|-----------------------|-------|-------------|-----------------------|-------|-------------|------|------|------|
| 0 | 5.38×10 ⁻⁸ | 3 | 0 | 4.17×10 ⁻⁸ | 3 | 0 | 3.85×10 ⁻⁸ | 0.01 | 57000 | 0.1 | 0.3 | 0.04 |

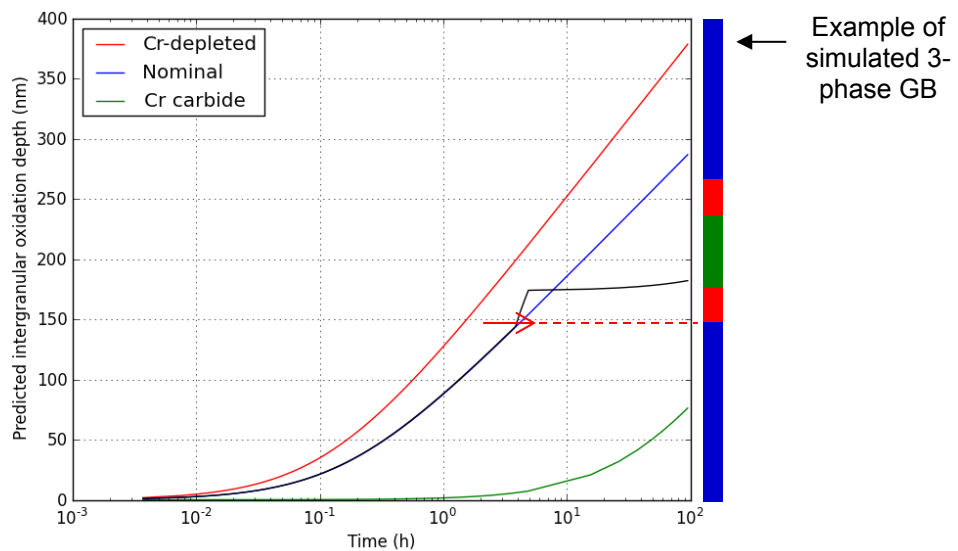


Figure 32 – Simulated oxide growth (dark curve) along a grain boundary (on the right) with Cr carbide (green portion) surrounded with two Cr-depleted zones (red portions). The blue portions correspond to a nominal Cr content. The red arrow illustrates the change in oxidation rate as soon as the intergranular oxidation front reaches the first interface (nominal/depleted). The change corresponds to the simple shift in time of the oxidation kinetics along the depleted phase up to the current time. Oxidation rates given at 320°C with DH = 30 ml.kg⁻¹ water.

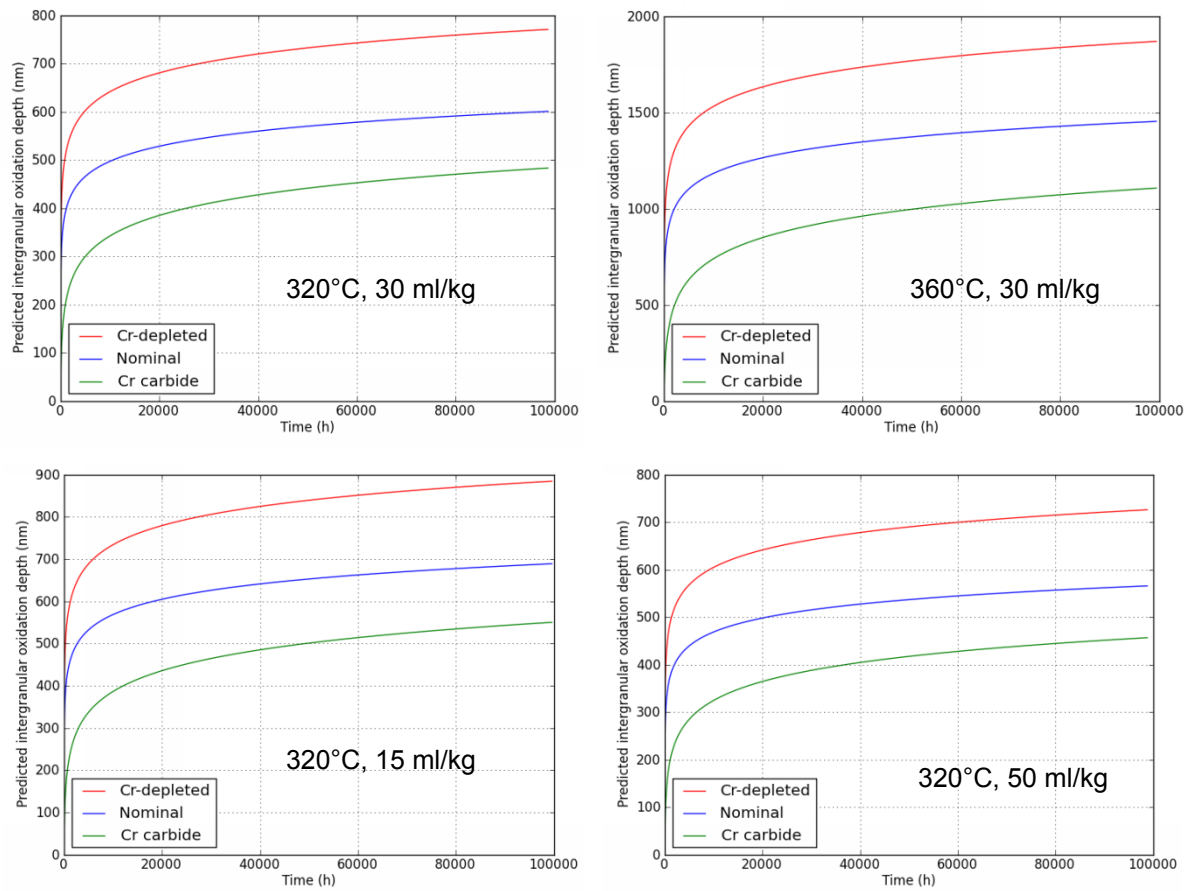


Figure 33 – Oxide growth kinetics along A182 intergranular Cr carbides, nominal grain boundaries and Cr depleted grain boundaries in hydrogenated primary water. Note that depth scales (Y-axes) are different.

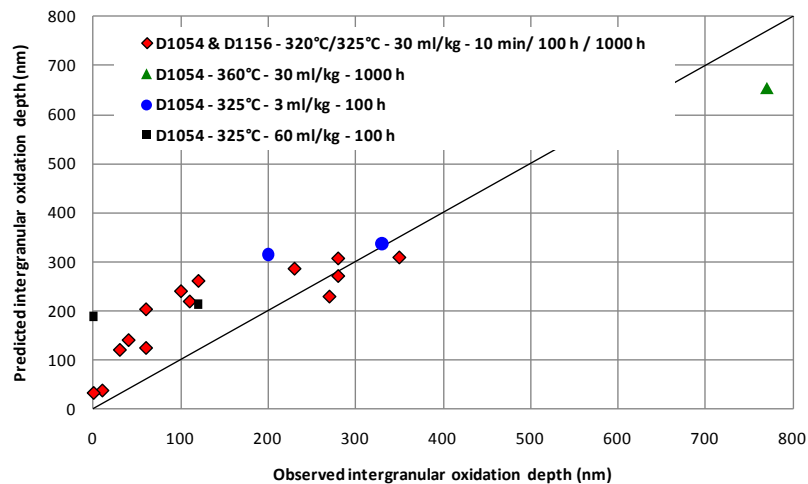


Figure 34 – Comparison between predicted and observed intergranular oxidation depths. A182 registered as RND-M-D-1054 and RND-M-D-1156.

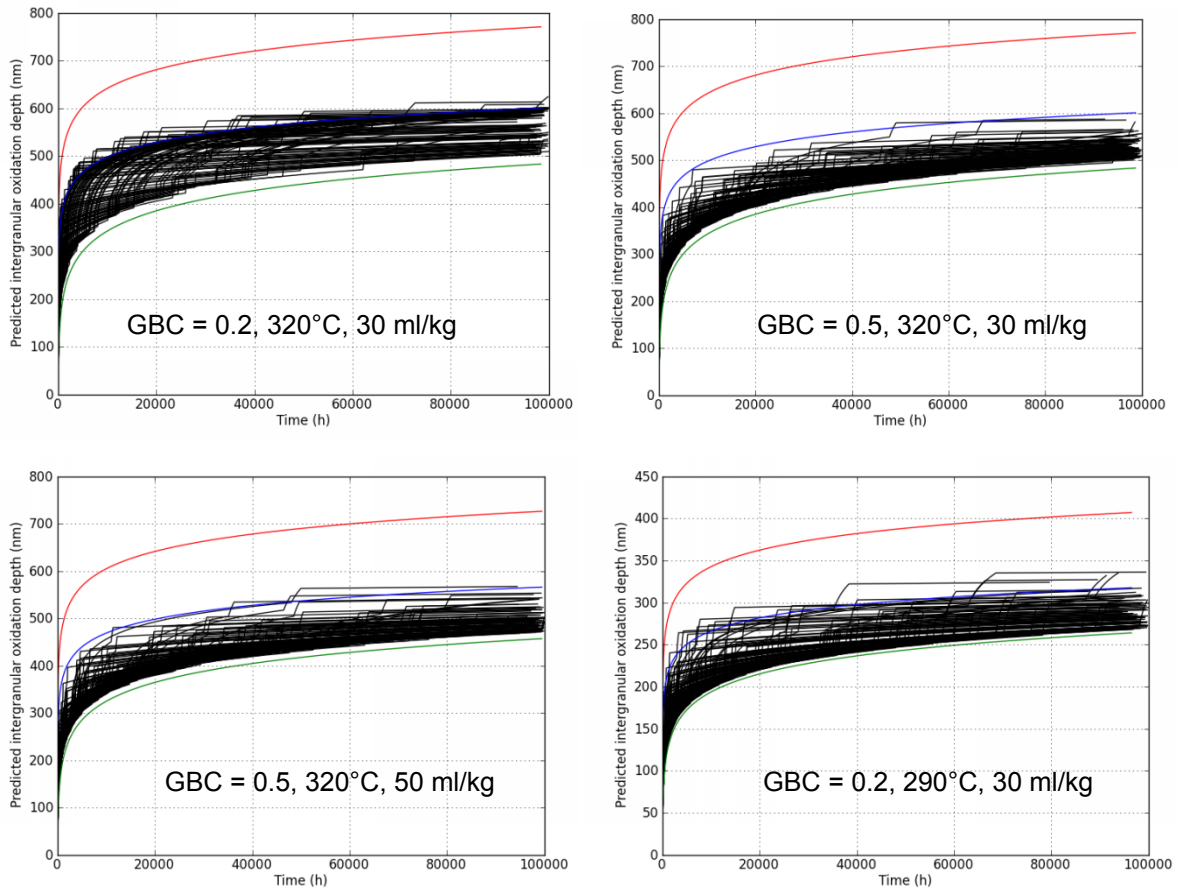


Figure 35 – Intergranular oxidation kinetics of a set of 100 grains boundaries (GBs) exposed to primary hydrogenated water [6]. Each dark curve corresponds to the oxidation kinetics of a GB, composed of three randomly distributed phases. In green: oxidation kinetics of a Cr-depleted GB; in blue: oxidation kinetics of a nominal (bulk) Cr content; in red: oxidation kinetics of a GB covered by a Cr carbide.

5.1.2.3. Stress concentration at grain boundaries

Crystal plasticity modeling is an appropriate approach to evaluate the stress concentrations at the grain boundaries of a polycrystalline aggregate, taking into account activation of slip systems. In the frame of small deformation assumption, the strain rate $\dot{\epsilon}$ can be decomposed into elastic $\dot{\epsilon}^e$ and plastic $\dot{\epsilon}^p$ parts (Equation 9).

$$\dot{\epsilon} = \dot{\epsilon}^e + \dot{\epsilon}^p \tag{Equation 9}$$

Considering that intragranular deformation is the main contribution, the plastic strain rate $\dot{\epsilon}^p$ in a grain is the sum of elementary shear rates $\dot{\gamma}^s$ extending over all active slip systems s (Equation 10):

$$\dot{\epsilon}^p = \sum_s \dot{\gamma}^s \tilde{m}^s \tag{Equation 10}$$

where \tilde{m}^s is the orientation tensor (Equation 11).

$$\tilde{m}^s = \frac{1}{2}(\bar{l}^s \otimes \bar{n}^s + \bar{n}^s \otimes \bar{l}^s) \tag{Equation 11}$$

| | | |
|-----|---|--|
| MAI | Quantitative evaluation of the EDF local model and the EPRI-NRC xLPR models of crack initiation of the weld metals of Alloy 600 (Alloys 82 and 182) | 6125-4501-2018-00583-EN Version 2.0 |
|-----|---|--|

where \bar{n}^s is the normal vector to the slip plane, \bar{l}^s is a vector corresponding to slip direction, and \otimes is the tensor product. Crystal plasticity models rely on the assumption that plastic deformation at low temperatures occurs by crystallographic slip following Schmid's law. The shear rate $\dot{\gamma}^s$ is linked to the motion of dislocations in active slip systems. The flow rule $\dot{\gamma}^s$ can be described by a phenomenological relation involving ingredients of interest: viscosity, isotropic and kinematic hardening. The resolved shear stress τ^s on a given slip system s is the projection (Equation 12) of the local stress tensor on \tilde{m}^s .

$$\tau^s = \tilde{\sigma} : \tilde{m}^s \quad \text{Equation 12}$$

After computation on a polycrystalline aggregate, in a first approach, the standard deviation (SD) of calculated local stresses σ can be correlated to the average stress $mean(\sigma)$ in the polycrystal (Equation 13), assuming a Gaussian distribution of local stresses.

$$SD(\sigma) = StressLinearCoef \times mean(\sigma) \quad \text{Equation 13}$$

The parameter *StressLinearCoef* is estimated thanks to finite element computations on a polycrystalline aggregate. Last, the largest stress levels are usually observed at grain boundaries. As a consequence, in the 'local' model, the tail of the assumed Gaussian stress distribution is assumed to be responsible for initiation.

The microstructure was simulated (Figure 36), involving 200 elongated grains, and 150000 nodes. The aggregate was meshed with tetrahedra. Hardening behavior (Equation 14) was calibrated on Alloy 82, assuming a Norton-like viscoplastic relation, where K_s is the viscosity constant and n_s is the stress sensitivity:

$$\dot{\gamma}^s = \left\langle \frac{|\tau^s - x^s| - \tau_c^s}{K_s} \right\rangle^{n_s} \frac{(\tau^s - x^s)}{|\tau^s - x^s|} \quad \text{Equation 14}$$

where x^s is the kinematic hardening, proportional to α^s (Equation 15 and Equation 16):

$$x^s = c \alpha^s \quad \text{Equation 15}$$

$$\dot{\alpha}^s = \dot{\gamma}^s - d\alpha^s |\dot{\gamma}^s| \quad \text{Equation 16}$$

where c is a constant. τ_c^s is the isotropic hardening, depending on the cumulated strain γ_{cum}^r (Equation 17 and Equation 18):

$$\tau_c^s = \tau_0 + Q \sum_r h_{rs} \left(1 - \exp(-b\gamma_{cum}^r) \right) \quad \text{Equation 17}$$

$$\gamma_{cum}^r = \int_t |\dot{\gamma}^r| dt \quad \text{Equation 18}$$

where h is the interaction matrix, describing the self-hardening (diagonal components) and the latent hardening (non-diagonal components) of the crystal slip systems. All components h_{rs} of h were normalized by the self-hardening components. Only five interaction coefficients h_{rs} exist in face cubic centered structures such as austenitic materials. When strain hardening is isotropic, h is independent of the active slip system. Therefore, in this situation $h_{rs} = 1$. Usually, self-hardening components are lower than latent components. Both isotropic and kinematic hardenings were considered to model the behavior of the material. However, in a first approach [27], it is assumed that $h_{rs} = 1$. Calculations were performed using EDF finite element modeling Code_Aster [28]. Parameters are given in Table 16. Computations were done with an isotropic elasticity (see moduli of elasticity E and Poisson's ratio ν in Table 16). Last, lattice rotation was considered, in order to update the orientation of the normal to the slip planes at each step of the computation. At the end of the calculation, $mean(\sigma) = 560$ MPa and *StressLinearCoef* = 0.25.

Table 16 – Parameters of the mechanical behavior (elasticity, plastic hardening).

| E (MPa) | ν | c | n_s | K_s | τ_0 (MPa) | Q (MPa) | h_{rs} | b | d |
|---------|-------|-----|-------|-------|----------------|---------|----------|-----|----|
| 164 955 | 0.33 | 450 | 6.505 | 31.6 | 132 | 37 | 1 | 3.9 | 20 |

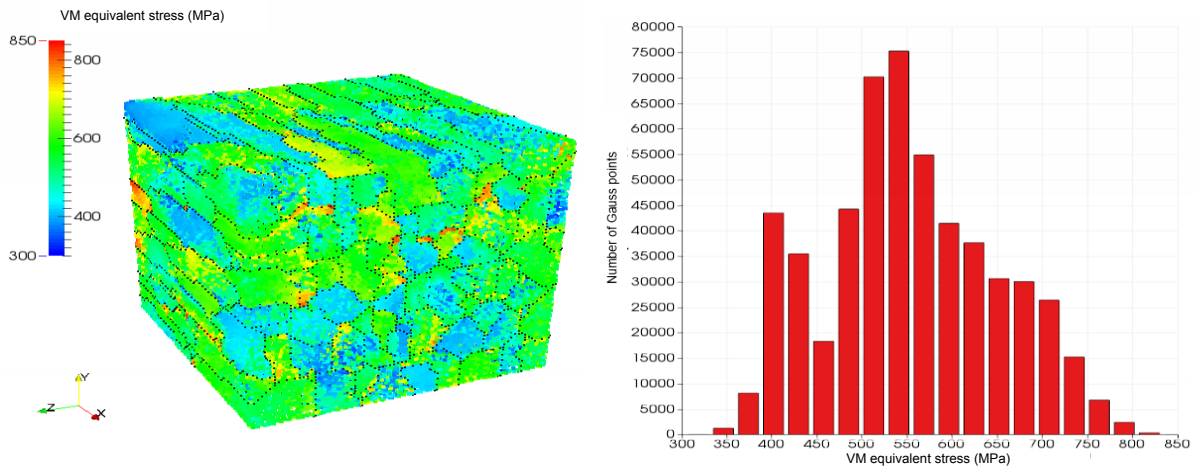


Figure 36 – Calculated von Mises stress in Alloy 82 polycrystalline aggregate. 3D view (left) and histogram (right).

5.1.2.4. Initiation criterion

The initiation is supposed to be possible as soon as a critical depth (p_c) of intergranular oxidation is reached. The initiation is assumed to possibly happen at an oxidized GB, as soon as the critical stress to failure (σ_c) is reached. The critical stress to fail oxidized grain boundaries was evaluated combining the experimental results of a tensile test with results of finite element modeling (FEM) on the polycrystalline aggregate. The procedure involved the following steps:

Oxidation of a non-stressed tensile specimen

A tensile specimen was cut in D1054 weld (T orientation) by electro-discharge machining, mechanically polished down to 1 μm and polished with colloidal silica for 30 to 40 minutes under a load of 20 N. The total length L_{GB} of GBs covering the central area A_{GB} of the specimen (2.25 mm²) was evaluated to 13.7 mm by Electron BackScatter Diffraction (EBSD) analysis excluding twin boundaries. Prior to the oxidation test, the specimen was ultrasonically cleaned in ethanol then in distilled water. The specimen was insulated from the Hastelloy (C-276) autoclave by oxidized Zircaloy to avoid galvanic coupling. Oxidation was conducted in a loop under open circuit conditions during 1000 h. The environment simulated PWR primary water (1000 ppm B as boric acid, 2 ppm Li as lithium hydroxide, 30 ml H₂.kg⁻¹ water) at 360°C.

Tensile test under vacuum at 360°C

The specimen was pulled using in-situ Scanning Electron Microscope (SEM) tensile machine MTEST5000W model (5 kN). The tensile test was stopped every 1% el. for detailed inspection of the surface of the specimen. The test was definitely stopped as soon as undisputable intergranular cracks were observed (Figure 37), after 6% el. when a stress of 500 MPa was reached. SEM examinations on cross sections showed that cracking happened within the intergranular oxide or at the metal/oxide interface (Figure 38).

Fraction of cracked grain boundaries

After tensile test on the oxidized specimen, the total length L_{CGB} of cracked grain boundaries on the analyzed area A_{CGB} (2.25 mm²) was visually estimated to 3.6 mm. The fraction f_{CGB} of cracked grain boundaries was estimated to 26% ($100 \times L_{CGB}/L_{GB}$). 13 GBs failed out of 21, 3 low angle GBs failed out of 7, while 10 high angle GBs failed out of 14.

Cracking criterion for oxidized grain boundaries

According to FEM computations on a polycrystalline aggregate, in a first approach, the local stresses σ in the microstructure can be modeled by a Gaussian distribution (Figure 36). For a mean stress of 500 MPa, the standard deviation (SD) of the local stresses was estimated thanks to Equation 13 with $S = 0.25$. The normal distribution of the corresponding stress is given in Figure 39.

Stresses usually exhibit wider distributions close to GBs. Therefore, it was assumed that sufficiently oxidized grain boundaries that failed were those subjected to the highest stress. In a first approach, only the lowest critical oxidation depth was considered: 200 to 400 nm, corresponding to 4% of the total length of cracked GBs, 1% of the total length of GBs. This preliminary evaluation was based on the examination of only 21 cross sections of different GBs. It was assumed that each examination of a cross section of a GB is representative of the entire GB (however, tomography would provide better evaluations). Using quantile functions, the stress representing 1% of the highest loaded GBs, would statistically correspond to about 790 MPa (Figure 39).

Finally, the initiation criterion at 360°C was supposed to be the critical stress of 790 MPa applied on a GB oxidized within the depth range of 200 nm-400 nm.

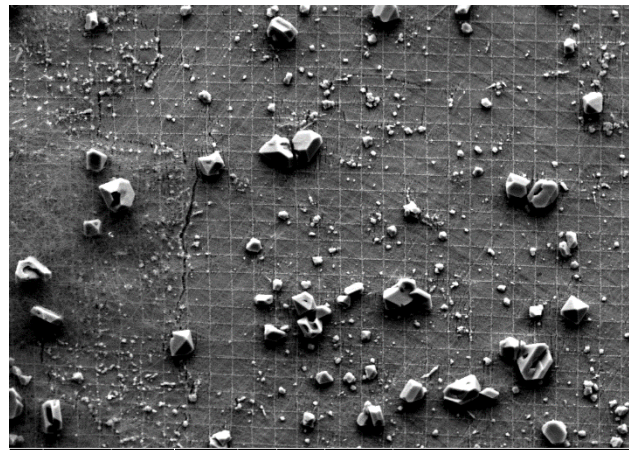


Figure 37 – SEM observation of cracked grain boundaries after the third loading (after 6% el.).

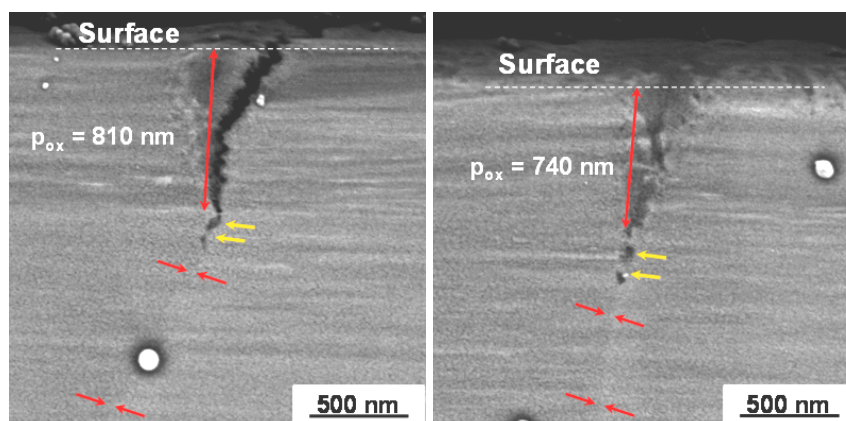


Figure 38 – SEM observation of cracked grain boundaries after the third loading (after 6% el.). Small red arrows indicate the position of the grain boundaries. Yellow arrows indicate the intergranular oxidation tips.

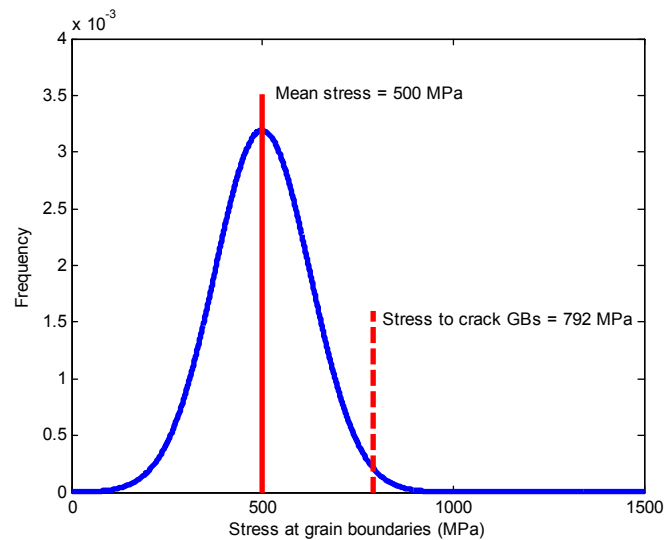


Figure 39 – Assumed Gaussian stress distribution at the surface of the tested specimen and stress to fail oxidized GBs at 360°C for a mean applied stress of 500 MPa. The stress threshold was estimated assuming that failure observed on 1% of the oxidized GBs (200 nm < oxidation depth < 400 nm) happened on the 1% most highly stressed GBs.

5.1.2.5. Former predictions

SCC kinetics were calculated (1D approach, without Code_Coriolis) for the A182 weld registered RND-M-D-1054, exhibiting a large susceptibility to initiation and crack growth. In agreement with the existing database (Table 9), the time to reach observed maximal crack depth was calculated for each specimen. The database involves a wide range of temperatures (325-360°C), stresses (380-660 MPa), durations (190-23770 h) and crack depths (0-1129 μm). However, the DH content was the same (30 ml.kg⁻¹).

As shown in Figure 40, the preliminary calibration of the parameters allow to reach relevant long times (>5000 h) to reach three short cracking (<100 μm) and one deep cracking (1 mm). Regarding short times, the prediction of the model is relevant for deep cracks (120 μm and 1.1 mm) but not realistic and non-conservative for very short cracks (5 and 12 μm). Regarding longer times and deeper cracks, the relative accuracy of the model is higher. The predicted time to reach the maximum SCC crack depth is much shorter than observed.

Last, no SCC was predicted for the conditions corresponding to the three tests for which no SCC was observed.

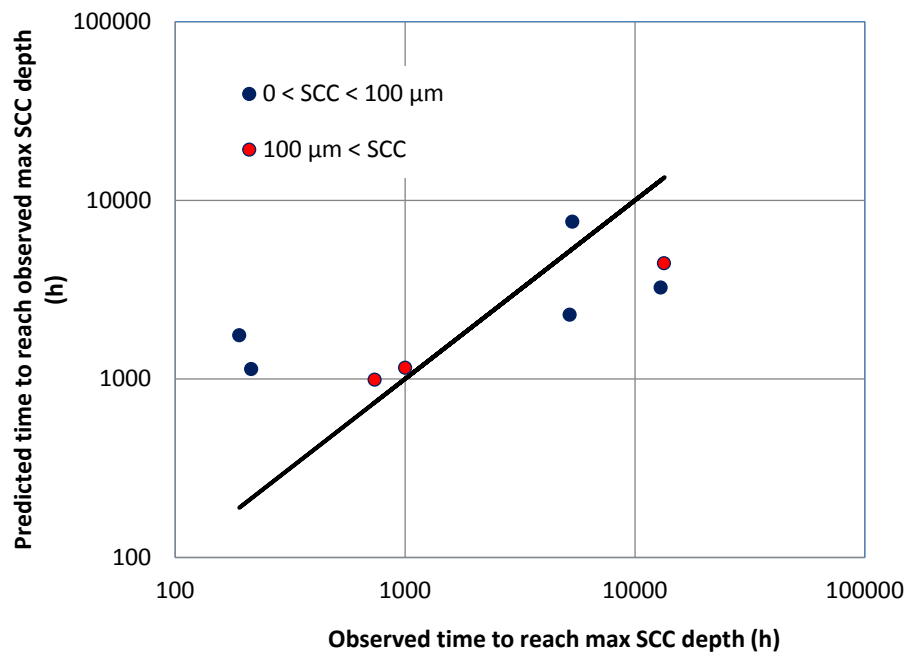


Figure 40 – Predicted (Local Model) versus experiment times to reach the maximal crack depths observed on RND-M-D-1054 weld.

5.1.2.6. Limitations

The 'local' model is based on a progressive weakening of GBs due to oxidation (incubation) leading to the mechanical failure of the highest stressed GB, followed by a slow then fast crack extension. The reliability of such a scenario still has to be proved.

As already shown in Figure 34, current fitted parameters on A182 overestimate short oxidation depths (< 250 nm) and under estimate the observed deep oxidation depths (780 nm). Therefore, using this model to predict SCC initiation may lead to overestimate the times to initiation. This result will be statistically considered and quantified in the near future.

Predictions of intergranular oxidation in A82 are probably overestimated because they rely, in a first approach, on parameters fitted on A182. As a consequence, predictions of SCC initiation in A82 will be over pessimistic (i.e., time to initiation underpredicted).

The proposed cracking criterion can be questioned: in a first approach, the criterion corresponds to a single critical stress associated to a single critical oxidation depth. However, detailed cross section examinations have shown that the probability to observe a cracked GBs increases when the oxidation depth increases (Figure 41). As a consequence, according to the followed methodology to estimate the stress to fail oxidized GBs, the critical stress to failure decreases when the oxidation depth increases (Figure 42). For oxidation depths within the range 200 nm-400 nm (4% of cracked GBs, 1% of GBs) the critical stress was evaluated to 790 MPa (stress to failure used in the current paper). The cumulated fraction of cracked GBs reaches 80% for the oxidation depth of 1 μm and 100% for the oxidation depth of 1.6 μm. It suggests that toughness may be more relevant than stress to define the cracking criterion. A 'pseudo' toughness k_c was calculated (Equation 19) using the critical stress σ_c to fail the fraction of cracked GBs oxidized for a depth p . The pseudo toughness of oxidized GBs was estimated within the range 16-23 MPa.m^{1/2}.

$$k_c = \sigma_c \sqrt{p} \quad \text{Equation 19}$$

The evaluation of the stress (or toughness) to fail oxidized GBs is a real challenge due to the very small extension of the oxide at GBs. Therefore, it is necessary to use different methodologies to evaluate it. For example, research is ongoing (Alloy 600) in Oxford University in order to fracture isolated GBs [29]. In addition, current approaches do not consider the possible effect of hydrogen and vacancies on

cracking. The effect of compressive stresses induced in the oxide by its growth within the metal should be considered. The presence of compressive oxide growth stresses could help to explain why no fracture of oxidized GBs is observed until 6% el. of the tensile specimen.

The use of the TEM to calibrate the GB oxidation rate model limits the database and therefore the validity of the model. Complementary techniques, such as Focused Ion Beam (FIB) tomography, may help to get necessary statistics in order to reach a convenient level of accuracy. The oxidation rate of chromium carbides and surrounding matrix has first to be strongly consolidated. Then, additional parameters could be considered:

- The absolute level of chromium content in the 'nominal' phase.
- The correlation between the chromium carbide precipitation and the nature of the grain boundary.
- The effect of plastic deformation (dislocations).
- The effect of stress (in absence of plastic strain).

Last, a physically based model (Point Defect Model ^[30]) could be preferred to the proposed empirical model.

Regarding the mechanical behavior, it would be necessary to validate the prediction of stress at the grain boundaries. Indeed, opening stresses play a major role in initiation. Furthermore, kinematic hardening has to be improved: the same set of parameters cannot predict properly strain-stress cycles of low and large strain amplitudes.

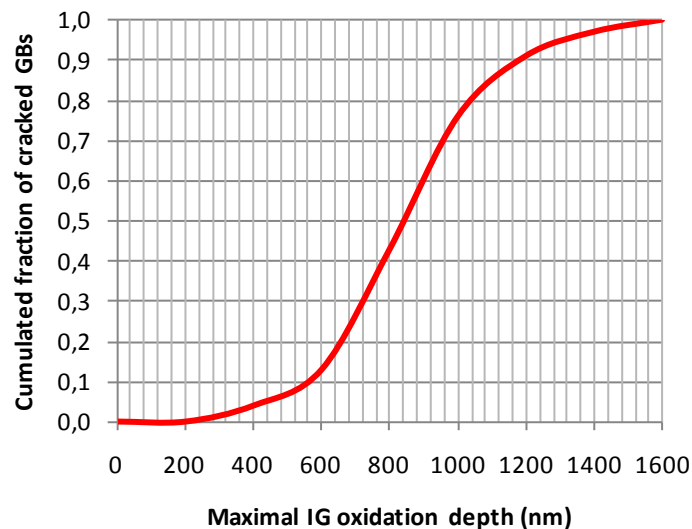


Figure 41 – Correlation between the fraction of cracked GBs and the maximal IG oxidation depth observed on cross sections after a tensile test on oxidized D1054 weld.

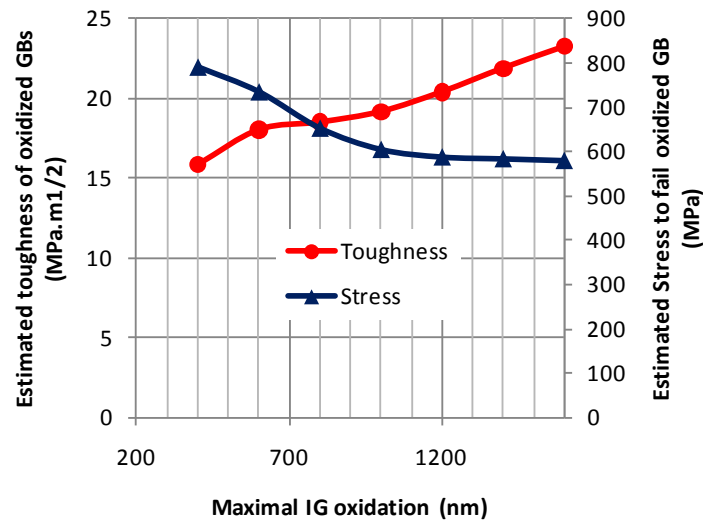


Figure 42 – Estimated cracking stress σ_c and toughness ($\sigma_c \times p^{1.2}$) of oxidized GBs versus maximal IG oxidation depth p observed on cross sections after a tensile test on oxidized D1054 weld.

5.1.3. xLPR initiation models

xLPR includes PWSCC initiation models, which provide time to crack initiation as an output. Three PWSCC initiation models were developed to address the significant level of modelling uncertainty associated with PWSCC initiation. These models include Direct Model 1 (discussed in Section 5.1.3.1), Direct Model 2 (discussed in Section 5.1.3.2), and the Weibull Model (discussed in Section 5.1.3.3). All three models assumed crack initiation to be a function of surface stress and operational temperature. Direct Model 2 further assumes that cold work and other mechanical properties influence crack initiation times.

The xLPR initiation models do not explicitly treat the evolution of micro-sized flaws but rather characterize their effect as “accumulating damage” leading to an initiation event defined as the existence of a flaw of engineering scale. Subsequent crack growth is treated in separate models. The xLPR initiation models, as currently calibrated, assume an initial flaw size on the order of a few mm^[31]. The recommended initial PWSCC crack depth input for xLPR runs is sampled from a log-normal distribution with a median of 1.5 mm, a log- μ of -6.50 [ln(m)], a log- σ of 0.35, and a lower truncation limit of 0.5 mm^[32]. The recommended initial flaw length input for xLPR runs is also log-normally distributed, with a median of 4.8 mm, a log- μ of -5.34 [ln(m)], and a log- σ of 0.8.

To accommodate multiple crack initiation sites on a single component/weldment, the xLPR program divides each component/weldment into multiple subunits and assumes a single axial and circumferential crack can initiate within each subunit.

Each of the xLPR PWSCC initiation models is developed to fit the following generalized model form^[30]:

$$t = \Lambda \cdot g(T, \sigma, \dots; Q, n, \dots) \quad \text{Equation 20}$$

Components of the generalized model form include:

- *Dependent variable (t)*: initiation time for flaws of engineering scale
- *Explanatory variables (e.g., T, σ)*: These are the independent model variables. They include stress conditions, material properties, and environmental properties, among others.
- *Effects model (g)*: The initiation functional model that defines the relationship between the independent model variables and the initiation time.
- *Effects model parameters (Q, n)*: The model parameters are used in the functional model to define the relationship between initiation time and the independent model variables. The Arrhenius model that uses a thermal activation energy, Q, is an example.
- *Failure time model random variable (Λ)*: Used to incorporate the statistical or probabilistic capability into the initiation model.

| | | |
|-----|---|--|
| MAI | Quantitative evaluation of the EDF local model and the EPRI-NRC xLPR models of crack initiation of the weld metals of Alloy 600 (Alloys 82 and 182) | 6125-4501-2018-00583-EN Version 2.0 |
|-----|---|--|

The xLPR PWSCC initiation models are empirically based, with effects model parameters fit to laboratory data and the failure time model calibrated to field data for Alloy 82/182/132 dissimilar metal piping butt welds.

5.1.3.1. Direct Model 1

Direct Model 1 is based on the ‘material index model’ [33, 34, 35]. This model incorporates dependencies relative to temperature and near-surface stress through the following effects model:

$$t = \Lambda_{cc} \cdot \Lambda_{wc} \cdot g(T, \sigma; Q, n) \quad \text{Equation 21}$$

$$g = e^{\frac{Q}{R_{gas}T}} \sigma^{-n}$$

The dependency with respect to temperature, T , is related through the Arrhenius model with an effects model parameter for activation energy, Q ; the chemical kinetics involved in PWSCC initiation accelerate with temperature. The dependency with respect to near-surface stress, σ , is related through a simple power-law form with an effects model parameter for the stress exponent, n ; surfaces exposed to higher stresses are generally more susceptible to PWSCC initiation.

Near-surface stress as discussed here refers to the stress beneath the thin surface cold-worked layer induced by surface grinding or machining that is usually present on the wetted surface of Alloy 82/182/132 PWR piping dissimilar metal piping butt welds [36]. As such, the near-surface stress includes weld residual stress (WRS) and normal operating loads, but excludes the effect of grinding or machining. Work by Scott [35] shows that the surface cold-worked layer is up to 100 or even 200 μm thick. The presence of this surface cold-worked layer, with the potential for very high tensile residual stresses in the layer, appears to be a key factor in much of the PWSCC experience. However, in the simplified treatment of stress presented here, the near-surface stress is the key determinant in whether a shallow defect initiated in the thin surface cold-worked layer will grow to engineering scale in the softer bulk (4) material over plant time scales.

Both failure time models are the reciprocal of distributed xLPR input parameters, which are assumed a priori to be log-normally distributed: (5)

$$\Lambda_{cc} = \frac{1}{A_{cc}} \quad \text{Equation 22}$$

$$A_{cc} \sim \log - N(0, \sigma_{A,cc})$$

$$\Lambda_{wc} = \frac{1}{A_{wc}} \quad \text{Equation 23}$$

$$A_{wc} \sim \log - N(\mu_{A,wc}, \sigma_{A,wc})$$

where the tilde (\sim) symbol can be interpreted as “is sampled from.” The $\log-\mu$ ($\mu_{A,wc}$) and $\log-\sigma$ ($\sigma_{A,cc}$ and $\sigma_{A,wc}$) terms are the hyperparameters of the overall Direct Model 1 failure time model.

Finally, the implementation of Direct Model 1 includes a near-surface stress threshold, σ_{th} , below which PWSCC initiation does not occur.

Inputs to Direct Model 1, as developed in xLPR-TR-CI-SCC-Calibration [37] are summarized in Table 17.

(4) The qualifier ‘bulk’ is used to distinguish the material surface phase from the bulk material phase beneath the surface phase.

(5) It is acknowledged that the reciprocal of a log-normally distributed variate is also log-normally distributed. However, the distinction between the parameter A and the failure time model Λ is important because the xLPR program accepts as input the value for A , not Λ .

| | | |
|-----|---|--|
| MAI | Quantitative evaluation of the EDF local model and the EPRI-NRC xLPR models of crack initiation of the weld metals of Alloy 600 (Alloys 82 and 182) | 6125-4501-2018-00583-EN Version 2.0 |
|-----|---|--|

Table 17 – Direct Model 1 Parameters ^[36]

| Description | Units | Characterization of Uncertainty | Distribution Parameters | Model Parameters |
|---|----------------------------------|---------------------------------|-------------------------|--------------------|
| Number of subunits | - | deterministic | best-estimate | 19 |
| Thermal activation energy | kJ/mol | deterministic | best-estimate | 185.0 |
| Inverse proportionality constant, A_{cc} (component-to-component) | - | distributed (epistemic) | type | Log-Normal |
| | | | log-norm μ | 0.00 |
| | | | log-norm σ | 2.89 |
| Inverse proportionality constant, A_{wc} (within-component) | (1/FPY) (1/MPa ⁵) | distributed (aleatory) | type | Log-Normal |
| | | | log-norm μ | -4.40 |
| | | | log-norm σ | 3.66 |
| Stress threshold | MPa | deterministic | best-estimate | 0.0 ⁽¹⁾ |
| Stress exponent | - | deterministic | best-estimate | 5.0 |

(1) The PWSCC initiation module of xLPR Version 2.0 does not allow the stress threshold input to be less than or equal to zero. Therefore, the Direct Model 1 stress threshold input to xLPR is set to an arbitrarily small positive value to emulate this value of 0 MPa.

5.1.3.2. Direct Model 2

Direct Model 2 is an implementation of the model developed in EPRI 1019032 ^[38] and 1025121 ^[39]. This model attempts to incorporate the effects of bulk cold work on stress corrosion cracking (SCC) susceptibility through the use of mechanical properties. The relatively complex effects model is given below:

$$t = \Lambda_{cc} \cdot \Lambda_{wc} \cdot g(T, \sigma, \sigma_{ys}, \sigma_{ult}, E, Q, z_1, z_2, v, w, q, a_{dm2}, b_{dm2}, c_{dm2}, k_{dm2})$$

$$g = Ge^{Q/R_{gas}T} \ln \left[\frac{D - z}{\frac{\sigma}{\sigma_{ys}} - z} \right] \quad \text{Equation 24}$$

$$G = m^{-q} \frac{\ln(D)}{\ln\left(\frac{D - z}{1 - z}\right)} \quad \text{Equation 25}$$

$$z = z_1 + z_2 \ln(\zeta) \quad \text{Equation 26}$$

$$D = v \cdot e^{w \cdot \zeta} \quad \text{Equation 27}$$

$$m = k_{dm2} \left(\frac{\sigma_{ys}}{E} \right)^{a_{dm2}} (\zeta - 1)^{b_{dm2}} (\zeta)^{c_{dm2}} \quad \text{Equation 28}$$

$$\zeta = \frac{\sigma_{ult}}{\sigma_{ys}} \quad \text{Equation 29}$$

Once more, the dependency with respect to temperature is related through the Arrhenius model. The dependency with respect to near-surface stress and bulk cold work effects is related as a function of near-surface stress, σ , material yield strength, σ_{ys} , ultimate tensile strength, σ_{ult} , and elastic modulus, E (all of which should reflect bulk mechanical properties below the surface cold-worked layer). By the convention established in EPRI 1019032, the mechanical property inputs to this model should represent room-temperature conditions). EPRI 1019032 can be consulted for a more in-depth discussion relating these equations to physical concepts.

The cold work effects parameters are based on laboratory testing of nickel-based alloy and austenitic stainless steel (SS) specimens presented in EPRI 1019032 [37] (see Table 18 ⁽⁶⁾).

For Direct Model 2, the failure time model is equivalent to a distributed xLPR input, which is assumed a

⁽⁶⁾ For Alloy 82/182, the value of the coefficient k was modified from 10.0 in EPRI 1019032 ^[24] to 8.2 in EPRI 1025121.

| | | |
|-----|---|--|
| MAI | Quantitative evaluation of the EDF local model and the EPRI-NRC xLPR models of crack initiation of the weld metals of Alloy 600 (Alloys 82 and 182) | 6125-4501-2018-00583-EN Version 2.0 |
|-----|---|--|

priori to be log-normally distributed:

$$\Lambda_{cc} = B_{cc}$$

$$B_{cc} \sim \log - N(0, \sigma_{B,cc})$$

Equation 30

$$\Lambda_{wc} = B_{wc}$$

$$B_{wc} \sim \log - N(\mu_{B,wc}, \sigma_{B,wc})$$

Equation 31

The log- μ ($\mu_{B,wc}$) and log- σ ($\sigma_{B,cc}$ and $\sigma_{B,wc}$) terms are the hyperparameters of the overall Direct Model 2 failure time model.

Like Direct Model 1, this model includes a near-surface stress threshold below which PWSCC initiation does not occur; however, in the case of Direct Model 2, it is a calculated quantity:

$$\sigma_{th} = z\sigma_{ys}$$

Equation 32

The initiation time prediction asymptotically approaches arbitrarily long times as near-surface stress approaches this threshold and is interpreted as infinite at or below this threshold (where Equation 24 is undefined).

Direct Model 2 also includes an upper near-surface stress above which PWSCC initiation occurs instantaneously:

$$\sigma_{max} = D\sigma_{ys}$$

Equation 33

The initiation time prediction approaches arbitrarily short times as near-surface stress approaches this threshold and is interpreted as zero at or above this threshold (where Equation 24 evaluates to a negative number).

Inputs to Direct Model 2, as developed in xLPR-TR-CI-SCC-Calibration [36] are summarized in Table 19.

Table 18 – Direct Model 2 Cold Work Parameters [36].

| Direct Model 2 Inputs for Ni-Based Alloys | | | | | | | | |
|---|-------|------|-----|-------|-----------|-----------|-----------|-----------|
| z_1 | z_2 | v | w | q | a_{dm2} | b_{dm2} | c_{dm2} | k_{dm2} |
| 0.350 | 0.333 | 0.66 | 0.5 | 0.375 | 0.25 | -0.75 | -0.25 | 8.2 |

Table 19 – Direct Model 2 Parameters [36].

| Description | Units | Characterization of Uncertainty | Distribution Parameters | Model Parameters |
|---|--------|---------------------------------|-------------------------|------------------|
| Number of subunits | - | deterministic | best-estimate | 19 |
| Thermal activation energy | kJ/mol | deterministic | best-estimate | 185.0 |
| Proportionality constant, B_{cc} (component-to-component) | - | distributed (epistemic) | type | Log-Normal |
| | | | log-norm μ | 0.00 |
| | | | log-norm σ | 1.49 |
| Proportionality constant, B_{wc} (within-component) | EFPY | distributed (aleatory) | type | Log-Normal |
| | | | log-norm μ | -28.43 |
| | | | log-norm σ | 1.91 |
| Cold work parameters | - | deterministic | best-estimate | see Table 18 |

5.1.3.3. Weibull Model

Akin to Direct Model 1, the Weibull model incorporates dependencies relative to temperature and near-surface stress:

$$t = \Lambda \cdot g(T, \sigma; Q, n, T_{ref}, \sigma_{ref})$$

$$g = \exp\left[\frac{Q}{R_{gas}}\left(\frac{1}{T} - \frac{1}{T_{ref}}\right)\right] \left(\frac{\sigma}{\sigma_{ref}}\right)^{-n}$$

Equation 34

The dependency with respect to temperature, T , is related through the Arrhenius model with effects model parameters for activation energy, Q , and reference temperature, T_{ref} . The dependency with respect to near-surface stress, σ , is related through a simple power-law form with effects model parameters for the stress exponent, n , and reference stress, σ_{ref} . The reference temperature and reference stress terms are constant scaling factors. They could be set to any arbitrary value, but they are set to 588.7 K (600°F) and 325 MPa, respectively, allowing the effects model to remain near one for

| | | |
|------------|---|--|
| MAI | Quantitative evaluation of the EDF local model and the EPRI-NRC xLPR models of crack initiation of the weld metals of Alloy 600 (Alloys 82 and 182) | 6125-4501-2018-00583-EN Version 2.0 |
|------------|---|--|

nominal conditions.

Like the Direct Models, the Weibull model includes a near-surface stress threshold below which PWSCC initiation is modeled not to occur; however, for the Weibull model this threshold is fixed at zero (i.e., no initiation within a compressive stress field).

As suggested by the name, the Weibull model features a failure time model that is assumed a priori to be Weibull distributed. In xLPR Version 2.1, the Weibull distribution is defined by the slope hyperparameter, β , and the vertical intercept hyperparameter, c . The vertical intercept hyperparameter is the intercept of the Weibull distribution in a Weibull plot ^[40]. The cumulative distribution function for this Weibull parameterization is stated in Equation 35.

$$\Lambda \sim W(\beta, c)$$

$$F_{\Lambda}(t; \beta, c) = 1 - \exp[-t^{\beta} \exp(c)] \quad \text{Equation 35}$$

This parameterization is in contrast with the more classical combination of slope and scale, θ . The scale hyperparameter can be related to the slope and vertical intercept hyperparameters through the following equation:

$$\theta = \exp[-c/\beta] \quad \text{Equation 36}$$

Finally, different from the Direct Models that use a within-component failure time model, the Weibull model includes an adjustment for the number of independent samples taken, N (e.g., twice the number of subunits in the case that both axial and circumferential crack initiation is treated simultaneously). This adjustment is included through the effects model as shown in Equation 37, which replaces Equation 34 and Equation 35.

$$t = \Lambda_{cc} \cdot g(T, \sigma, N; Q, n, T_{ref}, \sigma_{ref})$$

$$g = \exp\left[\frac{Q}{R_{gas}}\left(\frac{1}{T} - \frac{1}{T_{ref}}\right)\right] \left(\frac{\sigma}{\sigma_{ref}}\right)^{-n} N^{1/\beta_{cc}}$$

$$\Lambda_{cc} \sim W(\beta_{cc}, c_{cc})$$

$$F_{\Lambda_{cc}}(t; \beta_{cc}, c_{cc}) = 1 - \exp\left[-t^{\beta_{cc}} \exp(c_{cc})\right] \quad \text{Equation 37}$$

This adjustment results in initiation rates that have a scale that is invariant to the number of subunits ^[41]. Inputs to the Weibull Model, as developed in xLPR-TR-CI-SCC-Calibration ^[36] are summarized in Table 20.

| | | |
|-----|---|--|
| MAI | Quantitative evaluation of the EDF local model and the EPRI-NRC xLPR models of crack initiation of the weld metals of Alloy 600 (Alloys 82 and 182) | 6125-4501-2018-00583-EN Version 2.0 |
|-----|---|--|

Table 20 – Weibull Model Parameters ^[36].

| Description | Units | Characterization of Uncertainty | Distribution Parameters | Model Parameters |
|---|--------|---------------------------------|-------------------------|------------------|
| Number of subunits | - | deterministic | best-estimate | 19 |
| Thermal activation energy | kJ/mol | deterministic | best-estimate | 185.0 |
| Pivot time ^{1,2} | EPFY | deterministic | best-estimate | 10.4 |
| Percent of components with crack at pivot time ^{1,2} | % | deterministic | best-estimate | 10.0 |
| Vertical intercept error | - | distributed (epistemic) | type | Normal |
| | | | mean | 0.00 |
| | | | st dev | 0.38 |
| Weibull slope | - | distributed (epistemic) | type | Normal |
| | | | mean | 0.45 |
| | | | st dev | 0.08 |
| Correlation between vertical intercept error and Weibull slope ³ | - | deterministic | best-estimate | -0.800 |
| Stress exponent | - | deterministic | best-estimate | 5.0 |
| Reference temperature | K | deterministic | best-estimate | 588.7 |
| Reference stress | MPa | deterministic | best-estimate | 325.0 |

(1) The adjustment in Equation 37 requires that N is the number of independent samples taken (i.e., two times the number of subunits when both orientations are simulated). However, the implementation in xLPR uses the number of subunits, resulting in a factor of $2^{1/\beta}$ bias in the initiation time prediction. This bias has been corrected for in this table by subtracting $\ln(2)$ from the component-to-component vertical intercept.

(2) The pivot time and the percent of components with a crack at the pivot time are inputs to xLPR Version 2.0. These parameters may be interpreted as follows: given a best-estimate slope of 0.45 and a best-estimate vertical intercept of -3.30, the percent of components (10.0%) is expected to experience PWSCC by the pivot time (10.4 EPFY). They are directly related to the best-estimate vertical intercept (c) and slope (β) with a simple algebraic equation (e.g., Equation 35).

(3) Correlation expressed here refers to Pearson's correlation coefficient for two normal distributions.

5.2. Crack propagation

5.2.1. EDF Power law

The maximum crack growth rate \dot{a}_{max} calibrated at EDF is defined by Equation 38, where α is a constant depending on the loading/cracking directions in the weld (Table 21), f is a function depending on the stress intensity factor K , h is a function depending on ΔEcP , T is the temperature, Q is the activation energy and $R = 8.314 \text{ J.mol}^{-1}.\text{K}^{-1}$.

$$\dot{a}_{max} = \alpha \times f(K) \times h(\Delta EcP) \times e^{(-Q/RT)} \quad \text{Equation 38}$$

$h(\Delta EcP)$ (Equation 39) relies on results published by Morton ^[42]. It depends on temperature (K), dissolved hydrogen content and dissolved hydrogen content corresponding to the Ni/NiO equilibrium (Equation 8). h_0, h_1 are h_2 constant parameters ⁽⁷⁾.

$$h(\Delta EcP) = 1 + h_0 \times e^{\left[-\frac{1}{2} \left(\frac{\Delta EcP + h_1}{h_2} \right)^2 \right]} \quad \text{Equation 39}$$

Function f (Equation 40) gives the dependency to K in the fast crack growth regime, for $K \geq K_{ISCC}$.

$$f(K) = (K - K_{ISCC})^n \quad \text{Equation 40}$$

K_{ISCC} and n are parameters given in Table 21. According to Equation 40, $\dot{a}_{max} = 0$ when $K \leq K_{ISCC}$. Details on the relative positions of the EDF CGR upper bound and crack growth data are given in Appendix 1.

Figure 43 compares the predicted crack growth rates for EDF welds to the MRP-115 power law

⁽⁷⁾ $h_0 = 3.604$, $h_1 = 11.33$ and $h_2 = 43.36$.

($K_{ISCC} = 0$). When $K < 8 \text{ MPa.m}^{1/2}$, EPRI law is much more conservative than EDF laws. As soon as $K > 8 \text{ MPa.m}^{1/2}$, crack growth rates predicted with EDF laws are significantly higher than CGR predicted with MRP-115 for TS and LS orientations. For the TL orientation, the CGR predicted by MRP-115 is higher than the CGR predicted by EDF law as soon as K values are higher than $30 \text{ MPa.m}^{1/2}$.

The EDF power law will not be used in the current study because it was shown that such a law can lead to major errors in predictions: no crack extension being predicted while observation demonstrates 1 mm-deep SCC in A600 initiation specimen [1].

In a first approach, based on open literature [43,44], the crack growth rate in A82 has been shown to be 2.6 times slower than in A182. As a consequence, $\alpha(A82) = \alpha(A182) / 2.6$.

Table 21 – Material parameters as a function of orientation [45].

| Material | Orientation | $\alpha \text{ (}\mu\text{m.h}^{-1}\text{)}$ | $K_{ISCC} \text{ (MPa.m}^{1/2}\text{)}$ | n | $Q \text{ (kJ.mol}^{-1}\text{)}$ |
|--------------|-------------|--|---|------|----------------------------------|
| RND-M-D-1054 | TL | 4.0×10^4 | 8 | 0.34 | 65 |
| | LS | 1.0×10^5 | | | |
| | TS | 1.6×10^5 | | | |
| RND-M-D-711 | TL | 1.6×10^4 | 8 | 0.34 | 65 |
| | LS | 4.0×10^4 | | | |
| | TS | 6.2×10^4 | | | |

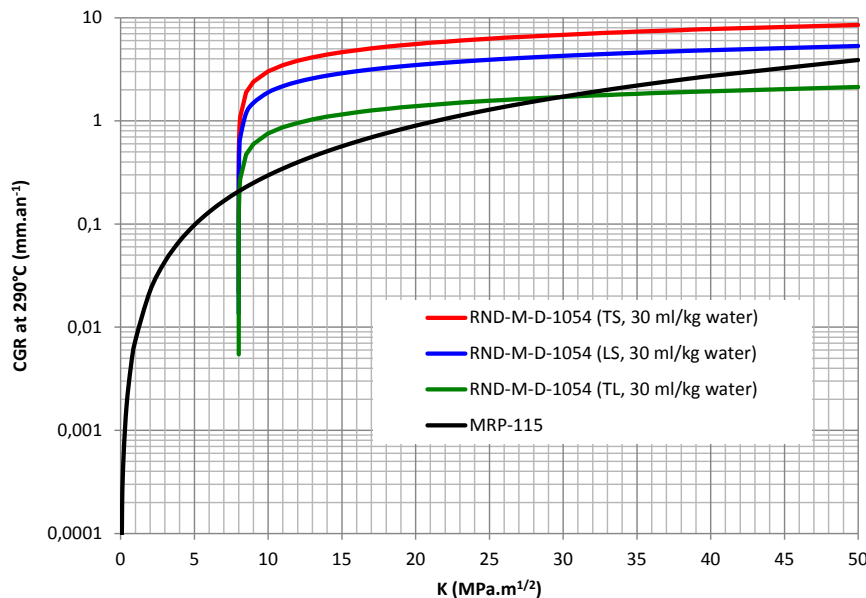


Figure 43 – Crack growth rates predicted at 290°C in primary hydrogenated water (30 ml.kg⁻¹) with a power law. Alloy 182 registered RND-M-D-1054 (along TS, LS and TL orientations) versus MRP-115.

5.2.2. EDF sigmoid law

The sigmoid crack extension law (upper bound) is given in Equation 41. It depends on K (in $\text{MPa.m}^{1/2}$), T (in K) and ΔEcP (in V) via h , and strain via g . $cgr11$ is the activation energy for crack growth CGR (in $\mu\text{m.h}^{-1}$).

$$cgr = cgr1 \times f(K) \times g(\varepsilon) \times h(\Delta EcP) \times \exp\left(\frac{-cgr11}{R \times T}\right) \quad \text{Equation 41}$$

where $cgr1$ is constant (depending on cracking direction in the weld). h depends on ΔEcP , as shown in Equation 44.

| | | |
|------------|---|--|
| MAI | Quantitative evaluation of the EDF local model and the EPRI-NRC xLPR models of crack initiation of the weld metals of Alloy 600 (Alloys 82 and 182) | 6125-4501-2018-00583-EN Version 2.0 |
|------------|---|--|

with
$$f(K) = \frac{K^{cgr2}}{1 + \exp[-cgr3 \times (K - cgr4)]}$$
 Equation 42

and
$$g(\varepsilon) = 1 + cgr5 \times (\varepsilon + |cgr7|) + cgr6 \times (\varepsilon + |cgr7|)^2$$
 Equation 43

and
$$h(\Delta EcP) = 1 + cgr8 \times \exp\left(-\frac{1}{2}\left(\frac{\Delta EcP + cgr9}{cgr10}\right)^2\right)$$
 Equation 44

where
$$\Delta EcP = 1000 \times \frac{R \times T}{2 \times F} \times \ln\left(\frac{DH}{DH_{Ni/NiO}}\right)$$
 Equation 45

with
$$DH_{Ni/NiO} = ecp1 \times \exp(ecp2 \times T)$$
 Equation 46

The sigmoid law (Equation 41) delivering the crack extension rate if given in Figure 45. The f_H dependency to hydrogen and associated ΔEcP is based on parameters proposed by Young [46]. Parameters were fitted as follows:

- Fast crack growth regime and K transition from slow to fast crack growth regime in agreement with the original CGR law (calibrated on fatigue pre-cracked Compact Tension specimens).
- Slow crack extension regime: in agreement with results of initiation tests on round tensile specimens.

The calibrated parameters for the weld registered RND-M-D-1054 are given in Table 22. The relative positions of the disposition sigmoid curves are similar to power law ones, including with regards to the MRP-115 law (Figure 44). Nevertheless, the introduction of the slow crack growth regime decreases the gap between EDF and EPRI models when $K < 10 \text{ MPa.m}^{1/2}$, even if CGR predicted by MRP-115 remains higher than EDF predictions. The crack growth rate in A82 has been shown to be 2.6 times slower than in A182. As a consequence, $cgr1(A82) = cgr1(A182) / 2.6$.

Details on the relative positions of the EDF CGR upper bound and crack growth data are given in Appendix 1.

Table 22 – Parameters of the crack growth rate model for A182 registered as RND-M-D-1054.

| Orientation | cgr1 | cgr2 | cgr3 | cgr4 | cgr5 | cgr6 | cgr7 | cgr8 | cgr9 | cgr10 | cgr11 | ecp1 | ecp2 |
|-------------|-------------------|------|------|------|------|------|------|-------|-------|-------|-------|--------------------|--------|
| TL | 2.2×10^4 | 0.5 | 0.5 | 12 | 15 | 0 | 0 | 3.604 | 11.33 | 43.36 | 65000 | 2×10^{-6} | 0.0256 |
| LS | 5.4×10^4 | | | | | | | | | | | | |
| TS | 8.5×10^4 | | | | | | | | | | | | |

Table 23 – Parameters of the crack growth rate model for A82 registered as RND-M-D-711.

| Orientation | cgr1 | cgr2 | cgr3 | cgr4 | cgr5 | cgr6 | cgr7 | cgr8 | cgr9 | cgr10 | cgr11 | ecp1 | ecp2 |
|-------------|-------------------|------|------|------|------|------|------|-------|-------|-------|-------|--------------------|--------|
| TL | 7.7×10^3 | 0.5 | 0.5 | 12 | 15 | 0 | 0 | 3.604 | 11.33 | 43.36 | 65000 | 2×10^{-6} | 0.0256 |
| LS | 2.1×10^4 | | | | | | | | | | | | |
| TS | 3.3×10^4 | | | | | | | | | | | | |

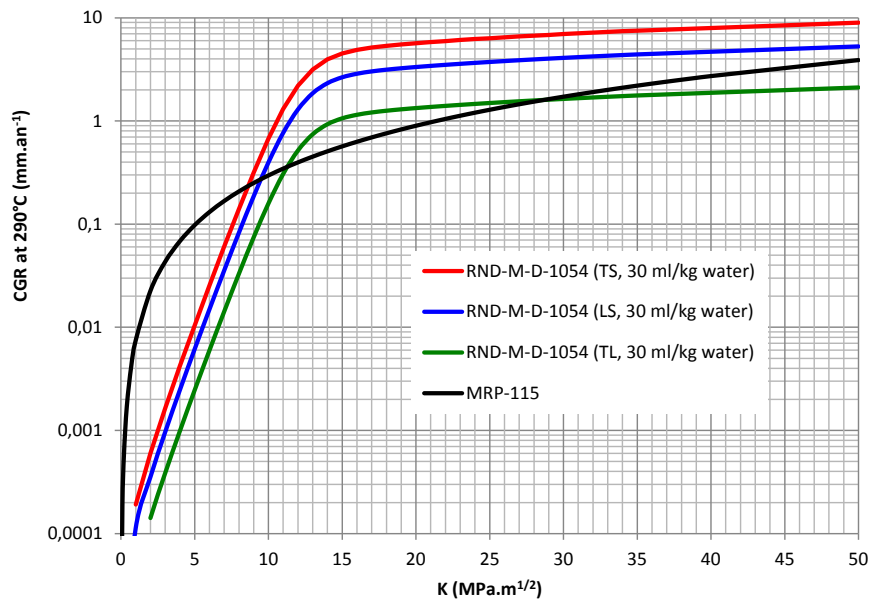


Figure 44 – Crack growth rates predicted at 290°C in primary hydrogenated water (30 ml.kg⁻¹). Alloy 182 registered RND-M-D-1054 (along TS, LS and TL orientations) versus MRP-115.

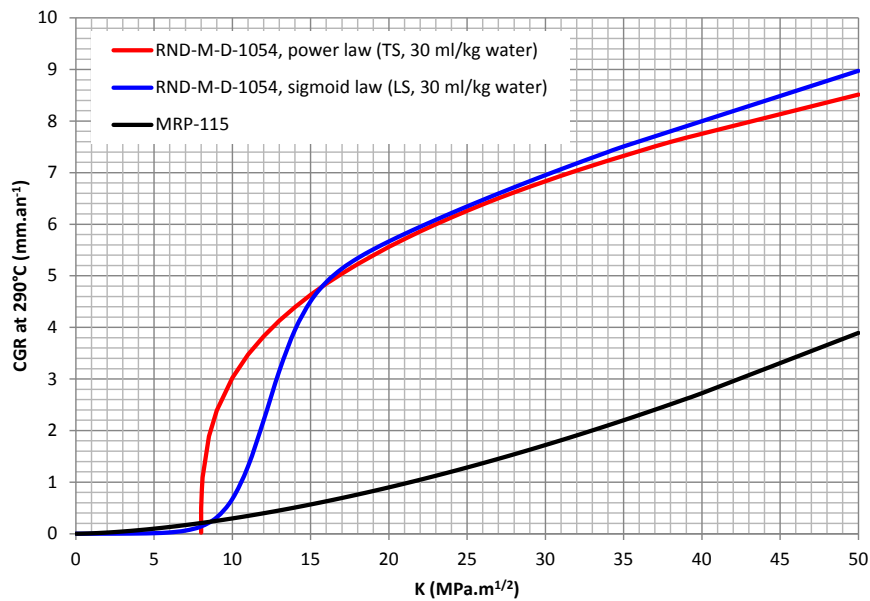


Figure 45 – Assumed crack extension rate in hydrogenated (30 ml.kg⁻¹) primary water at 325°C. Parameters calibrated on as-welded material registered RND-M-D-1054, along LS direction. Original EDF K-threshold crack growth law (in red) and MRP-115 are given for comparison.

6. Simulation of SCC tests with Code_Coriolis

6.1. Modeling of the specimens

The geometry and the mesh of the specimens have been modelled using Salomé software [27]. A finer mesh size was imposed at the outer surface, especially in the fillet of the specimen, to guarantee a sufficient number of nodes in volume, for the SCC simulation, especially close to the surface. Nevertheless, a specific procedure (mesh refinement) supports avoidance of major effects of mesh size in Code_Coriolis.

The model of the **TL2-type specimen** is shown in Figure 46. The mesh (Figure 47) involves 177870 nodes and 114099 quadratic elements (tetrahedrons with 10 nodes). 36080 nodes are at the surface where a contact with water is assigned in Code_Coriolis calculations.

The model of the **TRC-type specimen** is shown in Figure 48. The mesh (Figure 49) involves 35518 nodes and 20389 quadratic elements (tetrahedrons with 10 nodes). 4864 nodes are at the surface in contact with water.

The model of the **PNNL-type specimen** is shown in Figure 50. The mesh (Figure 51) involves 24526 nodes and 15123 quadratic elements (tetrahedrons with 10 nodes). 1937 nodes are at the surface in contact with water.



Figure 46 – Model of the TL2-type specimen.

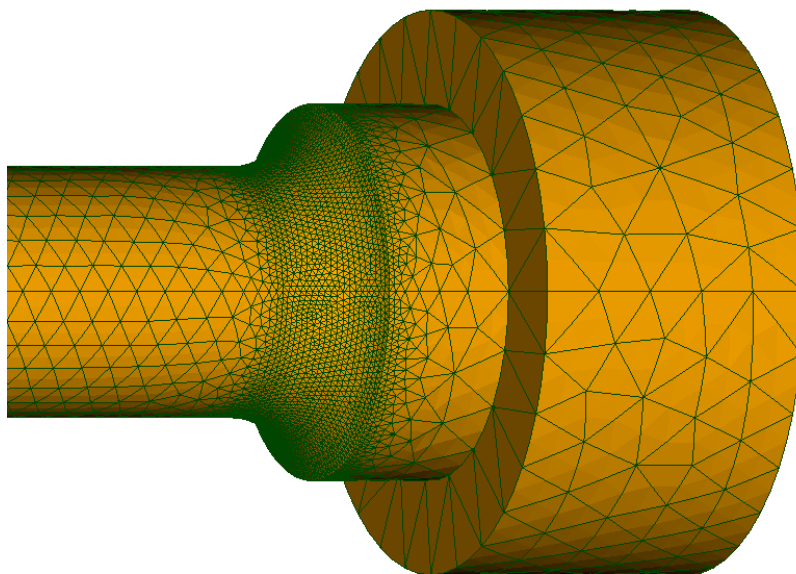


Figure 47 – Mesh of the TL2-type specimen.

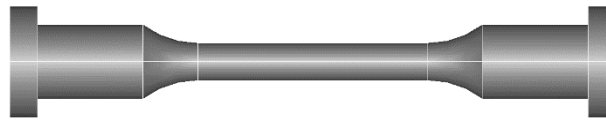


Figure 48 – Model of the TRC-type specimen.



Figure 49 – Mesh of the TRC-type specimen.

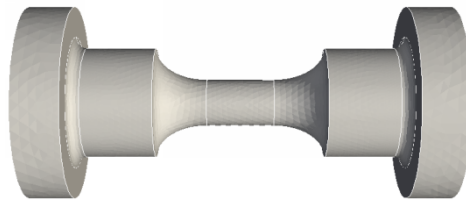


Figure 50 – Model of the PNNL-type specimen.

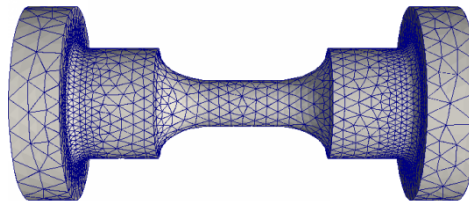


Figure 51 – Mesh of the PNNL-type specimen.

6.2. Modeling of the loading

Finite Element Modelling (FEM) was performed using Code_Aster v13.2 [27].

6.2.1. Boundary conditions

No displacement was allowed on one side of each specimen. At the opposite side a displacement along the axis of the specimen was imposed. The value of the final elongation imposed for each specimen is given in Table 24. For example:

- Figure 52 illustrates the displacement imposed on the right side of the TL2-type specimen #1383-11.
- Figure 53 illustrates the displacement imposed on the right side of the TRC-type specimen #1383-01-T.
- Figure 54 illustrates the displacement imposed on the right side of the PNNL-type specimen #IN168.

Table 24 – Elongations imposed on specimens.

| Specimen type | Specimen | Imposed elongation (mm) | Axial stress in the shank (MPa) |
|---------------|----------|-------------------------|---------------------------------|
| TL2 | 1383-20 | 1.154 | 392 |
| | 1383-23 | 1.901 | 400 |
| | 1383-22 | 1.901 | 400 |
| | 1383-27 | 5.753 | 453 |
| | 1383-26 | 11.39 | 521 |
| | 1383-19 | 5.824 | 450 |
| | 1383-16 | 0.724 | 380 |
| | 1588-16 | 27.09 | 700 |
| | 1383-21 | 23.34 | 660 |
| | 1383-28 | 16.77 | 590 |
| | 1383-29 | 5.540 | 448 |
| | 1383-11 | 0.320 | 350 |
| 1383-CEA | 0.320 | 350 | |
| TRC | 1383-01T | 0.640 | 406 |
| | 1383-02T | 0.094 | 316 |
| | 1383-03T | 0.154 | 333 |
| | 1383-04T | 0.375 | 376 |
| | D711-BS4 | 2.556 | 545 |
| PNNL | IN166 | 0.071 | 563 |
| | IN167 | 0.069 | 552 |
| | IN168 | 0.068 | 547 |
| | IN194 | 0.074 | 581 |
| | IN195 | 0.073 | 575 |
| | IN196 | 0.071 | 567 |
| | IN169 | 0.068 | 541 |
| | IN170 | 0.067 | 536 |
| | IN171 | 0.067 | 534 |
| | IN191 | 0.069 | 553 |
| | IN192 | 0.070 | 559 |
| | IN193 | 0.070 | 555 |
| | IN233 | 0.066 | 532 |
| | IN234 | 0.066 | 529 |
| IN235 | 0.066 | 532 | |



Figure 52 – Displacement field imposed on the TL2-type specimen #1383-11.

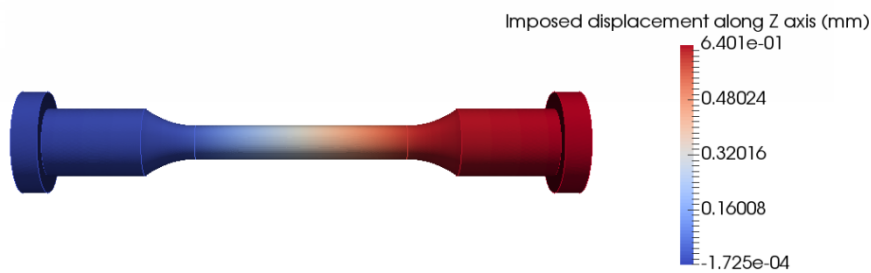


Figure 53 – Displacement field imposed on the TRC-type specimen #1383-01T.

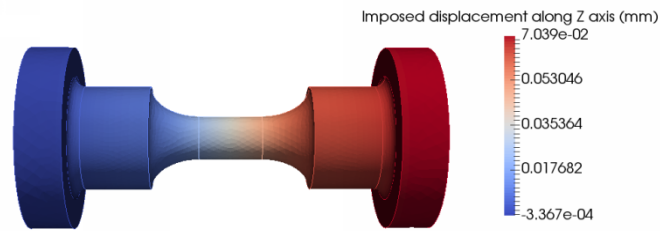


Figure 54 – Displacement field imposed on the PNNL-type specimen #IN168.

6.2.2. Stress and strain fields at the surface exposed to water

The maximal values of the von Mises and the principal stress reached at the surface of the specimens are detailed in Table 25. The von Mises stress is relevant for comparison with the stress measured during tensile tests. The maximal principal stress ($\max(\sigma^I)$) is relevant with regards to cracking; $\max(\sigma^I)$ is used by Code_Coriolis to predict initiation.

Stress and strain fields reached in specimen 1883-11 are illustrated in Figure 55 to Figure 57. Maximal von Mises stress in the shank is around 351 MPa, in agreement with the experimental value (Table 9). $\max(\sigma^I)$ reaches 497 MPa and is located at the head/shank junction. For comparison, the von Mises stress reaches 383 MPa at the same location. The maximal equivalent strain is around 3.3×10^{-3} (Figure 57). The design of the TL2-type specimen significantly promotes stress concentrations in the fillets. As a consequence, SCC initiation should be enhanced at this location.

Figure 58 and Figure 59 show that limited stress concentrations are reached in TRC- and PNNL-type specimens. Such designs are more convenient for SCC studies.

Table 25 – Maximal von Mises and principal stress reached at the surface of the specimens.

| Specimen | Max. von Mises equivalent stress (MPa) | Max. principal stress (MPa) |
|----------|--|-----------------------------|
| 1383-20 | 417 | 556 |
| 1383-23 | 424 | 568 |
| 1383-22 | 464 | 577 |
| 1383-27 | 464 | 577 |
| 1383-26 | 549 | 643 |
| 1383-19 | 464 | 614 |
| 1383-16 | 408 | 542 |
| 1588-16 | 730 | 907 |
| 1383-21 | 693 | 845 |
| 1383-28 | 622 | 817 |
| 1383-29 | 461 | 612 |
| 1383-11 | 383 | 497 |
| 1383-CEA | 383 | 497 |
| 1383-01T | 400 | 441 |
| 1383-02T | 317 | 408 |
| 1383-03T | 331 | 414 |
| 1383-04T | 370 | 419 |
| IN166 | 561 | 586 |
| IN167 | 551 | 575 |
| IN168 | 546 | 569 |
| IN194 | 570 | 596 |
| IN195 | 568 | 592 |
| IN196 | 564 | 588 |
| IN169 | 541 | 564 |
| IN170 | 536 | 558 |
| IN171 | 534 | 556 |
| IN191 | 551 | 576 |
| IN192 | 557 | 582 |
| IN193 | 553 | 578 |
| IN233 | 532 | 554 |
| IN234 | 530 | 552 |
| IN235 | 532 | 554 |

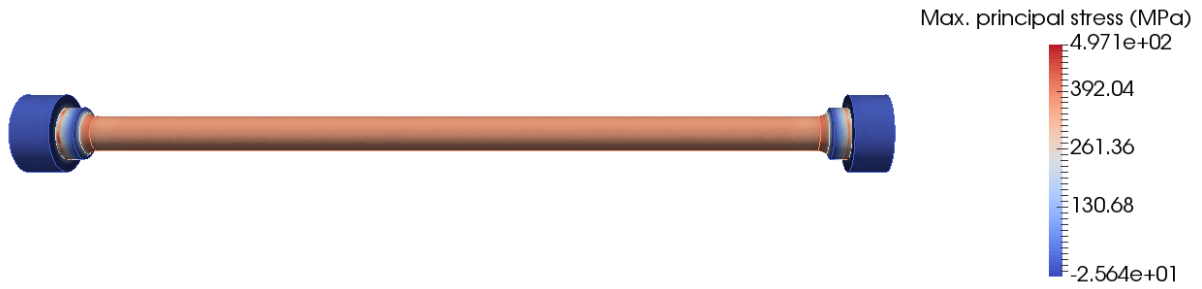


Figure 55 – Von Mises equivalent stress field in the TL2-type specimen #1383-11.

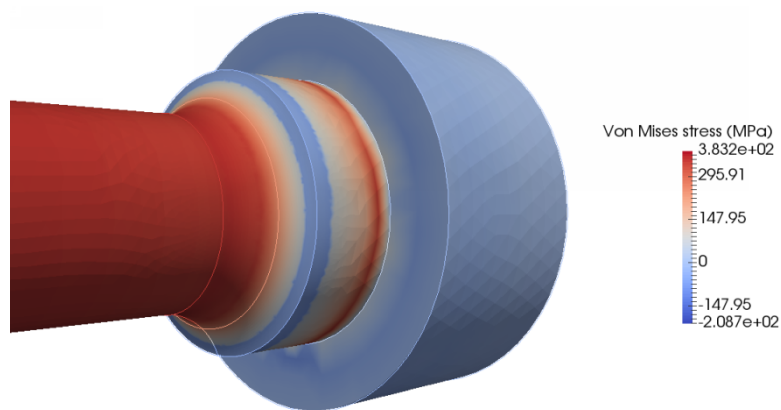


Figure 56 – Von Mises equivalent stress field in the TL2-type specimen #1383-11. Detailed view of the fillet.

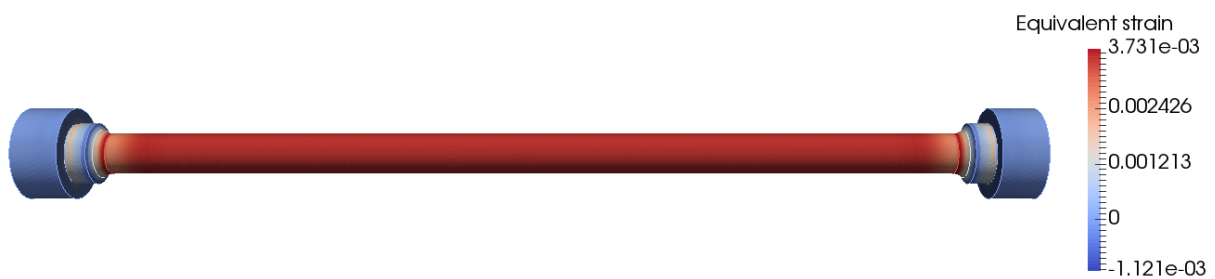


Figure 57 – Von Mises equivalent strain field in the TL2-type specimen #1383-11.

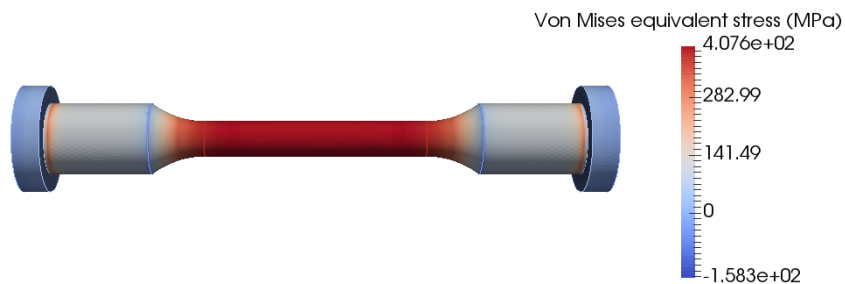


Figure 58 – Von Mises equivalent stress field in the TRC-type specimen #1383-01T.

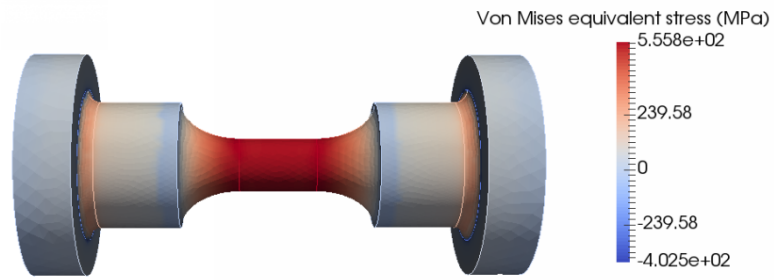


Figure 59 – Von Mises equivalent stress field in the PNNL-type specimen #IN168.

6.2.3. Calculation of K

In a first approach, K was calculated with the maximal principal stress σ and the crack depth a as follow:

$$K = 1.122 \times \sigma \times \sqrt{\pi a} \quad \text{Equation 47}$$

| | | |
|-----|---|--|
| MAI | Quantitative evaluation of the EDF local model and the EPRI-NRC xLPR models of crack initiation of the weld metals of Alloy 600 (Alloys 82 and 182) | 6125-4501-2018-00583-EN Version 2.0 |
|-----|---|--|

6.3. Algorithm for SCC prediction with Code_Coriolis

The algorithm to predict SCC is a coupling of previous behaviors. It follows the assumed successive stages of IGSCC as shown in Figure 60.

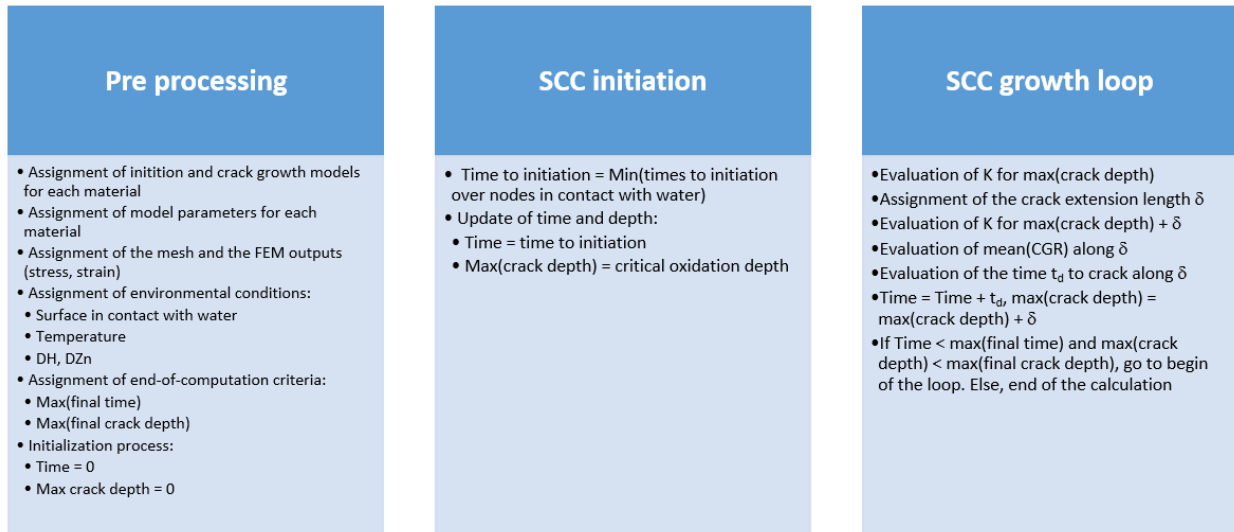


Figure 60 – General algorithm for the SCC computations with Code_Coriolis.

6.4. SCC predictions relying on the index initiation model and the sigmoid propagation law

Under the constraints of the Index Initiation Model, initiation was defined as the time to reach a crack depth of 5 μm , the lowest depth observed on cross sections after testing on EDF Alloy 182 registered RND-M-D-1054. Any observed crack depth beyond 5 μm was attributed to crack growth and modeled accordingly. The PNNL-tested specimens were monitored by DCPD with a detection threshold approximately 150 μm deep and the time to DCPD detection was less than the total testing time. Crack depths were not directly measured in cross section so the observed time to DCPD detection was defined as initiation with an assumed crack depth of 150 μm . Therefore, this assumed depth of 150 μm was modeled as a combination of initiation and crack growth.

6.4.1. Results on Alloy 182 registered RND-M-D-1054

Results of SCC predictions are given and compared to experimental results in Table 26. Details on SCC simulation results can be found in Appendix 2 for each specimen. For example, regarding the simulation of the test on specimen 1383-16 when the **index model** is coupled with the sigmoid law:

- Initiation is predicted after 2317 h, at the head/shank junction (Figure 61, Figure 62). The maximum principal stress at the initiation site is 428 MPa, which is significantly higher than the expected axial stress of 350 MPa in the shank. The histogram of the times to initiation (Figure 63) exhibits two peaks of time to initiation (one for the junction, one for the shank). The time to initiation field suggests that the design of the specimen is not convenient: it promotes initiation in areas other than the shank.
- The crack growth path followed by the tip of the main crack is shown (in transparency) in Figure 64. The crack extended in the shank, due to the lower stress in depth offered in the junction. The cracking kinetics is shown in Figure 65. The transition from slow to fast crack growth regime, when $K = K_{1SCC} = 12 \text{ MPa}\cdot\text{m}^{1/2}$, occurred after 4027 h. The transition happened at a depth of 199 μm , for a crack growth rate of 1.71 $\mu\text{m}\cdot\text{h}^{-1}$. At the experiment crack depth of 40 μm , $K = 5.4 \text{ MPa}\cdot\text{m}^{1/2}$ and $\text{CGR} = 0.08 \mu\text{m}\cdot\text{h}^{-1}$. Figure 66 shows the evolution of K with depth along the main cracking path. Figure 67 shows the crack growth law followed along the same

path. Both slow and fast regimes are involved. Figure 68 shows the initial stress level (before cracking) along the cracking path.

- The predicted time to reach 40 µm (experiment max crack depth) is 3592 h, which is about 1.5 time longer than testing time. Unfortunately, the prediction is not conservative.

Table 26 and Table 27 summarize results of the full data set. When initiation is predicted, most of the cracking time is dedicated to the slow crack growth. The time spent in the fast crack growth regime is very limited except for the tests on specimens 1383-21 and 1588-16 experiencing the highest stress.

Transitions from slow to fast crack growth regime happen at depths higher than ≈100 µm, except for the three highly loaded specimens.

A comparison of SCC predictions with observations is presented in Figure 69. Seven predictions out of thirteen are not conservative. Nevertheless, a large difference between observation and prediction is noticed only in three cases corresponding to very short crack depths. It means that parameters of the models have to be revised. Two ways of improvement can be easily proposed to better match observation:

- Adjust the material index.
- Improvement of the slow crack growth regime: current times spent in this regime can be several times higher than the full time to reach the maximal crack depth. It means that the slow crack growth rate is significantly underestimated. This correction will help to recover the conservatism of predictions.

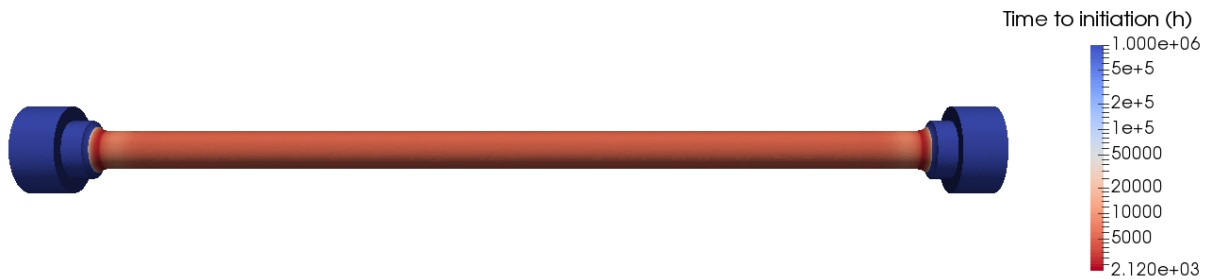


Figure 61 – Time to initiation field predicted for specimen 1383-16 (EDF weld registered RND-M-D-1054). Code_Coriolis prediction relying on the index model and the sigmoid growth law.

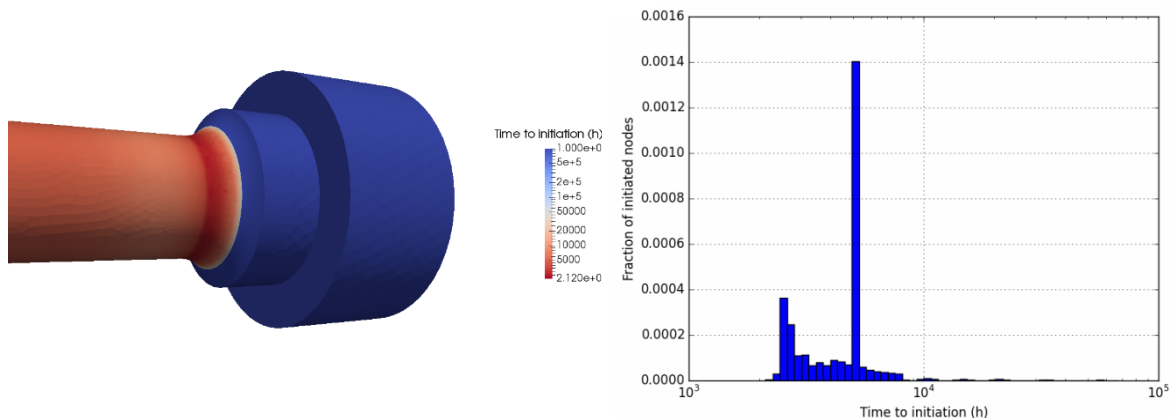


Figure 62 – Time to initiation field predicted for specimen 1383-16 (EDF weld registered RND-M-D-1054). Code_Coriolis prediction relying on the index model and the sigmoid growth law. Detailed view at the head/shank junction.

Figure 63 – Histogram of times to initiation predicted for specimen 1383-16 (EDF weld registered RND-M-D-1054). Code_Coriolis prediction relying on the index model and the sigmoid growth law.



Figure 64 – Crack growth path followed by the tip of the main crack predicted for specimen 1383-16 (EDF weld registered RND-M-D-1054). Code_Coriolis prediction relying on the index model and the sigmoid growth law. Detailed view at the head/shank junction.

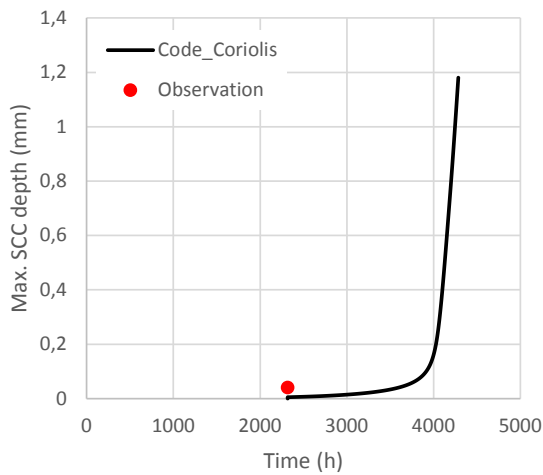


Figure 65 – Cracking kinetics predicted for specimen 1383-16 (EDF weld registered RND-M-D-1054). Code_Coriolis prediction relying on the index model and the sigmoid growth law.

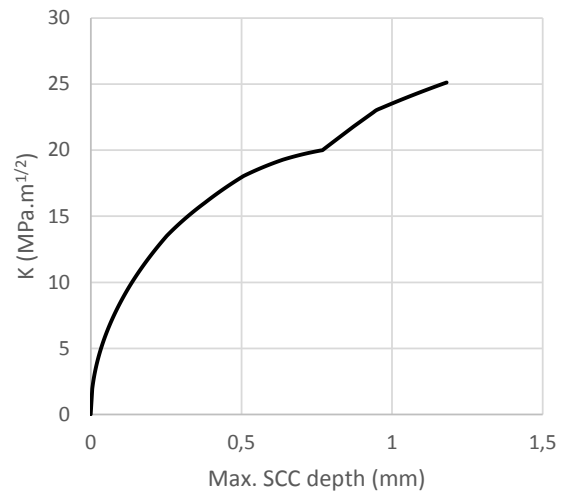


Figure 66 – K versus depth at the tip of the main crack predicted for specimen 1383-16 (EDF weld registered RND-M-D-1054). Code_Coriolis prediction relying on the index model and the sigmoid growth law.

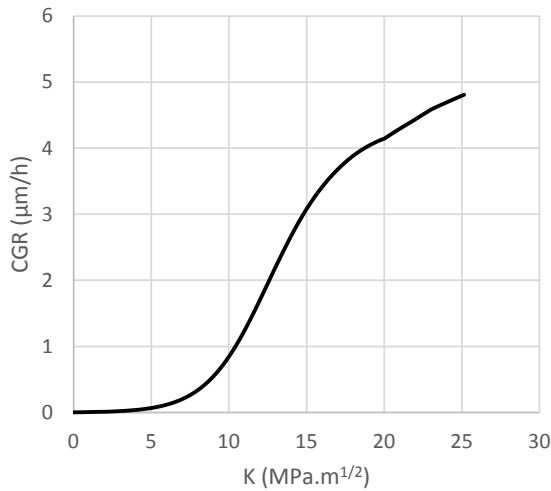


Figure 67 – Crack growth rate versus K at the tip of the main crack predicted for specimen 1383-16 (EDF weld registered RND-M-D-1054). Code_Coriolis prediction relying on the index model and the sigmoid growth law.

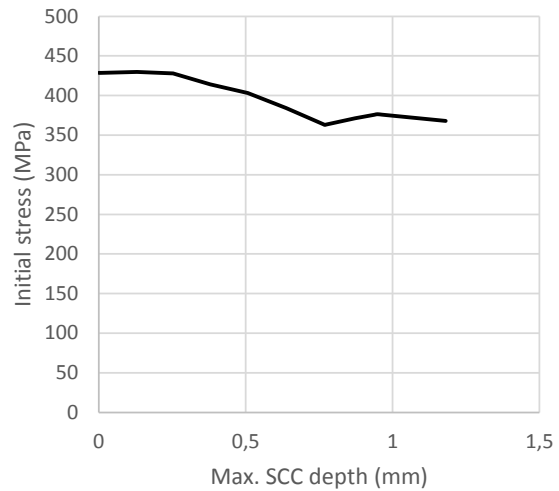


Figure 68 – Stress versus depth at the tip of the main crack predicted for specimen 1383-16 (EDF weld registered RND-M-D-1054). Code_Coriolis prediction relying on the index model and the sigmoid growth law.

Table 26 – Code_Coriolis predictions of the cracking times, depths and growth rates. EDF weld registered RND-M-D-1054. Simulations relying on the index model and the sigmoid growth law.

| Specimen | Experiment | | Simulation | | | | | | | | |
|----------|--------------|------------------|-----------------------|------------------------|--------------------------|-------------------------------|---------------------------------|---------------------------------|--|--|---|
| | Duration (h) | Crack depth (µm) | Initiation depth (µm) | Time to initiation (h) | Time to reach 150 µm (h) | Time to K _{1scc} (h) | Depth at K _{1scc} (µm) | CGR at K _{1scc} (µm/h) | Time to reach the experiment crack depth (h) | K for the experiment crack depth (MPa.m ^{1/2}) | CGR for the experiment crack depth (µm/h) |
| 1383-11 | 13365 | 1060 | 5 | 3811 | 5894 | 5970 | 234 | 1.65 | 6210 | 21.6 | 4.35 |
| 1383-16 | 12933 | 40 | 5 | 2317 | 3992 | 4027 | 199 | 1.71 | 3592 | 5.4 | 0.08 |
| 1383-19 | 5335 | 40 | 5 | 4880 | 7424 | 7476 | 185 | 0.8 | 6767 | 6 | 0.06 |
| 1383-20 | 722 | 0 | 5 | 1923 | 3452 | 3478 | 189 | 1.77 | 1923 | 0 | 0 |
| 1383-21 | 737 | 1129 | 5 | 422 | 748 | 732 | 75 | 3.09 | 855 | 46.9 | 13.43 |
| 1383-22 | 13456 | 0 | 5 | 1923 | 3452 | 3478 | 189 | 1.77 | 1923 | 0 | 0 |
| 1383-23 | 8626 | 0 | 5 | 1923 | 3452 | 3478 | 189 | 1.77 | 1923 | 0 | 0 |
| 1383-26 | 214 | 5 | 5 | 2271 | 3269 | 3255 | 123 | 1.61 | 2271 | 0 | 0 |
| 1383-27 | 190 | 12 | 5 | 5441 | 7385 | 7383 | 148 | 1.04 | 6241 | 3.4 | 0 |
| 1383-28 | 1000 | 120 | 5 | 176 | 425 | 418 | 98 | 5.24 | 421 | 13.2 | 6.94 |
| 1383-29 | 5200 | 50 | 5 | 874 | 1996 | 2018 | 183 | 1.79 | 1772 | 6.6 | 0 |
| 1383-CEA | 23771 | 1060 | 5 | 6699 | 9403 | 9502 | 234 | 1.27 | 9814 | 21.6 | 3.35 |
| 1588-16 | 120 | 1200 | 5 | 45 | 147 | 141 | 65 | 8.37 | 188 | 50.4 | 37.39 |

Table 27 – Code_Coriolis prediction of the duration of cracking stages. EDF weld registered RND-M-D-1054. Simulations relying on the index model and the sigmoid growth law.

| Specimen | Experiment | | Simulation | | | | DCPD detection |
|----------|--------------|------------------|--|------------------------|-----------------------------|-----------------------------|----------------|
| | Duration (h) | Crack depth (µm) | Time to reach the experiment crack depth (h) | Time to initiation (%) | Time in slow CGR regime (%) | Time in fast CGR regime (%) | |
| 1383-11 | 13365 | 1060 | 6210 | 61 | 35 | 4 | Yes |
| 1383-16 | 12933 | 40 | 3592 | 65 | 35 | 0 | No |
| 1383-19 | 5335 | 40 | 6767 | 72 | 28 | 0 | No |
| 1383-20 | 722 | 0 | 1923 | 100 | 0 | 0 | No |
| 1383-21 | 737 | 1129 | 855 | 49 | 36 | 14 | Yes |
| 1383-22 | 13456 | 0 | 1923 | 100 | 0 | 0 | No |
| 1383-23 | 8626 | 0 | 1923 | 100 | 0 | 0 | No |
| 1383-26 | 214 | 5 | 2271 | 100 | 0 | 0 | No |
| 1383-27 | 190 | 12 | 6241 | 87 | 13 | 0 | No |
| 1383-28 | 1000 | 120 | 421 | 42 | 57 | 1 | No |
| 1383-29 | 5200 | 50 | 1772 | 49 | 51 | 0 | No |
| 1383-CEA | 23771 | 1060 | 9814 | 68 | 29 | 3 | Yes |
| 1588-16 | 120 | 1200 | 188 | 24 | 51 | 25 | Yes |

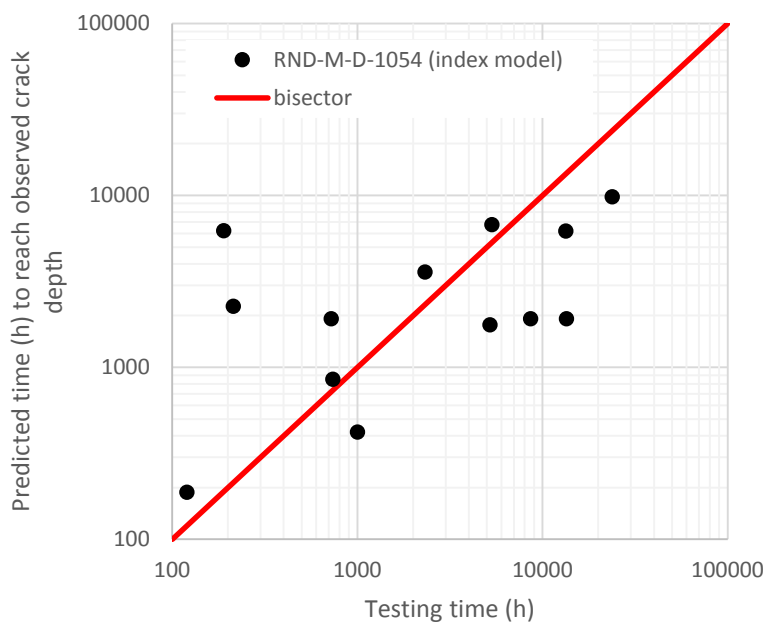


Figure 69 – Comparison between predicted time to reach experiment crack depth and testing time. EDF weld registered RND-M-D-1054. Code_Coriolis predictions relying on the index model and the sigmoid growth law.

6.4.2. Results on Alloy 82 registered RND-M-D-711

Results of SCC predictions are given and compared to experimental results in Table 28. The fastest cracking was predicted on specimen 1383-01T:

- Initiation is predicted after 35131 h, in the shank (Figure 70, Figure 71). The maximum principal

stress at the initiation site is of 403 MPa, which is very close to the expected axial stress of 406 MPa in the shank. The histogram of the times to initiation (Figure 72) exhibits a single peak of time to initiation, corresponding to the shank of the specimen. The tail of the histogram corresponds to longer times to initiation occurring at the head/shank junction. The initiation field confirms the convenient design of the specimen: initiation is promoted on the shank.

- The crack growth path followed by the tip of the main crack is shown (in transparency) in Figure 73. The crack extended in the shank. The cracking kinetics is shown in Figure 74. The transition from slow to fast crack growth regime, when $K = K_{1SCC} = 12 \text{ MPa}\cdot\text{m}^{1/2}$, occurred after 60803 h. The transition happened at a depth of 225 μm , for a crack growth rate of 0.14 $\mu\text{m}\cdot\text{h}^{-1}$. Figure 75 shows the evolution of K with depth along the main cracking path. Figure 76 shows the crack growth law followed along the same path. Only the slow regime is involved. Figure 77 illustrates the initial stress level (before cracking) along the cracking path.
- No cracking is predicted after 27,570 h, in agreement with the observation.

Table 28 and Table 29 summarize results of the full data set. When initiation is predicted, the cracking time dedicated to the slow crack growth is between 31% and 58% of the simulated time. Predicted times to DCPD detection are within the range 60,000 h to 356,000 h. None of the simulated cracks transitioned to the fast crack growth regime in less than 60,800 h.

More data is required to validate the current SCC models.

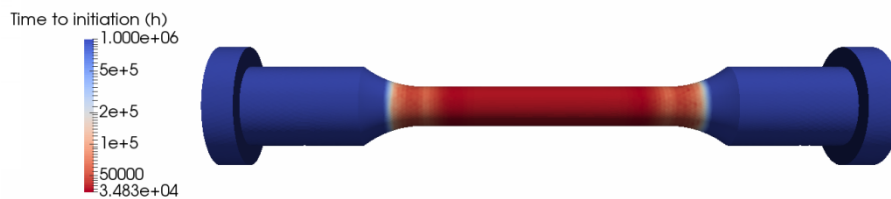


Figure 70 – Time to initiation field predicted for specimen 1383-01T (EDF weld registered RND-M-D-711). Code_Coriolis prediction relying on the index model and the sigmoid growth law.



Figure 71 – Time to initiation field predicted for specimen 1383-01T (EDF weld registered RND-M-D-711). Code_Coriolis prediction relying on the index model and the sigmoid growth law. Detailed view at the head/shank junction.

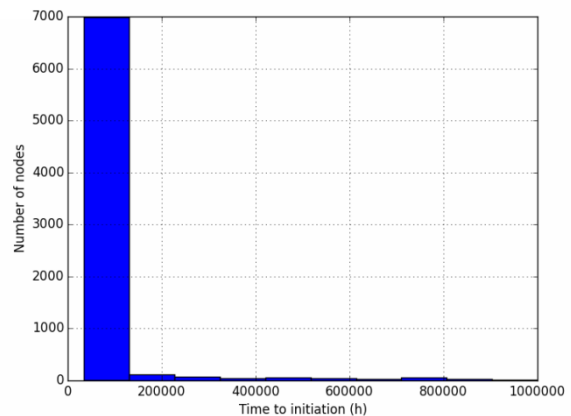


Figure 72 – Histogram of times to initiation predicted for specimen 1383-01T (EDF weld registered RND-M-D-711). Code_Coriolis prediction relying on the index model and the sigmoid growth law.

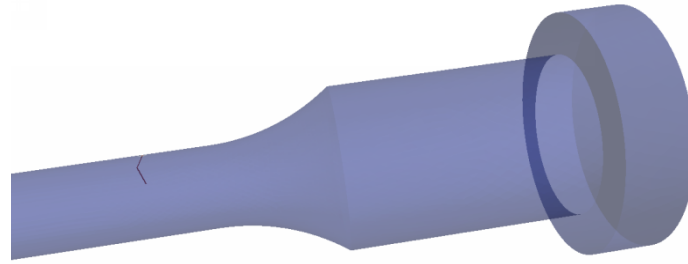


Figure 73 – Crack growth path followed by the tip of the main crack predicted for specimen 1383-01T (EDF weld registered RND-M-D-711). Code_Coriolis prediction relying on the index model and the sigmoid growth law. Detailed view at the head/shank junction.

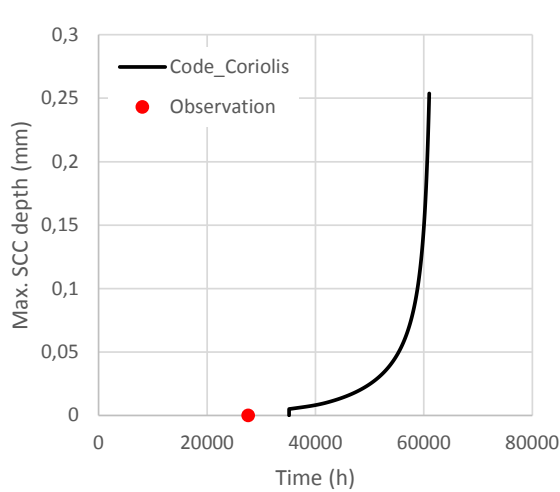


Figure 74 – Cracking kinetics predicted for specimen 1383-01T (EDF weld registered RND-M-D-711). Code_Coriolis prediction relying on the index model and the sigmoid growth law.

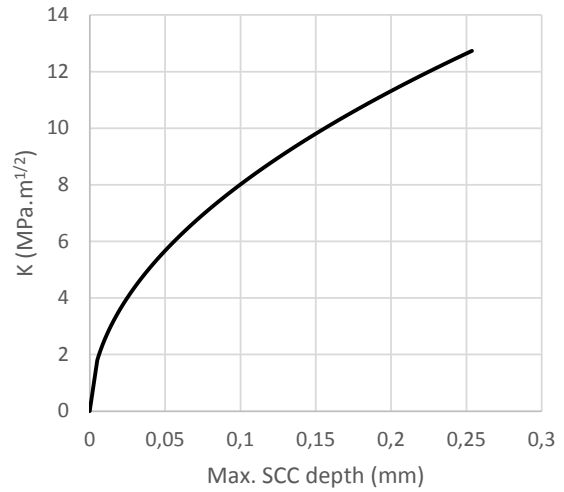


Figure 75 – K versus depth at the tip of the main crack predicted for specimen 1383-01T (EDF weld registered RND-M-D-711). Code_Coriolis prediction relying on the index model and the sigmoid growth law.

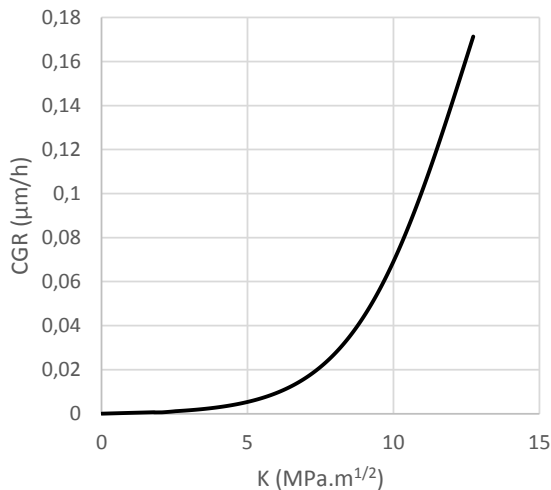


Figure 76 – Crack growth rate versus K at the tip of the main crack predicted for specimen 1383-01T (EDF weld registered RND-M-D-711). Code_Coriolis prediction relying on the index model and the sigmoid growth law.

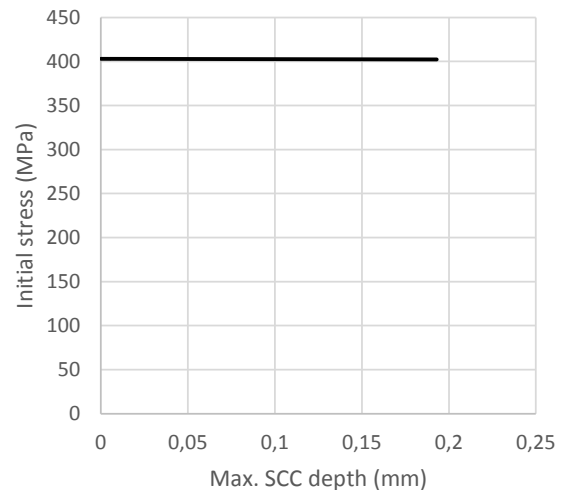


Figure 77 – Stress versus depth at the tip of the main crack predicted for specimen 1383-01T (EDF weld registered RND-M-D-711). Code_Coriolis prediction relying on the index model and the sigmoid growth law.

| | | |
|------------|---|--|
| MAI | Quantitative evaluation of the EDF local model and the EPRI-NRC xLPR models of crack initiation of the weld metals of Alloy 600 (Alloys 82 and 182) | 6125-4501-2018-00583-EN Version 2.0 |
|------------|---|--|

Table 28 – Code_Coriolis predictions of the cracking times, depths and growth rates. EDF weld registered RND-M-D-711. Simulations relying on the index model and the sigmoid growth law.

| Specimen | Experiment | | Simulation | | | | | | | | |
|-----------|--------------|------------------|-----------------------|------------------------|--------------------------|-------------------------------|---------------------------------|---------------------------------|--|--|---|
| | Duration (h) | Crack depth (µm) | Initiation depth (µm) | Time to initiation (h) | Time to reach 150 µm (h) | Time to K _{1scc} (h) | Depth at K _{1scc} (µm) | CGR at K _{1scc} (µm/h) | Time to reach the experiment crack depth (h) | K for the experiment crack depth (MPa.m ^{1/2}) | CGR for the experiment crack depth (µm/h) |
| 1383-01-T | 27570 | 0 | 5 | 35131 | 60017 | 60803 | 225 | 0.14 | - | - | - |
| 1383-02-T | 27570 | 0 | 5 | 151761 | 355944 | - | - | - | - | - | - |
| 1383-03-T | 27570 | 0 | 5 | 99984 | 144354 | 147508 | 319 | 0.11 | - | - | - |
| 1383-04-T | 27570 | 0 | 5 | 61126 | 94465 | 96050 | 265 | 0.13 | - | - | - |

Table 29 – Code_Coriolis prediction of the duration of cracking stages. EDF weld registered RND-M-D-711. Simulations relying on the index model and the sigmoid growth law.

| Specimen | Experiment | | Simulation | | | | |
|-----------|--------------|------------------|--|------------------------|-----------------------------|-----------------------------|----------------|
| | Duration (h) | Crack depth (µm) | Time to reach the experiment crack depth (h) | Time to initiation (%) | Time in slow CGR regime (%) | Time in fast CGR regime (%) | DCPD detection |
| 1383-01-T | 27570 | 0 | 35131 | 58 | 42 | 0 | No |
| 1383-02-T | 27570 | 0 | 151761 | 42 | 58 | 0 | No |
| 1383-03-T | 27570 | 0 | 99984 | 69 | 31 | 0 | No |
| 1383-04-T | 27570 | 0 | 61126 | 64 | 36 | 0 | No |

6.4.3. Results on PNNL Alloy 182 registered Studsvik 8001231

Results of SCC predictions are given and compared to experimental results in Table 30. Details on SCC simulation results can be found in Appendix 2 for each specimen. For example, regarding the simulation of the test on specimen IN171 when the **index model** is coupled with the sigmoid law:

- Initiation is predicted after 433 h, at the shank of the specimen (Figure 78 and Figure 79). The maximum principal stress at the initiation site is of 548 MPa, which is consistent with the expected axial stress of 534 MPa in the shank. The histogram of the times to initiation (Figure 80) exhibits two peaks of time to initiation, the first one corresponding to the shank. The time to initiation field suggests that the design of the specimen is convenient: it promotes initiation on the shank.
- The crack growth path followed by the tip of the main crack is shown (in transparency) in Figure 81. The crack extended in the shank, under a slightly decreasing stress. The cracking kinetics is shown in Figure 82. The transition from slow to fast crack growth regime, when $K = K_{1SCC} = 12 \text{ MPa}\cdot\text{m}^{1/2}$, occurred after 719 h. The transition happened at a depth of 128 μm , for a crack growth rate of 5.3 $\mu\text{m}\cdot\text{h}^{-1}$. At the experiment crack depth of 150 μm , $K = 12.9 \text{ MPa}\cdot\text{m}^{1/2}$ and $\text{CGR} = 6.7 \mu\text{m}\cdot\text{h}^{-1}$. Figure 83 shows the evolution of K with depth along the main cracking path. Figure 84 shows the crack growth law followed along the same path. Both slow and fast regimes are involved. Figure 85 shows the initial stress level (before cracking) along the cracking path.
- The predicted time to reach 150 μm (experiment crack depth to DCPD detection) is 723 h, which is about four times shorter than DCPD time to detection during testing. Therefore, the prediction underestimates the time to reach the crack depth at DCPD detection.

Table 30 and Table 31 summarize results of the full data set. The crack depths were not observed on cross sections after testing. Therefore, the comparison between experiment and simulation is limited to the comparison between the experiment and predicted times to DCPD detection, corresponding to a crack depth of 150 μm . Simulated times to reach a crack depth of 150 μm range from 572 h to 756 h. The depth criterion to stop the simulations was 200 μm . Typically, 50% of the simulated time (630 to 820 h) was dedicated to initiation, 35% was spent in the slow crack growth regime and 10% was dedicated to the fast crack growth.

Transitions from slow to fast crack growth regime happen at depths around 110-130 μm . The DCPD detection is predicted for specimens #IN171 and #IN235, in agreement with the observation. DCPD detection is also predicted for specimen #IN169 which is not consistent with the observation (Table 12).

A comparison of SCC predictions with observations is presented in Figure 86. The predicted times to reach the DCPD detection fall within a narrow range, due to the fact that applied loads are very close. By contrast, actual times to DCPD detections spread from 30 h to 2957 h. Nevertheless, the median time is at 62 h demonstrating that early initiation often occurs. Predictions are usually not conservative, showing that parameters of the models have to be tuned to better fit the susceptibility to SCC of this weld.

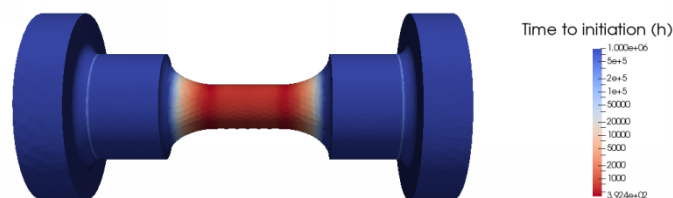


Figure 78 – Time to initiation field predicted for specimen IN171 (PNNL weld registered Studsvik 8001231). Code_Coriolis prediction relying on the index model and the sigmoid growth law.

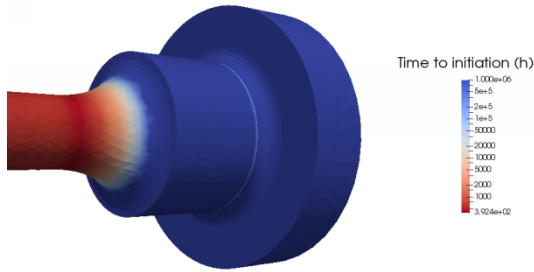


Figure 79 – Time to initiation field predicted for specimen IN171 (PNNL weld registered Studsvik 8001231). Code_Coriolis prediction relying on the index model and the sigmoid growth law. Detailed view at the head/shank junction.

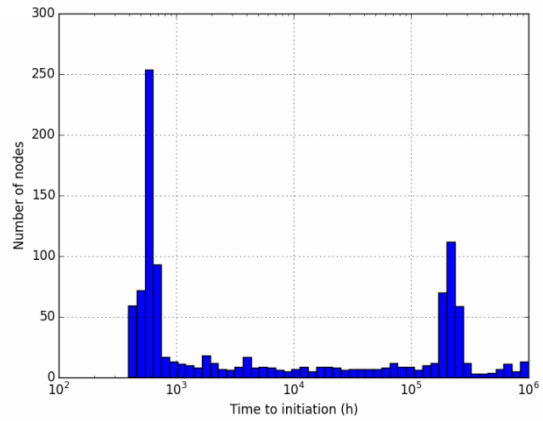


Figure 80 – Histogram of times to initiation predicted for specimen IN171 (PNNL weld registered Studsvik 8001231). Code_Coriolis prediction relying on the index model and the sigmoid growth law.

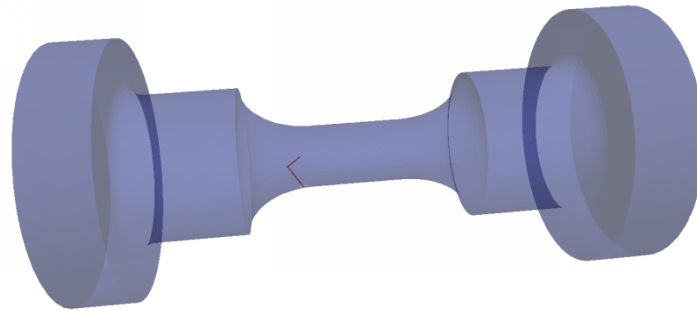


Figure 81 – Crack growth path followed by the tip of the main crack predicted for specimen IN171 (PNNL weld registered Studsvik 8001231). Code_Coriolis prediction relying on the index model and the sigmoid growth law. Detailed view at the head/shank junction.

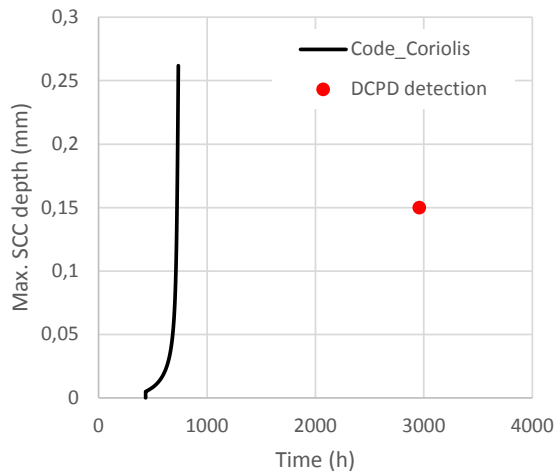


Figure 82 – Cracking kinetics predicted for specimen IN171 (PNNL weld registered Studsvik 8001231). Code_Coriolis prediction relying on the index model and the sigmoid growth law.

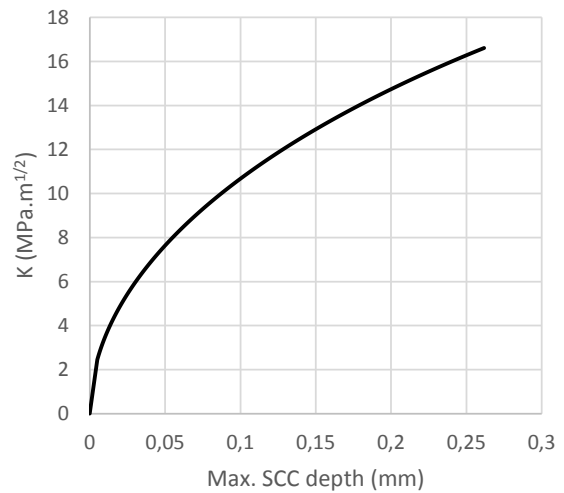


Figure 83 – K versus depth at the tip of the main crack predicted for specimen IN171 (PNNL weld registered Studsvik 8001231). Code_Coriolis prediction relying on the index model and the sigmoid growth law.

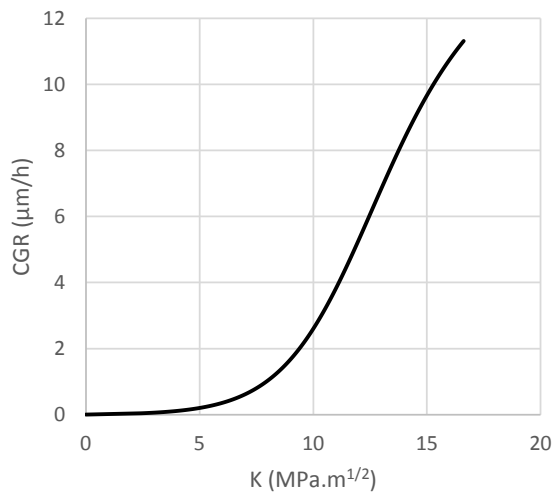


Figure 84 – Crack growth rate versus K at the tip of the main crack predicted for specimen IN171 (PNNL weld registered Studsvik 8001231). Code_Coriolis prediction relying on the index model and the sigmoid growth law.

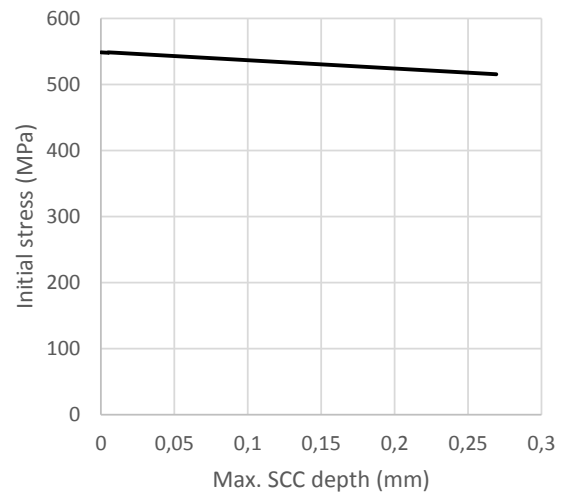


Figure 85 – Stress versus depth at the tip of the main crack predicted for specimen IN171 (PNNL weld registered Studsvik 8001231). Code_Coriolis prediction relying on the index model and the sigmoid growth law.

Table 30 – Code_Coriolis predictions of the cracking times, depths and growth rates. PNNL weld registered Studsvik 8001231. Simulations relying on the index model and the sigmoid growth law. NA: not available.

| Specimen | Experiment | | Simulation | | | | | | | | |
|----------|--------------|------------------|-----------------------|------------------------|--------------------------|------------------------|--------------------------|--------------------------|--|--|---|
| | Duration (h) | Crack depth (µm) | Initiation depth (µm) | Time to initiation (h) | Time to reach 150 µm (h) | Time to K_{1scc} (h) | Depth at K_{1scc} (µm) | CGR at K_{1scc} (µm/h) | Time to reach the experiment crack depth (h) | K for the experiment crack depth (MPa.m ^{1/2}) | CGR for the experiment crack depth (µm/h) |
| IN169 | 5126 | NA | 5 | 395 | 674 | 670 | 125 | 5.3 | - | - | - |
| IN170 | 30 | NA | 5 | 423 | 709 | 705 | 127 | 5.3 | - | - | - |
| IN171 | 2957 | NA | 5 | 433 | 723 | 719 | 128 | 5.3 | - | - | - |
| IN191 | 83 | NA | 5 | 343 | 603 | 598 | 116 | 5.3 | - | - | - |
| IN192 | 41 | NA | 5 | 319 | 572 | 566 | 113 | 5.3 | - | - | - |
| IN193 | 41 | NA | 5 | 334 | 592 | 587 | 115 | 5.3 | - | - | - |
| IN233 | 30 | NA | 5 | 444 | 736 | 733 | 129 | 5.3 | - | - | - |
| IN234 | 725 | NA | 5 | 459 | 756 | 752 | 131 | 5.3 | - | - | - |
| IN235 | 910 | NA | 5 | 444 | 736 | 733 | 129 | 5.3 | - | - | - |

Table 31 – Code_Coriolis prediction of the duration of cracking stages. PNNL weld registered Studsvik 8001231. Simulations relying on the index model and the sigmoid growth law. NA: not available.

| Specimen | Experiment | | Simulation | | | | |
|----------|--------------|------------------|--|------------------------|-----------------------------|-----------------------------|----------------|
| | Duration (h) | Crack depth (µm) | Time to reach the experiment crack depth (h) | Time to initiation (%) | Time in slow CGR regime (%) | Time in fast CGR regime (%) | DCPD detection |
| IN169 | 5126 | NA | 737 | 54 | 37 | 9 | Yes |
| IN170 | 30 | NA | 773 | 55 | 36 | 9 | Yes |
| IN171 | 2957 | NA | 786 | 55 | 36 | 9 | Yes |
| IN191 | 83 | NA | 662 | 52 | 39 | 10 | Yes |
| IN192 | 41 | NA | 630 | 51 | 39 | 10 | Yes |
| IN193 | 41 | NA | 651 | 51 | 39 | 10 | Yes |
| IN233 | 30 | NA | 800 | 56 | 36 | 8 | Yes |
| IN234 | 725 | NA | 820 | 56 | 36 | 8 | Yes |
| IN235 | 910 | NA | 800 | 56 | 36 | 8 | Yes |

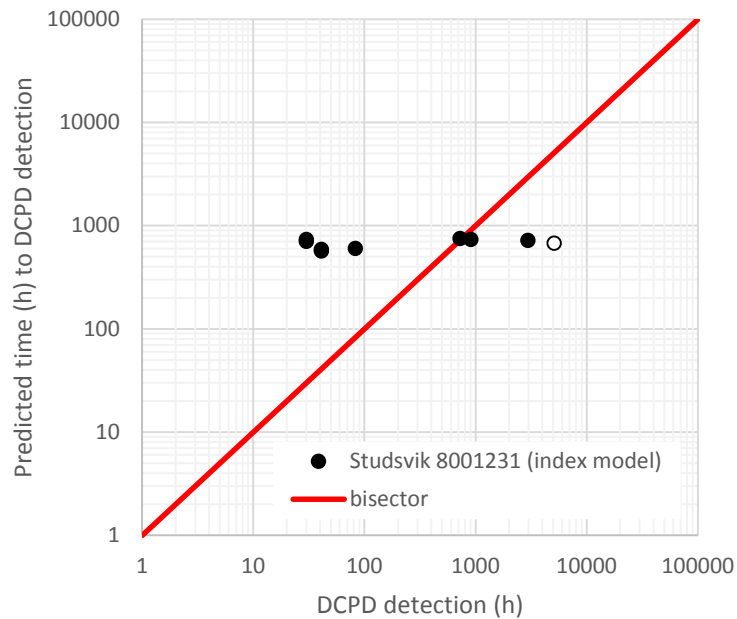


Figure 86 – Comparison between predicted time to reach experiment crack depth and testing time. PNNL weld registered Studsvik 8001231. Code_Coriolis predictions relying on the index model and the sigmoid growth law. Open symbol: no DCPD detection during testing (#IN169). Closed symbols: DCPD detection during testing.

6.4.4. Results on PNNL Alloy 182 registered KAPL 823030

Results of SCC predictions are given and compared to experimental results in Table 32. Details on SCC simulation results can be found in Appendix 2 for each specimen. For example, regarding the simulation of the test on specimen IN194 when the **index model** is coupled with the sigmoid law:

- Initiation is predicted after 274 h, at the shank of the specimen (Figure 87 and Figure 88). The maximum principal stress at the initiation site is 586 MPa, which is in good agreement with the expected axial stress of 581 MPa in the shank. The histogram of the times to initiation (Figure 89) exhibits three peaks of time to initiation, the first one corresponding to the shank. The time to initiation field suggests that the design of the specimen is convenient: it promotes initiation on the shank.
- The crack growth path followed by the tip of the main crack is shown (in transparency) in Figure 90. The crack extended in the shank, under a slightly decreasing stress. The cracking kinetics is shown in Figure 91. The transition from slow to fast crack growth regime, when $K = K_{1SCC} = 12 \text{ MPa}\cdot\text{m}^{1/2}$, occurred after 506 h. The transition happened at a depth of 108 μm , for a crack growth rate of 1.72 $\mu\text{m}\cdot\text{h}^{-1}$. At the experiment crack depth of 150 μm , $K = 14.0 \text{ MPa}\cdot\text{m}^{1/2}$ and CGR = 8.4 $\mu\text{m}\cdot\text{h}^{-1}$. Figure 92 shows the evolution of K with depth along the main cracking path. Figure 93 shows the crack growth law followed along the same path. Both slow and fast regimes are involved. Figure 94 displays the initial stress level (before cracking) along the cracking path.
- The predicted time to reach 150 μm (experiment crack depth to DCPD detection) is 512 h, which is more than 3 times shorter than DCPD time to detection during testing. Therefore, the prediction underestimate the time to DCPD detection.

Table 32 and Table 33 summarize results of the full data set. The crack depths were not observed on cross sections after testing. Therefore, the comparison between experiment and simulation is limited to the comparison between the experiment and predicted times to DCPD detection, corresponding to a crack depth of 150 μm . Simulated times to reach a crack depth of 150 μm range from 512 h to 640 h. The depth criterion to stop the simulations was 200 μm . Typically, 50% of the simulated time (569 to 703 h) was dedicated to initiation, 40% was spent in the slow crack growth regime and 10% was dedicated to the fast crack growth.

Transitions from the slow to fast crack growth regime happen at depths around 110-120 μm . The DCPD detection predictions are in agreement with the observation.

A comparison of SCC predictions with observations is presented in Figure 95. Predicted times to reach the DCPD detection fall within a narrow range because applied loads are very close. By contrast, actual times to DCPD detections spread from 30 h to 1635 h, with a median time at 1625 h demonstrating that early initiation may occurs. 50% of the predictions are underestimating the cracking, showing that parameters of the models have to be tuned to better fit the susceptibility to SCC of this weld.

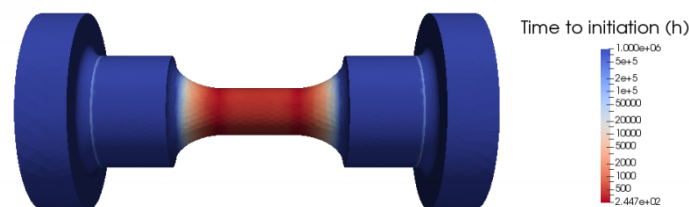


Figure 87 – Time to initiation field predicted for specimen IN194 (PNNL weld registered KAPL 823030). Code_Coriolis prediction relying on the index model and the sigmoid growth law.

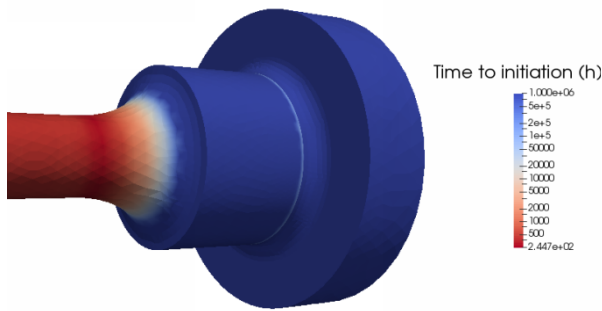


Figure 88 – Time to initiation field predicted for specimen IN194 (PNNL weld registered KAPL 823030). Code_Coriolis prediction relying on the index model and the sigmoid growth law. Detailed view at the head/shank junction.

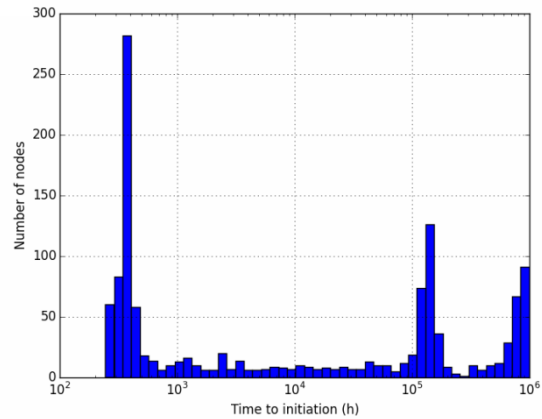


Figure 89 – Histogram of times to initiation predicted for specimen IN194 (PNNL weld registered KAPL 823030). Code_Coriolis prediction relying on the index model and the sigmoid growth law.

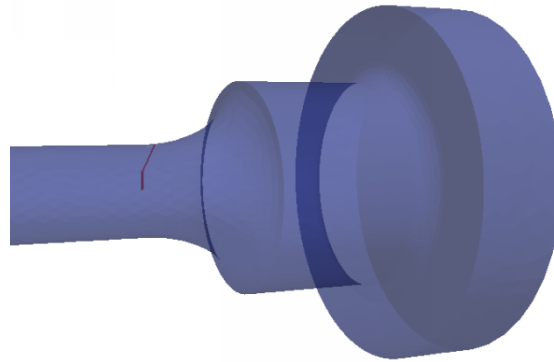


Figure 90 – Crack growth path followed by the tip of the main crack predicted for specimen IN194 (PNNL weld registered KAPL 823030). Code_Coriolis prediction relying on the index model and the sigmoid growth law. Detailed view at the head/shank junction.

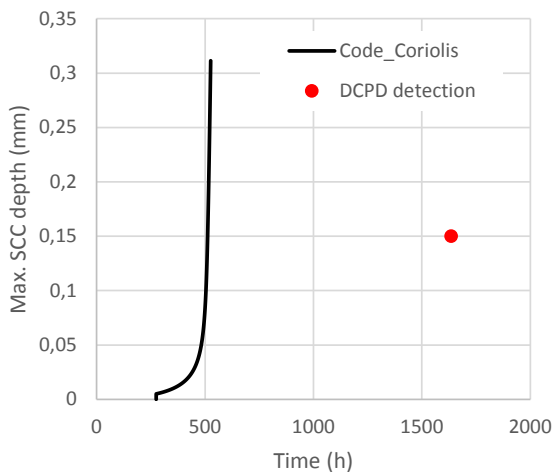


Figure 91 – Cracking kinetics predicted for specimen IN194 (PNNL weld registered KAPL 823030). Code_Coriolis prediction relying on the index model and the sigmoid growth law.

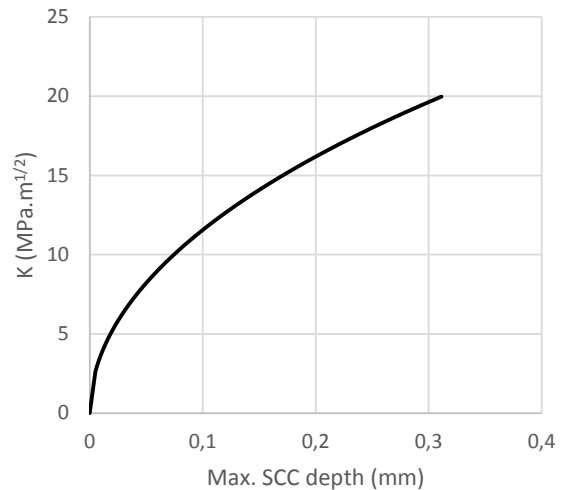


Figure 92 – K versus depth at the tip of the main crack predicted for specimen IN194 (PNNL weld registered KAPL 823030). Code_Coriolis prediction relying on the index model and the sigmoid growth law.

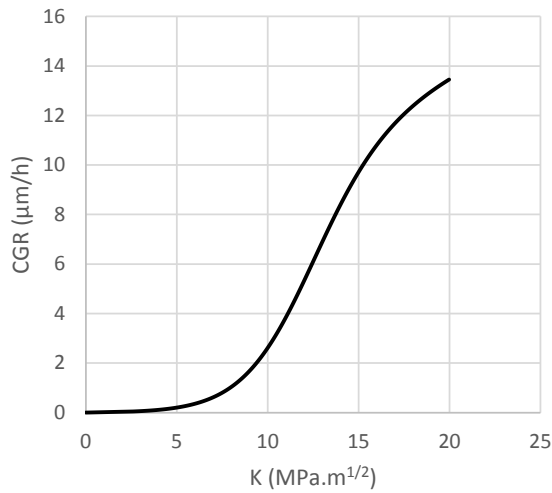


Figure 93 – Crack growth rate versus K at the tip of the main crack predicted for specimen IN194 (PNNL weld registered KAPL 823030). Code_Coriolis prediction relying on the index model and the sigmoid growth law.

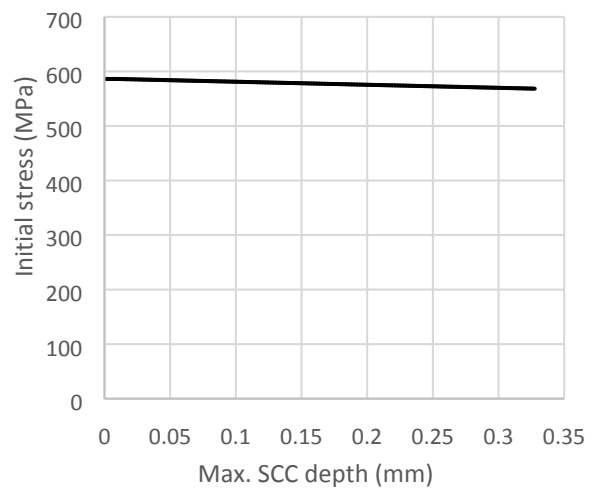


Figure 94 – Stress versus depth at the tip of the main crack predicted for specimen IN194 (PNNL weld registered KAPL 823030). Code_Coriolis prediction relying on the index model and the sigmoid growth law.

Table 32 – Code_Coriolis predictions of the cracking times, depths and growth rates. PNNL weld registered KAPL 823030. Simulations relying on the index model and the sigmoid growth law. NA: not available.

| Specimen | Experiment | | Simulation | | | | | | | | |
|----------|--------------|------------------|-----------------------|------------------------|--------------------------|-------------------------------|---------------------------------|---------------------------------|--|--|---|
| | Duration (h) | Crack depth (µm) | Initiation depth (µm) | Time to initiation (h) | Time to reach 150 µm (h) | Time to K _{1scc} (h) | Depth at K _{1scc} (µm) | CGR at K _{1scc} (µm/h) | Time to reach the experiment crack depth (h) | K for the experiment crack depth (MPa.m ^{1/2}) | CGR for the experiment crack depth (µm/h) |
| IN166 | 30 | NA | 5 | 305 | 554 | 548 | 112 | 5,31 | - | - | - |
| IN167 | 30 | NA | 5 | 346 | 607 | 602 | 116 | 5,30 | - | - | - |
| IN168 | 113 | NA | 5 | 369 | 640 | 636 | 122 | 5,30 | - | - | - |
| IN194 | 1635 | NA | 5 | 274 | 512 | 506 | 108 | 5,31 | - | - | - |
| IN195 | 1625 | NA | 5 | 284 | 524 | 518 | 109 | 5,31 | - | - | - |
| IN196 | 1642 | NA | 5 | 297 | 542 | 537 | 111 | 5,31 | - | - | - |

Table 33 – Code_Coriolis prediction of the duration of cracking stages. PNNL weld registered KAPL 823030. Simulations relying on the index model and the sigmoid growth law. NA: not available.

| Specimen | Experiment | | Simulation | | | | |
|----------|--------------|------------------|--|------------------------|-----------------------------|-----------------------------|----------------|
| | Duration (h) | Crack depth (µm) | Time to reach the experiment crack depth (h) | Time to initiation (%) | Time in slow CGR regime (%) | Time in fast CGR regime (%) | DCPD detection |
| IN166 | 30 | NA | 612 | 50 | 40 | 10 | Yes |
| IN167 | 30 | NA | 666 | 52 | 38 | 10 | Yes |
| IN168 | 113 | NA | 703 | 52 | 38 | 10 | Yes |
| IN194 | 1635 | NA | 569 | 48 | 41 | 11 | Yes |
| IN195 | 1625 | NA | 582 | 49 | 40 | 11 | Yes |
| IN196 | 1642 | NA | 600 | 50 | 40 | 11 | Yes |

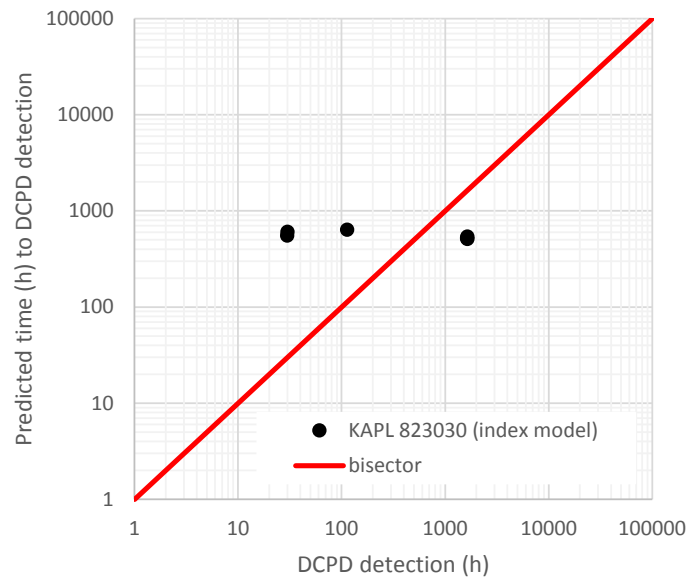


Figure 95 – Comparison between predicted time to reach the experiment crack depth and testing time. PNNL weld registered KAPL 823030. Code_Coriolis predictions relying on the index model and the sigmoid growth law.

6.5. SCC predictions relying on the local initiation model and the sigmoid propagation law

Under the constraints of the Local Initiation Model, initiation was defined as the time to fail a grain boundary oxidized on a depth of 200 nm, in agreement with observations on EDF Alloy 182 registered RND-M-D-1054. An initiation depth of 200 nm was assumed and any observed crack depth beyond 200 nm was attributed to crack growth and modeled accordingly. The PNNL-tested specimens were monitored by DCPD with a detection threshold approximately 150 μm deep and the time to DCPD detection was less than the total testing time. Crack depths were not directly measured in cross section so the observed time to DCPD detection was defined as initiation with an assumed crack depth of 150 μm . Therefore, this assumed depth of 150 μm was modeled as a combination of initiation and crack growth.

6.5.1. Results on Alloy 182 registered RND-M-D-1054

Results of SCC predictions are given and compared to experimental results in Table 34. Details on SCC simulation results can be found in Appendix 2 for each specimen. For example, regarding the simulation of the test on specimen 1383-16 when the **local model** is coupled with the sigmoid law:

- Initiation is predicted after 2 h, at the head/shank junction (Figure 96, Figure 97). The maximum principal stress at the initiation site is of 411 MPa, which is significantly higher than the expected axial stress of 350 MPa in the shank. The histogram of the times to initiation (Figure 98) exhibits two peaks of time to initiation (one for the junction, one for the shank). The time to initiation field suggests that the design of the specimen is not convenient because it promotes initiation in areas other than the shank. However, the probability to initiate within the shank cannot be fully excluded.
- The crack growth path followed by the tip of the main crack is shown (in transparency) in Figure 99. The crack extended in the shank, under a decreasing stress. The cracking kinetics is shown in Figure 100. The transition from slow to fast crack growth regime, when $K = K_{1\text{SCC}} = 12 \text{ MPa}\cdot\text{m}^{1/2}$, occurred after 2972 h. The transition happened at a depth of 223 μm , for a crack growth rate of 1.73 $\mu\text{m}\cdot\text{h}^{-1}$. At the experiment crack depth of 40 μm , $K = 5.2 \text{ MPa}\cdot\text{m}^{1/2}$ and CGR = 0.07 $\mu\text{m}\cdot\text{h}^{-1}$. Figure 101 shows the evolution of K with depth along the main cracking path. Figure 102 shows the crack growth law followed along the same path. Both slow and fast

regimes are involved. Figure 103 shows the initial stress level (before cracking) along the cracking path.

- The predicted time to reach 40 µm (experiment max crack depth) is 2436 h, which is very close to the testing time. Therefore, the prediction is good.

Table 34 and Table 35 summarize results of the full data set. When initiation is predicted, most of the cracking time is dedicated to the slow crack growth. The longest time spent in the fast crack growth regime is limited to 17%.

Initiation is always predicted, including for the lowest applied stress (350 MPa) for which no crack was reported after optical microscopy on cross sections. Complementary examinations at higher magnifications may be relevant, to confirm the actual absence of initiation and to evaluate the intergranular oxide depth.

Transitions from slow to fast crack growth regime happen at depths ranging from 73 µm to 563 µm.

A comparison of SCC predictions with observations is presented in Figure 104. Current predictions overestimate the time to reach the experiment crack depth when the testing time was lower than 1000 h. For longer testing times, the predicted times are close or shorter than the experiment times. Therefore, the current local model seems more convenient for SCC predictions under long exposures to the primary water than for brief exposures.

Parameters of the models could be revised to better match observation:

- Improvement of the slow crack growth regime: current times spent in this regime can be significantly larger than the full time to reach the experiment maximal crack depth. It means that the slow crack growth rate is underestimated. This correction will help to more accurately predict the time to experiment crack depth.
- Improvement of the intergranular oxidation kinetics, based on complementary surface examinations. Indeed, current intergranular oxidation kinetics may be overestimated.
- Improvement of the initiation criterion:
 - The stress to fail oxidized grain boundaries may be underestimated: new cracking tests should be performed.
 - The stress concentration at grain boundaries may be overestimated: new FEM calculations on polycrystalline aggregates should be conducted.

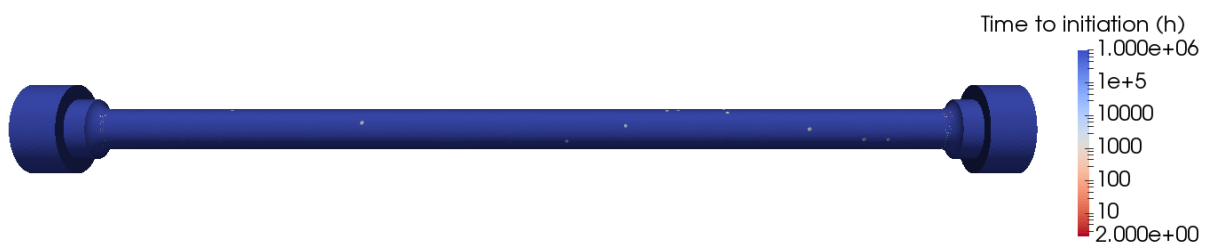


Figure 96 – Time to initiation field predicted for specimen 1383-16 (EDF weld registered RND-M-D-1054). Code_Coriolis prediction relying on the local model and the sigmoid growth law.

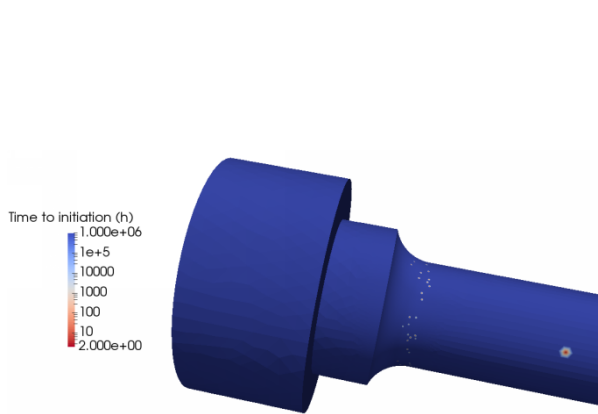


Figure 97 – Time to initiation field predicted for specimen 1383-16 (EDF weld registered RND-M-D-1054). Code_Coriolis prediction relying on the local model and the sigmoid growth law. Detailed view at the head/shank junction.

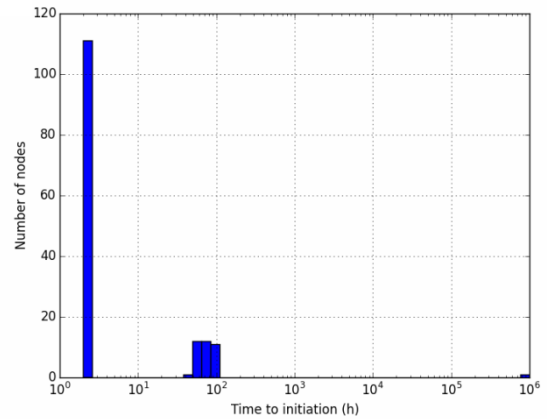


Figure 98 – Histogram of times to initiation predicted for specimen 1383-16 (EDF weld registered RND-M-D-1054). Code_Coriolis prediction relying on the local model and the sigmoid growth law.

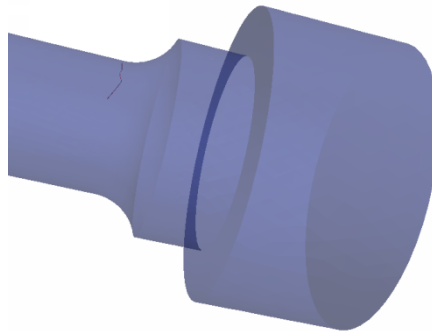


Figure 99 – Crack growth path followed by the tip of the main crack predicted for specimen 1383-16 (EDF weld registered RND-M-D-1054). Code_Coriolis prediction relying on the local model and the sigmoid growth law. Detailed view at the head/shank junction.

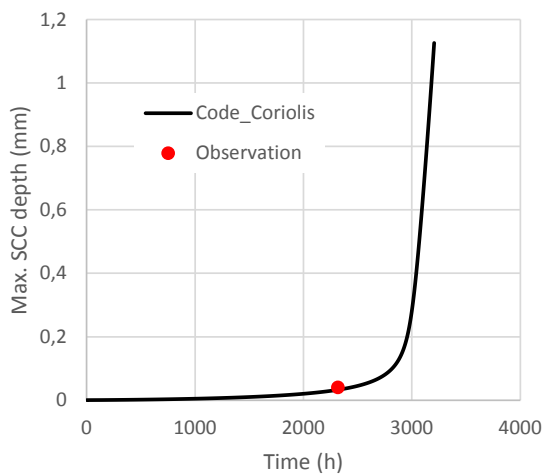


Figure 100 – Cracking kinetics predicted for specimen 1383-16 (EDF weld registered RND-M-D-1054). Code_Coriolis prediction relying on the local model and the sigmoid growth law.

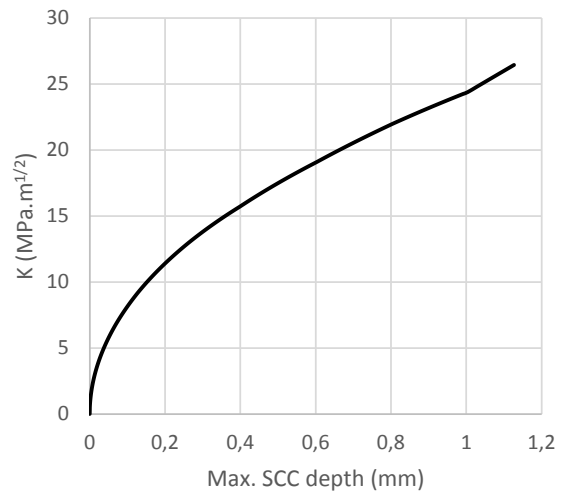


Figure 101 – K versus depth at the tip of the main crack predicted for specimen 1383-16 (EDF weld registered RND-M-D-1054). Code_Coriolis prediction relying on the local model and the sigmoid growth law.

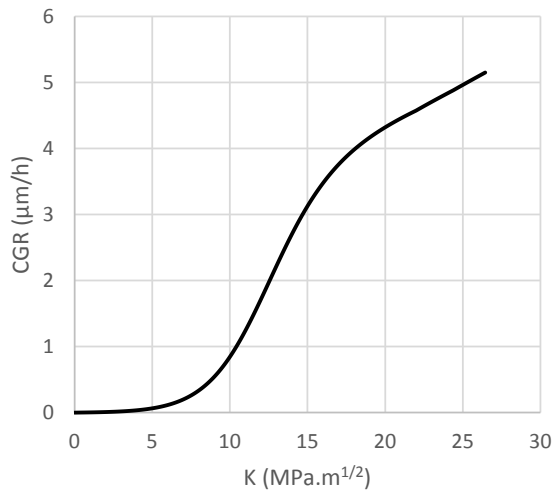


Figure 102 – Crack growth rate versus K at the tip of the main crack predicted for specimen 1383-16 (EDF weld registered RND-M-D-1054). Code_Coriolis prediction relying on the local model and the sigmoid growth law.

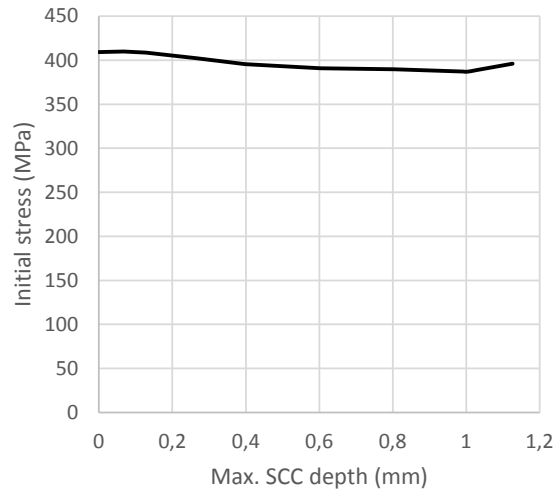


Figure 103 – Stress versus depth at the tip of the main crack predicted for specimen 1383-16 (EDF weld registered RND-M-D-1054). Code_Coriolis prediction relying on the local model and the sigmoid growth law.

Table 34 – Code_Coriolis predictions of the cracking times, depths and growth rates. EDF weld registered RND-M-D-1054. Simulations relying on the local model and the sigmoid growth law.

| Specimen | Experiment | | Simulation | | | | | | | | |
|----------|--------------|------------------|-----------------------|------------------------|--------------------------|-------------------------------|---------------------------------|---------------------------------|--|--|---|
| | Duration (h) | Crack depth (µm) | Initiation depth (µm) | Time to initiation (h) | Time to reach 150 µm (h) | Time to K _{1scc} (h) | Depth at K _{1scc} (µm) | CGR at K _{1scc} (µm/h) | Time to reach the experiment crack depth (h) | K for the experiment crack depth (MPa.m ^{1/2}) | CGR for the experiment crack depth (µm/h) |
| 1383-11 | 13365 | 1060 | 0.2 | 2 | 3254 | 3330 | 233 | 1.66 | 3578 | 21.4 | 4.32 |
| 1383-16 | 12933 | 40 | 0.2 | 2 | 2912 | 2972 | 223 | 1.73 | 2436 | 5.2 | 0.07 |
| 1383-19 | 5335 | 40 | 0.2 | 37 | 8643 | 11249 | 563 | 0.8 | 6756 | 4.6 | 0.02 |
| 1383-20 | 722 | 0 | 0.2 | 2 | 2623 | 2659 | 199 | 1.78 | 2 | 0 | 0 |
| 1383-21 | 737 | 1129 | 0.2 | 37 | 2833 | 2887 | 196 | 0.94 | 3440 | 29.1 | 2.7 |
| 1383-22 | 13456 | 0 | 0.2 | 2 | 2674 | 2725 | 224 | 2.08 | 2 | 0 | 0 |
| 1383-23 | 8626 | 0 | 0.2 | 2 | 2621 | 2666 | 218 | 2.06 | 2 | 0 | 0 |
| 1383-26 | 214 | 5 | 0.2 | 37 | 1888 | 1878 | 133 | 1.66 | 856 | 2.3 | 0 |
| 1383-27 | 190 | 12 | 0.2 | 37 | 3542 | 3553 | 164 | 1.09 | 2185 | 3.2 | 0 |
| 1383-28 | 1000 | 120 | 0.2 | 2 | 1694 | 1714 | 184 | 1.87 | 1670 | 10.2 | 1.02 |
| 1383-29 | 5200 | 50 | 0.2 | 2 | 1529 | 1533 | 159 | 2.45 | 1391 | 6.6 | 0.24 |
| 1383-CEA | 23771 | 1060 | 0.2 | 4 | 4258 | 4359 | 235 | 1.27 | 4694 | 19.7 | 3.15 |
| 1588-16 | 120 | 1200 | 0.2 | 2 | 210 | 204 | 73 | 8.21 | 246 | 48.2 | 38.3 |

Table 35 – Code_Coriolis prediction of the duration of cracking stages. EDF weld registered RND-M-D-1054. Simulations relying on the local model and the sigmoid growth law.

| Specimen | Experiment | | Simulation | | | | DCPD detection |
|----------|--------------|------------------|--|------------------------|-----------------------------|-----------------------------|----------------|
| | Duration (h) | Crack depth (µm) | Time to reach the experiment crack depth (h) | Time to initiation (%) | Time in slow CGR regime (%) | Time in fast CGR regime (%) | |
| 1383-11 | 13365 | 1060 | 3578 | 0 | 93 | 7 | Yes |
| 1383-16 | 12933 | 40 | 2436 | 0 | 100 | 0 | No |
| 1383-19 | 5335 | 40 | 6756 | 1 | 99 | 0 | No |
| 1383-20 | 722 | 0 | 2 | 100 | 0 | 0 | No |
| 1383-21 | 737 | 1129 | 3440 | 1 | 83 | 16 | Yes |
| 1383-22 | 13456 | 0 | 2 | 100 | 0 | 0 | No |
| 1383-23 | 8626 | 0 | 2 | 100 | 0 | 0 | No |
| 1383-26 | 214 | 5 | 856 | 4 | 96 | 0 | No |
| 1383-27 | 190 | 12 | 2185 | 2 | 98 | 0 | No |
| 1383-28 | 1000 | 120 | 1670 | 0 | 100 | 0 | No |
| 1383-29 | 5200 | 50 | 1391 | 0 | 100 | 0 | No |
| 1383-CEA | 23771 | 1060 | 4694 | 0 | 93 | 7 | Yes |
| 1588-16 | 120 | 1200 | 246 | 1 | 82 | 17 | Yes |

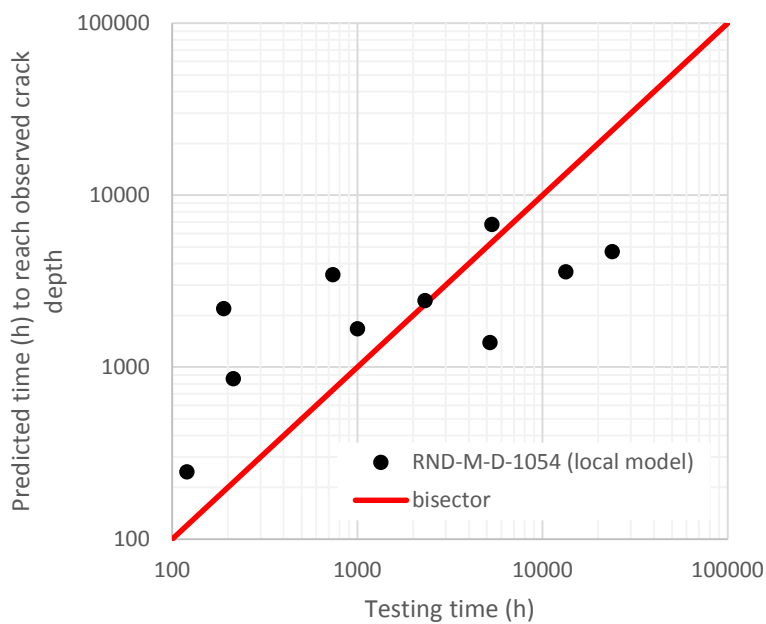


Figure 104 – Comparison between predicted time to reach the experiment crack depth and testing time. EDF weld registered RND-M-D-1054. Code_Coriolis predictions relying on the local model and the sigmoid growth law.

6.5.2. Results on Alloy 82 registered RND-M-D-711

Results of SCC predictions are given and compared to experimental results in Table 36. Details on SCC simulation results can be found in Appendix 2 for each specimen. For example, regarding the simulation of the test on specimen 1383-01T when the **local model** is coupled with the sigmoid law:

- Initiation is predicted after 2 h, on the shank, close to the fillet (Figure 105, Figure 106). The maximum principal stress at the initiation site is 377 MPa, which is lower than the expected axial stress of 406 MPa in the shank. The histogram of the times to initiation (Figure 107) shows that initiation can occur early. Initiation sites are all located on the shank.
- The crack growth path followed by the tip of the main crack is shown (in transparency) in Figure 108. The cracking kinetics is shown in Figure 109. The transition from the slow to fast crack growth regime ($K = 12 \text{ MPa}\cdot\text{m}^{1/2}$) occurred after only 3839 h. The transition happened at a depth of 227 μm , for a crack growth rate of 1.41 $\mu\text{m}\cdot\text{h}^{-1}$. Figure 110 shows the evolution of K with depth along the main cracking path. Figure 111 shows the crack growth law followed along the same path. Both slow and fast regimes are involved. Figure 112 shows the initial stress level (before cracking) along the cracking path. The cracking kinetics is too rapid to be realistic due to the too fast crack growth rate.
- The predicted time to reach a 150 μm -deep crack (DCPD detectable) is 3757 h.

Table 36 and Table 37 summarize results of the full data set. When initiation is predicted (specimen #1383-01-T), the cracking time is almost fully dedicated to the slow crack growth. The DCPD detection is predicted.

Predictions are not fully consistent with observations: a fast cracking is predicted on specimen #1383-01-T while no cracking was noticed during testing after more than 27000 h. The overestimation of the cracking kinetics may be due to the overestimation of the grain boundary oxidation kinetics. Regarding the three other specimens, no initiation is predicted, in agreement with the experiment. More data are required to validate the current local model and to better fit the crack growth parameters: a larger activation energy ($140 \text{ kJ}\cdot\text{mol}^{-1}$) and a lower dependency to K may be more relevant.



Figure 105 – Time to initiation field predicted for specimen 1383-01T (EDF weld registered RND-M-D-711). Code_Coriolis prediction relying on the local model and the sigmoid growth law.



Figure 106 – Time to initiation field predicted for specimen 1383-01T (EDF weld registered RND-M-D-711). Code_Coriolis prediction relying on the local model and the sigmoid growth law. Detailed view at the head/shank junction.

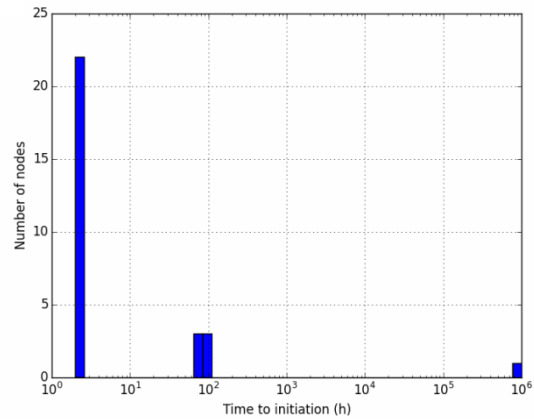


Figure 107 – Histogram of times to initiation predicted for specimen 1383-01T (EDF weld registered RND-M-D-711). Code_Coriolis prediction relying on the local model and the sigmoid growth law.



Figure 108 – Crack growth path followed by the tip of the main crack predicted for specimen 1383-01T (EDF weld registered RND-M-D-711). Code_Coriolis prediction relying on the local model and the sigmoid growth law. Detailed view at the head/shank junction.

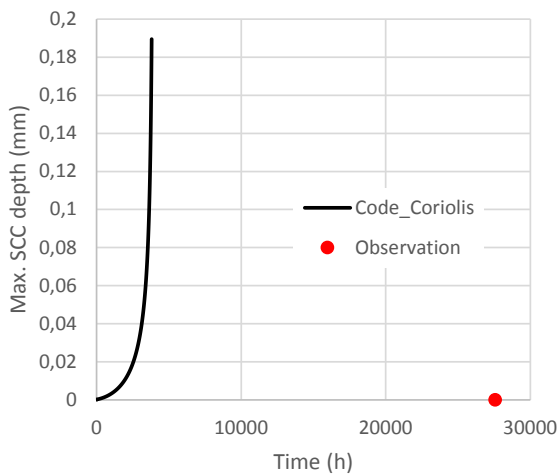


Figure 109 – Cracking kinetics predicted for specimen 1383-01T (EDF weld registered RND-M-D-711). Code_Coriolis prediction relying on the local model and the sigmoid growth law.

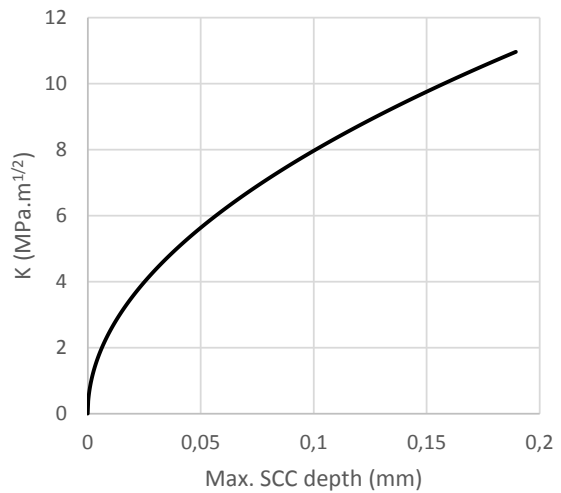


Figure 110 – K versus depth at the tip of the main crack predicted for specimen 1383-01T (EDF weld registered RND-M-D-711). Code_Coriolis prediction relying on the local model and the sigmoid growth law.

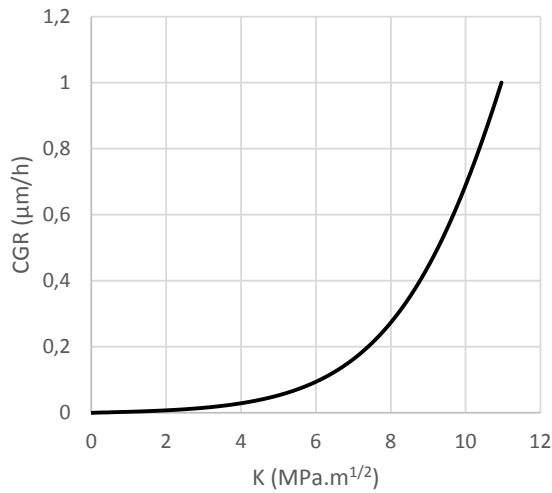


Figure 111 – Crack growth rate versus K at the tip of the main crack predicted for specimen 1383-01T (EDF weld registered RND-M-D-711). Code_Coriolis prediction relying on the local model and the sigmoid growth law.

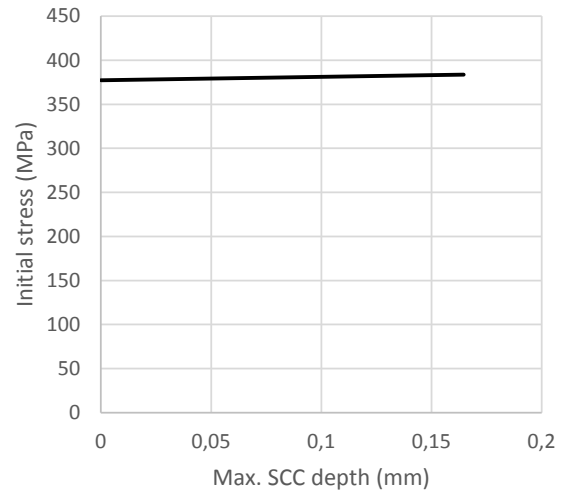


Figure 112 – Stress versus depth at the tip of the main crack predicted for specimen 1383-01T (EDF weld registered RND-M-D-711). Code_Coriolis prediction relying on the local model and the sigmoid growth law.

Table 36 – Code_Coriolis predictions of the cracking times, depths and growth rates. EDF weld registered RND-M-D-711. Simulations relying on the local model and the sigmoid growth law.

| Specimen | Experiment | | Simulation | | | | | | | | |
|-----------|--------------|------------------|-----------------------|------------------------|--------------------------|-------------------------------|---------------------------------|---------------------------------|--|--|---|
| | Duration (h) | Crack depth (µm) | Initiation depth (µm) | Time to initiation (h) | Time to reach 150 µm (h) | Time to K _{1SCC} (h) | Depth at K _{1SCC} (µm) | CGR at K _{1SCC} (µm/h) | Time to reach the experiment crack depth (h) | K for the experiment crack depth (MPa.m ^{1/2}) | CGR for the experiment crack depth (µm/h) |
| 1383-01-T | 27570 | 0 | 0.2 | 2 | 3757 | 3839 | 227 | 1,41 | 3817 | 11,3 | 1,11 |
| 1383-02-T | 27570 | 0 | 0.2 | +∞ | - | - | - | - | - | 0 | 0 |
| 1383-03-T | 27570 | 0 | 0.2 | +∞ | - | - | - | - | - | 0 | 0 |
| 1383-04-T | 27570 | 0 | 0.2 | +∞ | - | - | - | - | - | 0 | 0 |

Table 37 – Code_Coriolis prediction of the duration of cracking stages. EDF weld registered RND-M-D-711. Simulations relying on the local model and the sigmoid growth law.

| Specimen | Experiment | | Simulation | | | | |
|-----------|--------------|------------------|--|------------------------|-----------------------------|-----------------------------|----------------|
| | Duration (h) | Crack depth (µm) | Time to reach the experiment crack depth (h) | Time to initiation (%) | Time in slow CGR regime (%) | Time in fast CGR regime (%) | DCPD detection |
| 1383-01-T | 27570 | 0 | 3817 | 0 | 100 | 0 | Yes |
| 1383-02-T | 27570 | 0 | - | - | - | - | - |
| 1383-03-T | 27570 | 0 | - | - | - | - | - |
| 1383-04-T | 27570 | 0 | - | - | - | - | - |

6.5.3. Results on PNNL Alloy 182 registered Studsvik 8001231

Results of SCC predictions are given and compared to experimental results in Table 38. Details on SCC simulation results can be found in Appendix 2 for each specimen. For example, regarding the simulation of the test on specimen IN171 when the **local model** is coupled with the sigmoid law:

- Initiation is predicted after 2 h, at the shank of the specimen (Figure 113 and Figure 114). The maximum principal stress at the initiation site is of 543 MPa, which is consistent with the expected axial stress of 534 MPa in the shank. The histogram of the times to initiation (Figure 115) exhibits two peaks of time to initiation, the first one corresponding to the shank. The time to initiation field suggests that initiation can occur everywhere in the shank.
- The crack growth path followed by the tip of the main crack is shown (in transparency) in Figure 116. The crack extended in the shank, under a slightly decreasing stress. The cracking kinetics is shown in Figure 117. The transition from the slow to fast crack growth regime, when $K = K_{1SCC} = 12 \text{ MPa}\cdot\text{m}^{1/2}$, occurred after 538 h. The transition happened at a depth of 126 μm , for a crack growth rate of 5.3 $\mu\text{m}\cdot\text{h}^{-1}$. At the experiment crack depth of 150 μm , $K = 13.1 \text{ MPa}\cdot\text{m}^{1/2}$ and $\text{CGR} = 7.0 \mu\text{m}\cdot\text{h}^{-1}$. Figure 118 shows the evolution of K with depth along the main cracking path. Figure 119 shows the crack growth law followed along the same path. Both slow and fast regimes are involved. Figure 120 shows the initial stress level (before cracking) along the cracking path.
- The predicted time to reach 150 μm (experiment max crack depth) is 542 h, which is about six times shorter than the DCPD time to detection during testing. Therefore, the prediction underestimates the time to reach the crack depth at DCPD detection.

Table 38 and Table 39 summarize results of the full data set. The crack depths were not observed on cross sections after testing. Therefore, the comparison between experiment and simulation is limited to the comparison between the experiment and predicted times to DCPD detection, corresponding to a crack depth of 150 μm . Times to reach a simulated crack depth of 150 μm range from 495 h to 551 h. The depth criterion to stop the simulation was 200 μm . 90% of the simulation time was dedicated to the slow crack growth regime and 10% was dedicated to the fast crack growth.

Transitions from the slow to fast crack growth regime happen at depths around 120 μm . The absence of DCPD detection is predicted for five specimens, contrary to the observation.

A comparison of SCC predictions with observations is presented in Figure 121. Predicted times to reach the DCPD detection fall within a narrow range, due to the fact that applied loads are very close. By contrast, actual times to DCPD detections spread from 30 h to 2957 h with a median time at 62 h demonstrating that early initiation often occurs. Five predictions out of nine (corresponding to early detection during testing) overestimate the time to DCPD detection, showing that parameters of the models have to be tuned to better fit the susceptibility to SCC of this weld.



Figure 113 – Time to initiation field predicted for specimen IN171 (PNNL weld registered Studsvik 8001231). Code_Coriolis prediction relying on the local model and the sigmoid growth law.

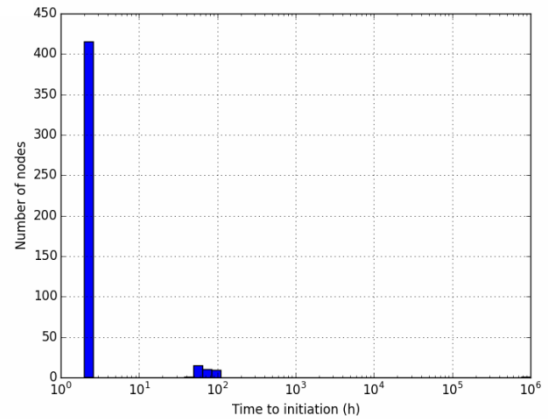
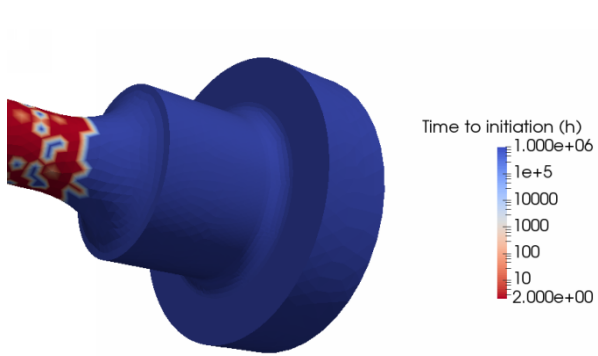


Figure 114 – Time to initiation field predicted for specimen IN171 (PNNL weld registered Studsvik 8001231). Code_Coriolis prediction relying on the local model and the sigmoid growth law. Detailed view at the head/shank junction.

Figure 115 – Histogram of times to initiation predicted for specimen IN171 (PNNL weld registered Studsvik 8001231). Code_Coriolis prediction relying on the local model and the sigmoid growth law.

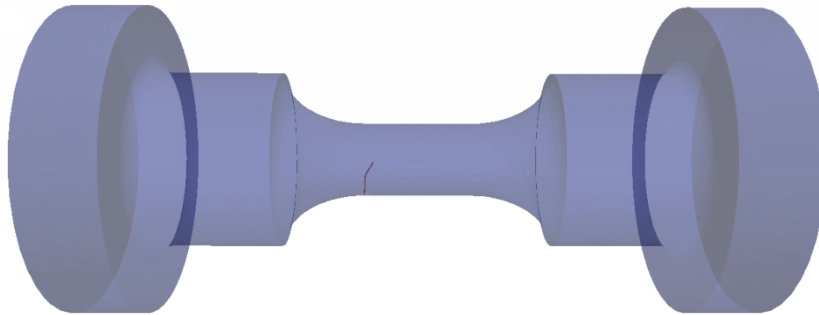


Figure 116 – Crack growth path followed by the tip of the main crack predicted for specimen IN171 (PNNL weld registered Studsvik 8001231). Code_Coriolis prediction relying on the local model and the sigmoid growth law. Detailed view at the head/shank junction.

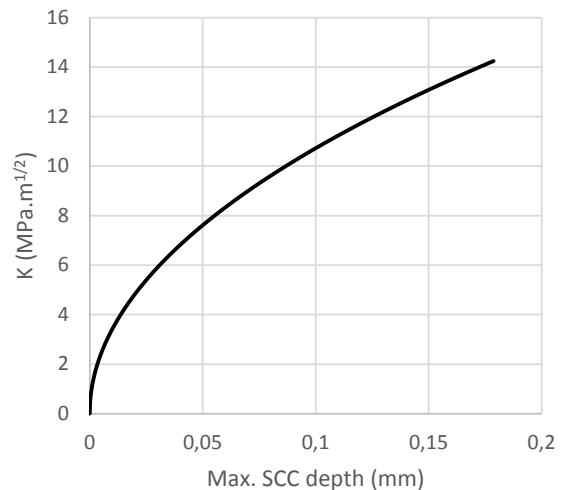
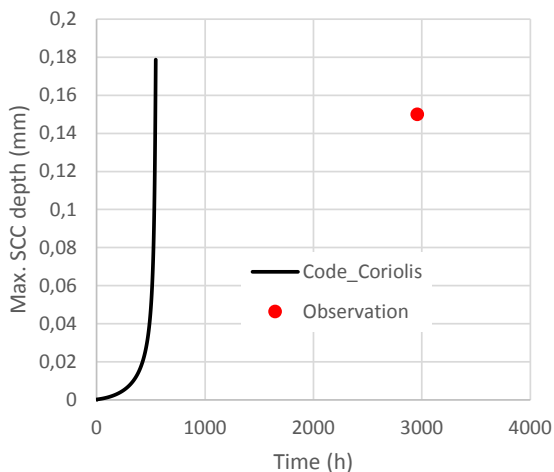


Figure 117 – Cracking kinetics predicted for specimen IN171 (PNNL weld registered Studsvik 8001231). Code_Coriolis prediction relying on the local model and the sigmoid growth law.

Figure 118 – K versus depth at the tip of the main crack predicted for specimen IN171 (PNNL weld registered Studsvik 8001231). Code_Coriolis prediction relying on the local model and the sigmoid growth law.

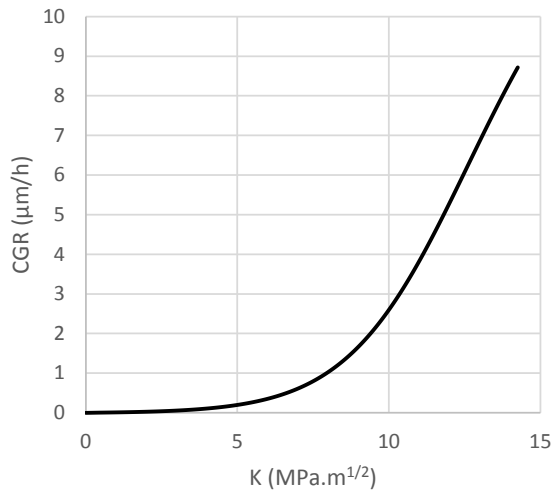


Figure 119 – Crack growth rate versus K at the tip of the main crack predicted for specimen IN171 (PNNL weld registered Studsvik 8001231). Code_Coriolis prediction relying on the local model and the sigmoid growth law.

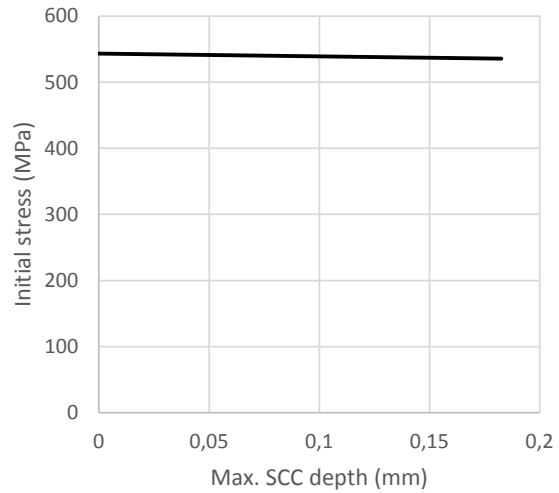


Figure 120 – Stress versus depth at the tip of the main crack predicted for specimen IN171 (PNNL weld registered Studsvik 8001231). Code_Coriolis prediction relying on the local model and the sigmoid growth law.

Table 38 – Code_Coriolis predictions of the cracking times, depths and growth rates. PNNL weld registered Studsvik 8001231. Simulations relying on the local model and the sigmoid growth law. NA: not available.

| Specimen | Experiment | | Simulation | | | | | | | | |
|----------|--------------|------------------|-----------------------|------------------------|--------------------------|-------------------------------|---------------------------------|---------------------------------|--|--|---|
| | Duration (h) | Crack depth (µm) | Initiation depth (µm) | Time to initiation (h) | Time to reach 150 µm (h) | Time to K _{1scc} (h) | Depth at K _{1scc} (µm) | CGR at K _{1scc} (µm/h) | Time to reach the experiment crack depth (h) | K for the experiment crack depth (MPa.m ^{1/2}) | CGR for the experiment crack depth (µm/h) |
| IN169 | 5126 | NA | 0.2 | 2 | 527 | 523 | 122 | 5.3 | - | - | - |
| IN170 | 30 | NA | 0.2 | 2 | 538 | 533 | 125 | 5.3 | - | - | - |
| IN171 | 2957 | NA | 0.2 | 2 | 542 | 538 | 126 | 5.3 | - | - | - |
| IN191 | 83 | NA | 0.2 | 2 | 506 | 501 | 118 | 5.3 | - | - | - |
| IN192 | 41 | NA | 0.2 | 2 | 495 | 489 | 115 | 5.3 | - | - | - |
| IN193 | 41 | NA | 0.2 | 2 | 502 | 497 | 117 | 5.3 | - | - | - |
| IN233 | 30 | NA | 0.2 | 2 | 546 | 542 | 127 | 5.3 | - | - | - |
| IN234 | 725 | NA | 0.2 | 2 | 551 | 547 | 128 | 5.3 | - | - | - |
| IN235 | 910 | NA | 0.2 | 2 | 546 | 542 | 127 | 5.3 | - | - | - |

Table 39 – Code_Coriolis prediction of the duration of cracking stages. PNNL weld registered Studsvik 8001231. Simulations relying on the local model and the sigmoid growth law. NA: not available.

| Specimen | Experiment | | Simulation | | | | |
|----------|--------------|------------------|--|------------------------|-----------------------------|-----------------------------|----------------|
| | Duration (h) | Crack depth (µm) | Time to reach the experiment crack depth (h) | Time to initiation (%) | Time in slow CGR regime (%) | Time in fast CGR regime (%) | DCPD detection |
| IN169 | 5126 | NA | 587 | 0 | 89 | 11 | Yes |
| IN170 | 30 | NA | 598 | 0 | 89 | 11 | Yes |
| IN171 | 2957 | NA | 602 | 0 | 89 | 11 | Yes |
| IN191 | 83 | NA | 564 | 0 | 88 | 11 | Yes |
| IN192 | 41 | NA | 553 | 0 | 88 | 12 | Yes |
| IN193 | 41 | NA | 561 | 0 | 88 | 11 | Yes |
| IN233 | 30 | NA | 606 | 0 | 89 | 11 | Yes |
| IN234 | 725 | NA | 612 | 0 | 89 | 11 | Yes |
| IN235 | 910 | NA | 606 | 0 | 89 | 11 | Yes |

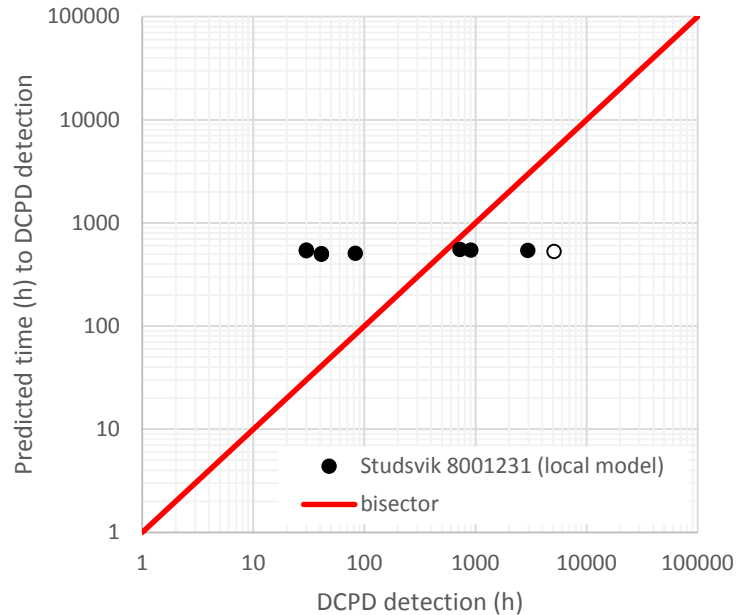


Figure 121 – Comparison between predicted time to reach the experiment crack depth and testing time. PNNL weld registered Studsvik 8001231. Code_Coriolis predictions relying on the local model and the sigmoid growth law. Closed symbols: DCPD detection, open symbol: no DCPD detection during experiment.

6.5.4. Results on PNNL Alloy 182 registered KAPL 823030

Results of SCC predictions are given and compared to experimental results in Table 40. Details on SCC simulation results can be found in Appendix 2 for each specimen. For example, regarding the simulation of the test on specimen IN194 when the **local model** is coupled with the sigmoid law:

- Initiation is predicted after 2 h, at the shank of the specimen (Figure 122 and Figure 123). The maximum principal stress at the initiation site is of 579 MPa, which is slightly lower than the expected axial stress of 581 MPa in the shank. The histogram of the times to initiation (Figure 124) exhibits a single peak corresponding to the shank, where initiation occur homogeneously.
- The crack growth path followed by the tip of the main crack is shown (in transparency) in Figure 125. The crack extended in the shank, under a slightly decreasing stress. The cracking kinetics is shown in Figure 126. The transition from the slow to fast crack growth regime, when $K = K_{1SCC} = 12 \text{ MPa}\cdot\text{m}^{1/2}$, occurred after 469 h. The transition happened at a depth of 110 μm , for a crack growth rate of 5.3 $\mu\text{m}\cdot\text{h}^{-1}$. At the crack depth of 150 μm , $K = 14.0 \text{ MPa}\cdot\text{m}^{1/2}$ and $\text{CGR} = 8.4 \mu\text{m}\cdot\text{h}^{-1}$. Figure 127 shows the evolution of K with depth along the main cracking path. Figure 128 shows the crack growth law followed along the same path. Both slow and fast regimes are involved. Figure 129 shows the initial stress level (before cracking) along the cracking path.
- The predicted time to reach 150 μm (experiment max crack depth) is 475 h, which is about 3.4 times shorter than DCPD time to detection during testing. Therefore, the prediction overestimates the cracking rate.

Table 40 and Table 41 summarize results of the full data set. The crack depths were not observed on cross sections after testing. Therefore, the comparison between experiment and simulation is limited to the comparison between the experiment and predicted times to DCPD detection, corresponding to a crack depth of 150 μm . Times to reach a simulated depth of 150 μm range from 477 h to 517 h. The depth criterion to stop the simulation was 200 μm . The simulated time (532 to 576 h) is shared between the slow crack growth regime (90%) and the fast crack growth (10%).

Transitions from the slow to fast crack growth regime happen at depths around 110-120 μm .

A comparison of SCC predictions with observations is presented in Figure 130. Predicted times to reach the DCPD detection fall within a narrow range, because applied loads are very close. By contrast, actual times to DCPD detections spread from 30 h to 1635 h, with a median time at 1625 h demonstrating that early initiation may occur. Predictions are not conservative, showing that parameters of the models have to be tuned to better fit the susceptibility to SCC of this weld.



Figure 122 – Time to initiation field predicted for specimen IN194 (PNNL weld registered KAPL 823030). Code_Coriolis prediction relying on the local model and the sigmoid growth law.

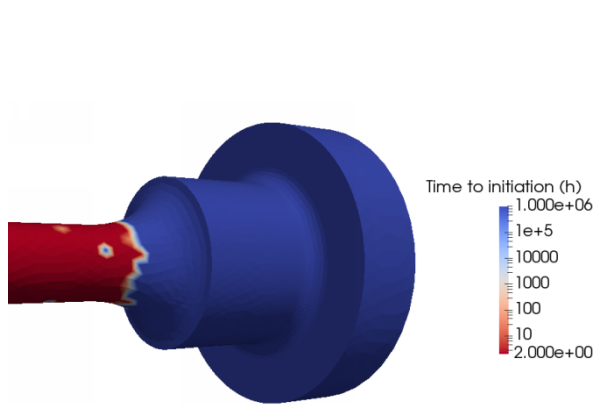


Figure 123 – Time to initiation field predicted for specimen IN194 (PNNL weld registered KAPL 823030). Code_Coriolis prediction relying on the local model and the sigmoid growth law. Detailed view at the head/shank junction.

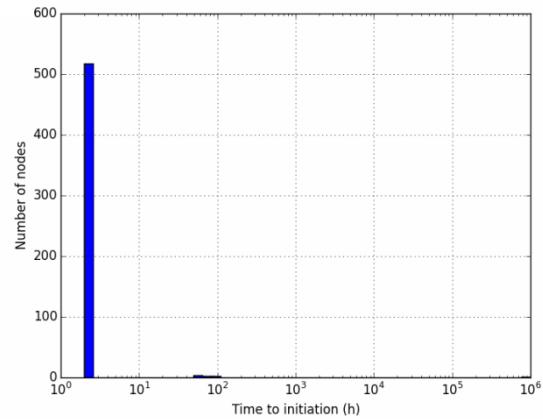


Figure 124 – Histogram of times to initiation predicted for specimen IN194 (PNNL weld registered KAPL 823030). Code_Coriolis prediction relying on the local model and the sigmoid growth law.

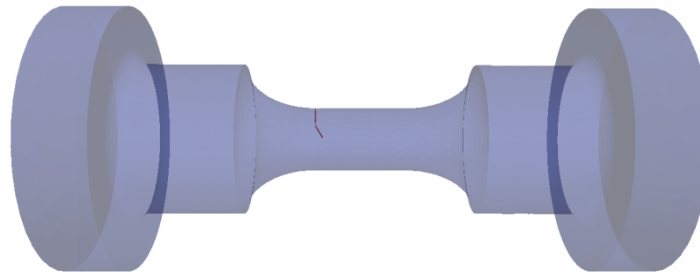


Figure 125 – Crack growth path followed by the tip of the main crack predicted for specimen IN194 (PNNL weld registered KAPL 823030). Code_Coriolis prediction relying on the local model and the sigmoid growth law. Detailed view at the head/shank junction.

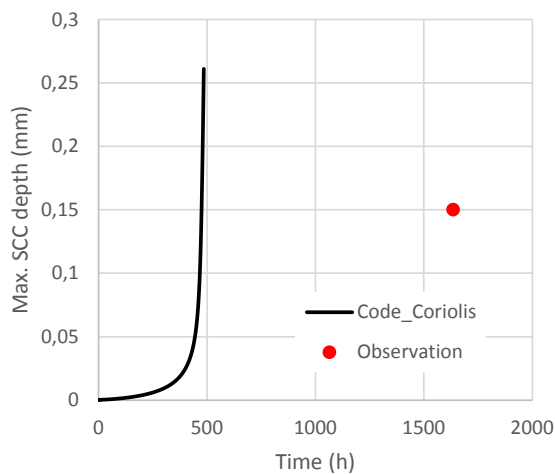


Figure 126 – Cracking kinetics predicted for specimen IN194 (PNNL weld registered KAPL 823030). Code_Coriolis prediction relying on the local model and the sigmoid growth law.

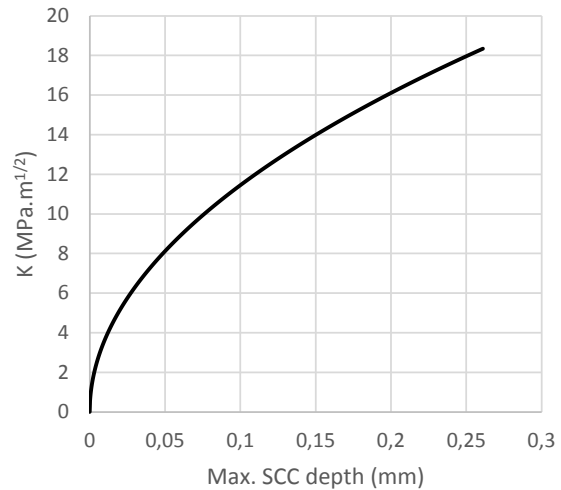


Figure 127 – K versus depth at the tip of the main crack predicted for specimen IN194 (PNNL weld registered KAPL 823030). Code_Coriolis prediction relying on the local model and the sigmoid growth law.

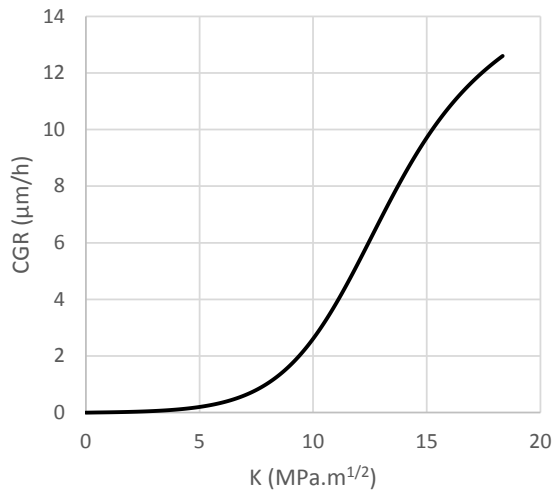


Figure 128 – Crack growth rate versus K at the tip of the main crack predicted for specimen IN194 (PNNL weld registered KAPL 823030). Code_Coriolis prediction relying on the local model and the sigmoid growth law.

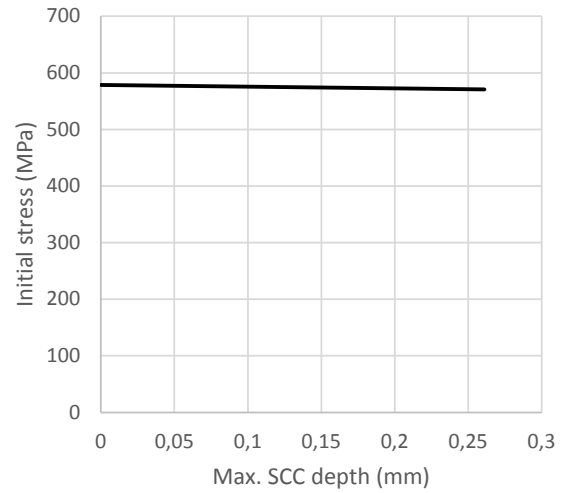


Figure 129 – Stress versus depth at the tip of the main crack predicted for specimen IN194 (PNNL weld registered KAPL 823030). Code_Coriolis prediction relying on the local model and the sigmoid growth law.

Table 40 – Code_Coriolis predictions of the cracking times, depths and growth rates. PNNL weld registered KAPL 823030. Simulations relying on the local model and the sigmoid growth law.

| Specimen | Experiment | | Simulation | | | | | | | | |
|----------|--------------|------------------|-----------------------|------------------------|--------------------------|-------------------------------|---------------------------------|---------------------------------|--|--|---|
| | Duration (h) | Crack depth (µm) | Initiation depth (µm) | Time to initiation (h) | Time to reach 150 µm (h) | Time to K _{1scc} (h) | Depth at K _{1scc} (µm) | CGR at K _{1scc} (µm/h) | Time to reach the experiment crack depth (h) | K for the experiment crack depth (MPa.m ^{1/2}) | CGR for the experiment crack depth (µm/h) |
| IN166 | 30 | NA | 0,2 | 2 | 488 | 482 | 113 | 5.31 | - | - | - |
| IN167 | 30 | NA | 0,2 | 2 | 507 | 502 | 118 | 5.31 | - | - | - |
| IN168 | 113 | NA | 0,2 | 2 | 517 | 512 | 120 | 5.31 | - | - | - |
| IN194 | 1635 | NA | 0,2 | 2 | 475 | 469 | 110 | 5.32 | - | - | - |
| IN195 | 1625 | NA | 0,2 | 2 | 477 | 472 | 111 | 5.32 | - | - | - |
| IN196 | 1642 | NA | 0,2 | 2 | 482 | 476 | 112 | 5.31 | - | - | - |

Table 41 – Code_Coriolis prediction of the duration of cracking stages. PNNL weld registered KAPL 823030. Simulations relying on the local model and the sigmoid growth law.

| Specimen | Experiment | | Simulation | | | | | DCPD detection |
|----------|--------------|------------------|--|------------------------|-----------------------------|-----------------------------|-----|----------------|
| | Duration (h) | Crack depth (µm) | Time to reach the experiment crack depth (h) | Time to initiation (%) | Time in slow CGR regime (%) | Time in fast CGR regime (%) | | |
| IN166 | 30 | NA | 546 | 0 | 88 | 12 | Yes | |
| IN167 | 30 | NA | 566 | 0 | 88 | 11 | Yes | |
| IN168 | 113 | NA | 576 | 0 | 89 | 11 | Yes | |
| IN194 | 1635 | NA | 532 | 0 | 88 | 12 | Yes | |
| IN195 | 1625 | NA | 535 | 0 | 88 | 12 | Yes | |
| IN196 | 1642 | NA | 540 | 0 | 88 | 12 | Yes | |

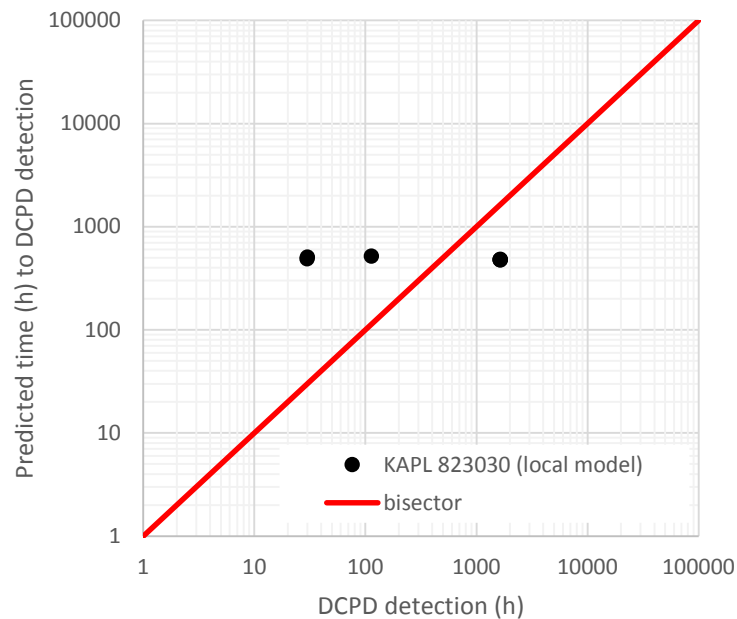


Figure 130 – Comparison between predicted time to reach the experiment crack depth and testing time. PNNL weld registered KAPL 823030. Code_Coriolis predictions relying on the index model and the sigmoid growth law.

6.6. Comparison of Code_Coriolis models and PWSCC initiation test data with xLPR initiation models

Initiation time predictions were made using each of the three xLPR models: Direct Model 1, Direct Model 2, and the Weibull Model. Sections 5.1.3.1, 5.1.3.2, and 5.1.3.3 discuss the model forms and recommended input parameters for each of these models in detail. The PWSCC initiation time predictions for each of the studied welds are presented in Section 6.6.1 through 6.6.4.

In the results shown, Direct Model 1 and Weibull model predictions are generally plotted as curves at constant temperature and material properties. However, several specimens were tested at a temperature that differs from the typical test temperature of 360°C. Direct Model 1 and Weibull Model predictions for these specimens are plotted as points. All xLPR PWSCC initiation time predictions from Direct Model 2 are plotted as points, with predictions made using specimen-specific inputs, including test temperature, applied stress, and material properties. For all xLPR models, the 50th percentile of all distributed failure time model parameters was applied. Implications of these comparisons made at the 50th percentile for distributed inputs are discussed further in Section 7.3.

It is noted that xLPR initiation time predictions correspond to the existence of a flaw of engineering scale, with an initial flaw size on the order of a few millimeters. As stated in Section 5.1.3, the PWSCC initial flaw distributions modelled in xLPR assume a median initial flaw depth of 1.5 mm. These results are compared with Code_Coriolis predictions for time to 150 µm (unless stated otherwise). It is also noted that DCPD detection of PWSCC initiation during testing occurs at an estimated depth of 150 µm, so Code_Coriolis predictions for time to 150 µm should provide a slightly more direct comparison.

6.6.1. Results Comparison of Alloy 182 registered RND-M-D-1054

Initiation predictions for each of the xLPR initiation models, for both Code_Coriolis models (presented as time to 150 µm), and initiation test results for Alloy 182 weld registered as RND-M-D-1054 as a function of applied stress are presented in Figure 131.

The Direct Model 1 and Weibull Model predictions that are plotted as lines represent predictions for a test temperature of 360°C. Five of the specimens were tested at temperatures below 360°C. The Direct Model 1 and Weibull Model predictions for these specimens are plotted as points. All Direct Model 2

predictions are made for the specimen-specific material properties and test conditions.

Generally, the Code_Coriolis models predict shorter initiation times and are thus more conservative than the xLPR models except Direct Model 2. At applied stresses less than 550 MPa, the Local Model typically predicts shorter initiation times than the Index Model. At stresses greater than 550 MPa, the Index Model predicts shorter initiation times than the Local Model. Direct Model 1 predicts the longest initiation times in almost all cases and therefore is the least conservative. The Weibull model predictions are slightly shorter than the Direct Model 1 predictions in all cases. The Index and Local Models predicted shorter initiation times than the observed test times for the specimens that initiated at 350 MPa, while both DM1 and the Weibull models predicted longer initiation times than the observed test times. All models except Direct Model 2 predicted longer initiation times than the observed test times for the specimens that initiated at applied stresses greater than 650 MPa. Direct Model 2 predictions produce the fastest times to initiation of all models, largely attributed to the application of the 50th percentile of distributed inputs, as is further discussed in Section 7.3. The stresses corresponding to the higher-stress specimens (1383-26, 1588-16, 1383-21, and 1383-28) are above the stress threshold for which Direct Model 2 predicts immediate initiation. Thus, the Direct Model 2 predictions for these higher-stress specimens are not plotted.

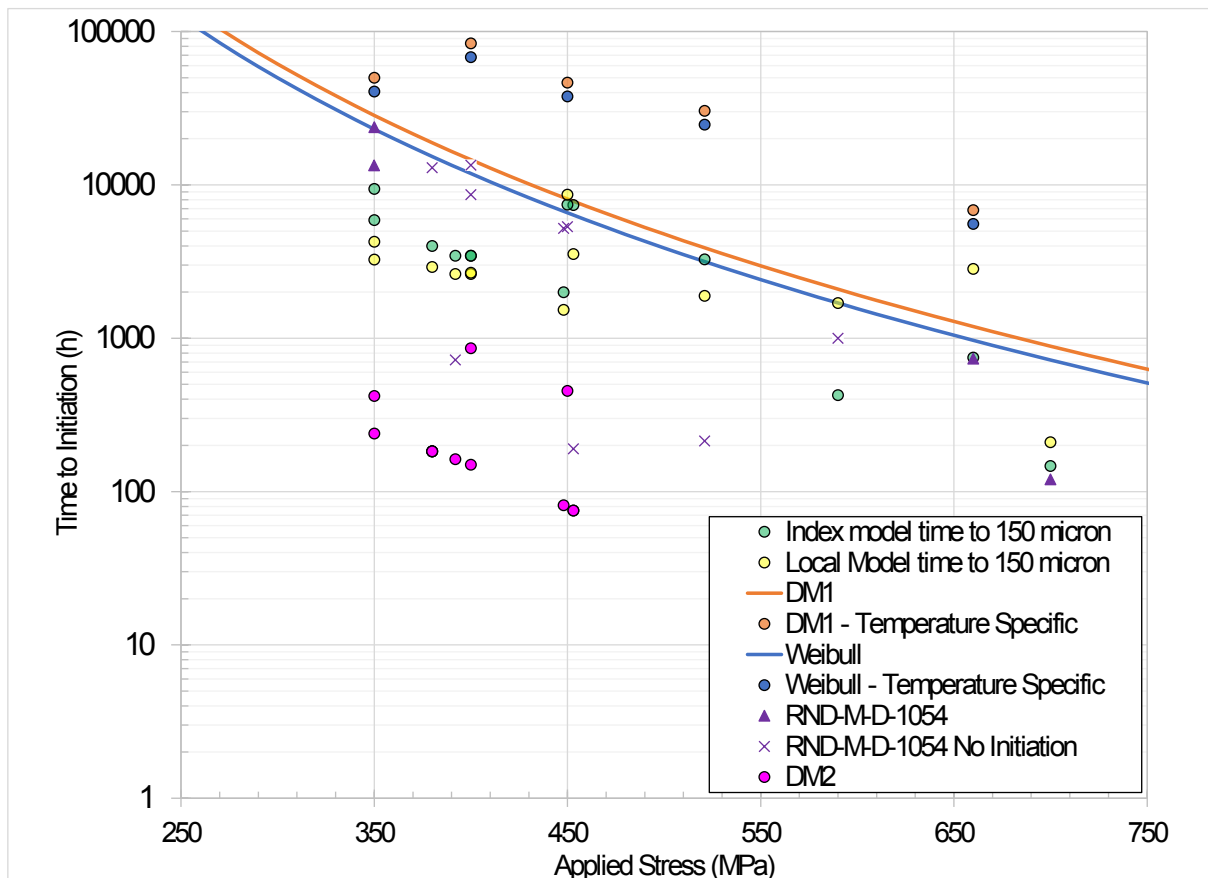


Figure 131 – Initiation predictions and observed initiation times for alloy 182 weld registered as RND-M-D-1054.

6.6.2. Results Comparison of Alloy 82 registered RND-M-D-711

Initiation predictions for each of the xLPR initiation models, initiation predictions for both Code_Coriolis models (for time to 150 μm), and initiation test results for the Alloy 82 weld registered as RND-M-D-711 as a function of applied stress are presented in Figure 132. While initiation was not observed in any of the four specimens, it is useful to compare the predictions for Alloy 82 welds. The Local Model does not predict initiation (predicts an infinite time to initiation) for all specimens except 1383-01T, so this is the only prediction shown in Figure 132. Because the Local Model only predicts initiation for one of the four specimens, it can be considered to be the least conservative model overall. The Index Model predicts

the longest initiation times among models that predict initiation of all specimens, with predictions that are greater than all xLPR models for all specimens. Direct Model 2 predicts the shortest times to initiation, at under 200 hours for all specimens (as is further discussed in Section 7.3). Both Direct Model 1 and the Weibull Model predict shorter initiation times than the Code_Coriolis models for a majority of specimens, and the Weibull Model predicts slightly shorter initiation times than Direct Model 1 for all specimens.

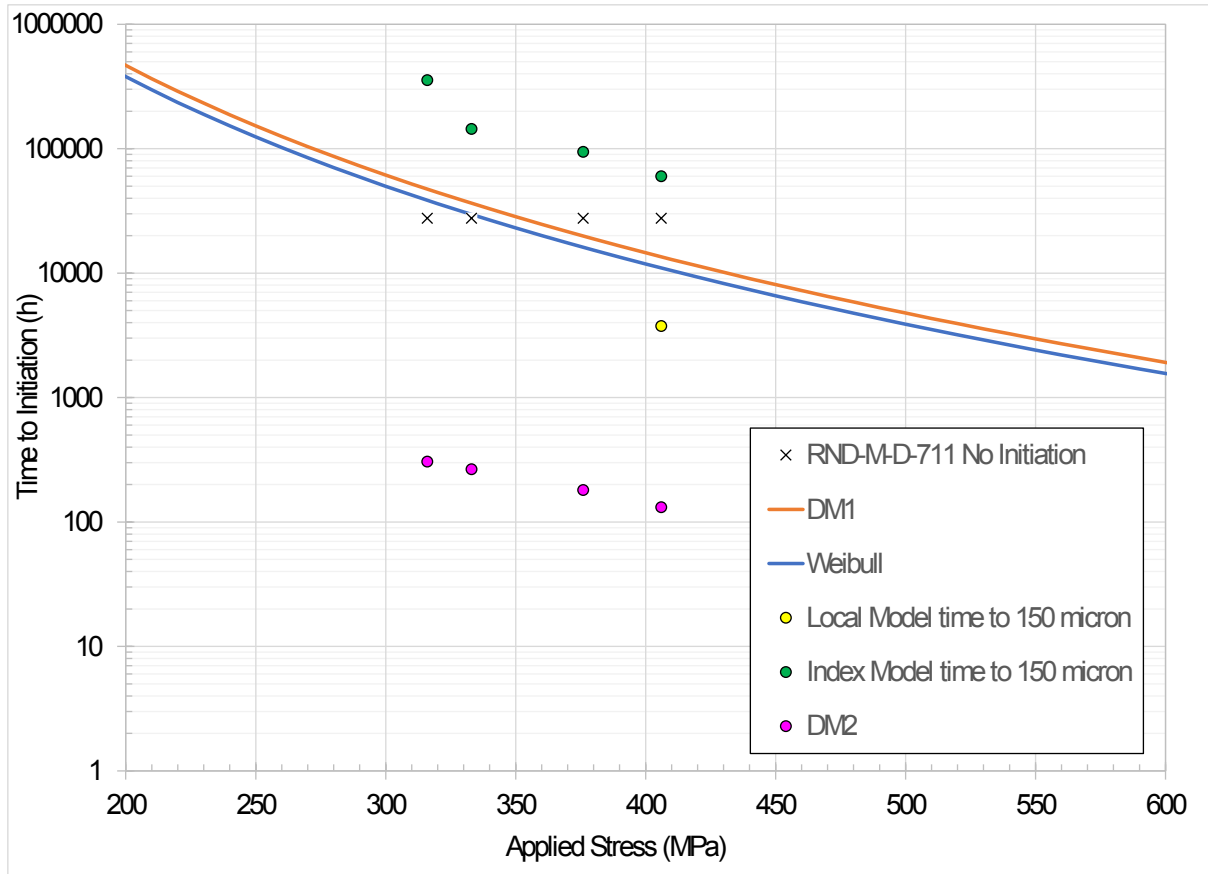


Figure 132 – Initiation predictions and observed initiation times for alloy 82 welds registered as RND-M-D-711.

6.6.3. Results Comparison of PNNL Alloy 182 registered Studsvik

Initiation predictions for each of the xLPR initiation models, initiation predictions for both Code_Coriolis models (for time to 150 μm), and PNNL initiation test results for Studsvik Alloy 182 specimens as a function of applied stress are presented in Figure 133.

The Local Model predicts shorter initiation times than the Index Model for all specimens. Direct Model 1 and the Weibull Model are less conservative than the Code_Coriolis models and predict longer times to initiation for all specimens. As is generally the case, Direct Model 1 is less conservative than the Weibull Model and predicts the longest times to initiation. As in almost all cases, Direct Model 2 predicts the shortest initiation times.

Almost all model predictions resulted in initiation times longer than the observed initiation times, as the majority of Studsvik weld specimens showed crack initiation in test times less than 100 hours. Direct Model 1 and the Weibull Model greatly overpredict the initiation times for these early initiation specimens. A potential cause for this discrepancy is discussed in Section 7.3.

Because the majority of the observed test times were less than 100 hours and Direct Model 2 predicts the shortest initiation times, Direct Model 2 is generally the most accurate. However, it is noted that the Direct Model 2 predictions are calculated using the 50th percentile of the failure time model parameters, which as discussed in Section 7.3 produces notably shorter predicted times to initiation at this percentile.

The Index Model and Weibull Model are more accurate for the Studsvik weld specimens with initiation times greater than 100 hours.

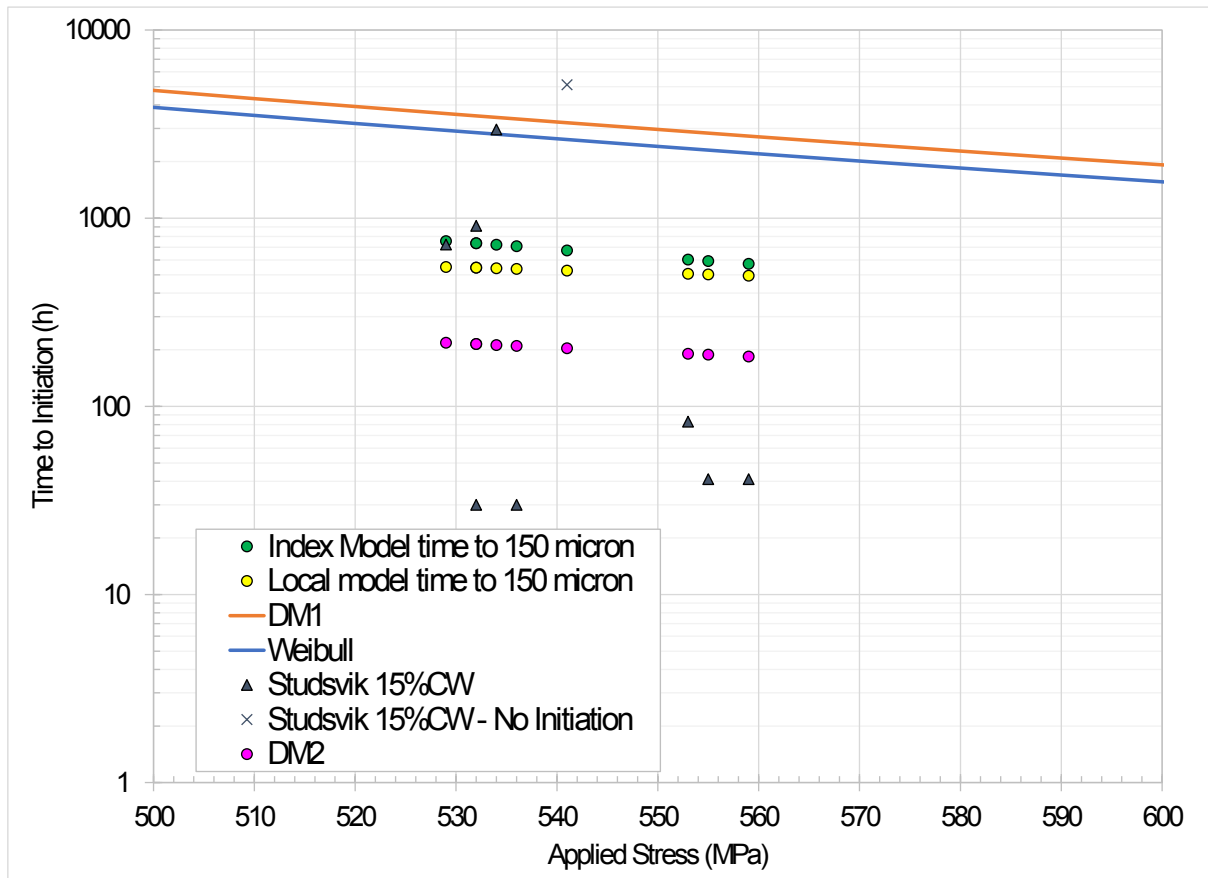


Figure 133 – Initiation predictions and observed initiation times for PNNL alloy 182 welds registered as Studsvik.

6.6.4. Results Comparison of PNNL Alloy 182 registered KAPL

Initiation predictions for each of the xLPR initiation models, initiation predictions for both Code_Coriolis models (for time to 150 μm), and PNNL initiation test results for KAPL Alloy 182 weld specimens as a function of applied stress are presented in Figure 134.

The Code_Coriolis models are generally more conservative (resulting in shorter initiation times) than the xLPR models except for Direct Model 2. The Code_Coriolis predictions for time to initiation are nearly 4 times shorter than the Weibull Model predictions and 5 times shorter than the Direct Model 1 predictions. The Local Model produces initiation times on the order of 500 hours, while the Index Model produces initiation times that are about 15% longer than those of the Local Model. As is the case for all weld types, Direct Model 1 predicts slightly longer initiation times than the Weibull Model, and Direct Model 2 predicts the shortest initiation times overall.

Of the six specimens that initiated, three initiated in about 100 hours or less. Direct Model 1 and the Weibull Model greatly overpredict the initiation times in these cases. The index model, local model, and Direct Model 2 also somewhat overpredicted the initiation time for these three specimens. A potential cause for this discrepancy is discussed in Section 7.3.

For the three welds that had longer initiation times, the Code_Coriolis models underpredicted initiation time by more than 1000 hours in all cases. Direct Model 1 predicted initiation times nearly 1000 hours greater than the observed test times, while the Weibull model was most accurate, overpredicting initiation times by about 500 hours. Direct Model 2 underpredicted the initiation times for these welds by nearly an order of magnitude.

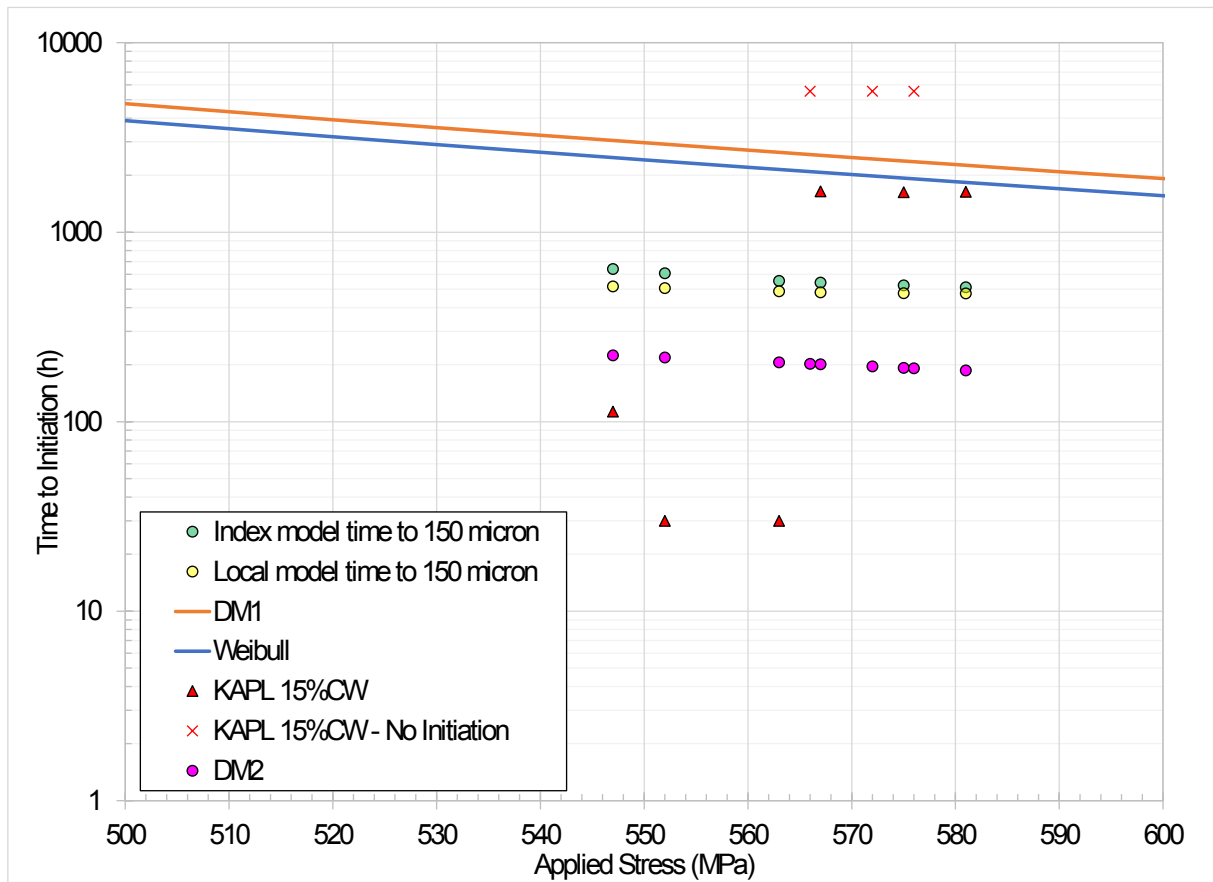


Figure 134 – Initiation predictions and observed initiation times for PNNL alloy 182 welds registered as KAPL.

| | | |
|-----|---|--|
| MAI | Quantitative evaluation of the EDF local model and the EPRI-NRC xLPR models of crack initiation of the weld metals of Alloy 600 (Alloys 82 and 182) | 6125-4501-2018-00583-EN Version 2.0 |
|-----|---|--|

7. Discussion

7.1. Index model

Predictions were all performed using the same set of parameters calibrated in a previous study without Code_Coriolis on the EDF weld registered RND-M-D-1054. The initiation depth associated with the time to initiation was assigned to 5 μm in computations.

The accuracy of the predictions was evaluated comparing the difference between the predicted and the experiment time to reach the maximal experiment crack depth as a function of this maximal experiment crack depth (Figure 135). Positive values indicate non-conservative predictions. The evaluation was not possible for tests on Studsvik and KAPL welds because crack depths were not measured on cross sections. The difference between prediction and observation is larger for crack depths lower than 40 μm , with a high probability to make non-conservative predictions, compared to cracks deeper than 1 mm. In addition, for deep cracks, predictions are always conservative. A good agreement between predictions and observations is noticed for the two deepest crack depths, and two predictions are over conservative. The accuracy of the predictions relying on the index model is conservative and acceptable for cracks deeper than 40 μm , in agreement with a previous study where only cracks deeper than 100 μm were considered to fit the material index.

Predictions are strongly affected by the value assigned to the initiation depth. Indeed, since the index model does not rely on a phenomenological cracking scenario, the initiation depth has to be arbitrary associated with the time to initiation. In the current study, the shortest crack depth observed under optical microscopy was considered: 5 μm . Figure 136 shows that changing this initiation depth to zero leads to highly overestimate the time to reach experiment crack depths. It means that using an ambiguous model where the initiation depth is not clearly defined can easily lead to wrong estimations of the cracking kinetics.

Regarding the Studsvik and KAPL cold worked welds, the accuracy of the predictions was evaluated comparing the difference between the predicted and the experiment time to reach the DCPD detection (a crack depth of 150 μm) as a function of the time to reach the detection (Figure 137). Positive values indicate non-conservative predictions. The evaluation was not possible for tests on EDF welds because no DCPD monitoring was performed and the testing time was not necessarily limited to short crack depths. Some predictions are not conservative, may be due to the fact that Studsvik and KAPL welds were cold worked prior to testing, or due to a higher susceptibility to SCC of these welds compared to the EDF weld RND-M-D-1054. Conservative predictions address tests that lasted more than 725 h. Parameters of the Studsvik and KAPL welds may be tuned if more data is available:

- Crack depth measurements.
- Slow crack growth rates measured on blunt notched or fatigue pre-cracked CT specimens, under low K.

The large spread of experimental times to reach the DCPD detection under the same load suggest a lack of metallurgical or microstructural consideration in the index model. However, the improvement of such an empirical model is unrealistic.

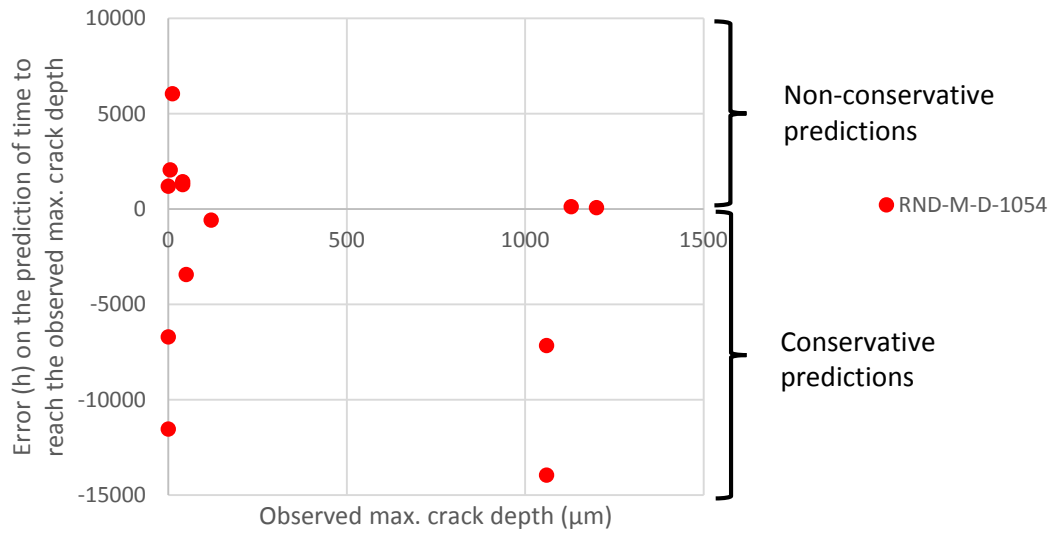


Figure 135 – Evaluation of the error in the prediction of the time to reach the experiment maximal crack depth, as a function of the maximal crack depth. Code_Coriolis predictions relying on the index model and the sigmoid growth law.

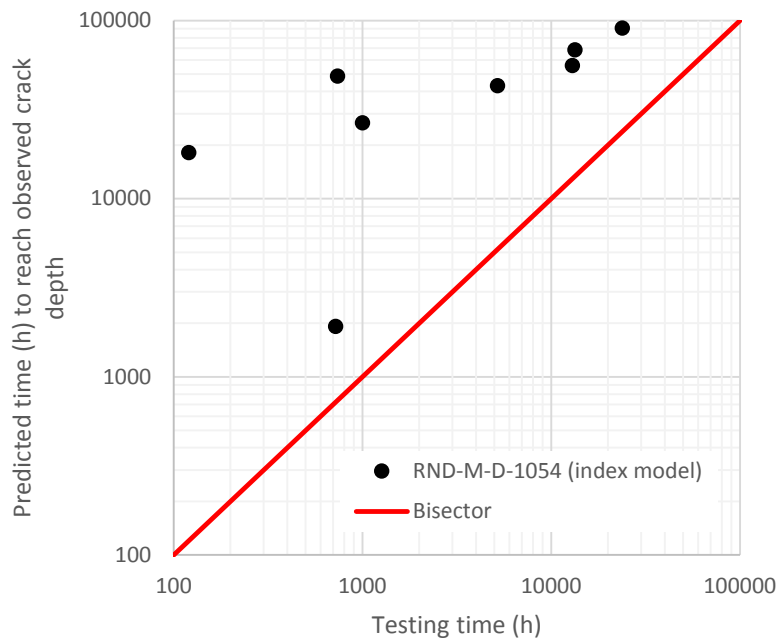


Figure 136 – Comparison between predicted time to reach experiment crack depth and testing time. EDF weld registered RND-M-D-1054. Code_Coriolis predictions relying on the index model and the sigmoid growth law. Initiation depth assigned to 0.

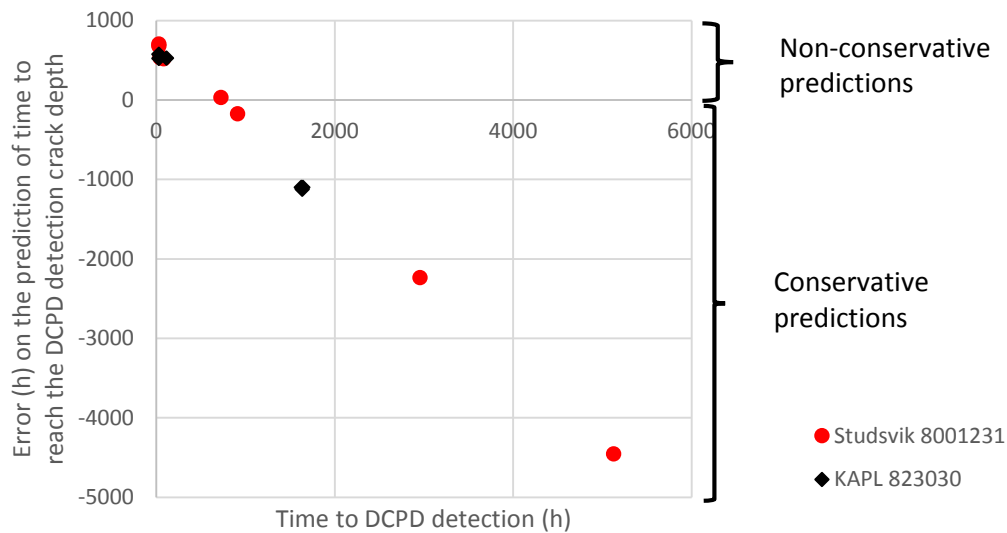


Figure 137 – Evaluation of the error in the prediction of the time to reach the DCPD detection (a crack depth of 150 μm), as a function of the time to reach the DCPD detection. Code_Coriolis predictions relying on the index model and the sigmoid growth law.

7.2. Local model

Predictions were all performed using the same set of parameters calibrated in a previous study without Code_Coriolis on the EDF weld registered RND-M-D-1054, except for the grain boundary coverage with chromium carbides (tuned for each material).

The accuracy of the predictions on weld RND-M-D-1054 was evaluated comparing the difference between the predicted and the experiment time to reach the maximal experiment crack depth as a function of this maximal experiment crack depth (Figure 138). A large difference between prediction and observation can be found for shallow (< 120 μm) and deep (> 1 mm) crack depths, with a significant probability to make non-conservative predictions. For the four cracks deeper than 1 mm, only one prediction (on specimen #1383-21) is not conservative. It could be due to the underestimation of the fast crack growth rate because specimen #1383-21 experienced the highest stress. Since PNNL tests demonstrated that initiation can occur in less than 30 h (which is considered representative of the material tested, but may not be entirely representative of material in nuclear power plant components), the fact that very short times to initiation are predicted by the local model is not the root cause of the lack of accuracy of the predictions. In addition, due to the fact that some of the testing times under low temperature or low applied stress were very long (more than 10,000 h) the underestimation of the slow crack growth rate is probably the main problem to fix. Complementary simulations may be done to better fit the slow crack growth regime and to guarantee conservative predictions. In return, overconservative predictions will be made using the index model, and an increase in the material index will be necessary to recover a reasonable conservative prediction. Last, very short time to initiation predicted by the local model should be validated by very short tests (from a couple of hours to tens of hours).

Regarding the Studsvik and KAPL cold worked welds, the accuracy of the predictions was evaluated comparing the difference between the predicted and the experiment time to reach the DCPD detection as a function of the time to reach the detection (Figure 139). Predictions related to very brief tests are not conservative. Since time to initiation prediction is not the root cause of the bad prediction, and that limited time was probably spent in the fast crack growth regime, it can be concluded that slow crack growth parameters have to be better tuned.

The large spread of experimental times to reach the DCPD detection under the same load suggest a lack of metallurgical or microstructural consideration in the crack propagation law.

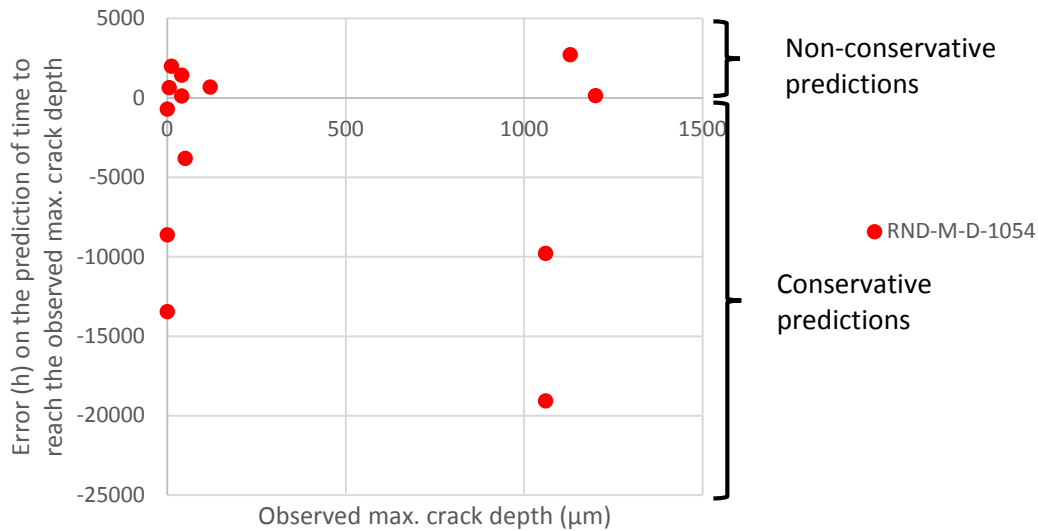


Figure 138 – Evaluation of the error in the prediction of the time to reach the experiment maximal crack depth, as a function of the maximal crack depth. Code_Coriolis predictions relying on the local model and the sigmoid growth law.

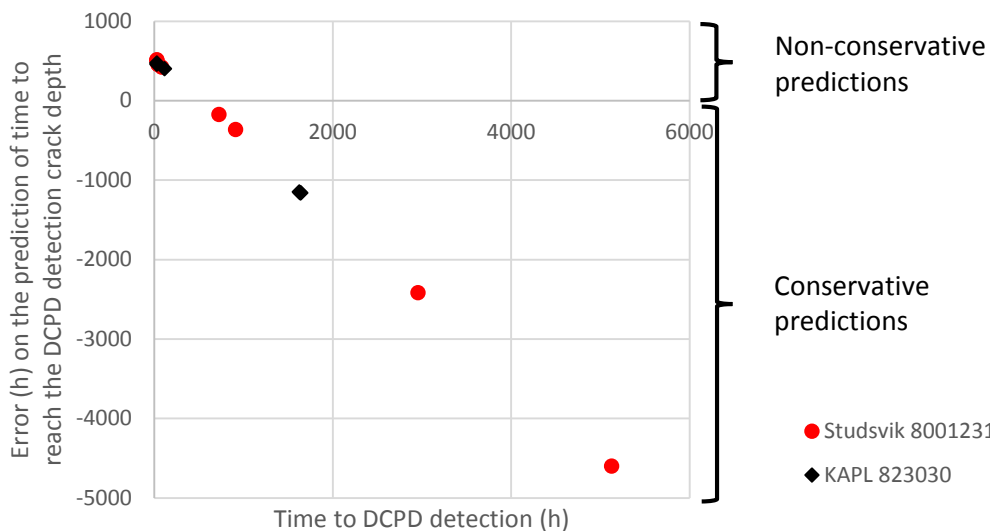


Figure 139 – Evaluation of the error in the prediction of the time to reach the DCPD detection (a crack depth of 150 µm), as a function of the time to reach the DCPD detection. Code_Coriolis predictions relying on the local model and the sigmoid growth law.

7.3. xLPR initiation models

Code_Coriolis initiation model predictions were benchmarked against the xLPR initiation model predictions for all initiation test data included in Section 4.2. This benchmarking was intended to develop a comparison of the relative accuracy and conservatism of the models. Figure 140 shows all xLPR and Code_Coriolis initiation predictions as well as initiation times for all specimens that initiated as a function of applied stress. Specimens that did not initiate in testing are not shown in this figure. Points with the same color represent predictions by a single model, and points with the same shape represent predictions for the same weld types. Points representing observed initiation times have unique colors and shapes for each weld type. The Direct Model 1 and Weibull model predictions shown as lines use the same test temperature (360°C, the temperature at which most specimens were tested) and uses

| | | |
|-----|---|--|
| MAI | Quantitative evaluation of the EDF local model and the EPRI-NRC xLPR models of crack initiation of the weld metals of Alloy 600 (Alloys 82 and 182) | 6125-4501-2018-00583-EN Version 2.0 |
|-----|---|--|

applied stress as the independent variable. For specimens at temperatures other than 360°C, the Direct Model 1 and Weibull model predictions are plotted as points of the same color.

Generally, the xLPR Direct Model 1 and Weibull Model predictions produce greater times to initiation (less conservative) than both the observed laboratory initiation times and Code_Coriolis model predictions. This is partially attributed to the differing definitions of initiation in the experiments and in each of the models. The output from Code_Coriolis used for this benchmarking was the time to a flaw depth of 150 µm, while the xLPR initiation models define initiation as the occurrence of a flaw of engineering scale, with a depth at least greater than 1 mm. Laboratory tests detected initiation at a range of flaw depths, but in the majority of cases, the flaw depths were significantly less than 1 mm. The PNNL-tested specimens were monitored by DCPD with a detection threshold approximately 150 µm deep.

It is noted that the xLPR Direct Model 1 and Weibull Model largely overestimate initiation times for KAPL and Studsvik specimens with initiation times under 100 hours⁽⁸⁾. The xLPR models were developed to represent the behavior of components in use in the field and not lab tested specimens. Specifically, although xLPR initiation effects model parameters (e.g., Q , n) were fit to laboratory data, the failure time model (Λ) was calibrated to field data for Alloy 82/182/132 dissimilar metal piping butt welds. Given the large difference between xLPR predictions, which represent field experience, and the observed laboratory initiation times for certain specimens, further investigation should be performed to determine whether the lab tested specimens with short initiation times (e.g., < 100 hours) are representative of material in plant components.

xLPR Direct Model 2 generally produces initiation times that are shorter (more conservative) than the observed initiation times, Code_Coriolis model predictions, Direct Model 1 predictions, and Weibull Model predictions. It is noted that the xLPR initiation models were calibrated to produce similar initiation times around the 80th percentile of each failure time distribution. As the 50th percentile of each distribution was used for calculating initiation times, it was expected that Direct Model 2 would result in an underprediction of initiation times for a majority of the specimens. The effect of the failure time distribution is discussed in detail in Section 7.4.

Apart from Direct Model 2, the Local Model predictions tend to be the most conservative of all the models. The Local Model has the shortest predicted time to a flaw depth of 150 µm for all RND-M-D-1054 weld specimens with applied stress lower than 530 MPa, KAPL specimens, and Studsvik specimens. The Index Model predicts shorter initiation times than both xLPR models, but predictions are on average 15-30% longer than predictions made using the Local Model.

The relative accuracy of the models in predicting crack initiation in laboratory specimens was evaluated by comparing the error between the predicted and observed initiation times for each specimen. Figure 141 shows the error in prediction time for each model as a function of applied stress, with all models evaluated at a temperature of 360°C. Note that the Code_Coriolis error data are calculated from the predicted times to reach a flaw depth of 150 µm. Also note that the error data for weld RND-M-D-1054 specimens 1383-11 and CEA have been omitted, as the error values are more than an order of magnitude greater than all other error data. Error for predictions from a single model are shown in the same color. Error for predictions from a single weld type are shown as the same shape.

The Code_Coriolis models tend to have the least error and are more likely to underpredict initiation times than Direct Model 1 or the Weibull Model. The Weibull Model error is smaller for KAPL weld specimens. The Weibull model error is also less than the Direct Model 1 error for all specimens. The Direct Model 2 error is smallest for the KAPL and Studsvik specimens, which had notably short initiation times (e.g., < 100 hours). As discussed in Section 7.4, Direct Model 2 produces very short initiation times when the 50th percentile of the failure time distribution is applied. Given that the xLPR models were calibrated near the 80th percentile of the failure time distributions, the relatively small error when applying the 50th percentile Direct Model 2 failure time distribution to these short initiation time (< 100 hours) specimens is not necessarily an indicator that it is the most accurate model. Applying the 80th percentile of the failure time distribution to all xLPR models would result in similar error among the xLPR models.

⁽⁸⁾ Direct Model 2 predicts initiation times similar to the Direct Model 1 and Weibull Model predictions when the recommended percentile of the failure time model parameters is used. Section 7.4 provides further detail on the agreement of the xLPR models.

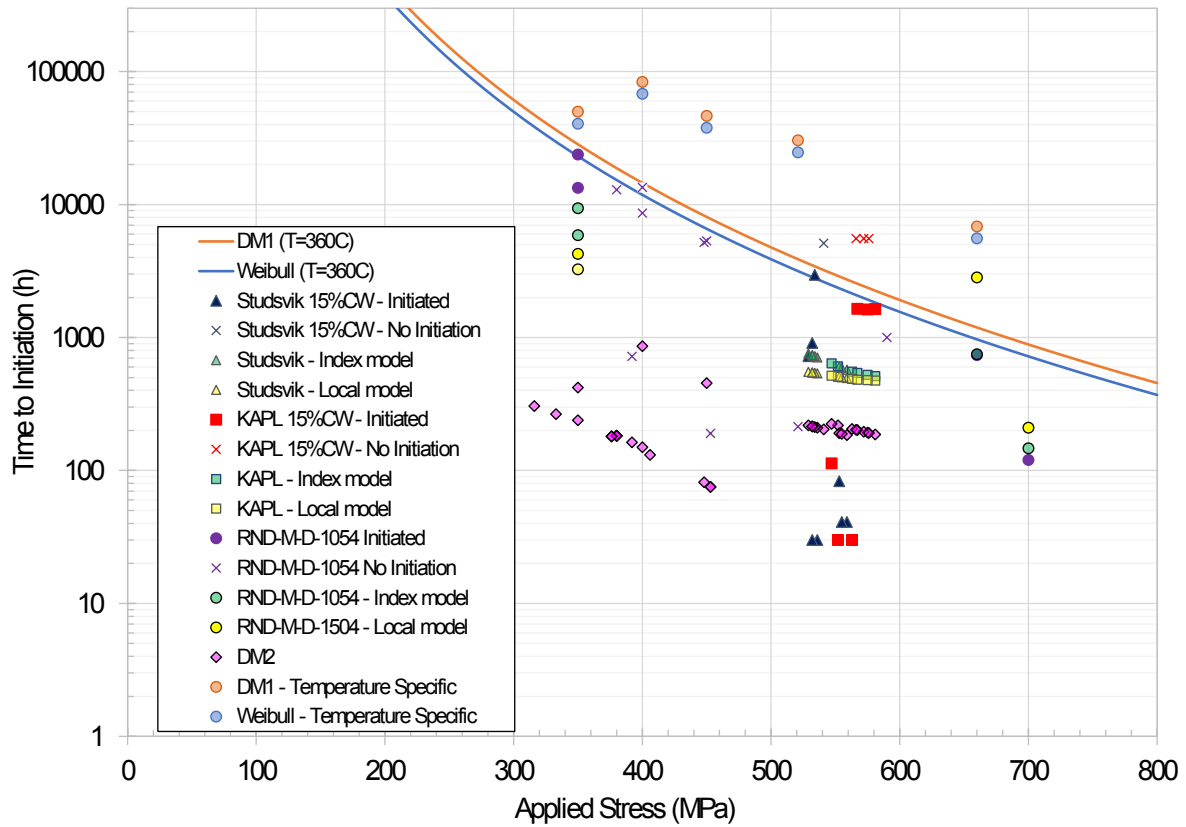


Figure 140 – Time to initiation for all initiated specimens and initiation time predictions by all models.

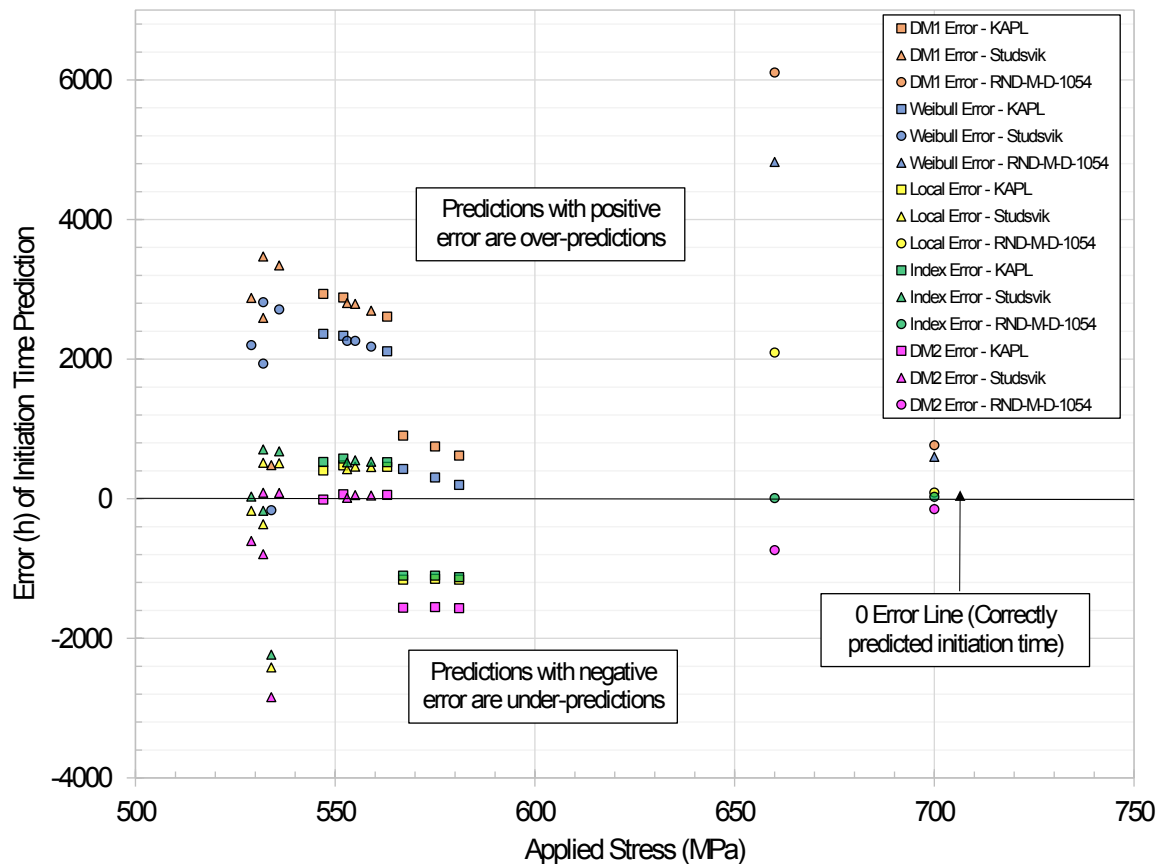


Figure 141 – Difference of predicted initiation time by all models and observed initiation time (Error) for all initiated specimens as a function of applied stress.

7.4. xLPR Model Calibration

Sections 6.6 and 7.3 discuss the comparison of the Code_Coriolis and xLPR crack initiation models. All xLPR predictions were made using the 50th percentile of the failure time model distributions. It was noted that almost all Direct Model 2 predictions were significantly lower (i.e., shorter times to initiation) than all other xLPR model predictions and Code_Coriolis predictions. This may be attributed to the methods employed when calibrating the failure time model parameters for the xLPR models.

The xLPR failure time model parameters are calibrated to data from Alloy 82/182 dissimilar metal piping butt welds in nuclear power plants. In accordance with this field experience, the models are in good agreement for lower cumulative probabilities of initiation (up to about 20%) for times to first initiation over a plant operating lifetime of 80 years. These initiation times approximately correspond to the 80th percentile of the distributed failure time model parameters used in each xLPR model. At lower percentiles, Direct Model 2 is much more conservative. As shown in Sections 6.6 and 7.3, when the 50th percentile of all distributions are used, Direct Model 2 produces notably shorter times to initiation than the other xLPR models, although the three models were calibrated to the same dataset. Figure 142 shows the xLPR model predictions for the applied stress used for all test specimens at the 80th percentile of the within component distributions for Direct Models 1 and 2 and the 80th percentile of the Weibull vertical intercept distribution. In this case, all the xLPR models are in good agreement.

xLPR initiation time predictions vary over orders of magnitude depending on the percentiles of the failure time distributions that are used. Figure 143 shows a scatter plot of 5000 predictions by each xLPR model at each applied stress. Figure 144 shows a violin plot of the same data. The distributed inputs to each xLPR model were randomly sampled for each of the 5000 predictions. Also shown in both figures are Index and Local Model predictions and the observed initiation times for all initiated specimens. The range of predictions produced by the xLPR models span over multiple orders of magnitude at each applied stress. Generally, Direct Model 1 has the largest variation for each applied stress. As discussed above, Direct Model 2 is more conservative at lower percentiles and over a larger range of percentiles

of the failure time distributions, so it is expected to predict shorter initiation times. Although the predictions span a wide range, Code_Coriolis predictions and observed initiation times appear to be in the middle ranges of the of xLPR predictions, suggesting there is some agreement between the Code_Coriolis models, xLPR models, and observed initiation times.

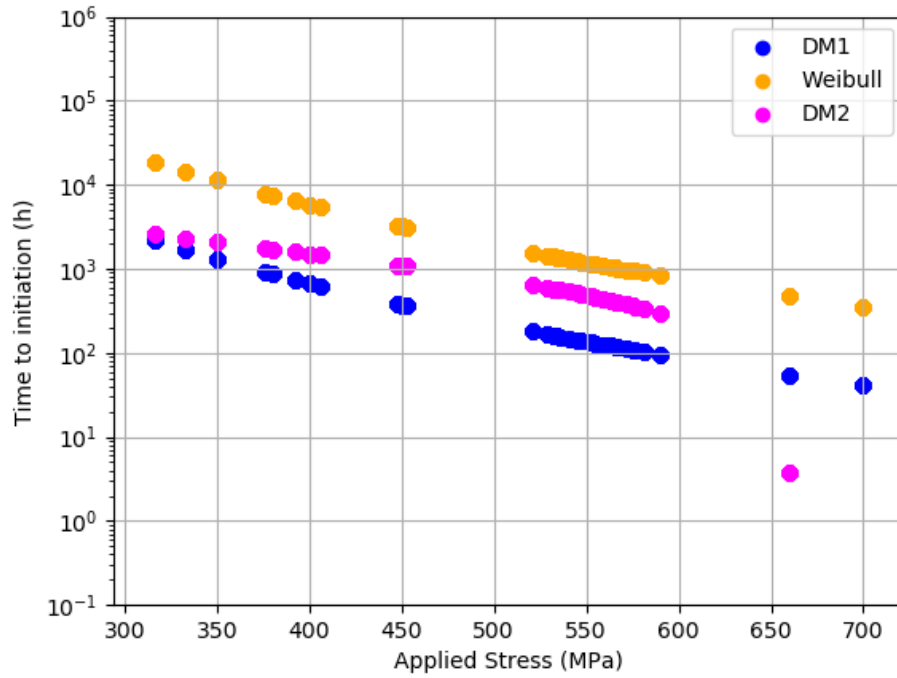


Figure 142 – xLPR model initiation predictions at the 80th percentile of input distributions.

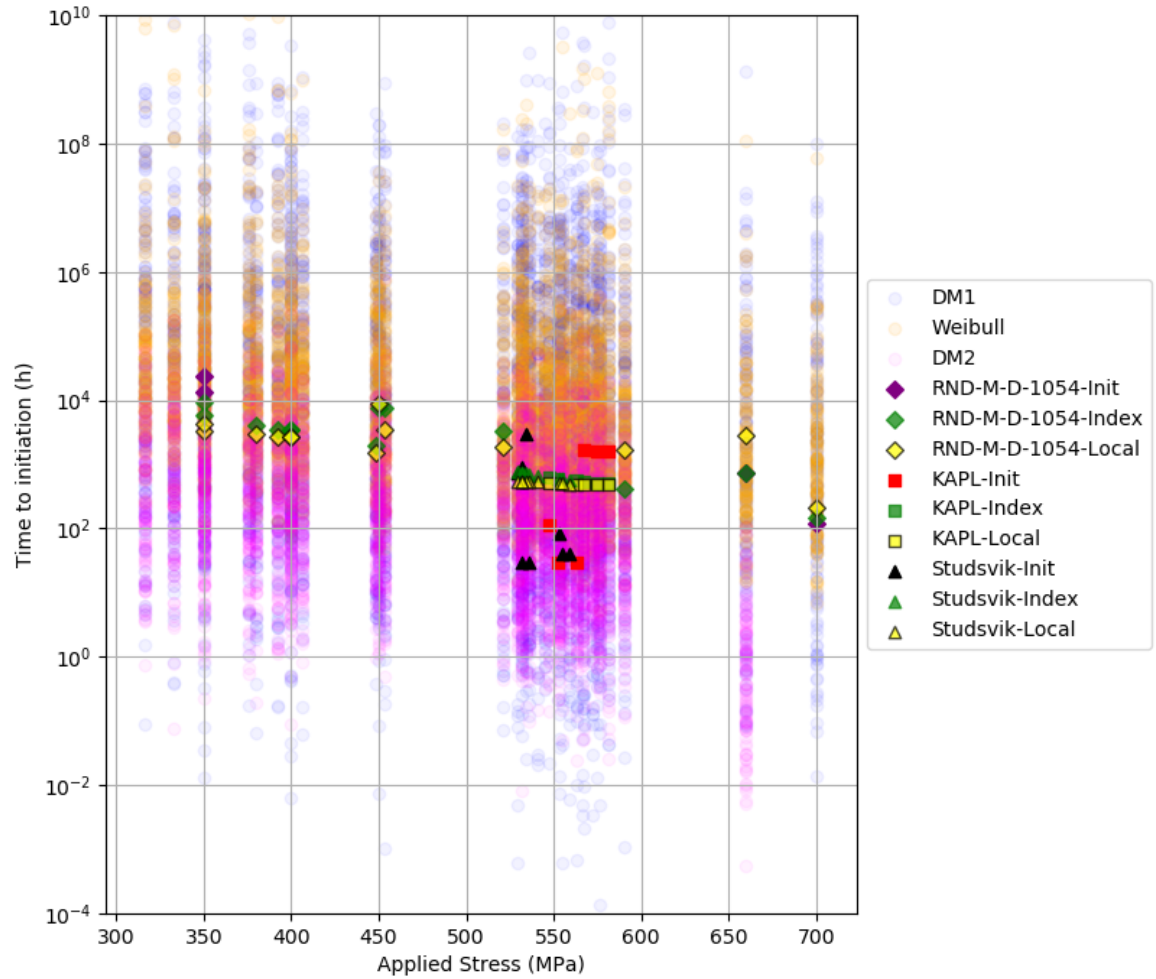


Figure 143 – xLPR model initiation predictions over range of distributed inputs.

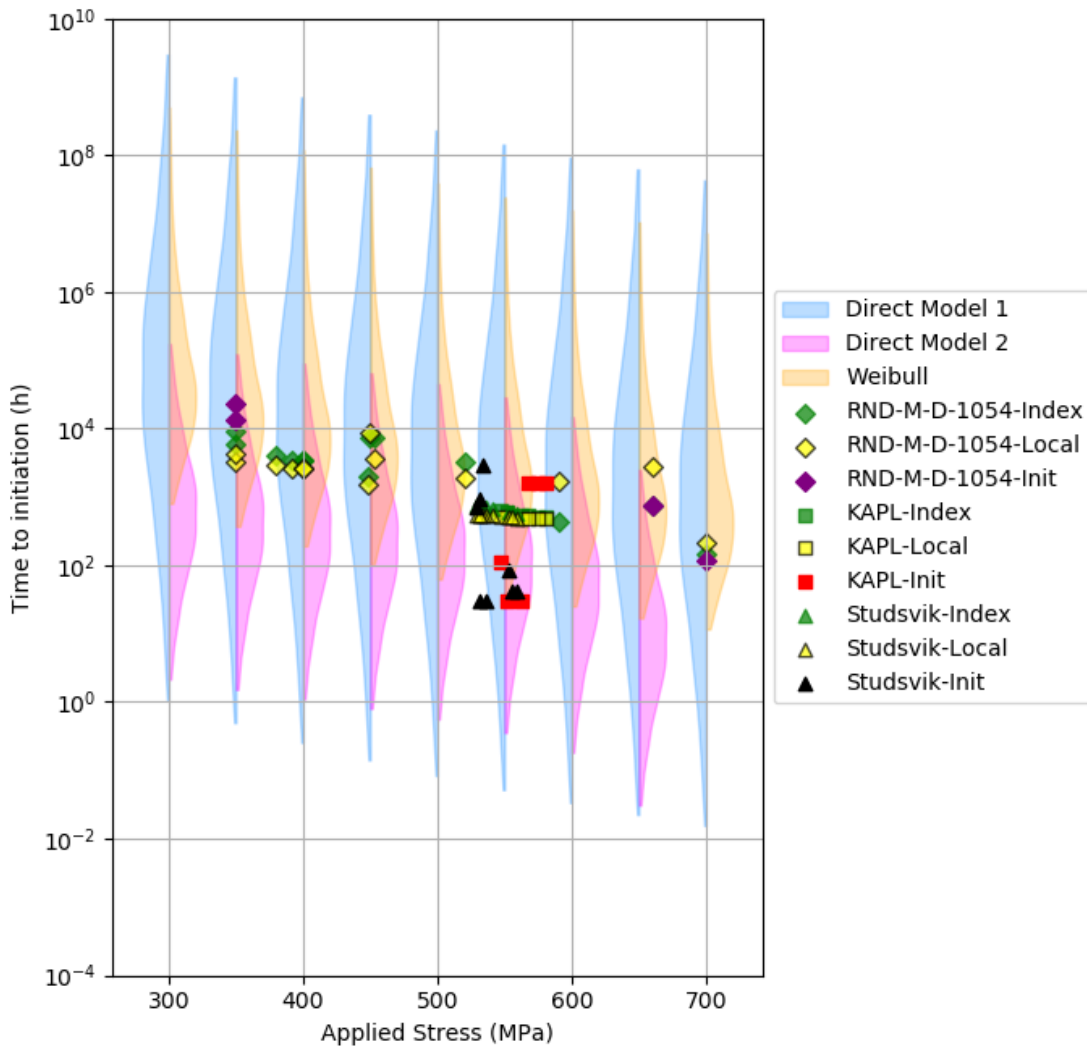


Figure 144 – Violin plot of xLPR model predictions over range of distributed inputs.

| | | |
|-----|---|--|
| MAI | Quantitative evaluation of the EDF local model and the EPRI-NRC xLPR models of crack initiation of the weld metals of Alloy 600 (Alloys 82 and 182) | 6125-4501-2018-00583-EN Version 2.0 |
|-----|---|--|

8. Conclusions and future work

Code_Coriolis (intermediate version v2.1.5) computations were performed in order to evaluate the accuracy of SCC predictions relying on two initiation models, coupled to the same sigmoid crack growth law:

- The index model: a fully empirical model. A large experimental SCC database is required for the calibration of parameters.
- The local model: a phenomenological model. SCC tests are not necessary to calibrate the model. They are required for the evaluation of predictions and can be used to optimize the crack growth model.

Current parameters allow conservative predictions of cracking kinetics for cracks deeper than 1 mm, if the index model is used. Parameters of the crack growth model should be tuned to guarantee conservative predictions using the local model.

Experiments performed by PNNL confirm that the time to initiation can be extremely short (less than 30 h), as predicted by the local model. These tests also show how microstructural or metallurgical parameters can affect initiation or the rate of cracking, at least in the slow crack growth regime. It is noted that although these observed extremely short times to initiation are considered representative of the material tested, it is possible that the material tested (15% cold forged) is not entirely representative of material in nuclear power plant components.

The simulation of PNNL tests, performed on cold worked welds, suggest that tested Studsvik and KAPL welds may have a larger susceptibility to SCC than EDF weld registered RND-M-D-1054. This weld was used to calibrate the EDF SCC model upper bounds. Therefore, complementary investigations may be useful to rank the susceptibilities of these three welds, considering at least the precipitation of chromium carbides and cold work, as well as the differences in environmental conditions tested and testing methodologies used.

Code_Coriolis initiation model predictions were benchmarked against the xLPR initiation model predictions for all available initiation test data. Generally, the xLPR Direct Model 1 and Weibull Model predictions produce greater times to initiation than both the observed laboratory initiation times and Code_Coriolis model predictions. This is partially attributed to the differing definitions of initiation in the experiments and in each of the models. xLPR Direct Model 2 generally produces initiation times that are shorter than the observed initiation times, Code_Coriolis model predictions, Direct Model 1 predictions, and Weibull Model predictions. The Code_Coriolis models tend to have the least error and are more likely to underpredict initiation times than Direct Model 1 or the Weibull Model. Almost all Direct Model 2 time to initiation predictions were significantly shorter than all other xLPR model predictions and Code_Coriolis predictions. This may be attributed to the methods employed when calibrating the failure time model parameters for the xLPR models.

Complementary tests and computations may be useful to better calibrate behaviors involved in the SCC:

- Oxidation tests, to improve the prediction of oxidation kinetics.
- Cracking tests of oxidized grain boundaries and crystal plasticity FEM, to improve the prediction of initiation.
- Crack growth tests under low K values, to better model the slow crack growth regime.

Existing models could be used to evaluate the susceptibility to PWSCC of Bottom Mounted Instrumentation nozzles (Figure 145). It may offer relevant guidelines for the improvement of models in agreement with industrial issues (surface finish effects) and factors of improvement based on mitigation (water chemistry, material replacement, peening). The simulation of components could also contribute to validate PWSCC models.

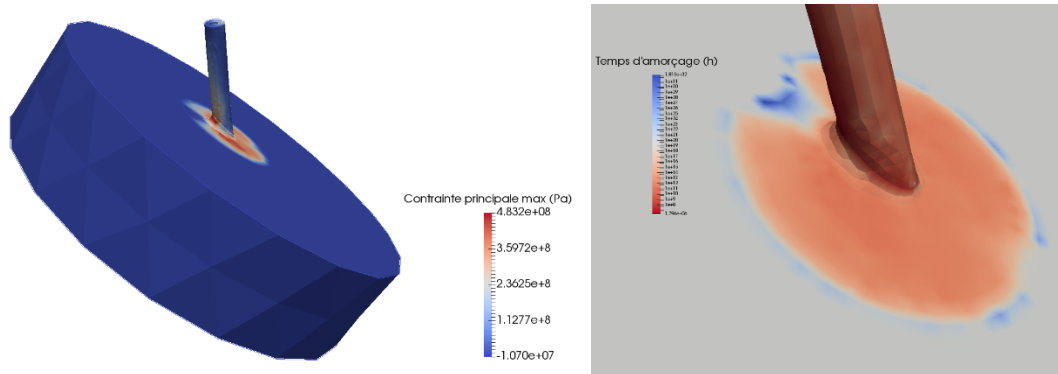


Figure 145 – Preliminary computation of the susceptibility to PWSCC of a peripheral BMI nozzle using Code_Coriolis v2.1.5 (intermediate version). Stress field (left) and time to initiation field (right) at the surface of the weld and the nozzle.

| | | |
|-----|---|--|
| MAI | Quantitative evaluation of the EDF local model and the EPRI-NRC xLPR models of crack initiation of the weld metals of Alloy 600 (Alloys 82 and 182) | 6125-4501-2018-00583-EN Version 2.0 |
|-----|---|--|

9. Cited documents

- [1] T. Couvant, 'Prediction of IGSCC as a FEM post analysis', 18th International Conference on environmental degradation of materials in nuclear systems-water reactors, Portland (Oregon), 2017.
- [2] T. Couvant, E. Burger, C. Thaury, C. Rainasse, 'Simulating the susceptibility to IGSCC of cold work 316 austenitic stainless steel exposed to primary water', 19th International Conference on environmental degradation of materials in nuclear systems-water reactors, Boston (Massachusetts) 2019.
- [3] <https://coriolis-test-8.pam-reted.fr/coriolis/#!/login>
- [4] T. Couvant, M. Dib, Y. Shen, C. Thaury, F. Oliveira, C. Rainasse, P. Grandclément, 'Toward a simulation of in-service SCC observed on Reactor Coolant Pump diffuser studs - A support to failure analyses', Fontevraud 9, Avignon (France), 2018.
- [5] T. Couvant, J. Caballero, C. Duhamel, J. Crépin, T. Maeguchi, 'Calibration of the Local IGSCC Engineering Model for Alloy 600', 18th International Conference on environmental degradation of materials in nuclear power systems – water reactors, Portland (USA), 2017.
- [6] T. Couvant, M. Wehbi, C. Duhamel, J. Crépin, R. Munier, 'Development of a local model to predict SCC: preliminary calibration of parameters for nickel alloys exposed to primary water', 17th International Conference on environmental degradation of materials in nuclear systems-water reactors, Ottawa (Canada), 2015.
- [7] T. Couvant, M. Wehbi, C. Vautier, 'SCC initiation models for nickel alloys 182/82 weld metals exposed to primary environment', EDF MAI report 6125-4501-2016-15869-EN, 2016.
- [8] T. Couvant, M. Wehbi, R. Munier, K. Sato, B. Martin-Cabanas, C. Vautier, 'Mechanical and oxidation behaviors of nickel weld Alloys 182 and 82 - Effect of welding conditions on microstructural parameters', EDF MAI report H-B60-2012-00926-EN, 2015.
- [9] K. Nakata, O. Okada, Y. Ueki, T. Kamino, 'Effect of thin foil thickness on measurement of grain boundary segregation with FEG-TEM/EDS in austenitic stainless steels', Journal of Electron Microscopy 47 (3), 1993.
- [10] R. Bandy, D. van Rooyen, 'Effect of thermal stabilization on the low temperature stress corrosion cracking of Inconel 600', Corrosion vol. 40, 1984.
- [11] A. Stein, A. McIlree, 'Relationship of annealing temperature and microstructure to primary side cracking of alloy steam generator tubing and the prediction of stress corrosion cracking in primary water', 2nd International Symposium on Environmental Degradation of Materials in Nuclear Power System-Water Reactors, Monterey (California), 1985.
- [12] Y. Rouillon, 'Essais de corrosion sous contrainte en eau pure et en milieu primaire de réacteurs à eau pressurisée sur tubes de générateurs de vapeur en alliages 600 et 690', note EDF EMA D588, 1985.
- [13] D. Garriga-Majo, 'Etude métallurgique de la corrosion sous contrainte en milieux aqueux de l'alliage 600 (NC15Fe)', PhD thesis, University of Paris-Sud, 1993.
- [14] J.D. Mithieux, F. Vaillant, 'Influence de la teneur en chrome et de la structure des alliages de nickel sur le comportement en corrosion sous contrainte en milieu primaire de REP', note EDF HT-44/97/020/A, 1997.
- [15] F. Vaillant, J.D. Mithieux, 'Influence of chromium content and microstructure on creep and PWSCC resistance of nickel base alloys', 9th International Symposium on Environmental Degradation of Materials in Nuclear Power System-Water Reactors, Newport Beach (California), 1999.
- [16] T. Couvant, L. Legras, T. Ghys, 'Interaction between strain localization and SCC in austenitic alloys exposed to PWR primary environment (contract EP-P22073/C10796) - Final report', EDF report H-T29-2010-00634-EN, 2012.

| | | |
|-----|---|--|
| MAI | Quantitative evaluation of the EDF local model and the EPRI-NRC xLPR models of crack initiation of the weld metals of Alloy 600 (Alloys 82 and 182) | 6125-4501-2018-00583-EN Version 2.0 |
|-----|---|--|

- [17] P. Crooker, 'Materials Reliability Program: Stress Corrosion Crack (SCC) Initiation Testing of Ni-Base Alloys for PWR Applications – Part 1 (MRP-426)', EPRI report 3002010761, 2017.
- [18] Data provided by M. Toloczko from PNNL.
- [19] P. Scott, P. Combrade, 'General corrosion and stress corrosion cracking of Alloy 600 in light water reactor primary coolants', *Journal of Nuclear Materials* 524, 340-375, 2019.
- [20] F. Vaillant et al., 'A review of weldability and SCC behaviors of Ni-base weld metals in laboratory PWR environment', 13rd International Conference on environmental degradation of materials in nuclear systems-water reactors, Whistler (Canada), 2007.
- [21] M. Wehbi, T. Couvant, C. Duhamel, J. Crépin, 'Oxidation of nickel-base welds 182 and 82 in simulated primary water of pressurised water reactors', *Materials at High Temperatures Vol 32*, No 1–2, 2015.
- [22] C. Duhamel, M. Wehbi, T. Couvant, J. Crepin, 'Grain Boundary Oxidation of Nickel Base Welds 182/82 in Simulated PWR Primary Water', 17th International Conference on environmental degradation of materials in nuclear systems-water reactors, Ottawa (Canada), 2015.
- [23] J. Caballero, J. Crépin, T. Couvant, C. Duhamel, 'Intergranular oxidation of Alloy 600 exposed to simulated PWR primary water', Eurocorr 2014, Pisa (Italy).
- [24] L. Thomas, M. Olszta, B. Johnson, S. Bruemmer, 'Microstructural characterization of primary water stress-corrosion cracks in Alloy 182 welds from PWR components and laboratory tests', 14th International Conference on Environmental Degradation of Materials in Nuclear Power Systems-Water Reactors, Virginia Beach (Virginia), 2009.
- [25] S. Attanasio, D. Morton, 'Measurement of the Nickel/Nickel Oxide Transition in Ni-Cr-Fe Alloys and Updated Data and Correlations to Quantify the Effect of Aqueous Hydrogen on Primary Water SCC', 11th International Conference on Environmental Degradation of Materials in Nuclear Power Systems-Water Reactors, Stevenson (Washington), 2003.
- [26] D. Morton, S. Attanasio, G. Young, 'Primary water SCC understanding and characterization through fundamental testing in the vicinity of the nickel/nickel oxide phase transition', 10th International Conference on Environmental Degradation of Materials in Nuclear Power Systems-Water Reactors, Lake Tahoe (California), 2001.
- [27] G. Cailletaud, 'A micromechanical approach to inelastic behaviour of metals', *International Journal of Plasticity*, Volume 8, Issue 1, 1992, Pages 55-73.
- [28] www.code-aster.org.
- [29] J. Dohr, 'Recent Insights in the Deformation and Fracture of Oxidized Grain Boundaries in Austenitic Alloys: A Synergistic Experimental and Finite Element Study', 17th International Conference on environmental degradation of materials in nuclear systems-water reactors, Ottawa (Canada), 2015.
- [30] A. Seyeux, V. Maurice, P. Marcus, 'Oxide Film Growth Kinetics on Metals and Alloys - I. Physical Model', *Journal of The Electrochemical Society*, 160 (6) C189-C196 (2013).
- [31] xLPR-MSGR-CI V1, PWSCC & Fatigue Crack Initiation Module Development, August 2016.
- [32] xLPR-SRD-CI-SCC V3.4, xLPR Software Requirements Description for Crack Initiation – PWSCC, December 2015.
- [33] C. Amzallag, S. L Hong, C. Pages, A. Gelpi, "Stress Corrosion Life Assessment of Alloy 600 PWR Components," *Proceedings of the Ninth International Symposium on Environmental Degradation of Materials in Nuclear Power Systems – Water Reactors*, pp. 243-250, The Minerals, Metals, and Materials Society, 1999.
- [34] F. Cattant, F. Vaillant, J. M. Boursier, and S. De-Vito, "Contribution of Hot and Cold Laboratory Investigations to the Resolution of EDF Alloys 600/182/82 PWSCC Issues," *Materials Reliability Program: Proceedings of the 2005 International PWSCC of Alloy 600 Conference and Exhibit Show (MRP-154)*, EPRI 1012089, Santa Anna Pueblo, New Mexico, 2005. [Freely available at

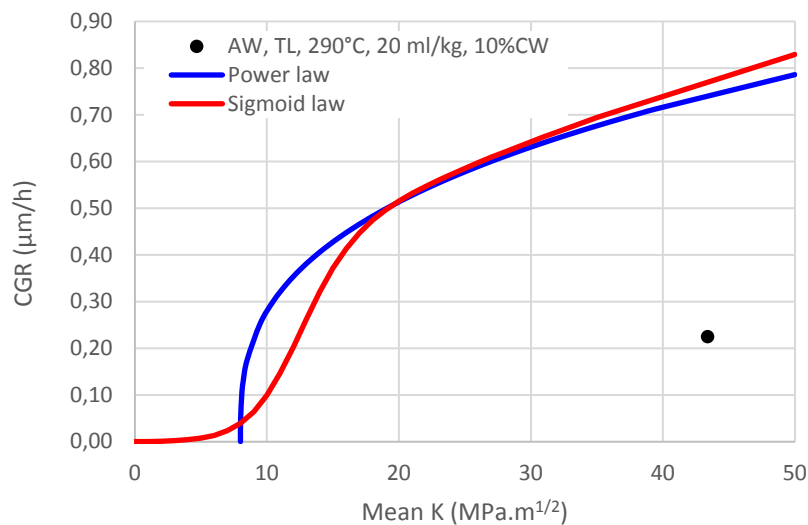
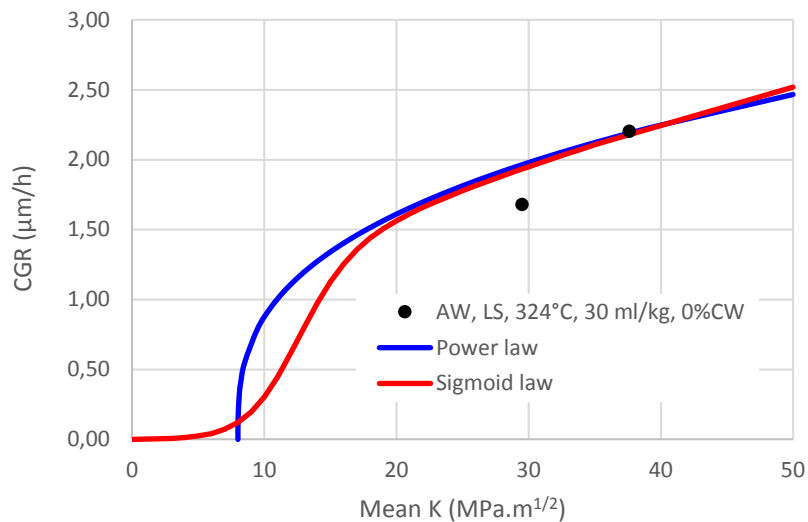
| | | |
|-----|---|--|
| MAI | Quantitative evaluation of the EDF local model and the EPRI-NRC xLPR models of crack initiation of the weld metals of Alloy 600 (Alloys 82 and 182) | 6125-4501-2018-00583-EN Version 2.0 |
|-----|---|--|

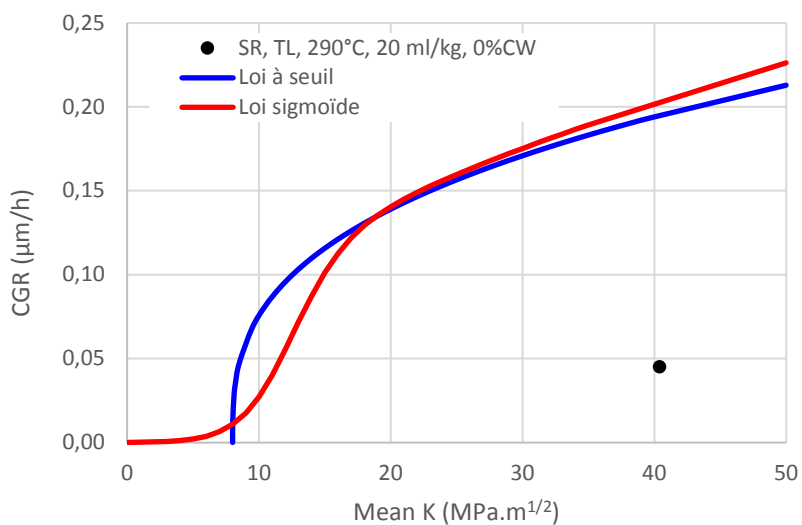
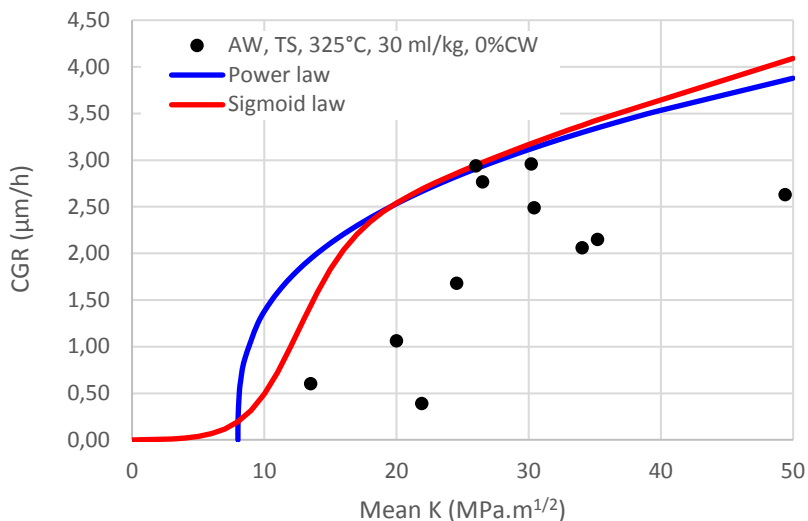
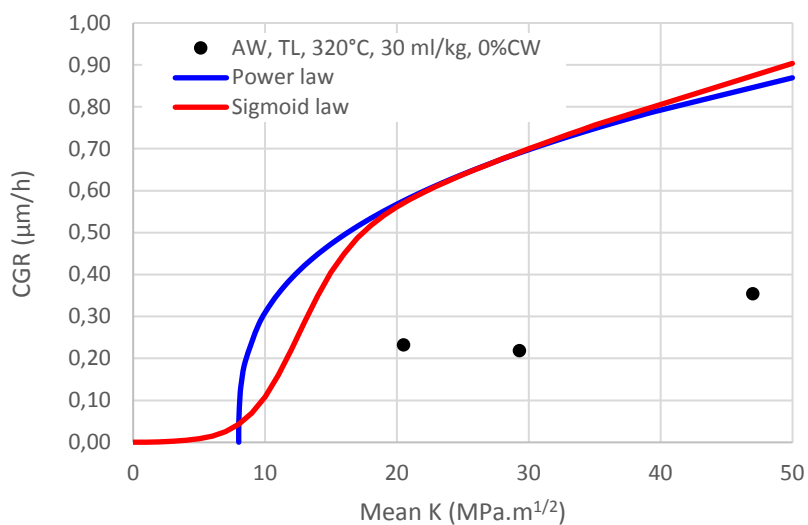
www.epri.com]

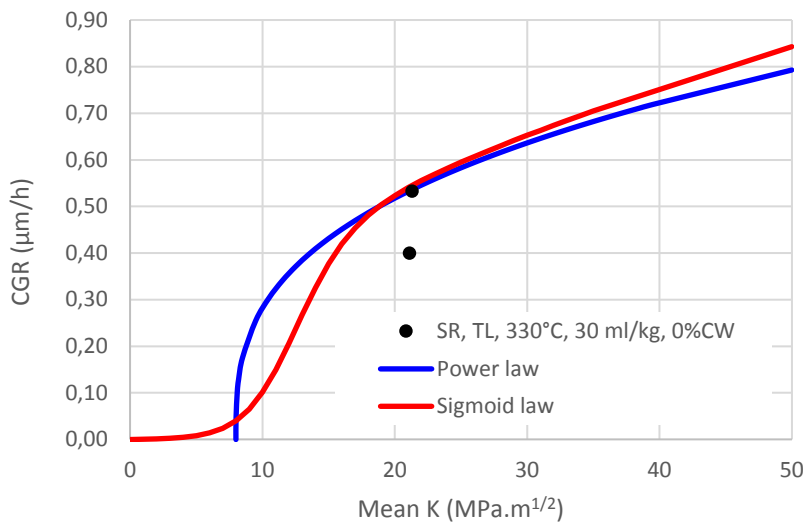
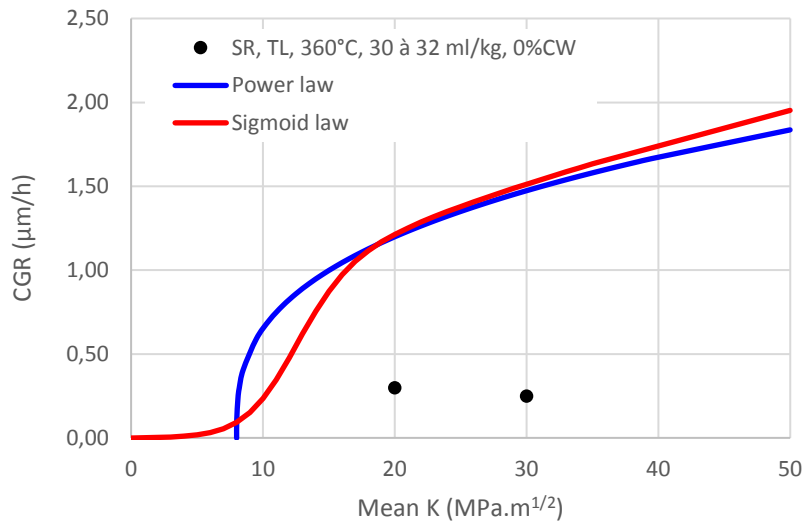
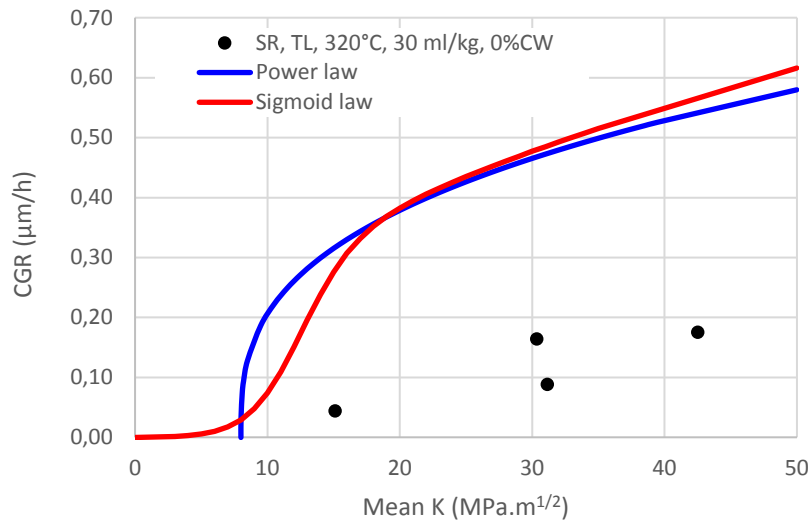
- [35] J. Daret, "Initiation of SCC in Alloy 600 Wrought Materials: A Laboratory and Statistical Evaluation," *Proceedings of the 12th International Conference on Environmental Degradation of Materials in Nuclear Power System – Water Reactors*, pp. 937-944, The Minerals, Metals & Materials Society, 2005.
- [36] P. Scott, et al., "Comparison of Laboratory and Field Experience of PWSCC in Alloy 182 Weld Metal," *Presented at the 13th International Conference on Environmental Degradation of Materials in Nuclear Power Systems*. Whistler, British Columbia, Canada, 2007.
- [37] xLPR-TR-CI-SCC-Calibration V2.0, PWSCC Initiation Model Parameter Development, Confirmatory Analyses, and Validation for xLPR Version 2.0, March 2017.
- [38] *Stress Corrosion Cracking Initiation Model for Stainless Steel and Nickel Alloys – Effects of Cold Work*. EPRI, Palo Alto, CA: 2009. 1019032. [Freely available at www.epri.com]
- [39]. Validation of Stress Corrosion Cracking Initiation Model for Stainless Steel and Nickel Alloys: Effects of Cold Work. EPRI, Palo Alto, CA: 2012. 1025121.
- [40] R. B. Abernethy, *The New Weibull Handbook*, Second Edition, Robert B. Abernethy, North Palm Beach, FL, 1996.
- [41] W. J. Shack and O. K. Chopra, "Statistical Initiation and Crack Growth Models for Stress Corrosion Cracking," *Proceedings of the 2007 ASME Pressure Vessels and Piping Division Conference*, San Antonio, TX, 2007.
- [42] D. Morton, S. Attanasio, G. Young, 'Primary Water SCC Understanding and Characterization Through Fundamental Testing in the vicinity of the Nickel/Nickel Oxide Phase Transition', *Proceedings of 10th International Conference on Environmental Degradation of Materials in Nuclear Power Systems-Water Reactors*, 2001.
- [43] W.J. Mills, C.M. Brown, 'Stress corrosion cracking growth rates for alloys 82H welds in high temperature water', *11th International Conference on Environmental Degradation of Materials in Nuclear Power Systems-Water Reactors*, Stevenson (WA), 2003.
- [44] D.J. Paraventi, W.C. Moshier, 'The effect of cold work and dissolved hydrogen in the stress corrosion cracking of alloy 82 and alloy 182 weld metal', *12th Int. Conf. on Environmental Degradation of Materials in Nuclear Power Systems-Water Reactors*, Snowbird (USA), 2005.
- [45] T. Couvant, 'Dossier de Synthèse des Zones en Inconel : chapitres R&D Matériaux', note EDF R&D 6125-2108-2018-02446-FR.
- [46] G. Young, W. Wilkening, D. Morton, E. Richey, N. Lewis, 'The mechanism and modeling of intergranular stress corrosion cracking of nickel-chromium-iron alloys exposed to high purity water', *12th International conference on environmental degradation of materials in nuclear power systems-water reactor*, 2005.

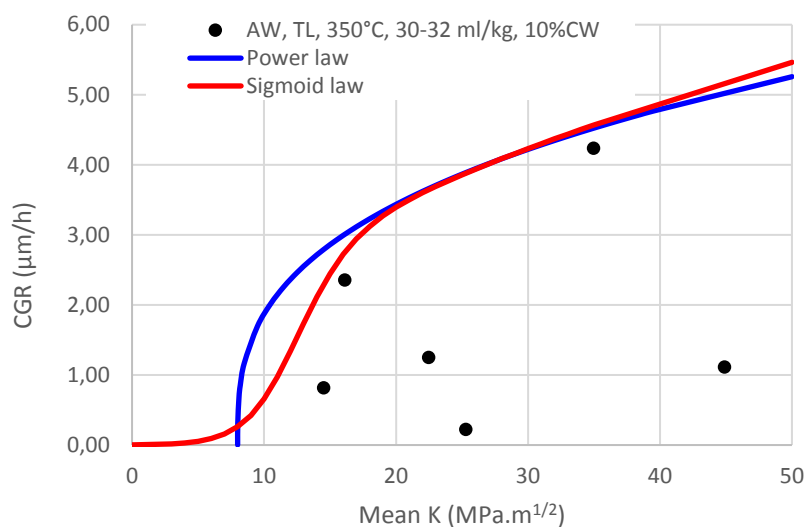
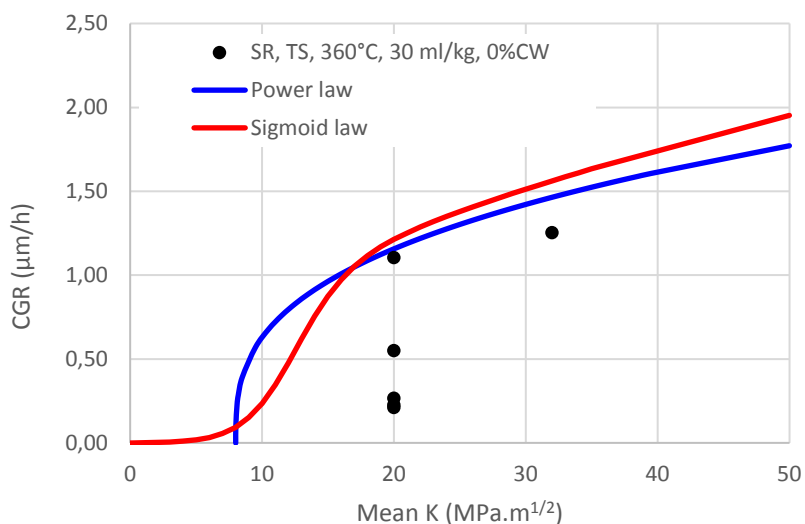
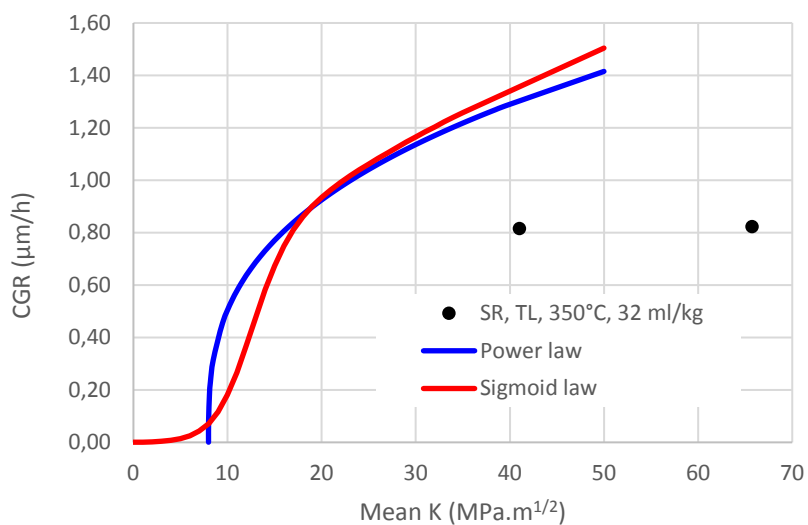
10. Appendix 1: CGR upper bounds vs. crack growth data on weld registered RND-M-D-1054

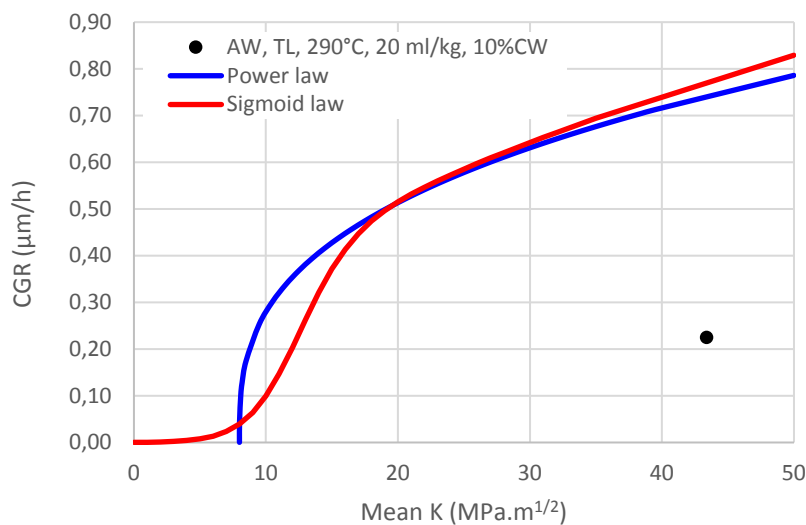
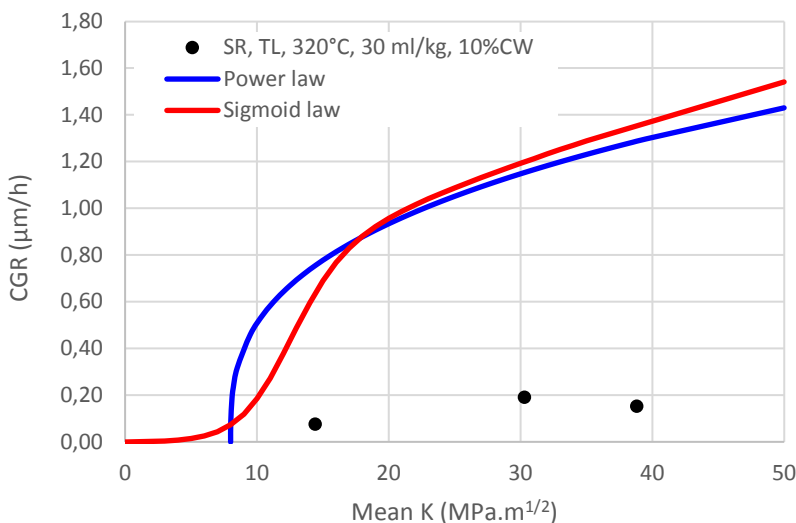
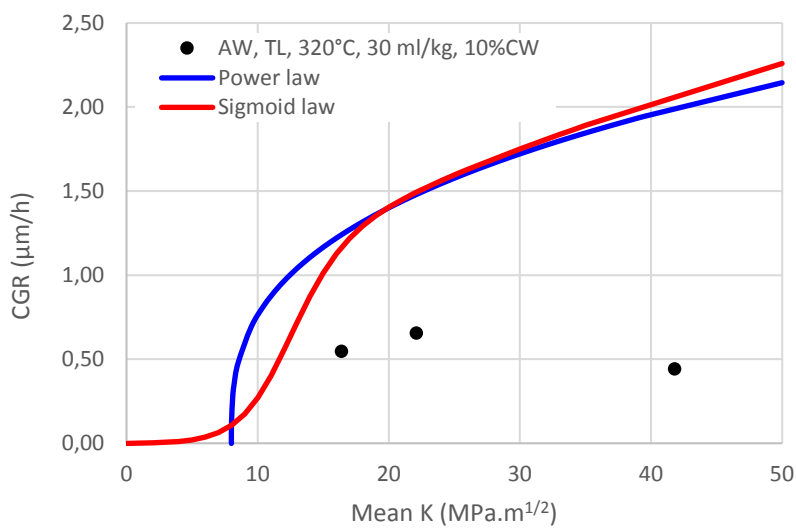
In the following, the EDF crack growth power laws (in blue) and sigmoid laws (in red) are compared with EDF crack growth experiments. Each figure corresponds to given experimental condition: stress relief heat treatment (TTD), cracking direction vs. loading direction (in the L, S and T axes of the weld), primary water temperature, dissolved hydrogen and cold work (CW) of the weld prior to testing.

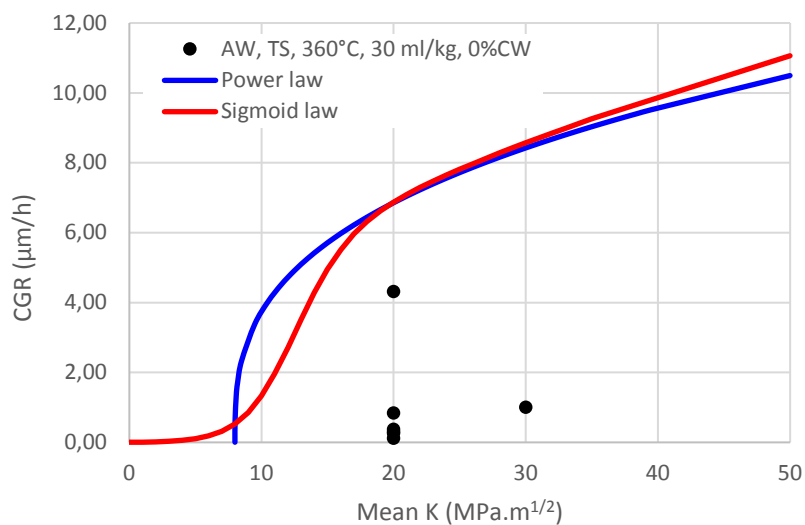
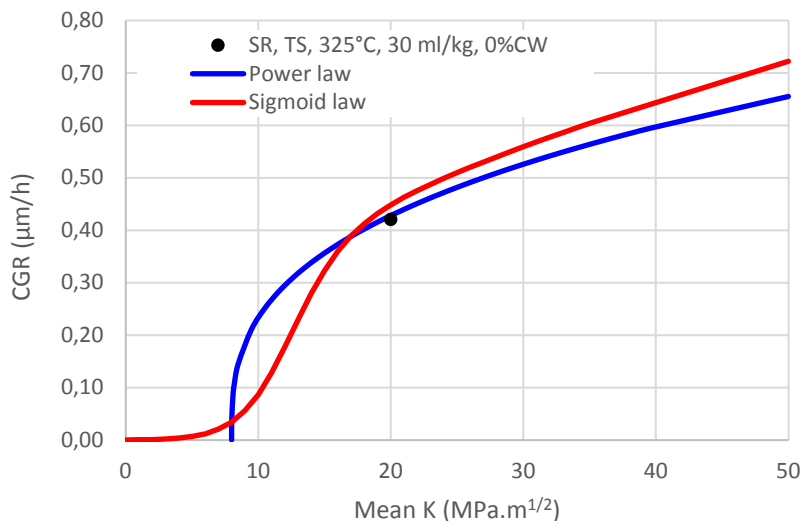
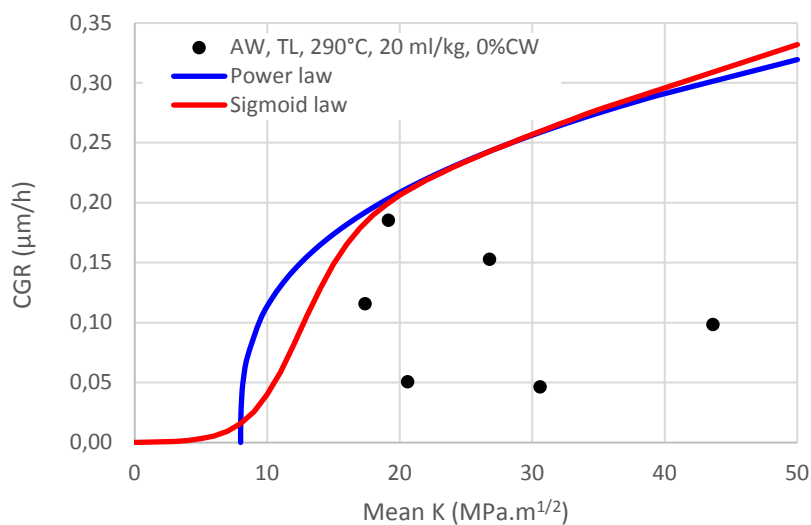












11. Appendix 2: Code_Coriolis main inputs/outputs

11.1. Simulations of the test on specimen 1383-11

11.1.1. Index initiation model with sigmoid CGR law

Parameters of the initiation model named 'index' (Code_Coriolis v2.1.5 intermediate version)

| init1 | init2 | init3 | init4 (j/mol) | init5 | init6 | Init_depth |
|-------|-------|-------|---------------|-------|------------------|------------|
| 1 | 6.8 | 1 | 185000 | 1 | 10 ⁻⁶ | 0.005 |

Parameters of the crack growth model named 'cgr_sigmoid_cw2_h' (Code_Coriolis v2.1.5 intermediate version)

| cgr1 | cgr2 | cgr3 | cgr4 | cgr5 | cgr6 | cgr7 | cgr8 | cgr9 | cgr10 | cgr11 | ecp1 | ecp2 |
|-------------------|------|------|------|------|------|------|-------|-------|-------|-------|--------------------|--------|
| 5×10 ⁴ | 0.5 | 0.66 | 12 | 15 | 0 | 0 | 3.604 | 11.33 | 43.36 | 65000 | 2×10 ⁻⁶ | 0.0256 |

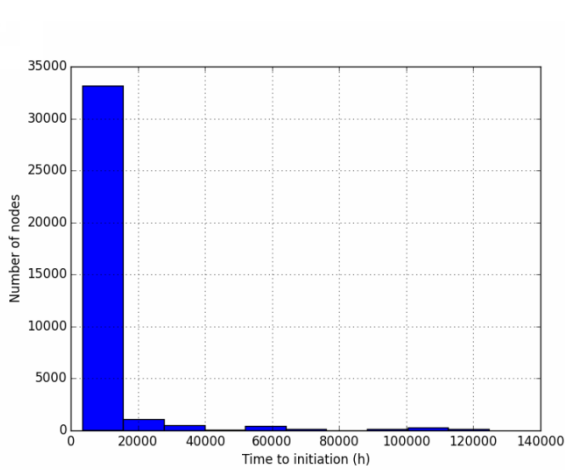


Figure 146 – Histogram of times to initiation predicted for specimen 1383-11, using the index model.

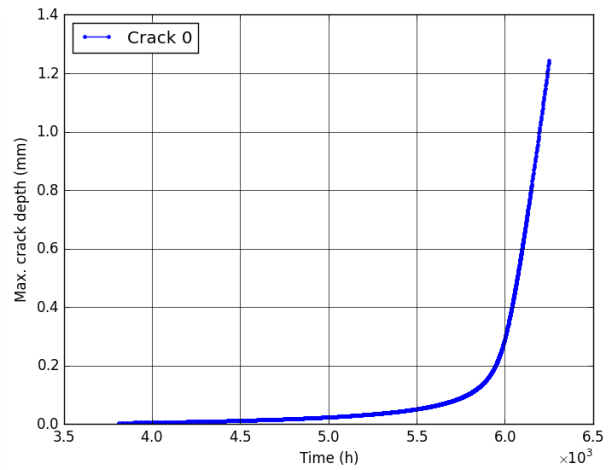


Figure 147 – Cracking kinetics predicted for specimen 1383-11, using the index model.

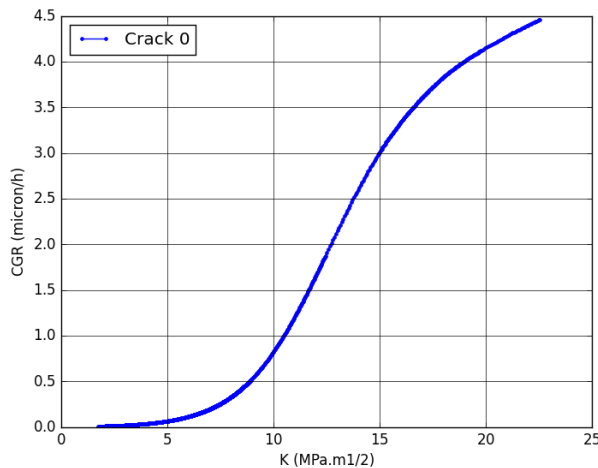


Figure 148 – Crack growth rate versus K at the tip of the main crack predicted for specimen 1383-11, using the index model.

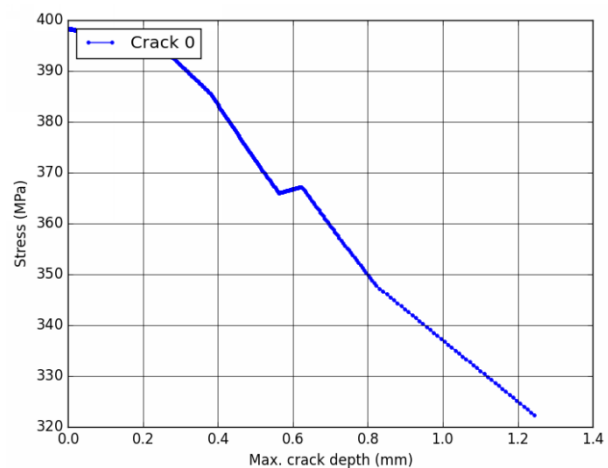


Figure 149 – Stress versus depth at the tip of the main crack predicted for specimen 1383-11, using the index model.

11.1.2. Local initiation model with sigmoid CGR law

Parameters of the initiation model named 'local_initiation_model' (Code_Coriolis v2.1.5 intermediate version)

| Grain boundaries | | | | | | | | | | | | |
|-------------------------------|--------------------------|----------------------|---------------|--------------------------|------------------|-------------|---------------------|-------|-------------|------|------|------|
| Densite (mm/mm ²) | SfTot (mm ²) | SpaceResolution (nm) | GBlength (nm) | GBResolution (joints/mm) | GBC | rC (nm) | zCr (nm) | | | | | |
| 10 | 1 | 1 | 200 | 10 | 0.2 | 30 | 30 | | | | | |
| Intergranular oxidation | | | | | | | | | | | | |
| x0nom (nm) | bnom | cnom | x0depl (nm) | bdepl | Cdepl | x0carb (nm) | bcarb | Ccarb | oxQ (J/mol) | oxg1 | oxg2 | oxg3 |
| 0 | 1.86×10 ⁷ | 3 | 0 | 2.4×10 ⁷ | 3 | 0 | 2.6×10 ⁷ | 0.01 | 57000 | 0.1 | 0.3 | 0.04 |
| Cracking criterion | | | | | | | | | | | | |
| Poxc (nm) | SigmaC (MPa) | | | | StressLinearCoef | | | | | | | |
| 200 | 790 | | | | 0.25 | | | | | | | |

Parameters of the crack growth model named 'cgr_sigmoid_cw2_h' (v2.1.5 intermediate version)

| cgr1 | cgr2 | cgr3 | cgr4 | cgr5 | cgr6 | cgr7 | cgr8 | cgr9 | cgr10 | cgr11 | ecp1 | ecp2 |
|-------------------|------|------|------|------|------|------|-------|-------|-------|-------|--------------------|--------|
| 5×10 ⁴ | 0.5 | 0.66 | 12 | 0 | 0 | 0 | 3.604 | 11.33 | 43.36 | 65000 | 2×10 ⁻⁶ | 0.0256 |

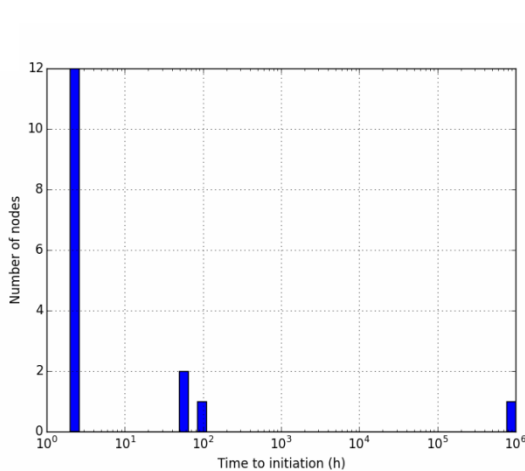


Figure 150 – Histogram of times to initiation predicted for specimen 1383-11, using the local model.

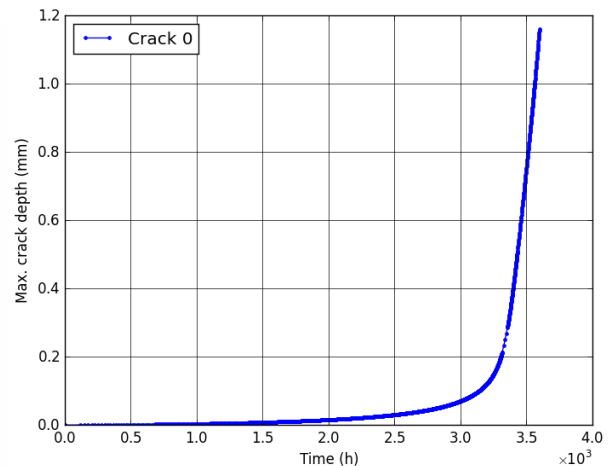


Figure 151 – Cracking kinetics predicted for specimen 1383-11, using the local model.

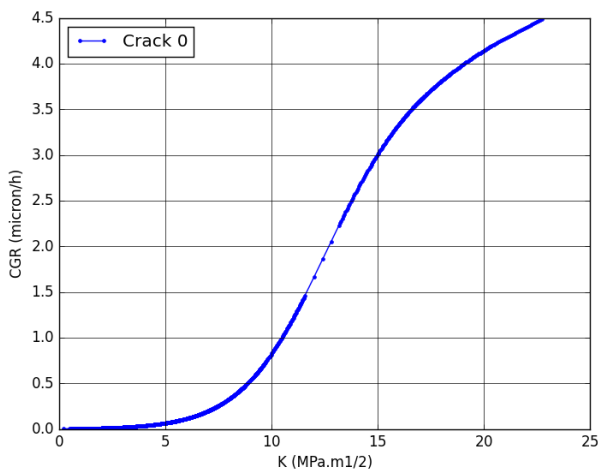


Figure 152 – Crack growth rate versus K at the tip of the main crack predicted for specimen 1383-11, using the local model.

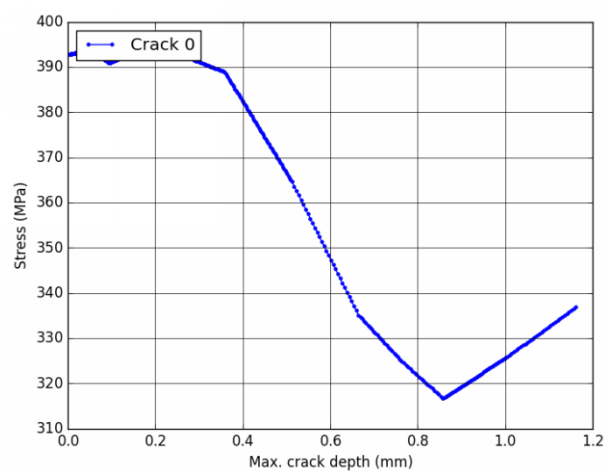


Figure 153 – Stress versus depth at the tip of the main crack predicted for specimen 1383-11, using the local model.

11.2. Simulations of the test on specimen 1383-16

11.2.1. Index initiation model with sigmoid CGR law

Parameters of the initiation model named 'index' (Code_Coriolis v2.1.5 intermediate version)

| init1 | init2 | init3 | init4 (j/mol) | init5 | init6 | Init_depth |
|-------|-------|-------|---------------|-------|------------------|------------|
| 1 | 6.8 | 1 | 185000 | 1 | 10 ⁻⁶ | 0.005 |

Parameters of the crack growth model named 'cgr_sigmoid_cw2_h' (Code_Coriolis v2.1.5 intermediate version)

| cgr1 | cgr2 | cgr3 | cgr4 | cgr5 | cgr6 | cgr7 | cgr8 | cgr9 | cgr10 | cgr11 | ecp1 | ecp2 |
|-------------------|------|------|------|------|------|------|-------|-------|-------|-------|--------------------|--------|
| 5×10 ⁴ | 0.5 | 0.66 | 12 | 15 | 0 | 0 | 3.604 | 11.33 | 43.36 | 65000 | 2×10 ⁻⁶ | 0.0256 |

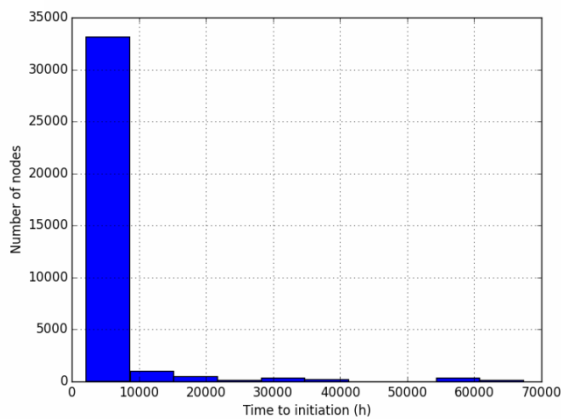


Figure 154 – Histogram of times to initiation predicted for specimen 1383-16, using the index model.

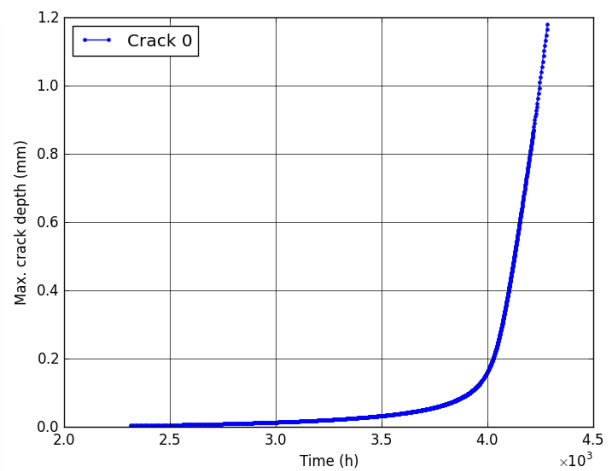


Figure 155 – Cracking kinetics predicted for specimen 1383-16, using the index model.

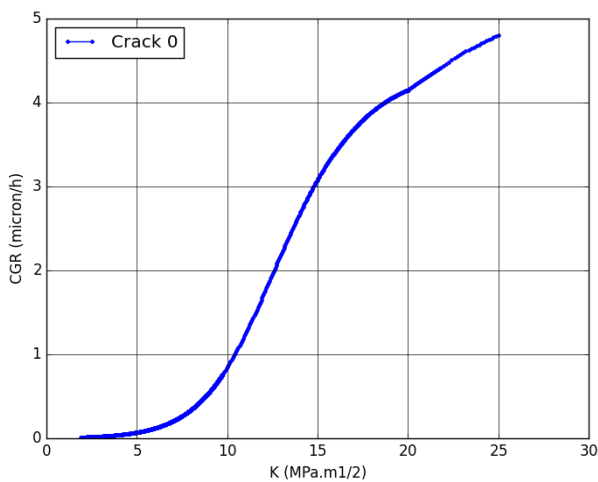


Figure 156 – Crack growth rate versus K at the tip of the main crack predicted for specimen 1383-16 using the index model.

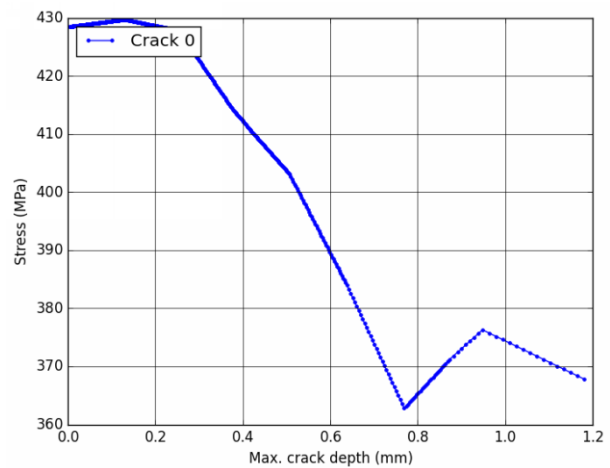


Figure 157 – Stress versus depth at the tip of the main crack predicted for specimen 1383-16, using the index model.

| | | |
|------------|---|--|
| MAI | Quantitative evaluation of the EDF local model and the EPRI-NRC xLPR models of crack initiation of the weld metals of Alloy 600 (Alloys 82 and 182) | 6125-4501-2018-00583-EN Version 2.0 |
|------------|---|--|

11.2.2. Local initiation model with sigmoid CGR law

Parameters of the initiation model named 'local_initiation_model' (Code_Coriolis v2.1.5 intermediate version)

| Grain boundaries | | | | | | | | | | | | |
|-------------------------------|--------------------------|----------------------|---------------|--------------------------|------------------|-------------|---------------------|-------|-------------|------|------|------|
| Densite (mm/mm ²) | SfTot (mm ²) | SpaceResolution (nm) | GBlength (nm) | GBResolution (joints/mm) | GBC | rC (nm) | zCr (nm) | | | | | |
| 10 | 1 | 1 | 200 | 10 | 0.2 | 30 | 30 | | | | | |
| Intergranular oxidation | | | | | | | | | | | | |
| x0nom (nm) | bnom | cnom | x0depl (nm) | bdepl | Cdepl | x0carb (nm) | bcarb | Ccarb | oxQ (J/mol) | oxg1 | oxg2 | oxg3 |
| 0 | 1.86×10 ⁷ | 3 | 0 | 2.4×10 ⁷ | 3 | 0 | 2.6×10 ⁷ | 0.01 | 57000 | 0.1 | 0.3 | 0.04 |
| Cracking criterion | | | | | | | | | | | | |
| Poxc (nm) | SigmaC (MPa) | | | | StressLinearCoef | | | | | | | |
| 200 | 790 | | | | 0.25 | | | | | | | |

Parameters of the crack growth model named 'cgr_sigmoid_cw2_h' (Code_Coriolis v2.1.5 intermediate version)

| cgr1 | cgr2 | cgr3 | cgr4 | cgr5 | cgr6 | cgr7 | cgr8 | cgr9 | cgr10 | cgr11 | ecp1 | ecp2 |
|-------------------|------|------|------|------|------|------|-------|-------|-------|-------|--------------------|--------|
| 5×10 ⁴ | 0.5 | 0.66 | 12 | 0 | 0 | 0 | 3.604 | 11.33 | 43.36 | 65000 | 2×10 ⁻⁶ | 0.0256 |

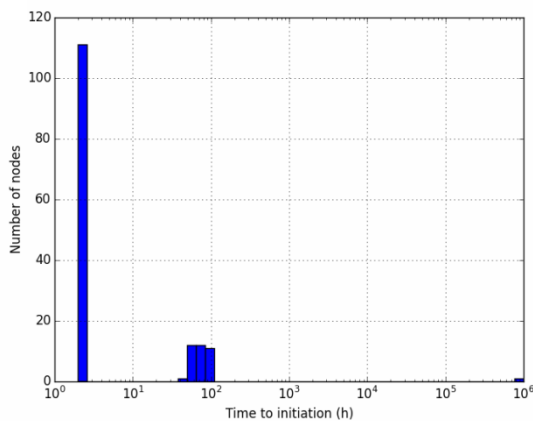


Figure 158 – Histogram of times to initiation predicted for specimen 1383-16, using the local model.

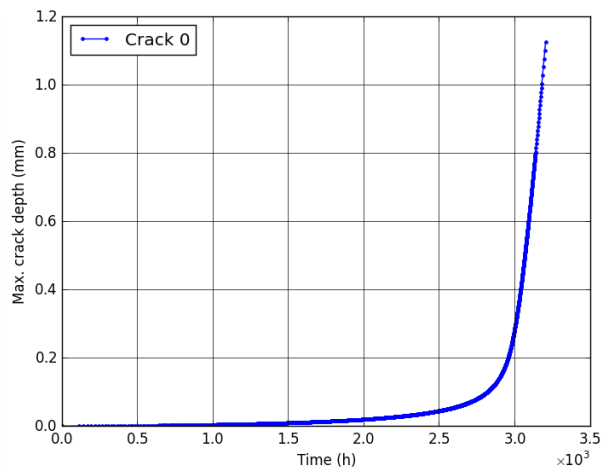


Figure 159 – Cracking kinetics predicted for specimen 1383-16, using the local model.

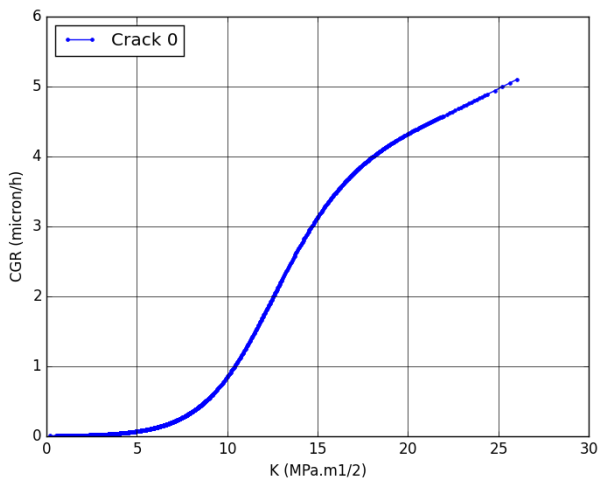


Figure 160 – Crack growth rate versus K at the tip of the main crack predicted for specimen 1383-16, using the local model.

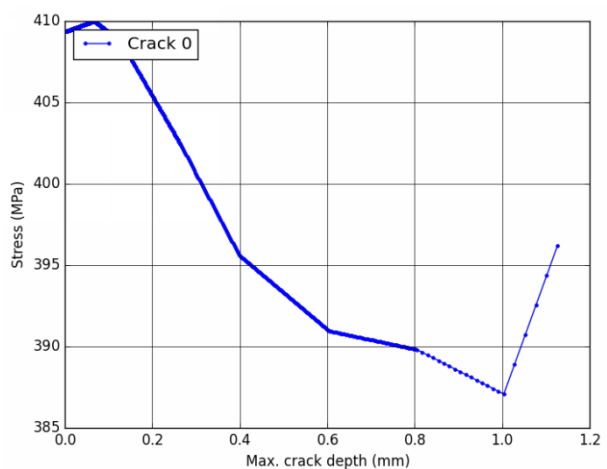


Figure 161 – Stress versus depth at the tip of the main crack predicted for specimen 1383-16, using the local model.

11.3. Simulations of the test on specimen 1383-19

11.3.1. Index initiation model with sigmoid CGR law

Parameters of the initiation model named 'index' (Code_Coriolis v2.1.5 intermediate version)

| init1 | init2 | init3 | init4 (j/mol) | init5 | init6 | Init_depth |
|-------|-------|-------|---------------|-------|------------------|------------|
| 1 | 6.8 | 1 | 185000 | 1 | 10 ⁻⁶ | 0.005 |

Parameters of the crack growth model named 'cgr_sigmoid_cw2_h' (Code_Coriolis v2.1.5 intermediate version)

| cgr1 | cgr2 | cgr3 | cgr4 | cgr5 | cgr6 | cgr7 | cgr8 | cgr9 | cgr10 | cgr11 | ecp1 | ecp2 |
|-------------------|------|------|------|------|------|------|-------|-------|-------|-------|--------------------|--------|
| 5×10 ⁴ | 0.5 | 0.66 | 12 | 15 | 0 | 0 | 3.604 | 11.33 | 43.36 | 65000 | 2×10 ⁻⁶ | 0.0256 |

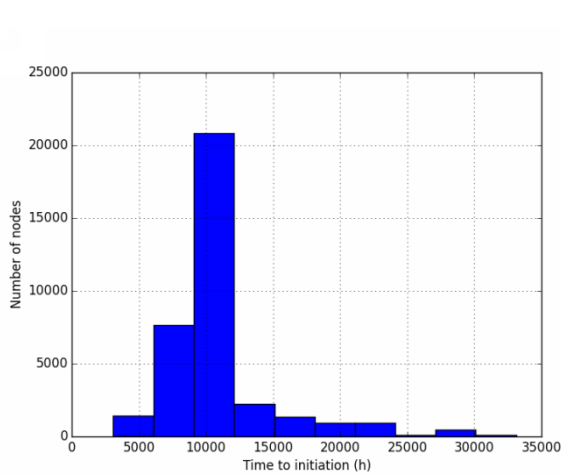


Figure 162 – Histogram of times to initiation predicted for specimen 1383-19, using the index model.

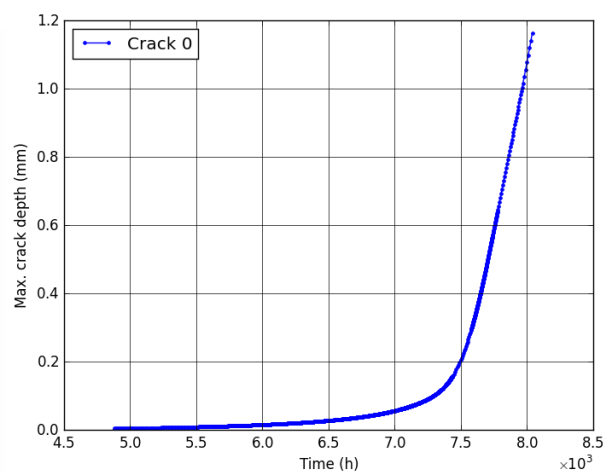


Figure 163 – Cracking kinetics predicted for specimen 1383-19, using the index model.

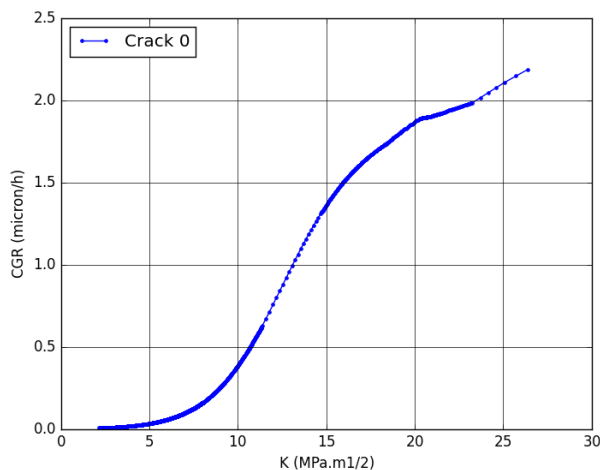


Figure 164 – Crack growth rate versus K at the tip of the main crack predicted for specimen 1383-19 using the index model.

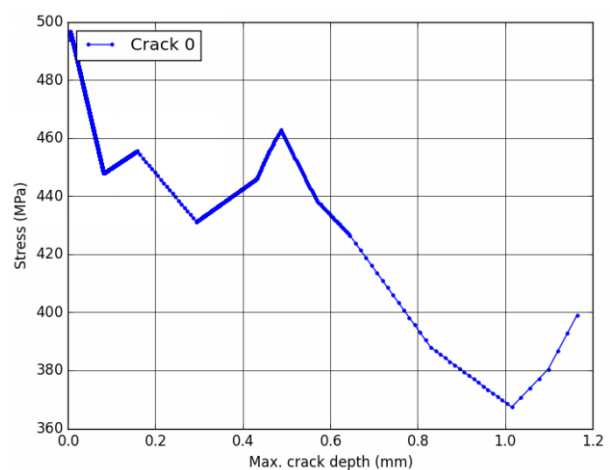


Figure 165 – Stress versus depth at the tip of the main crack predicted for specimen 1383-19, using the index model.

11.3.2. Local initiation model with sigmoid CGR law

Parameters of the initiation model named 'local_initiation_model' (Code_Coriolis v2.1.5)

| Grain boundaries | | | | | | | | | | | | |
|-------------------------------|--------------------------|----------------------|---------------|--------------------------|------------------|-------------|---------------------|-------|-------------|------|------|------|
| Densite (mm/mm ²) | SfTot (mm ²) | SpaceResolution (nm) | GBlength (nm) | GBResolution (joints/mm) | GBC | rC (nm) | zCr (nm) | | | | | |
| 10 | 1 | 1 | 200 | 10 | 0.2 | 30 | 30 | | | | | |
| Intergranular oxidation | | | | | | | | | | | | |
| x0nom (nm) | bnom | cnom | x0depl (nm) | bdepl | Cdepl | x0carb (nm) | bcarb | Ccarb | oxQ (J/mol) | oxg1 | oxg2 | oxg3 |
| 0 | 1.86×10 ⁷ | 3 | 0 | 2.4×10 ⁷ | 3 | 0 | 2.6×10 ⁷ | 0.01 | 57000 | 0.1 | 0.3 | 0.04 |
| Cracking criterion | | | | | | | | | | | | |
| Poxc (nm) | SigmaC (MPa) | | | | StressLinearCoef | | | | | | | |
| 200 | 790 | | | | 0.25 | | | | | | | |

Parameters of the crack growth model named 'cgr_sigmoid_cw2_h' (Code_Coriolis v2.1.5 intermediate version)

| cgr1 | cgr2 | cgr3 | cgr4 | cgr5 | cgr6 | cgr7 | cgr8 | cgr9 | cgr10 | cgr11 | ecp1 | ecp2 |
|-------------------|------|------|------|------|------|------|-------|-------|-------|-------|--------------------|--------|
| 5×10 ⁴ | 0.5 | 0.66 | 12 | 0 | 0 | 0 | 3.604 | 11.33 | 43.36 | 65000 | 2×10 ⁻⁶ | 0.0256 |

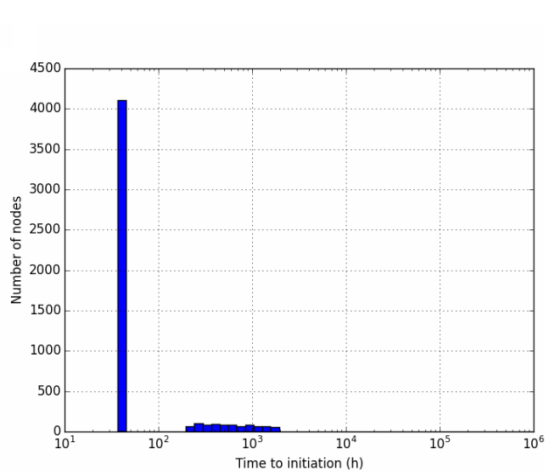


Figure 166 – Histogram of times to initiation predicted for specimen 1383-19, using the local model.

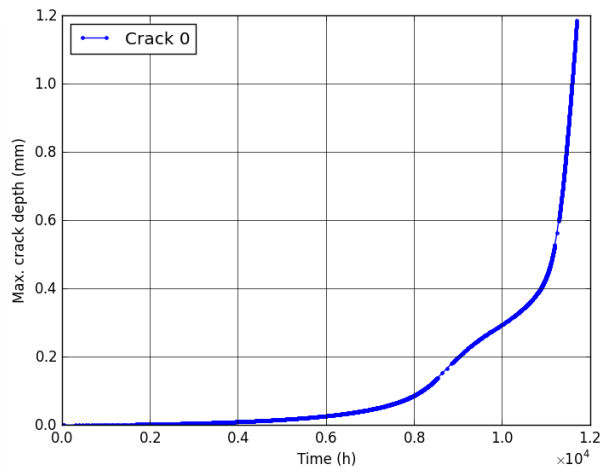


Figure 167 – Cracking kinetics predicted for specimen 1383-19, using the local model.

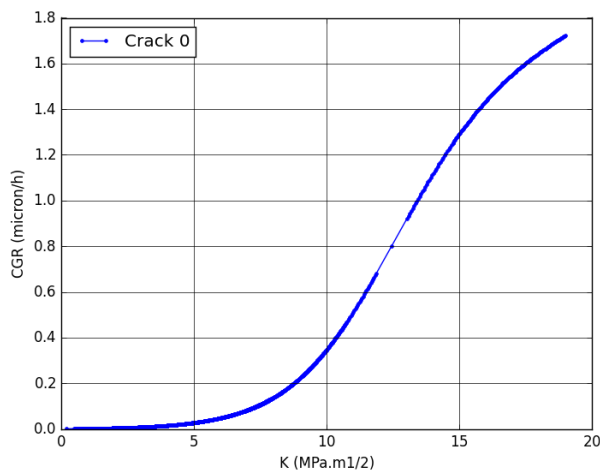


Figure 168 – Crack growth rate versus K at the tip of the main crack predicted for specimen 1383-19, using the local model.

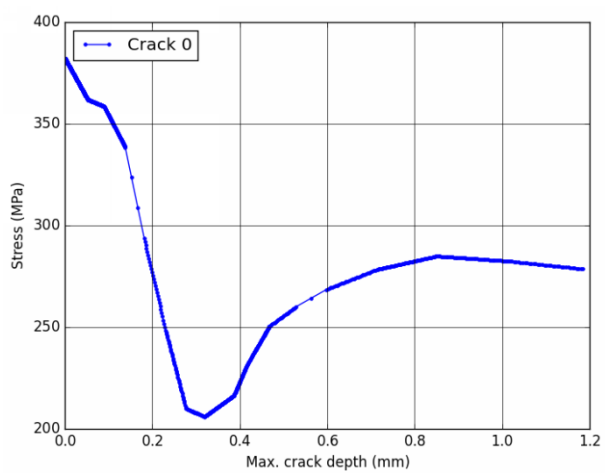


Figure 169 – Stress versus depth at the tip of the main crack predicted for specimen 1383-19, using the local model.

11.4. Simulations of the test on specimen 1383-20

11.4.1. Index initiation model with sigmoid CGR law

Parameters of the initiation model named 'index' (Code_Coriolis v2.1.5 intermediate version)

| init1 | init2 | init3 | init4 (j/mol) | init5 | init6 | Init_depth |
|-------|-------|-------|---------------|-------|------------------|------------|
| 1 | 6.8 | 1 | 185000 | 1 | 10 ⁻⁶ | 0.005 |

Parameters of the crack growth model named 'cgr_sigmoid_cw2_h' (Code_Coriolis v2.1.5 intermediate version)

| cgr1 | cgr2 | cgr3 | cgr4 | cgr5 | cgr6 | cgr7 | cgr8 | cgr9 | cgr10 | cgr11 | ecp1 | ecp2 |
|-------------------|------|------|------|------|------|------|-------|-------|-------|-------|--------------------|--------|
| 5×10 ⁴ | 0.5 | 0.66 | 12 | 15 | 0 | 0 | 3.604 | 11.33 | 43.36 | 65000 | 2×10 ⁻⁶ | 0.0256 |

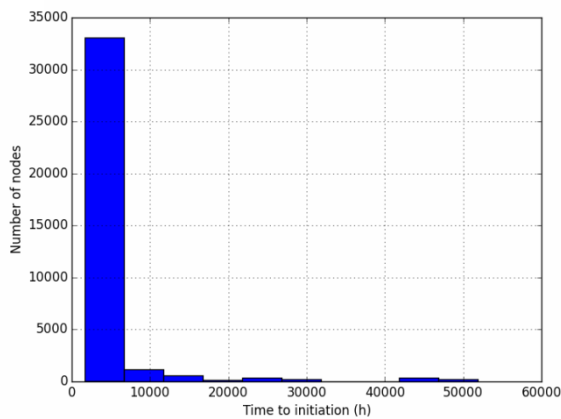


Figure 170 – Histogram of times to initiation predicted for specimen 1383-20, using the index model.

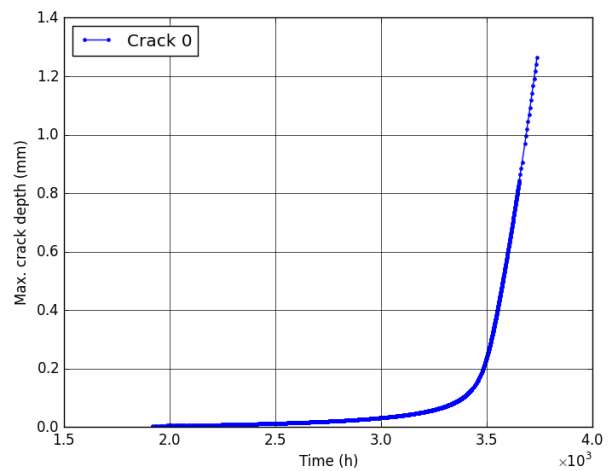


Figure 171 – Cracking kinetics predicted for specimen 1383-20, using the index model.

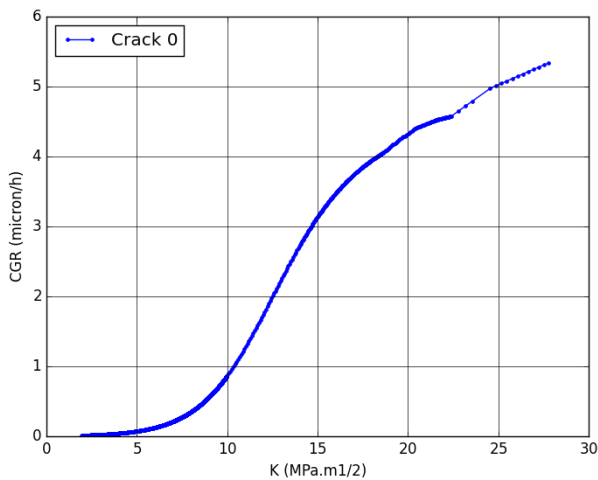


Figure 172 – Crack growth rate versus K at the tip of the main crack predicted for specimen 1383-20 using the index model.

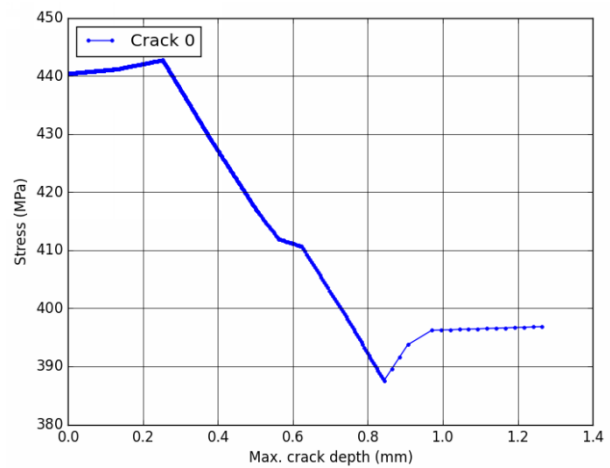


Figure 173 – Stress versus depth at the tip of the main crack predicted for specimen 1383-20, using the index model.

| | | |
|------------|---|--|
| MAI | Quantitative evaluation of the EDF local model and the EPRI-NRC xLPR models of crack initiation of the weld metals of Alloy 600 (Alloys 82 and 182) | 6125-4501-2018-00583-EN Version 2.0 |
|------------|---|--|

11.4.2. Local initiation model with sigmoid CGR law

Parameters of the initiation model named 'local_initiation_model' (Code_Coriolis v2.1.5 intermediate version)

| Grain boundaries | | | | | | | | | | | | |
|-------------------------------|--------------------------|----------------------|---------------|--------------------------|------------------|-------------|---------------------|-------|-------------|------|------|------|
| Densite (mm/mm ²) | SfTot (mm ²) | SpaceResolution (nm) | GBlength (nm) | GBResolution (joints/mm) | GBC | rC (nm) | zCr (nm) | | | | | |
| 10 | 1 | 1 | 200 | 10 | 0.2 | 30 | 30 | | | | | |
| Intergranular oxidation | | | | | | | | | | | | |
| x0nom (nm) | bnom | cnom | x0depl (nm) | bdepl | Cdepl | x0carb (nm) | bcarb | Ccarb | oxQ (J/mol) | oxg1 | oxg2 | oxg3 |
| 0 | 1.86×10 ⁷ | 3 | 0 | 2.4×10 ⁷ | 3 | 0 | 2.6×10 ⁷ | 0.01 | 57000 | 0.1 | 0.3 | 0.04 |
| Cracking criterion | | | | | | | | | | | | |
| Poxc (nm) | SigmaC (MPa) | | | | StressLinearCoef | | | | | | | |
| 200 | 790 | | | | 0.25 | | | | | | | |

Parameters of the crack growth model named 'cgr_sigmoid_cw2_h' (Code_Coriolis v2.1.5 intermediate version)

| | | | | | | | | | | | | |
|-------------------|------|------|------|------|------|------|-------|-------|-------|-------|--------------------|--------|
| cgr1 | cgr2 | cgr3 | cgr4 | cgr5 | cgr6 | cgr7 | cgr8 | cgr9 | cgr10 | cgr11 | ecp1 | ecp2 |
| 5×10 ⁴ | 0.5 | 0.66 | 12 | 0 | 0 | 0 | 3.604 | 11.33 | 43.36 | 65000 | 2×10 ⁻⁶ | 0.0256 |

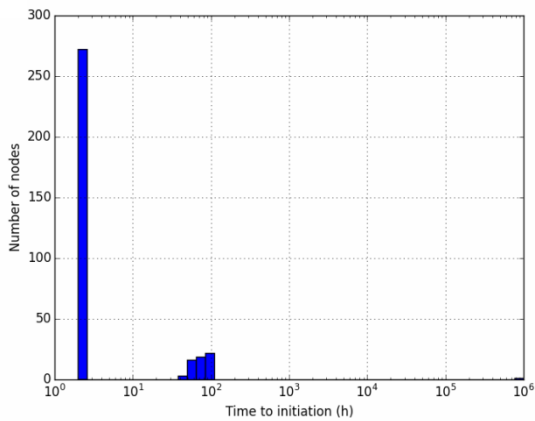


Figure 174 – Histogram of times to initiation predicted for specimen 1383-20, using the local model.

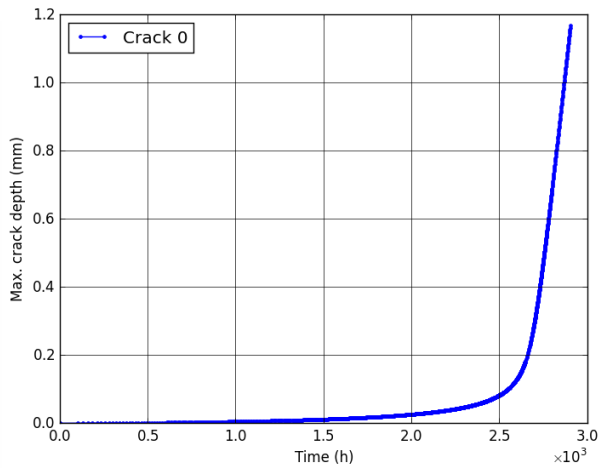


Figure 175 – Cracking kinetics predicted for specimen 1383-20, using the local model.

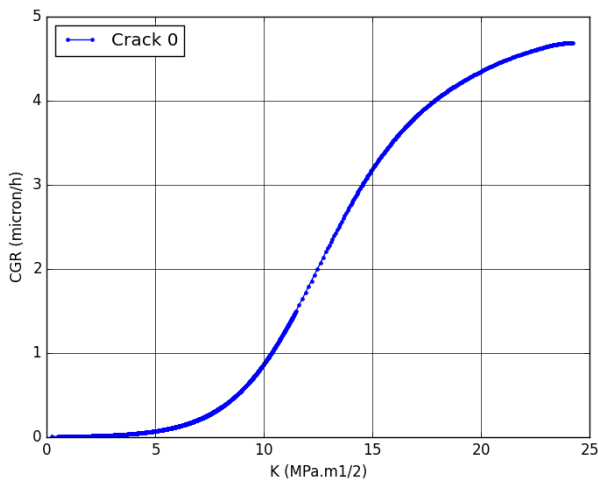


Figure 176 – Crack growth rate versus K at the tip of the main crack predicted for specimen 1383-20, using the local model.

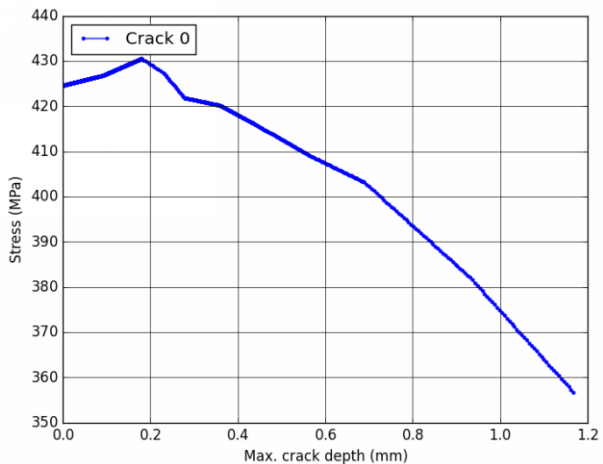


Figure 177 – Stress versus depth at the tip of the main crack predicted for specimen 1383-20, using the local model.

11.5. Simulations of the test on specimen 1383-21

11.5.1. Index initiation model with sigmoid CGR law

Parameters of the initiation model named 'index' (Code_Coriolis v2.1.5 intermediate version)

| init1 | init2 | init3 | init4 (j/mol) | init5 | init6 | Init_depth |
|-------|-------|-------|---------------|-------|------------------|------------|
| 1 | 6.8 | 1 | 185000 | 1 | 10 ⁻⁶ | 0.005 |

Parameters of the crack growth model named 'cgr_sigmoid_cw2_h' (Code_Coriolis v2.1.5 intermediate version)

| cgr1 | cgr2 | cgr3 | cgr4 | cgr5 | cgr6 | cgr7 | cgr8 | cgr9 | cgr10 | cgr11 | ecp1 | ecp2 |
|-------------------|------|------|------|------|------|------|-------|-------|-------|-------|--------------------|--------|
| 5×10 ⁴ | 0.5 | 0.66 | 12 | 15 | 0 | 0 | 3.604 | 11.33 | 43.36 | 65000 | 2×10 ⁻⁶ | 0.0256 |

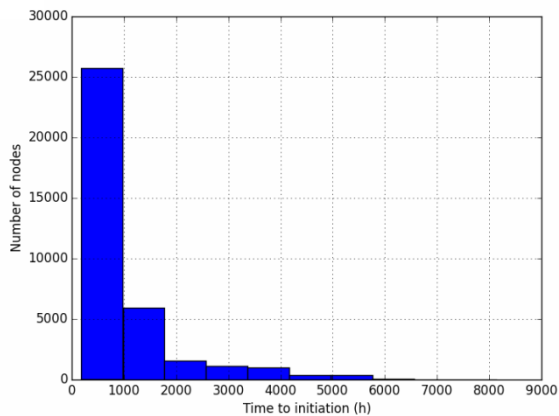


Figure 178 – Histogram of times to initiation predicted for specimen 1383-21, using the index model.

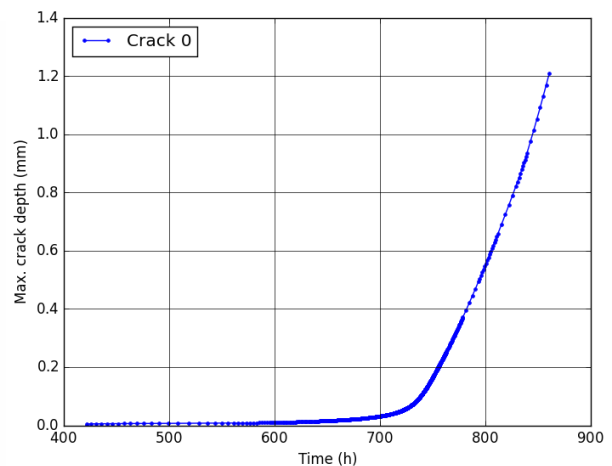


Figure 179 – Cracking kinetics predicted for specimen 1383-21, using the index model.

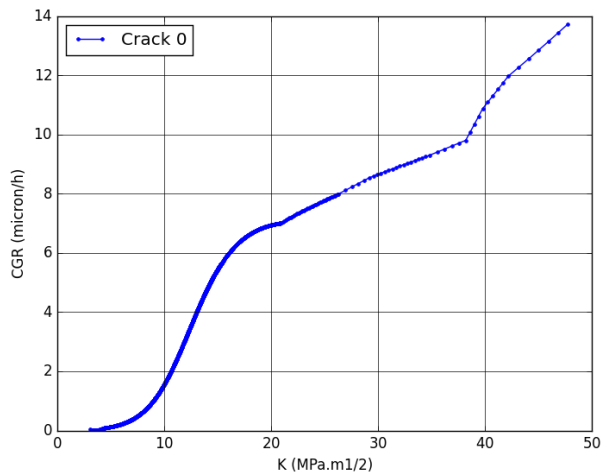


Figure 180 – Crack growth rate versus K at the tip of the main crack predicted for specimen 1383-21 using the index model.

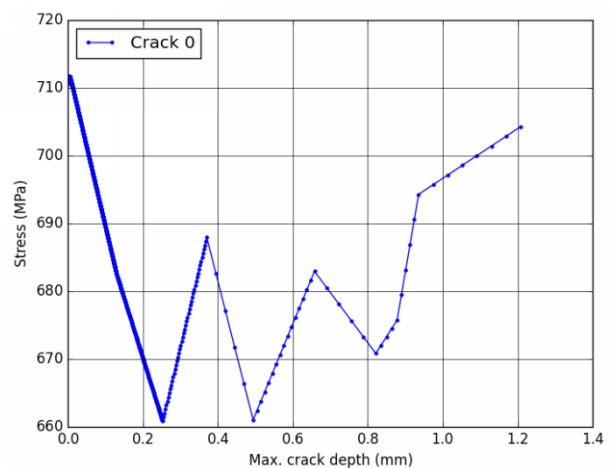


Figure 181 – Stress versus depth at the tip of the main crack predicted for specimen 1383-21, using the index model.

| | | |
|------------|---|--|
| MAI | Quantitative evaluation of the EDF local model and the EPRI-NRC xLPR models of crack initiation of the weld metals of Alloy 600 (Alloys 82 and 182) | 6125-4501-2018-00583-EN Version 2.0 |
|------------|---|--|

11.5.2. Local initiation model with sigmoid CGR law

Parameters of the initiation model named 'local_initiation_model' (Code_Coriolis v2.1.5 intermediate version)

| Grain boundaries | | | | | | | | | | | | |
|-------------------------------|--------------------------|----------------------|---------------|--------------------------|------------------|-------------|---------------------|-------|-------------|------|------|------|
| Densite (mm/mm ²) | SfTot (mm ²) | SpaceResolution (nm) | GBlength (nm) | GBResolution (joints/mm) | GBC | rC (nm) | zCr (nm) | | | | | |
| 10 | 1 | 1 | 200 | 10 | 0.2 | 30 | 30 | | | | | |
| Intergranular oxidation | | | | | | | | | | | | |
| x0nom (nm) | bnom | cnom | x0depl (nm) | bdepl | Cdepl | x0carb (nm) | bcarb | Ccarb | oxQ (J/mol) | oxg1 | oxg2 | oxg3 |
| 0 | 1.86×10 ⁷ | 3 | 0 | 2.4×10 ⁷ | 3 | 0 | 2.6×10 ⁷ | 0.01 | 57000 | 0.1 | 0.3 | 0.04 |
| Cracking criterion | | | | | | | | | | | | |
| Poxc (nm) | SigmaC (MPa) | | | | StressLinearCoef | | | | | | | |
| 200 | 790 | | | | 0.25 | | | | | | | |

Parameters of the crack growth model named 'cgr_sigmoid_cw2_h' (Code_Coriolis v2.1.5 intermediate version)

| cgr1 | cgr2 | cgr3 | cgr4 | cgr5 | cgr6 | cgr7 | cgr8 | cgr9 | cgr10 | cgr11 | ecp1 | ecp2 |
|-------------------|------|------|------|------|------|------|-------|-------|-------|-------|--------------------|--------|
| 5×10 ⁴ | 0.5 | 0.66 | 12 | 0 | 0 | 0 | 3.604 | 11.33 | 43.36 | 65000 | 2×10 ⁻⁶ | 0.0256 |

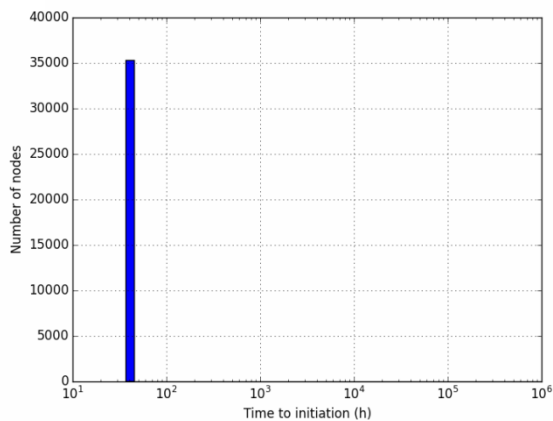


Figure 182 – Histogram of times to initiation predicted for specimen 1383-21, using the local model.

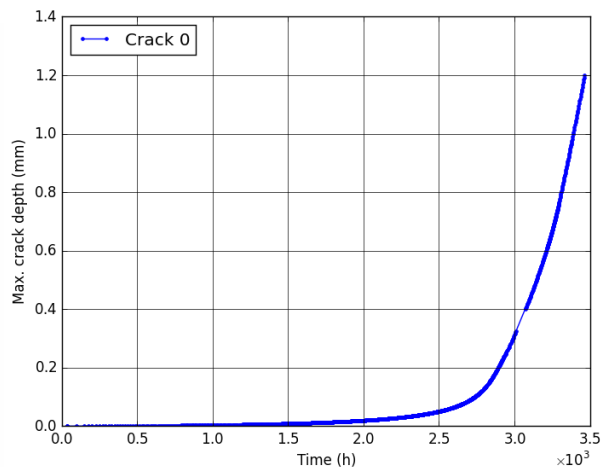


Figure 183 – Cracking kinetics predicted for specimen 1383-21, using the local model.

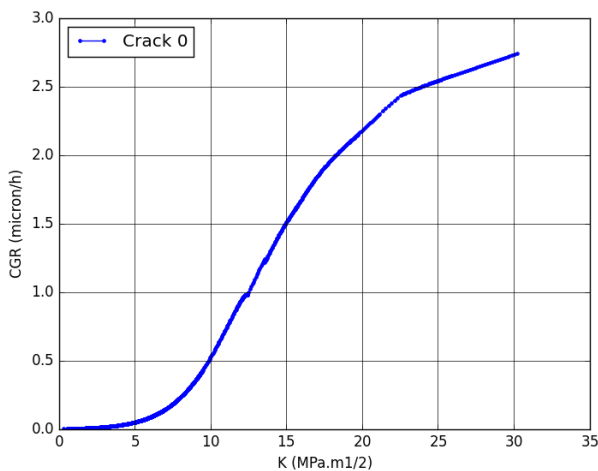


Figure 184 – Crack growth rate versus K at the tip of the main crack predicted for specimen 1383-21, using the local model.

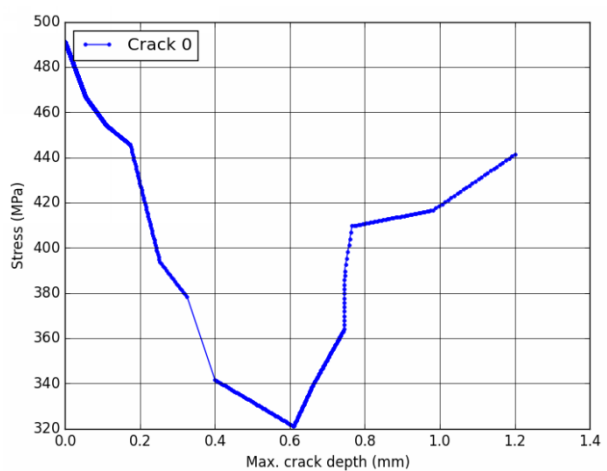


Figure 185 – Stress versus depth at the tip of the main crack predicted for specimen 1383-21, using the local model.

11.6. Simulations of the test on specimen 1383-22

11.6.1. Index initiation model with sigmoid CGR law

Parameters of the initiation model named 'index' (Code_Coriolis v2.1.5 intermediate version)

| init1 | init2 | init3 | init4 (j/mol) | init5 | init6 | Init_depth |
|-------|-------|-------|---------------|-------|------------------|------------|
| 1 | 6.8 | 1 | 185000 | 1 | 10 ⁻⁶ | 0.005 |

Parameters of the crack growth model named 'cgr_sigmoid_cw2_h' (Code_Coriolis v2.1.5 intermediate version)

| cgr1 | cgr2 | cgr3 | cgr4 | cgr5 | cgr6 | cgr7 | cgr8 | cgr9 | cgr10 | cgr11 | ecp1 | ecp2 |
|-------------------|------|------|------|------|------|------|-------|-------|-------|-------|--------------------|--------|
| 5×10 ⁴ | 0.5 | 0.66 | 12 | 15 | 0 | 0 | 3.604 | 11.33 | 43.36 | 65000 | 2×10 ⁻⁶ | 0.0256 |

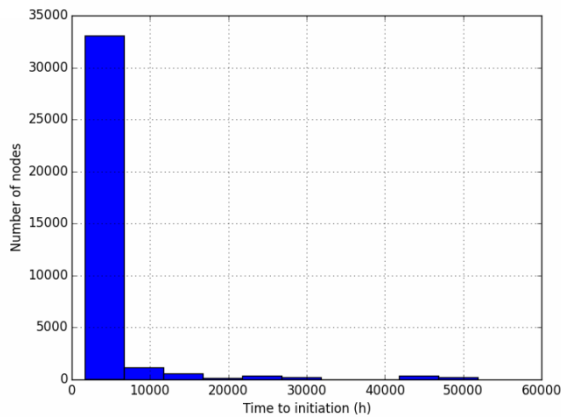


Figure 186 – Histogram of times to initiation predicted for specimen 1383-22, using the index model.

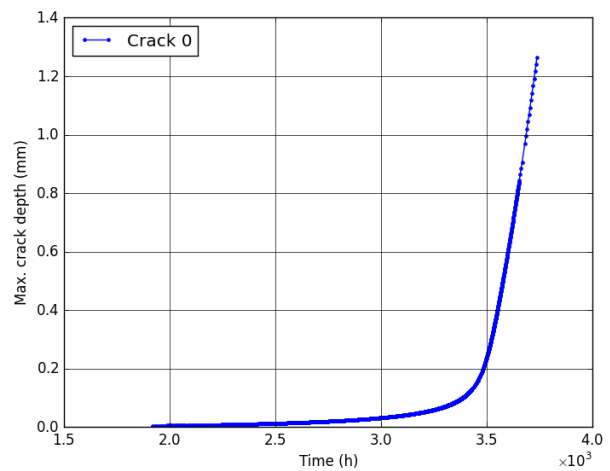


Figure 187 – Cracking kinetics predicted for specimen 1383-22, using the index model.

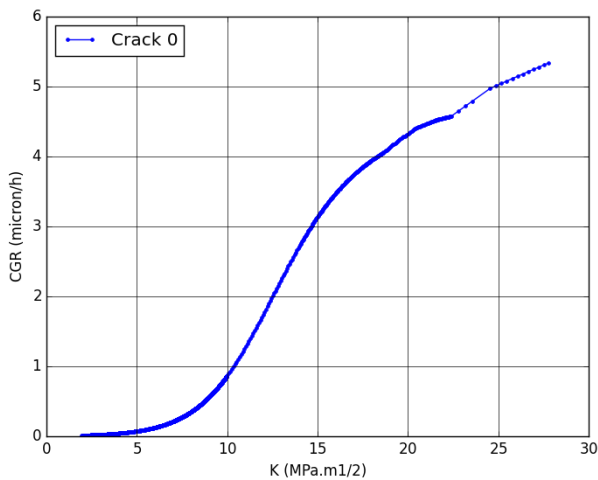


Figure 188 – Crack growth rate versus K at the tip of the main crack predicted for specimen 1383-22 using the index model.

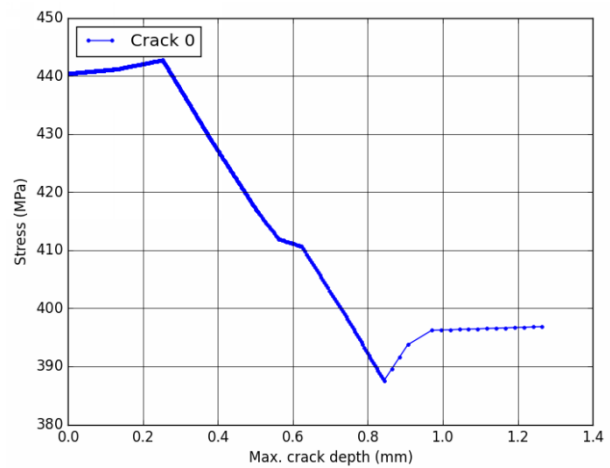


Figure 189 – Stress versus depth at the tip of the main crack predicted for specimen 1383-22, using the index model.

| | | |
|------------|---|--|
| MAI | Quantitative evaluation of the EDF local model and the EPRI-NRC xLPR models of crack initiation of the weld metals of Alloy 600 (Alloys 82 and 182) | 6125-4501-2018-00583-EN Version 2.0 |
|------------|---|--|

11.6.2. Local initiation model with sigmoid CGR law

Parameters of the initiation model named 'local_initiation_model' (Code_Coriolis v2.1.5 intermediate version)

| Grain boundaries | | | | | | | | | | | | |
|-------------------------------|--------------------------|----------------------|---------------|--------------------------|------------------|-------------|---------------------|-------|-------------|------|------|------|
| Densite (mm/mm ²) | SfTot (mm ²) | SpaceResolution (nm) | GBlength (nm) | GBResolution (joints/mm) | GBC | rC (nm) | zCr (nm) | | | | | |
| 10 | 1 | 1 | 200 | 10 | 0.2 | 30 | 30 | | | | | |
| Intergranular oxidation | | | | | | | | | | | | |
| x0nom (nm) | bnom | cnom | x0depl (nm) | bdepl | Cdepl | x0carb (nm) | bcarb | Ccarb | oxQ (J/mol) | oxg1 | oxg2 | oxg3 |
| 0 | 1.86×10 ⁷ | 3 | 0 | 2.4×10 ⁷ | 3 | 0 | 2.6×10 ⁷ | 0.01 | 57000 | 0.1 | 0.3 | 0.04 |
| Cracking criterion | | | | | | | | | | | | |
| Poxc (nm) | SigmaC (MPa) | | | | StressLinearCoef | | | | | | | |
| 200 | 790 | | | | 0.25 | | | | | | | |

Parameters of the crack growth model named 'cgr_sigmoid_cw2_h' (Code_Coriolis v2.1.5 intermediate version)

| cgr1 | cgr2 | cgr3 | cgr4 | cgr5 | cgr6 | cgr7 | cgr8 | cgr9 | cgr10 | cgr11 | ecp1 | ecp2 |
|-------------------|------|------|------|------|------|------|-------|-------|-------|-------|--------------------|--------|
| 5×10 ⁴ | 0.5 | 0.66 | 12 | 0 | 0 | 0 | 3.604 | 11.33 | 43.36 | 65000 | 2×10 ⁻⁶ | 0.0256 |

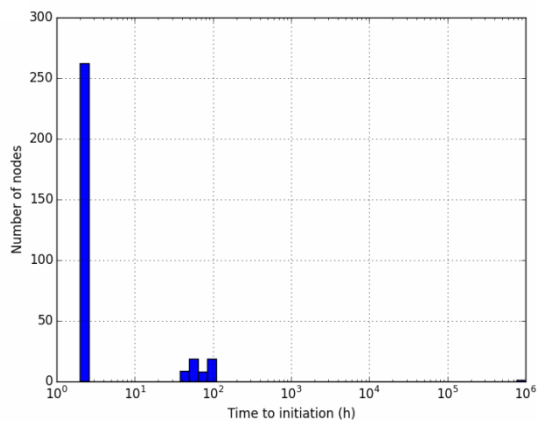


Figure 190 – Histogram of times to initiation predicted for specimen 1383-22, using the local model.

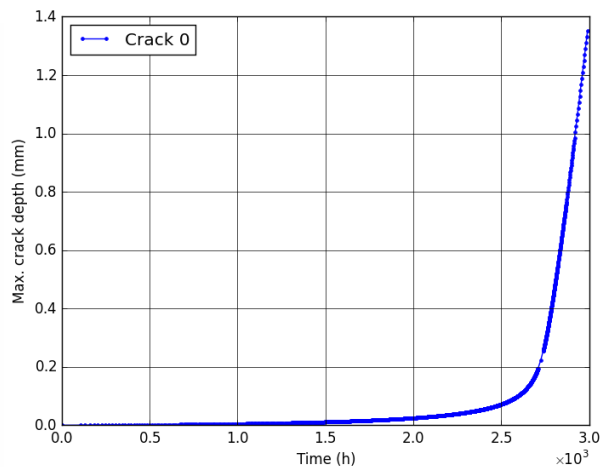


Figure 191 – Cracking kinetics predicted for specimen 1383-22, using the local model.

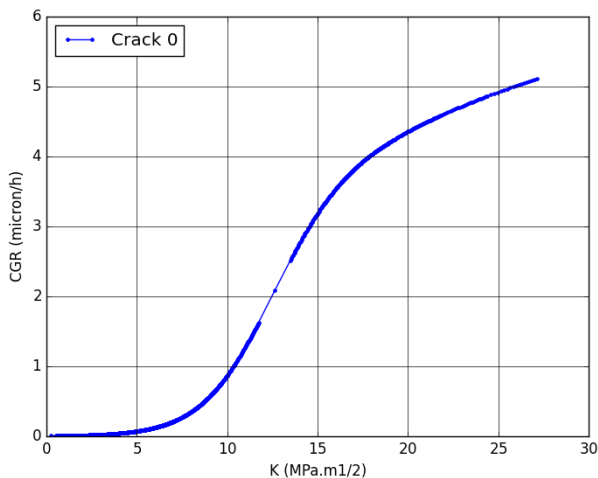


Figure 192 – Crack growth rate versus K at the tip of the main crack predicted for specimen 1383-22, using the local model.

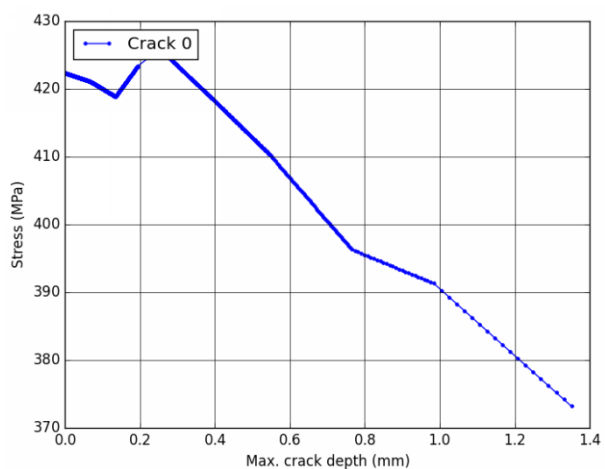


Figure 193 – Stress versus depth at the tip of the main crack predicted for specimen 1383-22, using the local model.

11.7. Simulations of the test on specimen 1383-23

11.7.1. Index initiation model with sigmoid CGR law

Parameters of the initiation model named 'index' (Code_Coriolis v2.1.5 intermediate version)

| init1 | init2 | init3 | init4 (j/mol) | init5 | init6 | Init_depth |
|-------|-------|-------|---------------|-------|------------------|------------|
| 1 | 6.8 | 1 | 185000 | 1 | 10 ⁻⁶ | 0.005 |

Parameters of the crack growth model named 'cgr_sigmoid_cw2_h' (Code_Coriolis v2.1.5 intermediate version)

| cgr1 | cgr2 | cgr3 | cgr4 | cgr5 | cgr6 | cgr7 | cgr8 | cgr9 | cgr10 | cgr11 | ecp1 | ecp2 |
|-------------------|------|------|------|------|------|------|-------|-------|-------|-------|--------------------|--------|
| 5×10 ⁴ | 0.5 | 0.66 | 12 | 15 | 0 | 0 | 3.604 | 11.33 | 43.36 | 65000 | 2×10 ⁻⁶ | 0.0256 |

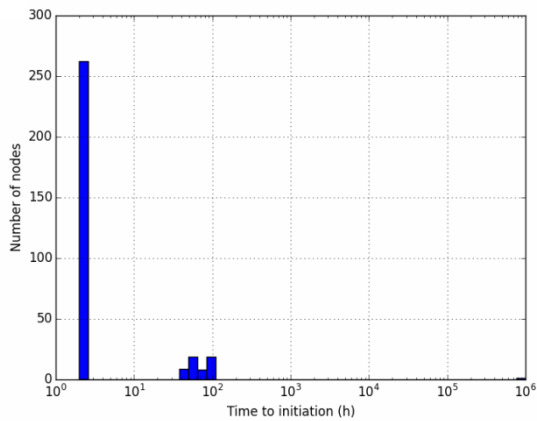


Figure 194 – Histogram of times to initiation predicted for specimen 1383-23, using the index model.

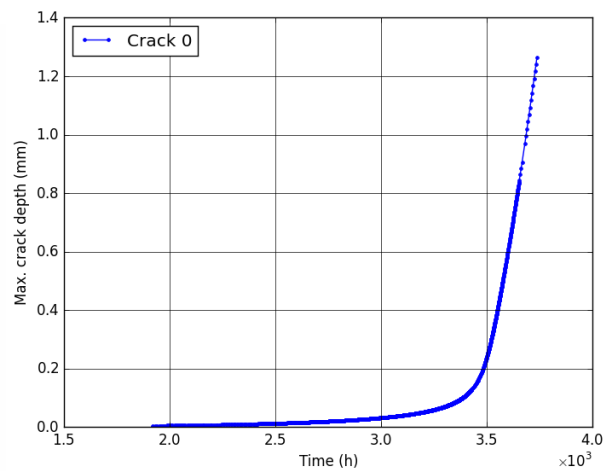


Figure 195 – Cracking kinetics predicted for specimen 1383-23, using the index model.

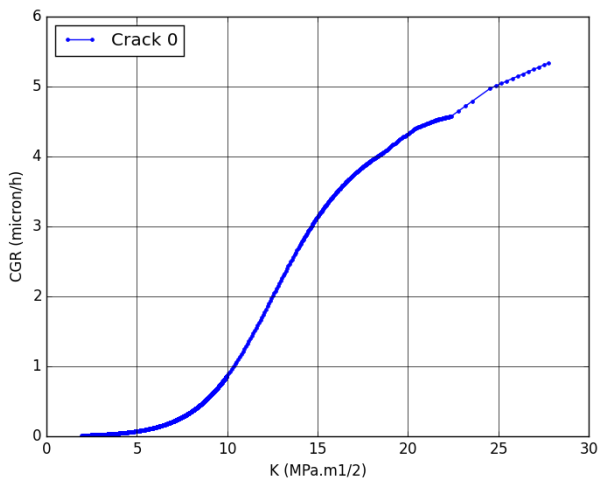


Figure 196 – Crack growth rate versus K at the tip of the main crack predicted for specimen 1383-23 using the index model.

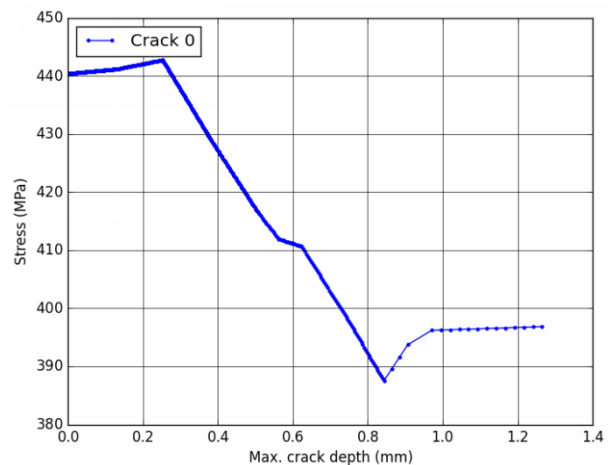


Figure 197 – Stress versus depth at the tip of the main crack predicted for specimen 1383-23, using the index model.

| | | |
|-----|---|--|
| MAI | Quantitative evaluation of the EDF local model and the EPRI-NRC xLPR models of crack initiation of the weld metals of Alloy 600 (Alloys 82 and 182) | 6125-4501-2018-00583-EN Version 2.0 |
|-----|---|--|

11.7.2. Local initiation model with sigmoid CGR law

Parameters of the initiation model named 'local_initiation_model' (Code_Coriolis v2.1.5 intermediate version)

| Grain boundaries | | | | | | | | | | | | |
|-------------------------------|--------------------------|----------------------|---------------|--------------------------|------------------|-------------|---------------------|-------|-------------|------|------|------|
| Densite (mm/mm ²) | SfTot (mm ²) | SpaceResolution (nm) | GBlength (nm) | GBResolution (joints/mm) | GBC | rC (nm) | zCr (nm) | | | | | |
| 10 | 1 | 1 | 200 | 10 | 0.2 | 30 | 30 | | | | | |
| Intergranular oxidation | | | | | | | | | | | | |
| x0nom (nm) | bnom | cnom | x0depl (nm) | bdepl | Cdepl | x0carb (nm) | bcarb | Ccarb | oxQ (J/mol) | oxg1 | oxg2 | oxg3 |
| 0 | 1.86×10 ⁷ | 3 | 0 | 2.4×10 ⁷ | 3 | 0 | 2.6×10 ⁷ | 0.01 | 57000 | 0.1 | 0.3 | 0.04 |
| Cracking criterion | | | | | | | | | | | | |
| Poxc (nm) | SigmaC (MPa) | | | | StressLinearCoef | | | | | | | |
| 200 | 790 | | | | 0.25 | | | | | | | |

Parameters of the crack growth model named 'cgr_sigmoid_cw2_h' (Code_Coriolis v2.1.5 intermediate version)

| cgr1 | cgr2 | cgr3 | cgr4 | cgr5 | cgr6 | cgr7 | cgr8 | cgr9 | cgr10 | cgr11 | ecp1 | ecp2 |
|-------------------|------|------|------|------|------|------|-------|-------|-------|-------|--------------------|--------|
| 5×10 ⁴ | 0.5 | 0.66 | 12 | 0 | 0 | 0 | 3.604 | 11.33 | 43.36 | 65000 | 2×10 ⁻⁶ | 0.0256 |

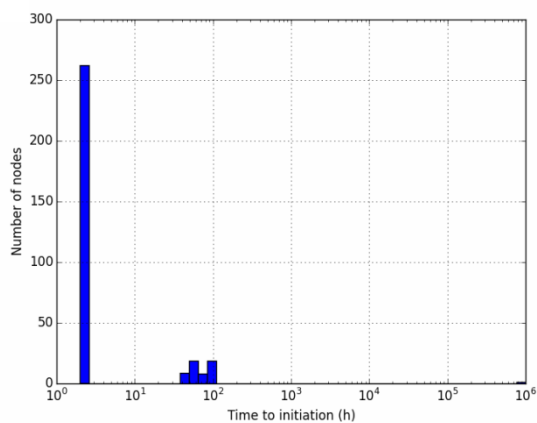


Figure 198 – Histogram of times to initiation predicted for specimen 1383-23, using the local model.

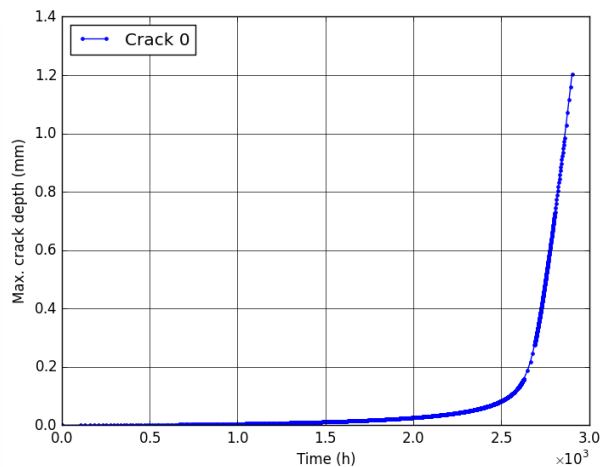


Figure 199 – Cracking kinetics predicted for specimen 1383-23, using the local model.

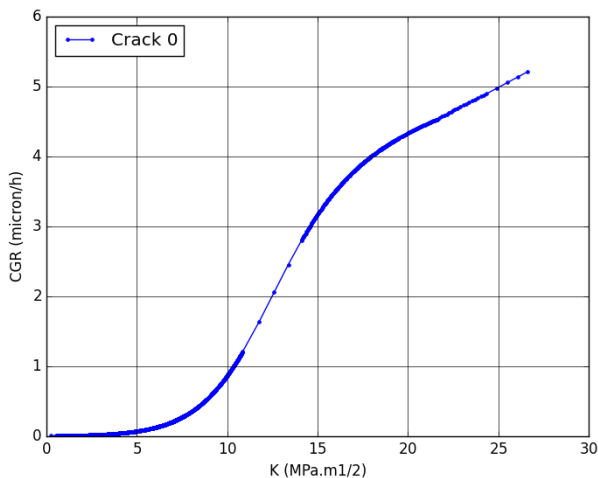


Figure 200 – Crack growth rate versus K at the tip of the main crack predicted for specimen 1383-23, using the local model.

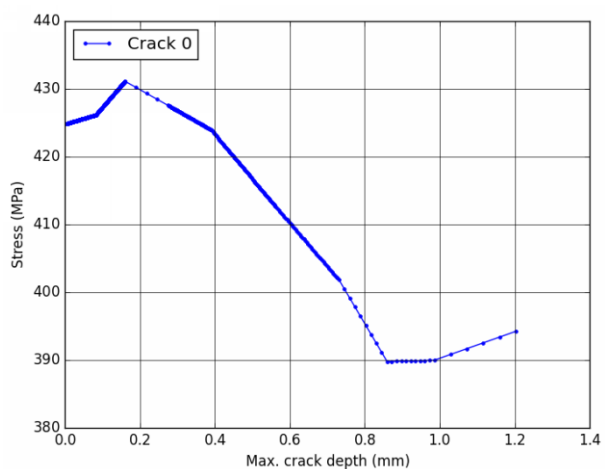


Figure 201 – Stress versus depth at the tip of the main crack predicted for specimen 1383-23, using the local model.

11.8. Simulations of the test on specimen 1383-26

11.8.1. Index initiation model with sigmoid CGR law

Parameters of the initiation model named 'index' (Code_Coriolis v2.1.5 intermediate version)

| init1 | init2 | init3 | init4 (j/mol) | init5 | init6 | Init_depth |
|-------|-------|-------|---------------|-------|------------------|------------|
| 1 | 6.8 | 1 | 185000 | 1 | 10 ⁻⁶ | 0.005 |

Parameters of the crack growth model named 'cgr_sigmoid_cw2_h' (Code_Coriolis v2.1.5 intermediate version)

| cgr1 | cgr2 | cgr3 | cgr4 | cgr5 | cgr6 | cgr7 | cgr8 | cgr9 | cgr10 | cgr11 | ecp1 | ecp2 |
|-------------------|------|------|------|------|------|------|-------|-------|-------|-------|--------------------|--------|
| 5×10 ⁴ | 0.5 | 0.66 | 12 | 15 | 0 | 0 | 3.604 | 11.33 | 43.36 | 65000 | 2×10 ⁻⁶ | 0.0256 |

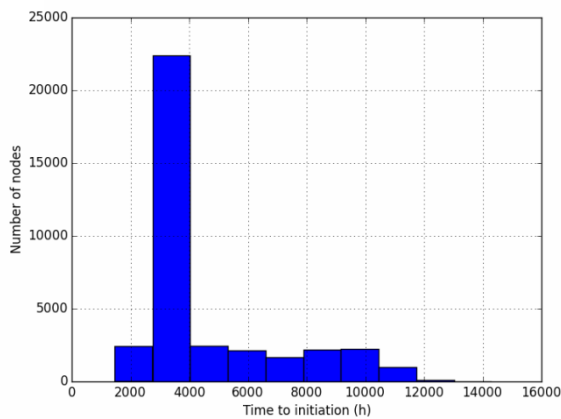


Figure 202 – Histogram of times to initiation predicted for specimen 1383-26, using the index model.

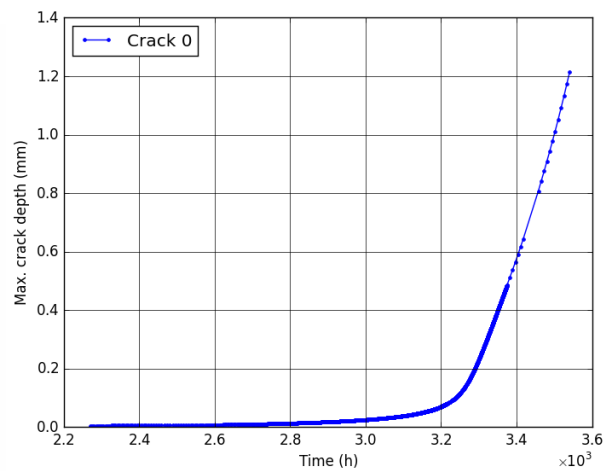


Figure 203 – Cracking kinetics predicted for specimen 1383-26, using the index model.

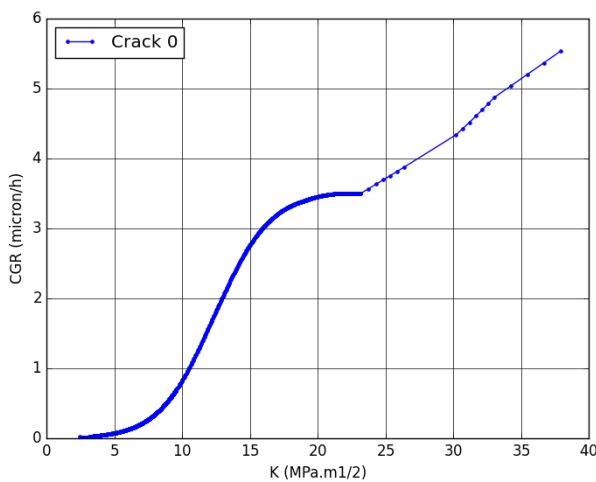


Figure 204 – Crack growth rate versus K at the tip of the main crack predicted for specimen 1383-26 using the index model.

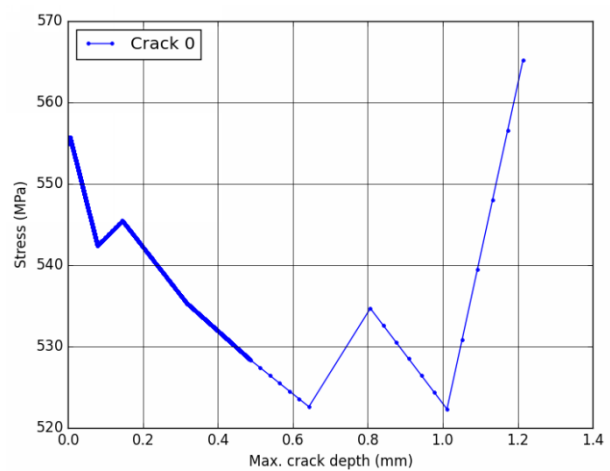


Figure 205 – Stress versus depth at the tip of the main crack predicted for specimen 1383-26, using the index model.

| | | |
|-----|---|--|
| MAI | Quantitative evaluation of the EDF local model and the EPRI-NRC xLPR models of crack initiation of the weld metals of Alloy 600 (Alloys 82 and 182) | 6125-4501-2018-00583-EN Version 2.0 |
|-----|---|--|

11.8.2. Local initiation model with sigmoid CGR law

Parameters of the initiation model named 'local_initiation_model' (Code_Coriolis v2.1.5 intermediate version)

| Grain boundaries | | | | | | | | | | | | |
|-------------------------------|--------------------------|----------------------|--------------|---------------------|--------------------------|------------------|---------------------|---------|-------------|------|------|------|
| Densite (mm/mm ²) | SfTot (mm ²) | SpaceResolution (nm) | | GBlength (nm) | GBResolution (joints/mm) | | GBC | rC (nm) | zCr (nm) | | | |
| 10 | 1 | 1 | | 200 | 10 | | 0.2 | 30 | 30 | | | |
| Intergranular oxidation | | | | | | | | | | | | |
| x0nom (nm) | bnom | cnom | x0depl (nm) | bdepl | Cdepl | x0carb (nm) | bcarb | Ccarb | oxQ (J/mol) | oxg1 | oxg2 | oxg3 |
| 0 | 1.86×10 ⁷ | 3 | 0 | 2.4×10 ⁷ | 3 | 0 | 2.6×10 ⁷ | 0.01 | 57000 | 0.1 | 0.3 | 0.04 |
| Cracking criterion | | | | | | | | | | | | |
| Poxc (nm) | | | SigmaC (MPa) | | | StressLinearCoef | | | | | | |
| 200 | | | 790 | | | 0.25 | | | | | | |

Parameters of the crack growth model named 'cgr_sigmoid_cw2_h' (Code_Coriolis v2.1.5 intermediate version)

| cgr1 | cgr2 | cgr3 | cgr4 | cgr5 | cgr6 | cgr7 | cgr8 | cgr9 | cgr10 | cgr11 | ecp1 | ecp2 |
|-------------------|------|------|------|------|------|------|-------|-------|-------|-------|--------------------|--------|
| 5×10 ⁴ | 0.5 | 0.66 | 12 | 0 | 0 | 0 | 3.604 | 11.33 | 43.36 | 65000 | 2×10 ⁻⁶ | 0.0256 |

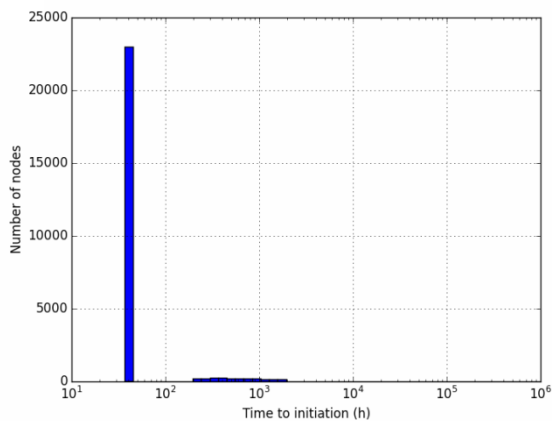


Figure 206 – Histogram of times to initiation predicted for specimen 1383-26, using the local model.

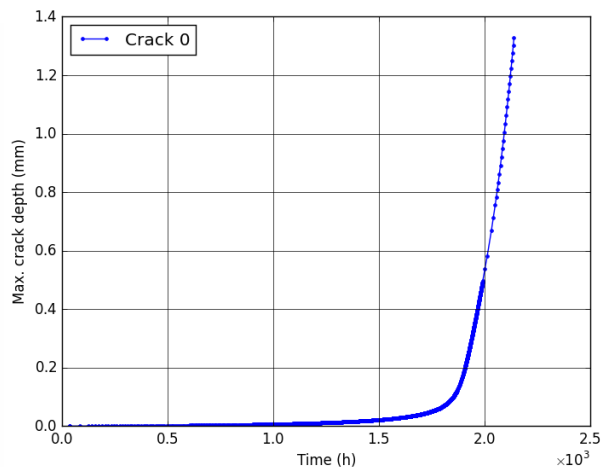


Figure 207 – Cracking kinetics predicted for specimen 1383-26, using the local model.

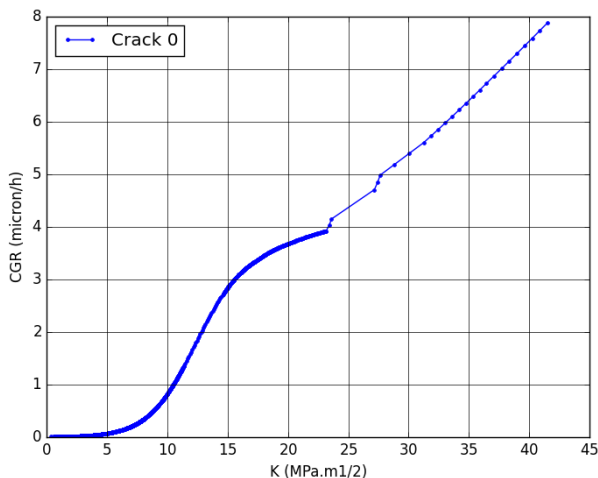


Figure 208 – Crack growth rate versus K at the tip of the main crack predicted for specimen 1383-26, using the local model.

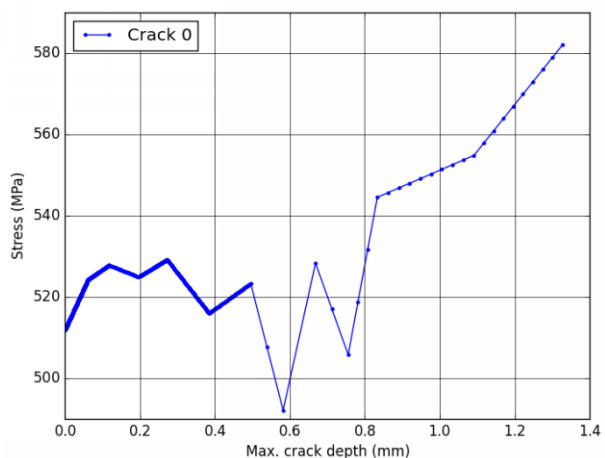


Figure 209 – Stress versus depth at the tip of the main crack predicted for specimen 1383-26, using the local model.

11.9. Simulations of the test on specimen 1383-27

11.9.1. Index initiation model with sigmoid CGR law

Parameters of the initiation model named 'index' (Code_Coriolis v2.1.5 intermediate version)

| init1 | init2 | init3 | init4 (j/mol) | init5 | init6 | Init_depth |
|-------|-------|-------|---------------|-------|------------------|------------|
| 1 | 6.8 | 1 | 185000 | 1 | 10 ⁻⁶ | 0.005 |

Parameters of the crack growth model named 'cgr_sigmoid_cw2_h' (Code_Coriolis v2.1.5 intermediate version)

| cgr1 | cgr2 | cgr3 | cgr4 | cgr5 | cgr6 | cgr7 | cgr8 | cgr9 | cgr10 | cgr11 | ecp1 | ecp2 |
|-------------------|------|------|------|------|------|------|-------|-------|-------|-------|--------------------|--------|
| 5×10 ⁴ | 0.5 | 0.66 | 12 | 15 | 0 | 0 | 3.604 | 11.33 | 43.36 | 65000 | 2×10 ⁻⁶ | 0.0256 |

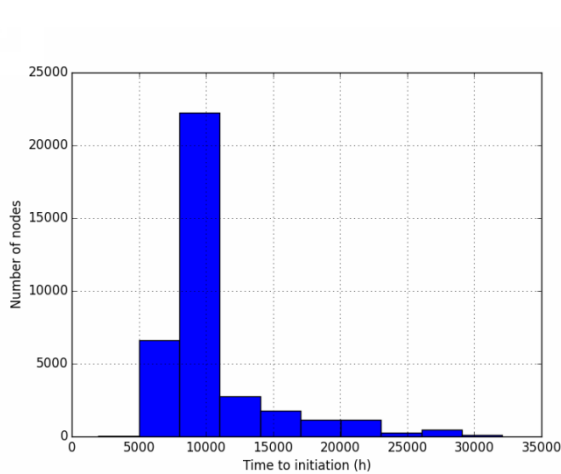


Figure 210 – Histogram of times to initiation predicted for specimen 1383-27, using the index model.

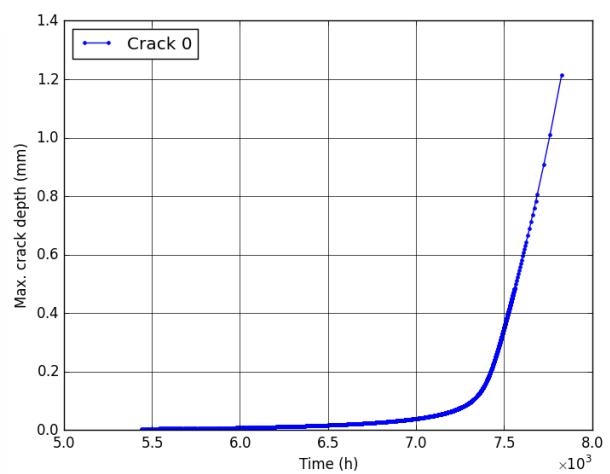


Figure 211 – Cracking kinetics predicted for specimen 1383-27, using the index model.

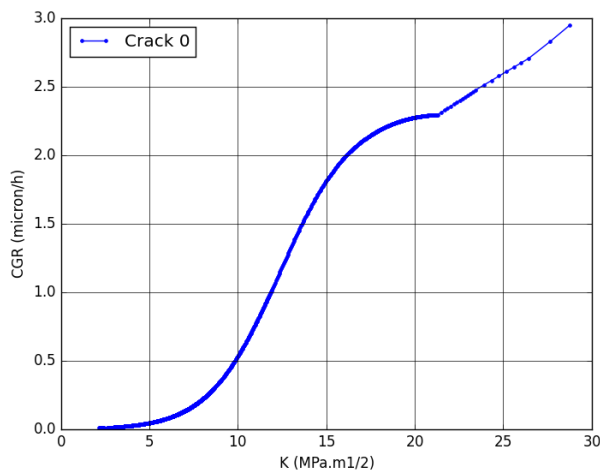


Figure 212 – Crack growth rate versus K at the tip of the main crack predicted for specimen 1383-27 using the index model.

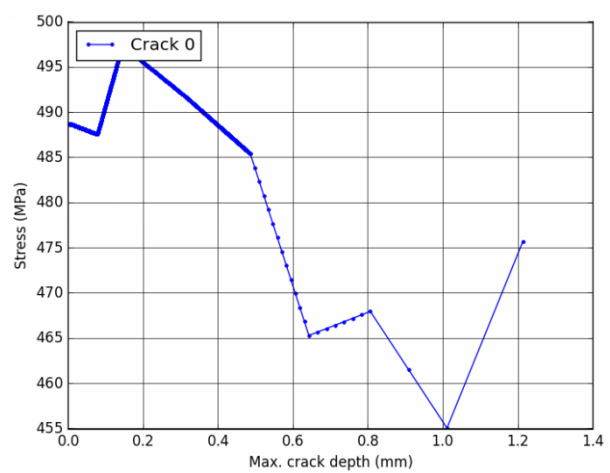


Figure 213 – Stress versus depth at the tip of the main crack predicted for specimen 1383-27, using the index model.

| | | |
|------------|---|--|
| MAI | Quantitative evaluation of the EDF local model and the EPRI-NRC xLPR models of crack initiation of the weld metals of Alloy 600 (Alloys 82 and 182) | 6125-4501-2018-00583-EN Version 2.0 |
|------------|---|--|

11.9.2. Local initiation model with sigmoid CGR law

Parameters of the initiation model named 'local_initiation_model' (Code_Coriolis v2.1.5 intermediate version)

| Grain boundaries | | | | | | | | | | | | |
|-------------------------------|--------------------------|----------------------|---------------|--------------------------|------------------|-------------|---------------------|-------|-------------|------|------|------|
| Densite (mm/mm ²) | SfTot (mm ²) | SpaceResolution (nm) | GBlength (nm) | GBResolution (joints/mm) | GBC | rC (nm) | zCr (nm) | | | | | |
| 10 | 1 | 1 | 200 | 10 | 0.2 | 30 | 30 | | | | | |
| Intergranular oxidation | | | | | | | | | | | | |
| x0nom (nm) | bnom | cnom | x0depl (nm) | bdepl | Cdepl | x0carb (nm) | bcarb | Ccarb | oxQ (J/mol) | oxg1 | oxg2 | oxg3 |
| 0 | 1.86×10 ⁷ | 3 | 0 | 2.4×10 ⁷ | 3 | 0 | 2.6×10 ⁷ | 0.01 | 57000 | 0.1 | 0.3 | 0.04 |
| Cracking criterion | | | | | | | | | | | | |
| Poxc (nm) | SigmaC (MPa) | | | | StressLinearCoef | | | | | | | |
| 200 | 790 | | | | 0.25 | | | | | | | |

Parameters of the crack growth model named 'cgr_sigmoid_cw2_h' (Code_Coriolis v2.1.5 intermediate version)

| cgr1 | cgr2 | cgr3 | cgr4 | cgr5 | cgr6 | cgr7 | cgr8 | cgr9 | cgr10 | cgr11 | ecp1 | ecp2 |
|-------------------|------|------|------|------|------|------|-------|-------|-------|-------|--------------------|--------|
| 5×10 ⁴ | 0.5 | 0.66 | 12 | 0 | 0 | 0 | 3.604 | 11.33 | 43.36 | 65000 | 2×10 ⁻⁶ | 0.0256 |

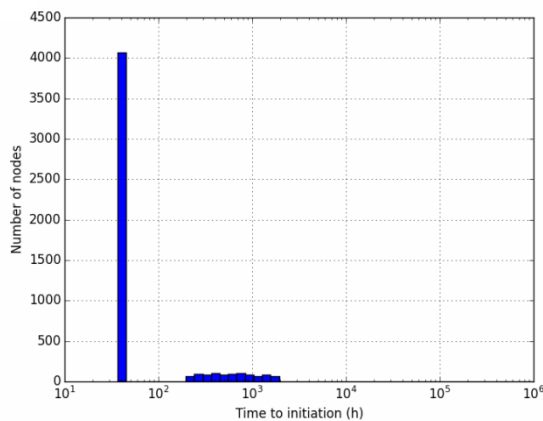


Figure 214 – Histogram of times to initiation predicted for specimen 1383-27, using the local model.

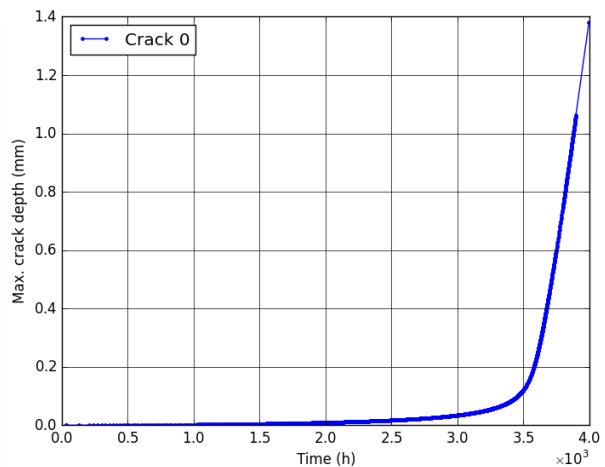


Figure 215 – Cracking kinetics predicted for specimen 1383-27, using the local model.

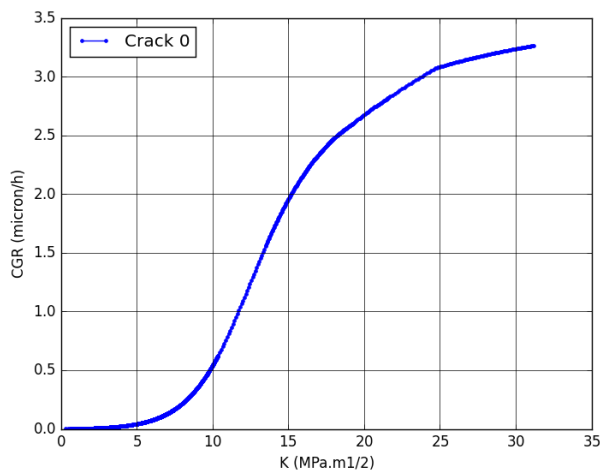


Figure 216 – Crack growth rate versus K at the tip of the main crack predicted for specimen 1383-27, using the local model.

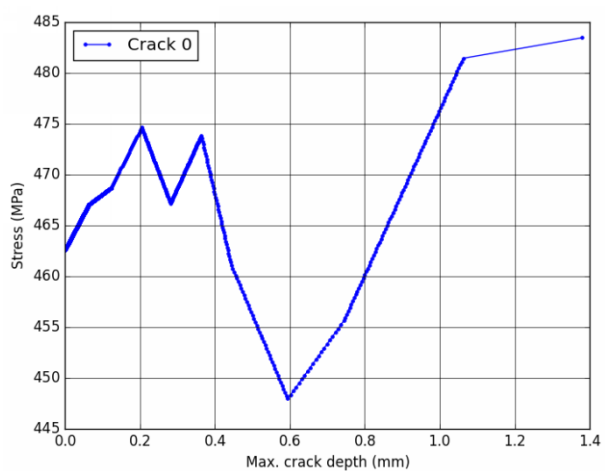


Figure 217 – Stress versus depth at the tip of the main crack predicted for specimen 1383-27, using the local model.

11.10. Simulations of the test on specimen 1383-28

11.10.1. Index initiation model with sigmoid CGR law

Parameters of the initiation model named 'index' (Code_Coriolis v2.1.5 intermediate version)

| init1 | init2 | init3 | init4 (j/mol) | init5 | init6 | Init_depth |
|-------|-------|-------|---------------|-------|------------------|------------|
| 1 | 6.8 | 1 | 185000 | 1 | 10 ⁻⁶ | 0.005 |

Parameters of the crack growth model named 'cgr_sigmoid_cw2_h' (Code_Coriolis v2.1.5 intermediate version)

| cgr1 | cgr2 | cgr3 | cgr4 | cgr5 | cgr6 | cgr7 | cgr8 | cgr9 | cgr10 | cgr11 | ecp1 | ecp2 |
|-------------------|------|------|------|------|------|------|-------|-------|-------|-------|--------------------|--------|
| 5×10 ⁴ | 0.5 | 0.66 | 12 | 15 | 0 | 0 | 3.604 | 11.33 | 43.36 | 65000 | 2×10 ⁻⁶ | 0.0256 |

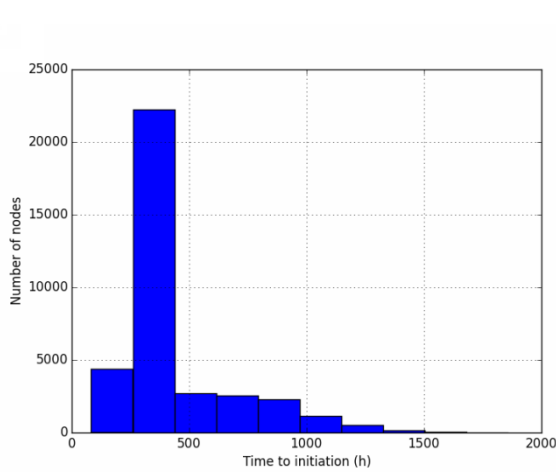


Figure 218 – Histogram of times to initiation predicted for specimen 1383-28, using the index model.

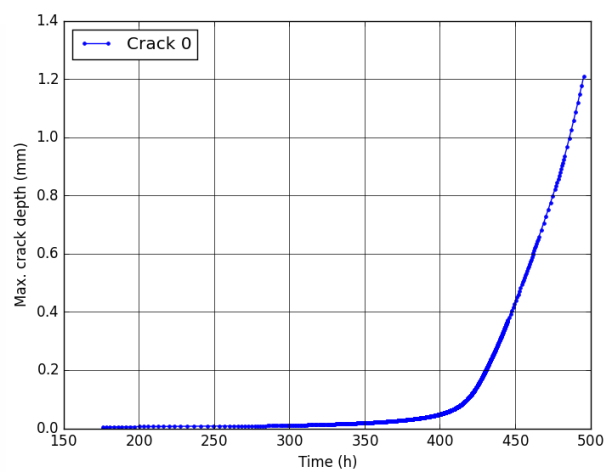


Figure 219 – Cracking kinetics predicted for specimen 1383-28, using the index model.

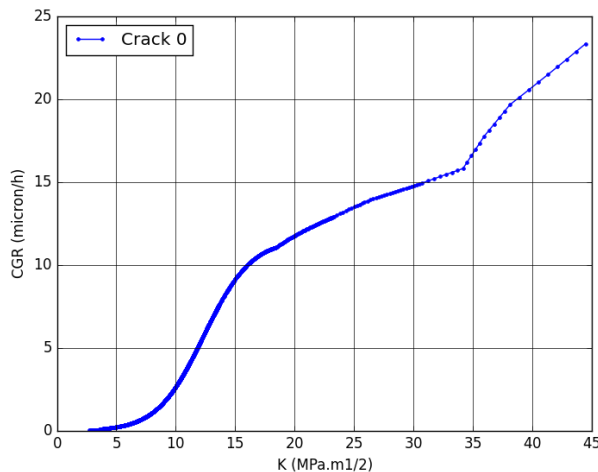


Figure 220 – Crack growth rate versus K at the tip of the main crack predicted for specimen 1383-28 using the index model.

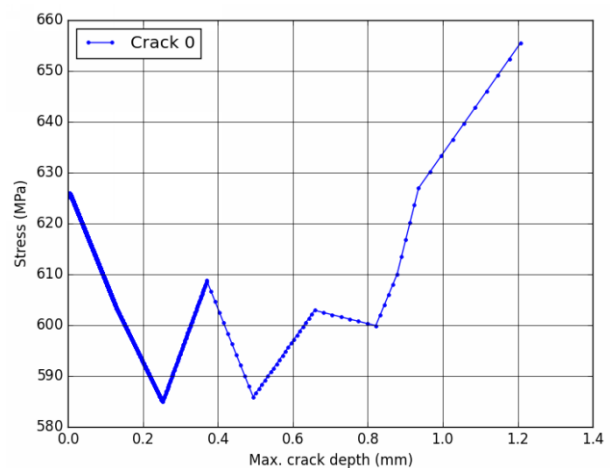


Figure 221 – Stress versus depth at the tip of the main crack predicted for specimen 1383-28, using the index model.

| | | |
|------------|---|--|
| MAI | Quantitative evaluation of the EDF local model and the EPRI-NRC xLPR models of crack initiation of the weld metals of Alloy 600 (Alloys 82 and 182) | 6125-4501-2018-00583-EN Version 2.0 |
|------------|---|--|

11.10.2. Local initiation model with sigmoid CGR law

Parameters of the initiation model named 'local_initiation_model' (Code_Coriolis v2.1.5 intermediate version)

| Grain boundaries | | | | | | | | | | | | |
|-------------------------------|--------------------------|----------------------|---------------|--------------------------|------------------|-------------|---------------------|-------|-------------|------|------|------|
| Densite (mm/mm ²) | SfTot (mm ²) | SpaceResolution (nm) | GBlength (nm) | GBResolution (joints/mm) | GBC | rC (nm) | zCr (nm) | | | | | |
| 10 | 1 | 1 | 200 | 10 | 0.2 | 30 | 30 | | | | | |
| Intergranular oxidation | | | | | | | | | | | | |
| x0nom (nm) | bnom | cnom | x0depl (nm) | bdepl | Cdepl | x0carb (nm) | bcarb | Ccarb | oxQ (J/mol) | oxg1 | oxg2 | oxg3 |
| 0 | 1.86×10 ⁷ | 3 | 0 | 2.4×10 ⁷ | 3 | 0 | 2.6×10 ⁷ | 0.01 | 57000 | 0.1 | 0.3 | 0.04 |
| Cracking criterion | | | | | | | | | | | | |
| Poxc (nm) | SigmaC (MPa) | | | | StressLinearCoef | | | | | | | |
| 200 | 790 | | | | 0.25 | | | | | | | |

Parameters of the crack growth model named 'cgr_sigmoid_cw2_h' (Code_Coriolis v2.1.5 intermediate version)

| cgr1 | cgr2 | cgr3 | cgr4 | cgr5 | cgr6 | cgr7 | cgr8 | cgr9 | cgr10 | cgr11 | ecp1 | ecp2 |
|-------------------|------|------|------|------|------|------|-------|-------|-------|-------|--------------------|--------|
| 5×10 ⁴ | 0.5 | 0.66 | 12 | 0 | 0 | 0 | 3.604 | 11.33 | 43.36 | 65000 | 2×10 ⁻⁶ | 0.0256 |

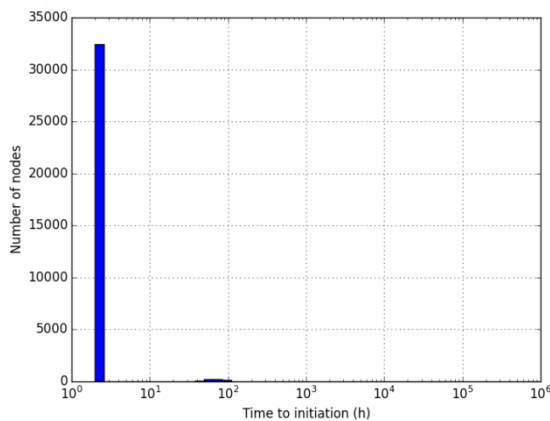


Figure 222 – Histogram of times to initiation predicted for specimen 1383-28, using the local model.

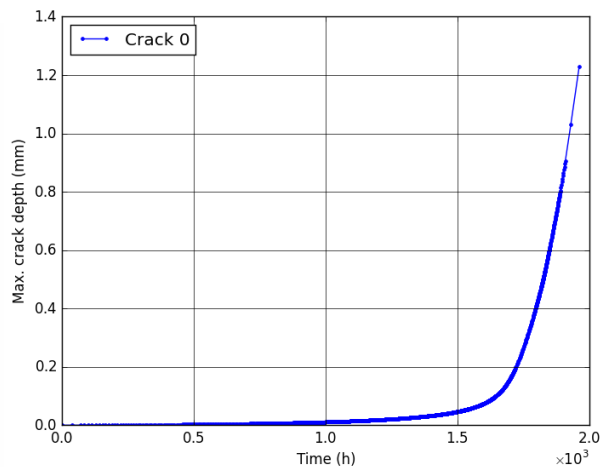


Figure 223 – Cracking kinetics predicted for specimen 1383-28, using the local model.

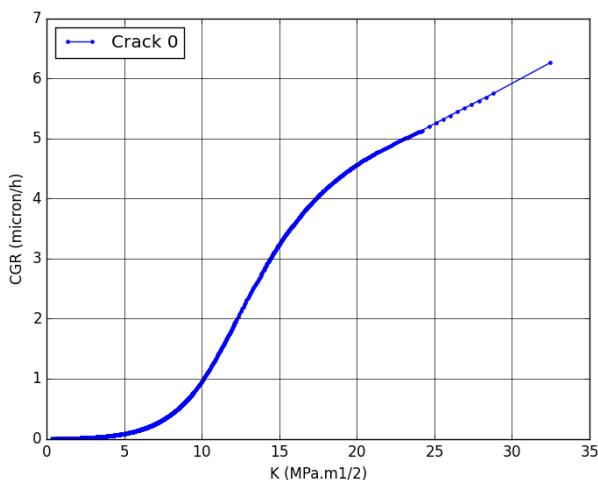


Figure 224 – Crack growth rate versus K at the tip of the main crack predicted for specimen 1383-28, using the local model.

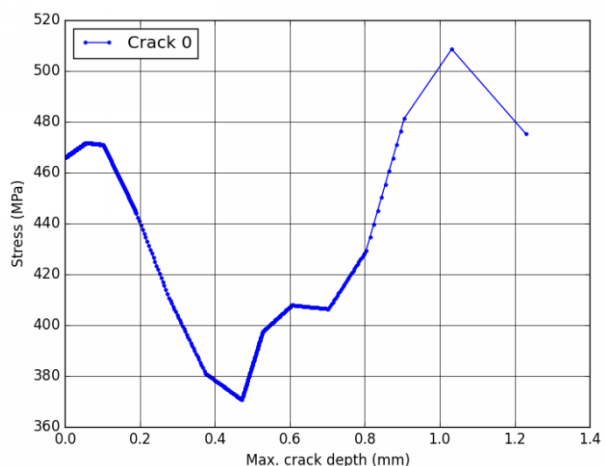


Figure 225 – Stress versus depth at the tip of the main crack predicted for specimen 1383-28, using the local model.

11.11. Simulations of the test on specimen 1383-29

11.11.1. Index initiation model with sigmoid CGR law

Parameters of the initiation model named 'index' (Code_Coriolis v2.1.5 intermediate version)

| init1 | init2 | init3 | init4 (J/mol) | init5 | init6 | Init_depth |
|-------|-------|-------|---------------|-------|------------------|------------|
| 1 | 6.8 | 1 | 185000 | 1 | 10 ⁻⁶ | 0.005 |

Parameters of the crack growth model named 'cgr_sigmoid_cw2_h' (Code_Coriolis v2.1.5 intermediate version)

| cgr1 | cgr2 | cgr3 | cgr4 | cgr5 | cgr6 | cgr7 | cgr8 | cgr9 | cgr10 | cgr11 | ecp1 | ecp2 |
|-------------------|------|------|------|------|------|------|-------|-------|-------|-------|--------------------|--------|
| 5×10 ⁴ | 0.5 | 0.66 | 12 | 15 | 0 | 0 | 3.604 | 11.33 | 43.36 | 65000 | 2×10 ⁻⁶ | 0.0256 |

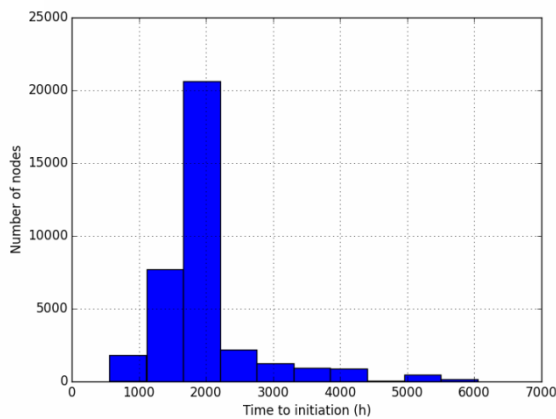


Figure 226 – Histogram of times to initiation predicted for specimen 1383-29, using the index model.

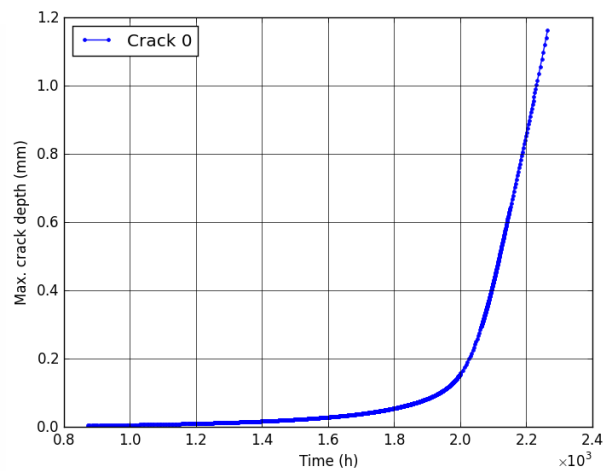


Figure 227 – Cracking kinetics predicted for specimen 1383-29, using the index model.

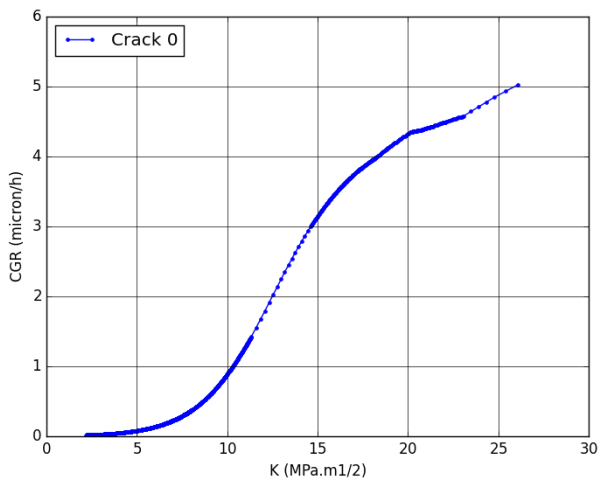


Figure 228 – Crack growth rate versus K at the tip of the main crack predicted for specimen 1383-29 using the index model.

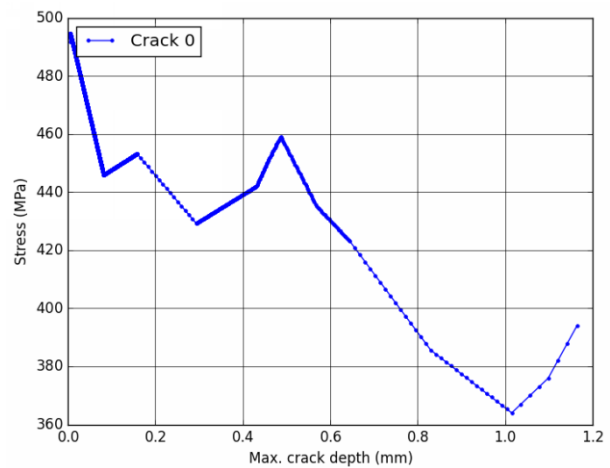


Figure 229 – Stress versus depth at the tip of the main crack predicted for specimen 1383-29, using the index model.

| | | |
|------------|---|--|
| MAI | Quantitative evaluation of the EDF local model and the EPRI-NRC xLPR models of crack initiation of the weld metals of Alloy 600 (Alloys 82 and 182) | 6125-4501-2018-00583-EN Version 2.0 |
|------------|---|--|

11.11.2. Local initiation model with sigmoid CGR law

Parameters of the initiation model named 'local_initiation_model' (Code_Coriolis v2.1.5 intermediate version)

| Grain boundaries | | | | | | | | | | | | |
|-------------------------------|--------------------------|----------------------|---------------|--------------------------|------------------|-------------|---------------------|-------|-------------|------|------|------|
| Densite (mm/mm ²) | SfTot (mm ²) | SpaceResolution (nm) | GBlength (nm) | GBResolution (joints/mm) | GBC | rC (nm) | zCr (nm) | | | | | |
| 10 | 1 | 1 | 200 | 10 | 0.2 | 30 | 30 | | | | | |
| Intergranular oxidation | | | | | | | | | | | | |
| x0nom (nm) | bnom | cnom | x0depl (nm) | bdepl | Cdepl | x0carb (nm) | bcarb | Ccarb | oxQ (J/mol) | oxg1 | oxg2 | oxg3 |
| 0 | 1.86×10 ⁷ | 3 | 0 | 2.4×10 ⁷ | 3 | 0 | 2.6×10 ⁷ | 0.01 | 57000 | 0.1 | 0.3 | 0.04 |
| Cracking criterion | | | | | | | | | | | | |
| Poxc (nm) | SigmaC (MPa) | | | | StressLinearCoef | | | | | | | |
| 200 | 790 | | | | 0.25 | | | | | | | |

Parameters of the crack growth model named 'cgr_sigmoid_cw2_h' (Code_Coriolis v2.1.5 intermediate version)

| cgr1 | cgr2 | cgr3 | cgr4 | cgr5 | cgr6 | cgr7 | cgr8 | cgr9 | cgr10 | cgr11 | ecp1 | ecp2 |
|-------------------|------|------|------|------|------|------|-------|-------|-------|-------|--------------------|--------|
| 5×10 ⁴ | 0.5 | 0.66 | 12 | 0 | 0 | 0 | 3.604 | 11.33 | 43.36 | 65000 | 2×10 ⁻⁶ | 0.0256 |

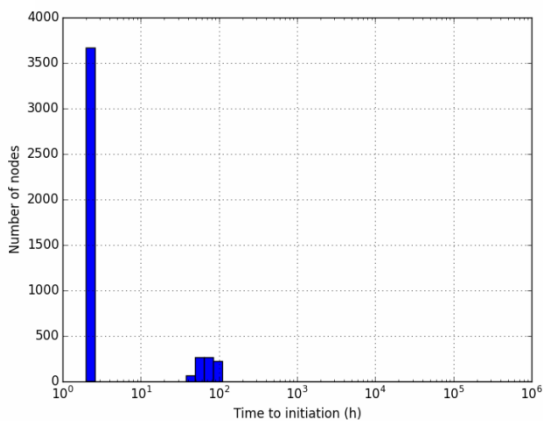


Figure 230 – Histogram of times to initiation predicted for specimen 1383-29, using the local model.

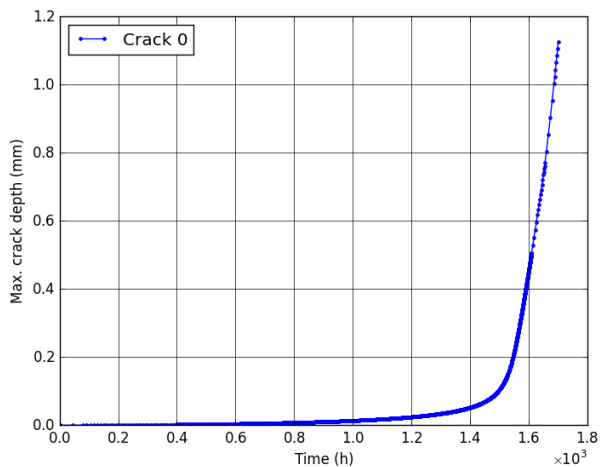


Figure 231 – Cracking kinetics predicted for specimen 1383-29, using the local model.

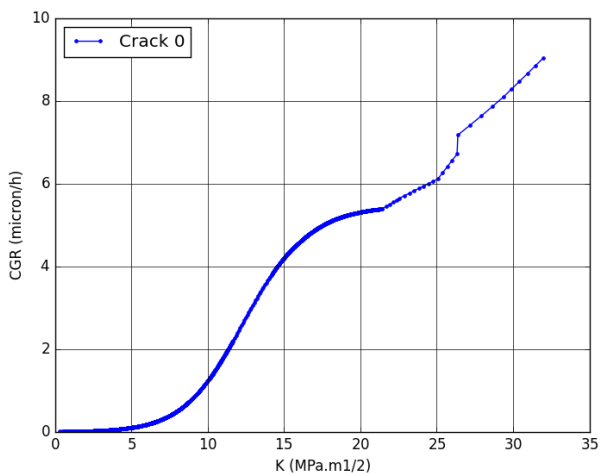


Figure 232 – Crack growth rate versus K at the tip of the main crack predicted for specimen 1383-29, using the local model.

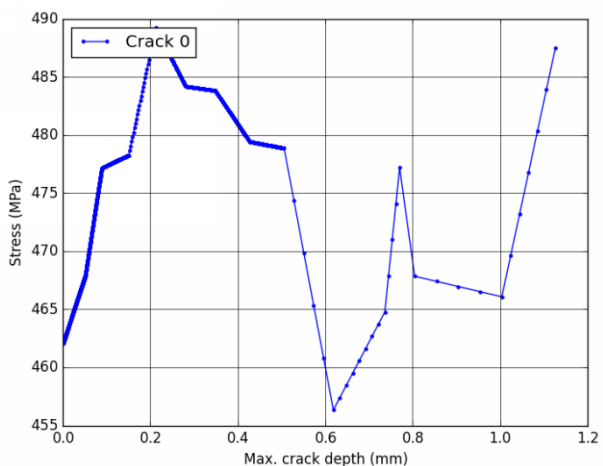


Figure 233 – Stress versus depth at the tip of the main crack predicted for specimen 1383-29, using the local model.

11.12. Simulations of the test on specimen 1383-CEA

11.12.1. Index initiation model with sigmoid CGR law

Parameters of the initiation model named 'index' (Code_Coriolis v2.1.5 intermediate version)

| init1 | init2 | init3 | init4 (j/mol) | init5 | init6 | Init_depth |
|-------|-------|-------|---------------|-------|------------------|------------|
| 1 | 6.8 | 1 | 185000 | 1 | 10 ⁻⁶ | 0.005 |

Parameters of the crack growth model named 'cgr_sigmoid_cw2_h' (Code_Coriolis v2.1.5 intermediate version)

| cgr1 | cgr2 | cgr3 | cgr4 | cgr5 | cgr6 | cgr7 | cgr8 | cgr9 | cgr10 | cgr11 | ecp1 | ecp2 |
|-------------------|------|------|------|------|------|------|-------|-------|-------|-------|--------------------|--------|
| 5×10 ⁴ | 0.5 | 0.66 | 12 | 15 | 0 | 0 | 3.604 | 11.33 | 43.36 | 65000 | 2×10 ⁻⁶ | 0.0256 |

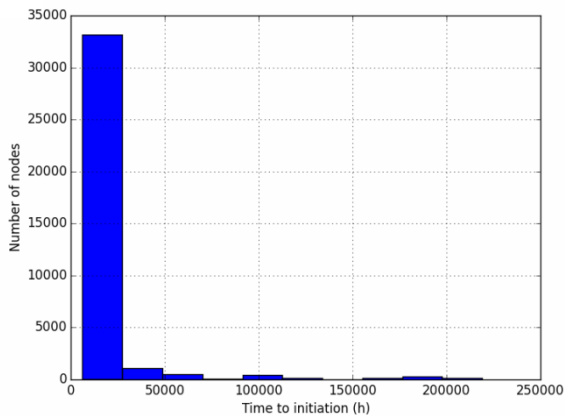


Figure 234 – Histogram of times to initiation predicted for specimen 1383-CEA, using the index model.

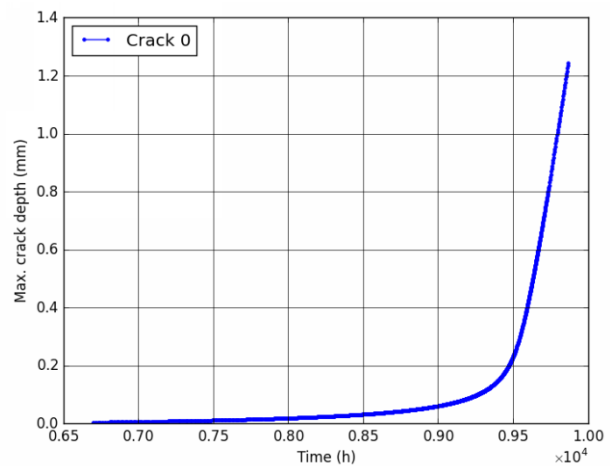


Figure 235 – Cracking kinetics predicted for specimen 1383-CEA, using the index model.

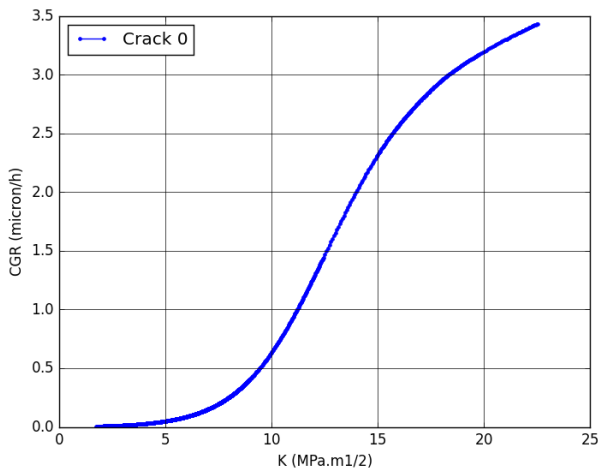


Figure 236 – Crack growth rate versus K at the tip of the main crack predicted for specimen 1383-CEA using the index model.

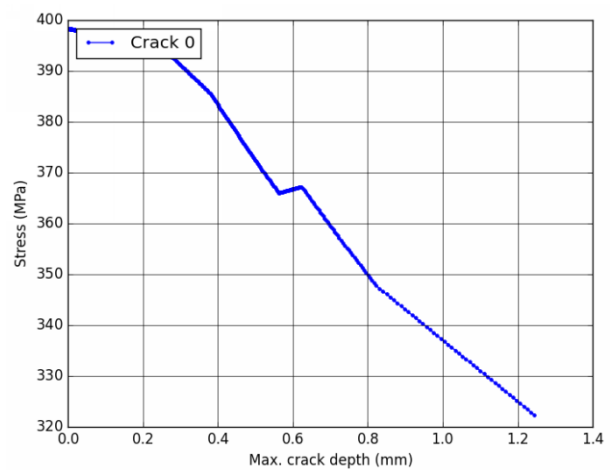


Figure 237 – Stress versus depth at the tip of the main crack predicted for specimen 1383-CEA, using the index model.

| | | |
|------------|---|--|
| MAI | Quantitative evaluation of the EDF local model and the EPRI-NRC xLPR models of crack initiation of the weld metals of Alloy 600 (Alloys 82 and 182) | 6125-4501-2018-00583-EN Version 2.0 |
|------------|---|--|

11.12.2. Local initiation model with sigmoid CGR law

Parameters of the initiation model named 'local_initiation_model' (Code_Coriolis v2.1.5 intermediate version)

| Grain boundaries | | | | | | | | | | | | |
|-------------------------------|--------------------------|----------------------|---------------|--------------------------|------------------|-------------|---------------------|-------|-------------|------|------|------|
| Densite (mm/mm ²) | SfTot (mm ²) | SpaceResolution (nm) | GBlength (nm) | GBResolution (joints/mm) | GBC | rC (nm) | zCr (nm) | | | | | |
| 10 | 1 | 1 | 200 | 10 | 0.2 | 30 | 30 | | | | | |
| Intergranular oxidation | | | | | | | | | | | | |
| x0nom (nm) | bnom | cnom | x0depl (nm) | bdepl | Cdepl | x0carb (nm) | bcarb | Ccarb | oxQ (J/mol) | oxg1 | oxg2 | oxg3 |
| 0 | 1.86×10 ⁷ | 3 | 0 | 2.4×10 ⁷ | 3 | 0 | 2.6×10 ⁷ | 0.01 | 57000 | 0.1 | 0.3 | 0.04 |
| Cracking criterion | | | | | | | | | | | | |
| Poxc (nm) | SigmaC (MPa) | | | | StressLinearCoef | | | | | | | |
| 200 | 790 | | | | 0.25 | | | | | | | |

Parameters of the crack growth model named 'cgr_sigmoid_cw2_h' (Code_Coriolis v2.1.5 intermediate version)

| | | | | | | | | | | | | |
|-------------------|------|------|------|------|------|------|-------|-------|-------|-------|--------------------|--------|
| cgr1 | cgr2 | cgr3 | cgr4 | cgr5 | cgr6 | cgr7 | cgr8 | cgr9 | cgr10 | cgr11 | ecp1 | ecp2 |
| 5×10 ⁴ | 0.5 | 0.66 | 12 | 0 | 0 | 0 | 3.604 | 11.33 | 43.36 | 65000 | 2×10 ⁻⁶ | 0.0256 |

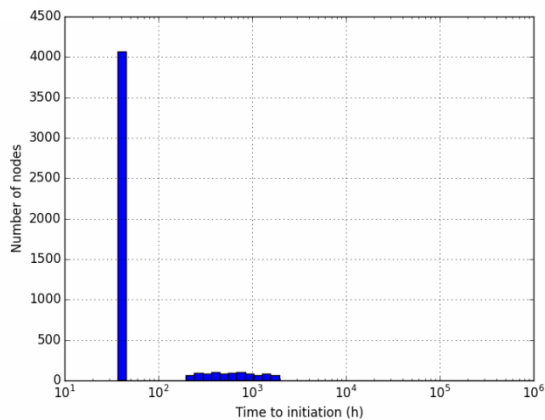


Figure 238 – Histogram of times to initiation predicted for specimen 1383-CEA, using the local model.

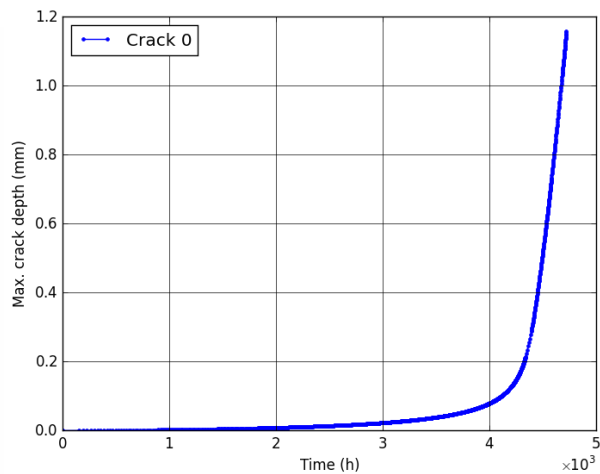


Figure 239 – Cracking kinetics predicted for specimen 1383-CEA, using the local model.

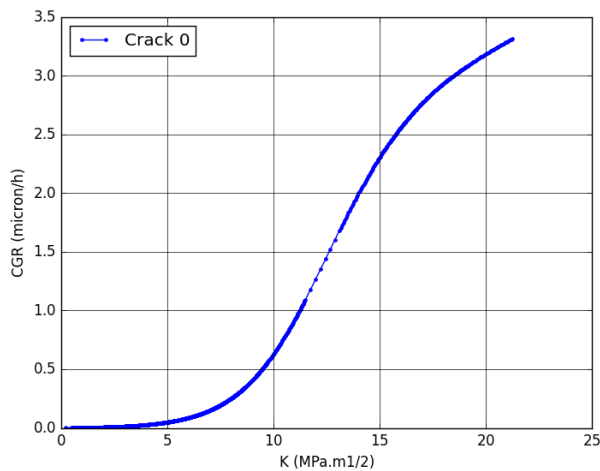


Figure 240 – Crack growth rate versus K at the tip of the main crack predicted for specimen 1383-CEA, using the local model.

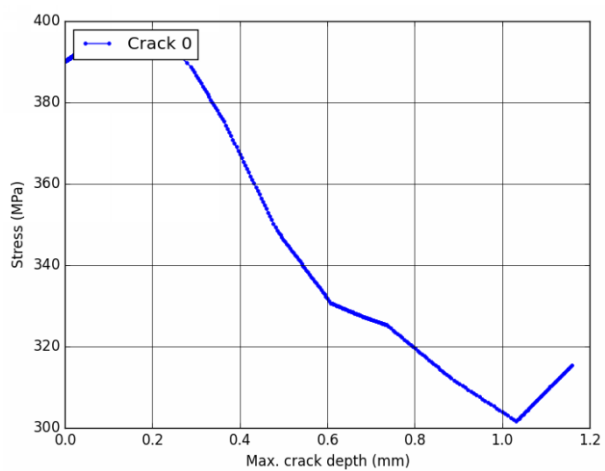


Figure 241 – Stress versus depth at the tip of the main crack predicted for specimen 1383-CEA, using the local model.

11.13. Simulations of the test on specimen 1588-16

11.13.1. Index initiation model with sigmoid CGR law

Parameters of the initiation model named 'index' (Code_Coriolis v2.1.5 intermediate version)

| init1 | init2 | init3 | init4 (j/mol) | init5 | init6 | Init_depth |
|-------|-------|-------|---------------|-------|------------------|------------|
| 1 | 6.8 | 1 | 185000 | 1 | 10 ⁻⁶ | 0.005 |

Parameters of the crack growth model named 'cgr_sigmoid_cw2_h' (Code_Coriolis v2.1.5 intermediate version)

| cgr1 | cgr2 | cgr3 | cgr4 | cgr5 | cgr6 | cgr7 | cgr8 | cgr9 | cgr10 | cgr11 | ecp1 | ecp2 |
|-------------------|------|------|------|------|------|------|-------|-------|-------|-------|--------------------|--------|
| 5×10 ⁴ | 0.5 | 0.66 | 12 | 15 | 0 | 0 | 3.604 | 11.33 | 43.36 | 65000 | 2×10 ⁻⁶ | 0.0256 |

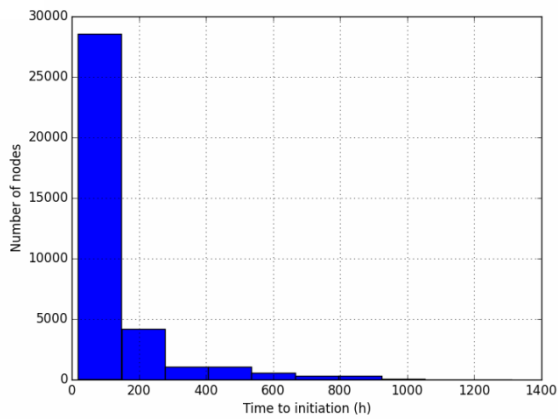


Figure 242 – Histogram of times to initiation predicted for specimen 1588-16, using the index model.

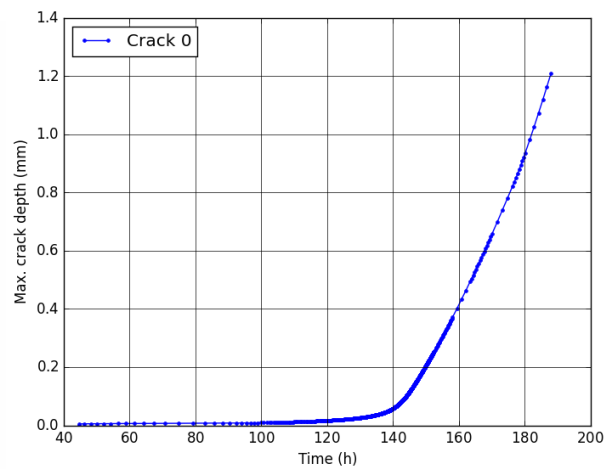


Figure 243 – Cracking kinetics predicted for specimen 1588-16, using the index model.

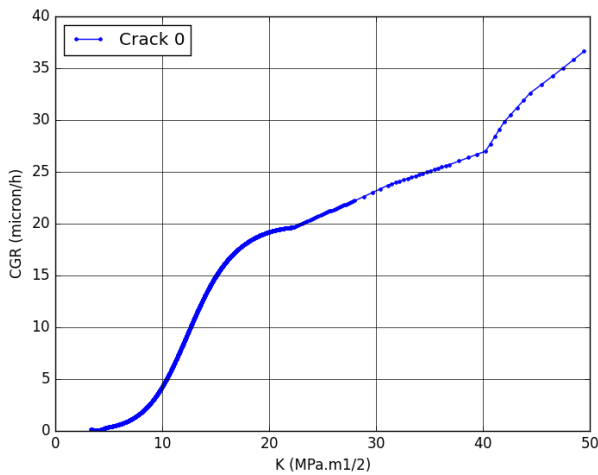


Figure 244 – Crack growth rate versus K at the tip of the main crack predicted for specimen 1588-16 using the index model.

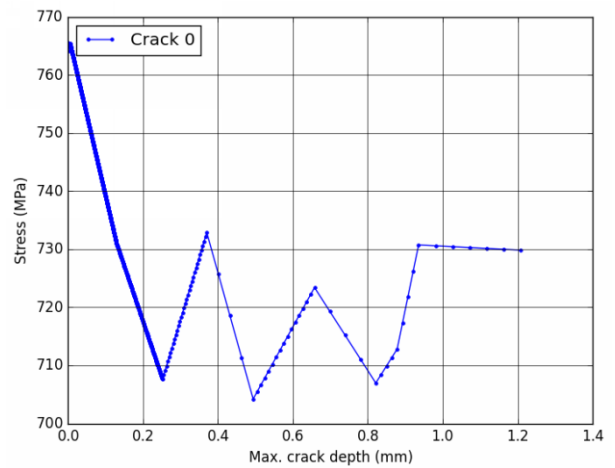


Figure 245 – Stress versus depth at the tip of the main crack predicted for specimen 1588-16, using the index model.

| | | |
|-----|---|--|
| MAI | Quantitative evaluation of the EDF local model and the EPRI-NRC xLPR models of crack initiation of the weld metals of Alloy 600 (Alloys 82 and 182) | 6125-4501-2018-00583-EN Version 2.0 |
|-----|---|--|

11.13.2. Local initiation model with sigmoid CGR law

Parameters of the initiation model named 'local_initiation_model' (Code_Coriolis v2.1.5 intermediate version)

| Grain boundaries | | | | | | | | | | | | |
|-------------------------------|--------------------------|----------------------|-------------|---------------------|--------------------------|-------------|---------------------|---------|-------------|------|------|------|
| Densite (mm/mm ²) | SfTot (mm ²) | SpaceResolution (nm) | | GBlength (nm) | GBResolution (joints/mm) | | GBC | rC (nm) | zCr (nm) | | | |
| 10 | 1 | 1 | | 200 | 10 | | 0.2 | 30 | 30 | | | |
| Intergranular oxidation | | | | | | | | | | | | |
| x0nom (nm) | bnom | cnom | x0depl (nm) | bdepl | Cdepl | x0carb (nm) | bcarb | Ccarb | oxQ (J/mol) | oxg1 | oxg2 | oxg3 |
| 0 | 1.86×10 ⁷ | 3 | 0 | 2.4×10 ⁷ | 3 | 0 | 2.6×10 ⁷ | 0.01 | 57000 | 0.1 | 0.3 | 0.04 |
| Cracking criterion | | | | | | | | | | | | |
| Poxc (nm) | | SigmaC (MPa) | | | StressLinearCoef | | | | | | | |
| 200 | | 790 | | | 0.25 | | | | | | | |

Parameters of the crack growth model named 'cgr_sigmoid_cw2_h' (Code_Coriolis v2.1.5 intermediate version)

| cgr1 | cgr2 | cgr3 | cgr4 | cgr5 | cgr6 | cgr7 | cgr8 | cgr9 | cgr10 | cgr11 | ecp1 | ecp2 |
|-------------------|------|------|------|------|------|------|-------|-------|-------|-------|--------------------|--------|
| 5×10 ⁴ | 0.5 | 0.66 | 12 | 0 | 0 | 0 | 3.604 | 11.33 | 43.36 | 65000 | 2×10 ⁻⁶ | 0.0256 |

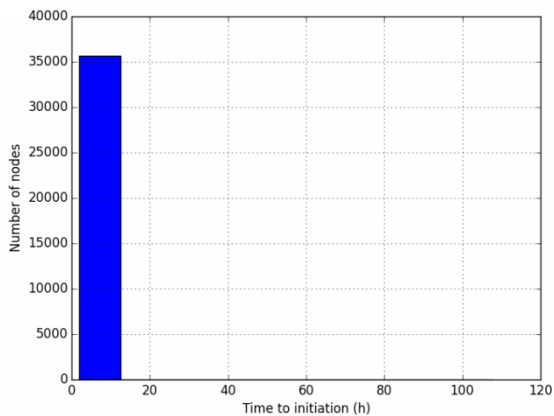


Figure 246 – Histogram of times to initiation predicted for specimen 1588-16, using the local model.

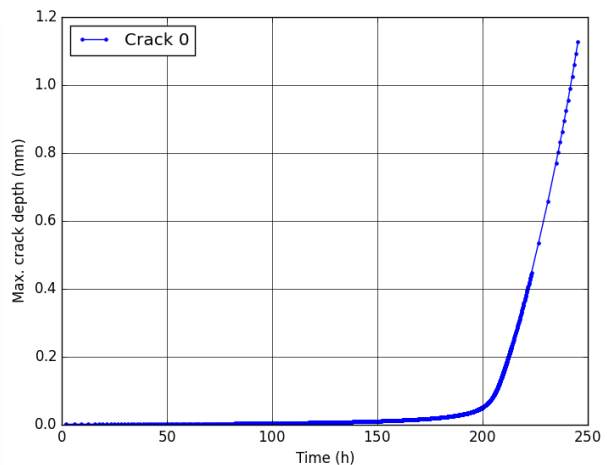


Figure 247 – Cracking kinetics predicted for specimen 1588-16, using the local model.

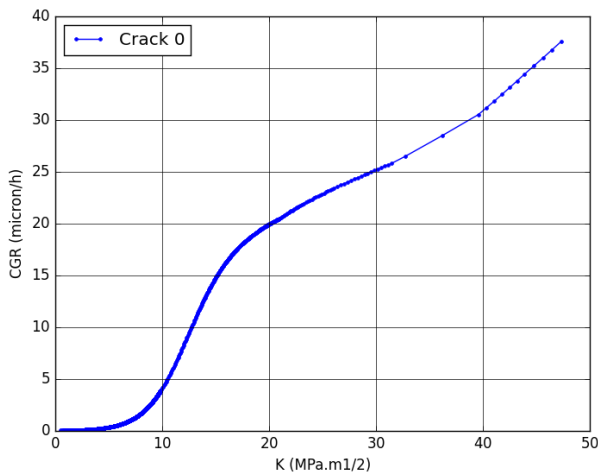


Figure 248 – Crack growth rate versus K at the tip of the main crack predicted for specimen 1588-16, using the local model.

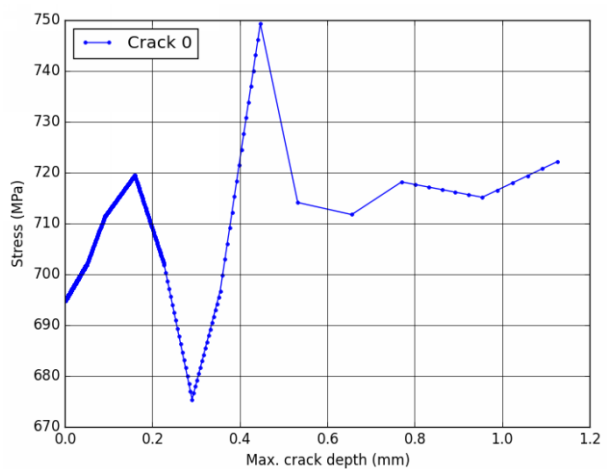


Figure 249 – Stress versus depth at the tip of the main crack predicted for specimen 1588-16, using the local model.

11.14. Simulations of the test on specimen IN169

11.14.1. Index initiation model with sigmoid CGR law

Parameters of the initiation model named 'index' (Code_Coriolis v2.1.5 intermediate version)

| init1 | init2 | init3 | init4 (j/mol) | init5 | init6 | Init_depth |
|-------|-------|-------|---------------|-------|------------------|------------|
| 1 | 6.8 | 1 | 185000 | 1 | 10 ⁻⁶ | 0.005 |

Parameters of the crack growth model named 'cgr_sigmoid_cw2_h' (Code_Coriolis v2.1.5 intermediate version)

| cgr1 | cgr2 | cgr3 | cgr4 | cgr5 | cgr6 | cgr7 | cgr8 | cgr9 | cgr10 | cgr11 | ecp1 | ecp2 |
|-------------------|------|------|------|------|------|------|-------|-------|-------|-------|--------------------|--------|
| 5×10 ⁴ | 0.5 | 0.66 | 12 | 15 | 0 | 0 | 3.604 | 11.33 | 43.36 | 65000 | 2×10 ⁻⁶ | 0.0256 |

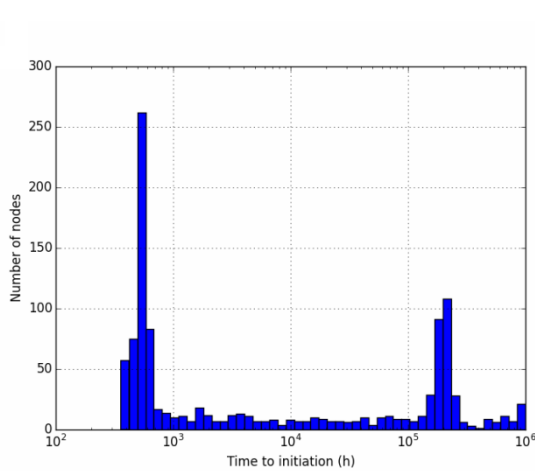


Figure 250 – Histogram of times to initiation predicted for specimen IN169, using the index model.

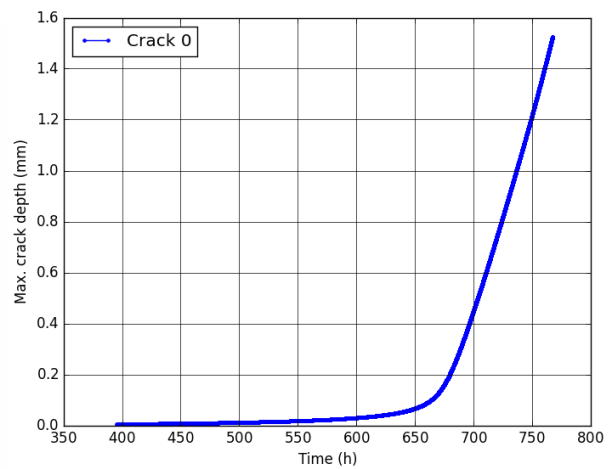


Figure 251 – Cracking kinetics predicted for specimen IN169, using the index model.

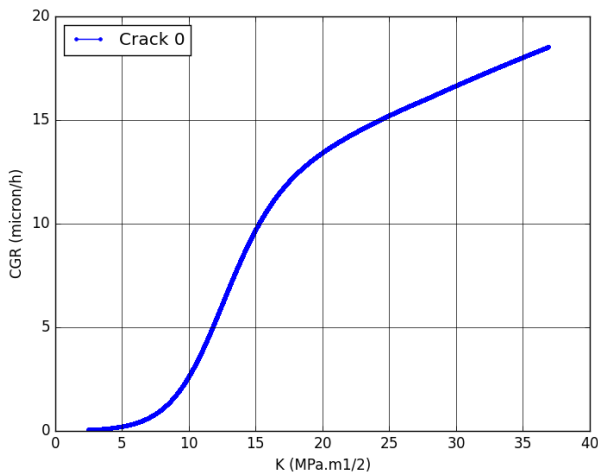


Figure 252 – Crack growth rate versus K at the tip of the main crack predicted for specimen IN169 using the index model.

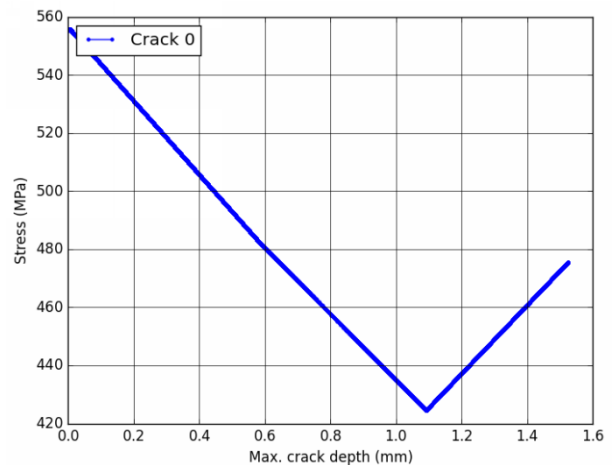


Figure 253 – Stress versus depth at the tip of the main crack predicted for specimen IN169, using the index model.

| | | |
|------------|---|--|
| MAI | Quantitative evaluation of the EDF local model and the EPRI-NRC xLPR models of crack initiation of the weld metals of Alloy 600 (Alloys 82 and 182) | 6125-4501-2018-00583-EN Version 2.0 |
|------------|---|--|

11.14.2. Local initiation model with sigmoid CGR law

Parameters of the initiation model named 'local_initiation_model' (Code_Coriolis v2.1.5 intermediate version)

| Grain boundaries | | | | | | | | | | | | |
|-------------------------------|--------------------------|----------------------|-------------|---------------------|--------------------------|-------------|---------------------|---------|-------------|------|------|------|
| Densite (mm/mm ²) | SfTot (mm ²) | SpaceResolution (nm) | | GBlength (nm) | GBResolution (joints/mm) | | GBC | rC (nm) | zCr (nm) | | | |
| 10 | 1 | 1 | | 200 | 10 | | 0.2 | 30 | 30 | | | |
| Intergranular oxidation | | | | | | | | | | | | |
| x0nom (nm) | bnom | cnom | x0depl (nm) | bdepl | Cdepl | x0carb (nm) | bcarb | Ccarb | oxQ (J/mol) | oxg1 | oxg2 | oxg3 |
| 0 | 1.86×10 ⁷ | 3 | 0 | 2.4×10 ⁷ | 3 | 0 | 2.6×10 ⁷ | 0.01 | 57000 | 0.1 | 0.3 | 0.04 |
| Cracking criterion | | | | | | | | | | | | |
| Poxc (nm) | | SigmaC (MPa) | | | StressLinearCoef | | | | | | | |
| 200 | | 790 | | | 0.25 | | | | | | | |

Parameters of the crack growth model named 'cgr_sigmoid_cw2_h' (Code_Coriolis v2.1.5 intermediate version)

| | | | | | | | | | | | | |
|-------------------|------|------|------|------|------|------|-------|-------|-------|-------|--------------------|--------|
| cgr1 | cgr2 | cgr3 | cgr4 | cgr5 | cgr6 | cgr7 | cgr8 | cgr9 | cgr10 | cgr11 | ecp1 | ecp2 |
| 5×10 ⁴ | 0.5 | 0.66 | 12 | 0 | 0 | 0 | 3.604 | 11.33 | 43.36 | 65000 | 2×10 ⁻⁶ | 0.0256 |

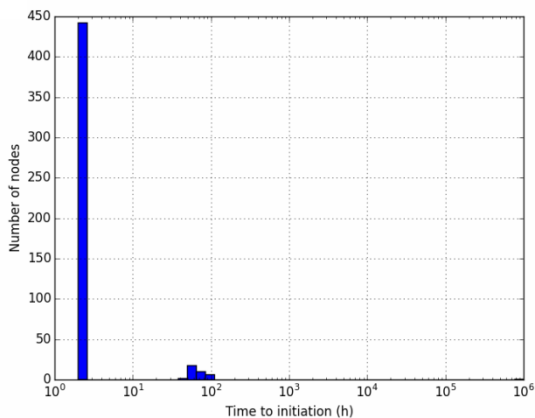


Figure 254 – Histogram of times to initiation predicted for specimen IN169, using the local model.

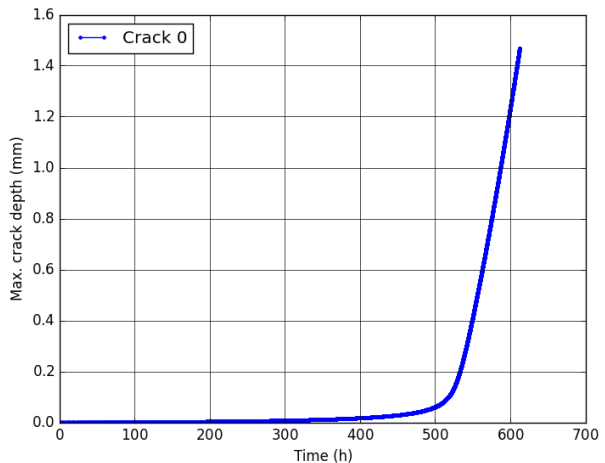


Figure 255 – Cracking kinetics predicted for specimen IN169, using the local model.

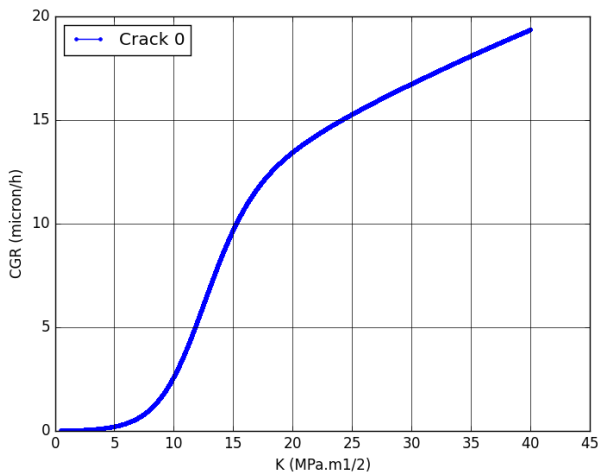


Figure 256 – Crack growth rate versus K at the tip of the main crack predicted for specimen IN169, using the local model.

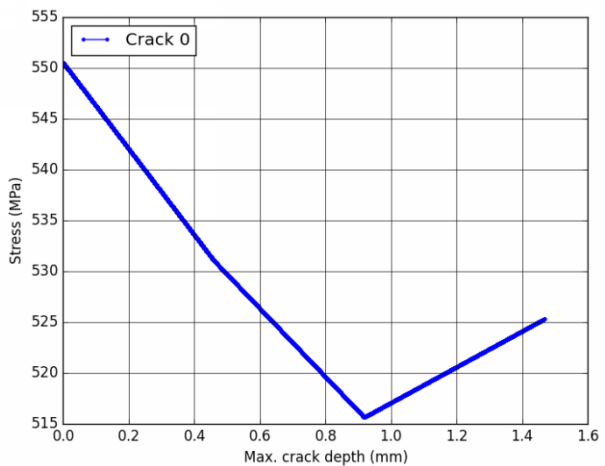


Figure 257 – Stress versus depth at the tip of the main crack predicted for specimen IN169, using the local model.

11.15. Simulations of the test on specimen IN170

11.15.1. Index initiation model with sigmoid CGR law

Parameters of the initiation model named 'index' (Code_Coriolis v2.1.5 intermediate version)

| init1 | init2 | init3 | init4 (j/mol) | init5 | init6 | Init_depth |
|-------|-------|-------|---------------|-------|------------------|------------|
| 1 | 6.8 | 1 | 185000 | 1 | 10 ⁻⁶ | 0.005 |

Parameters of the crack growth model named 'cgr_sigmoid_cw2_h' (Code_Coriolis v2.1.5 intermediate version)

| cgr1 | cgr2 | cgr3 | cgr4 | cgr5 | cgr6 | cgr7 | cgr8 | cgr9 | cgr10 | cgr11 | ecp1 | ecp2 |
|-------------------|------|------|------|------|------|------|-------|-------|-------|-------|--------------------|--------|
| 5×10 ⁴ | 0.5 | 0.66 | 12 | 15 | 0 | 0 | 3.604 | 11.33 | 43.36 | 65000 | 2×10 ⁻⁶ | 0.0256 |

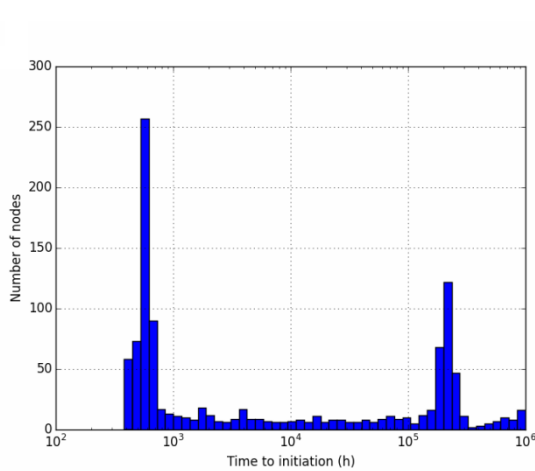


Figure 258 – Histogram of times to initiation predicted for specimen IN170, using the index model.

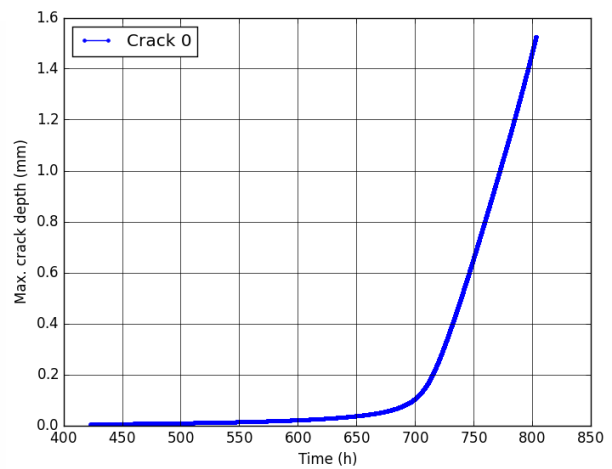


Figure 259 – Cracking kinetics predicted for specimen IN1709, using the index model.

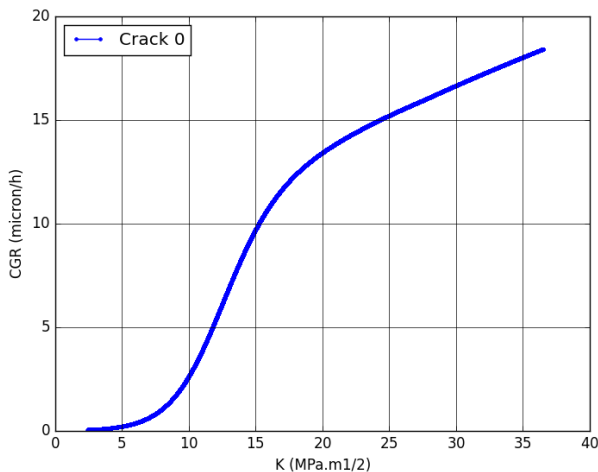


Figure 260 – Crack growth rate versus K at the tip of the main crack predicted for specimen IN170 using the index model.

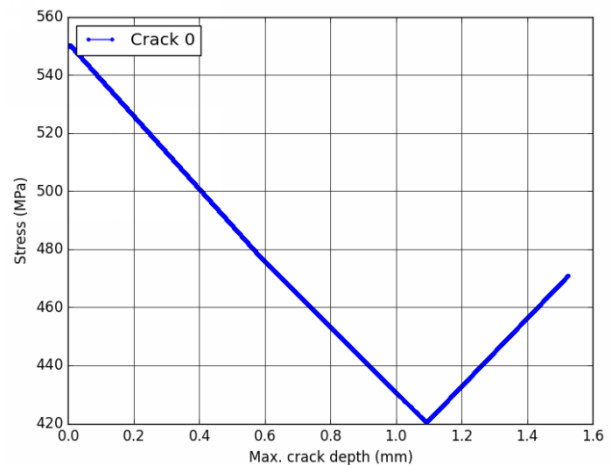


Figure 261 – Stress versus depth at the tip of the main crack predicted for specimen IN170, using the index model.

| | | |
|------------|---|--|
| MAI | Quantitative evaluation of the EDF local model and the EPRI-NRC xLPR models of crack initiation of the weld metals of Alloy 600 (Alloys 82 and 182) | 6125-4501-2018-00583-EN Version 2.0 |
|------------|---|--|

11.15.2. Local initiation model with sigmoid CGR law

Parameters of the initiation model named 'local_initiation_model' (Code_Coriolis v2.1.5 intermediate version)

| Grain boundaries | | | | | | | | | | | | |
|-------------------------------|--------------------------|----------------------|-------------|---------------------|--------------------------|-------------|---------------------|---------|-------------|------|------|------|
| Densite (mm/mm ²) | SfTot (mm ²) | SpaceResolution (nm) | | GBlength (nm) | GBResolution (joints/mm) | | GBC | rC (nm) | zCr (nm) | | | |
| 10 | 1 | 1 | | 200 | 10 | | 0.2 | 30 | 30 | | | |
| Intergranular oxidation | | | | | | | | | | | | |
| x0nom (nm) | bnom | cnom | x0depl (nm) | bdepl | Cdepl | x0carb (nm) | bcarb | Ccarb | oxQ (J/mol) | oxg1 | oxg2 | oxg3 |
| 0 | 1.86×10 ⁷ | 3 | 0 | 2.4×10 ⁷ | 3 | 0 | 2.6×10 ⁷ | 0.01 | 57000 | 0.1 | 0.3 | 0.04 |
| Cracking criterion | | | | | | | | | | | | |
| Poxc (nm) | | SigmaC (MPa) | | | StressLinearCoef | | | | | | | |
| 200 | | 790 | | | 0.25 | | | | | | | |

Parameters of the crack growth model named 'cgr_sigmoid_cw2_h' (Code_Coriolis v2.1.5 intermediate version)

| cgr1 | cgr2 | cgr3 | cgr4 | cgr5 | cgr6 | cgr7 | cgr8 | cgr9 | cgr10 | cgr11 | ecp1 | ecp2 |
|-------------------|------|------|------|------|------|------|-------|-------|-------|-------|--------------------|--------|
| 5×10 ⁴ | 0.5 | 0.66 | 12 | 0 | 0 | 0 | 3.604 | 11.33 | 43.36 | 65000 | 2×10 ⁻⁶ | 0.0256 |

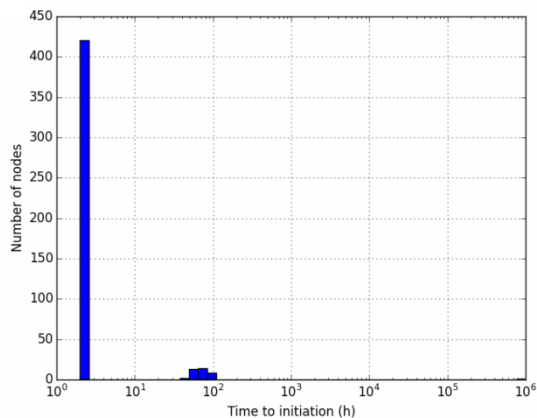


Figure 262 – Histogram of times to initiation predicted for specimen IN170, using the local model.

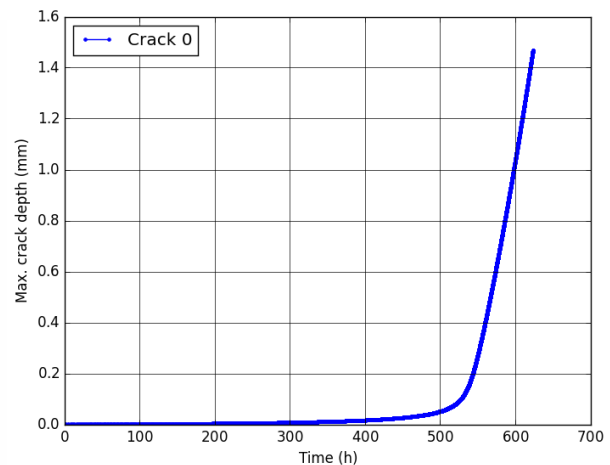


Figure 263 – Cracking kinetics predicted for specimen IN170, using the local model.

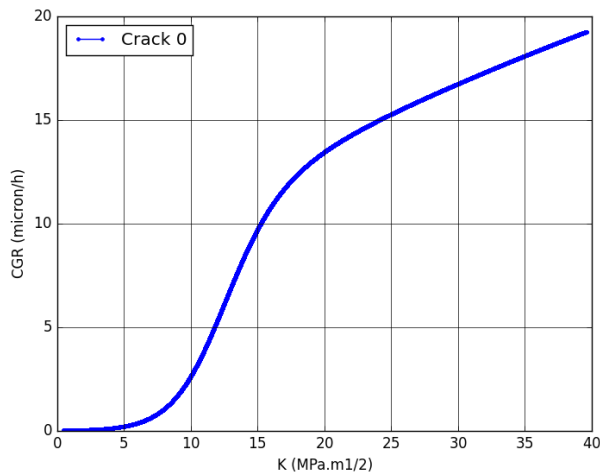


Figure 264 – Crack growth rate versus K at the tip of the main crack predicted for specimen IN170, using the local model.

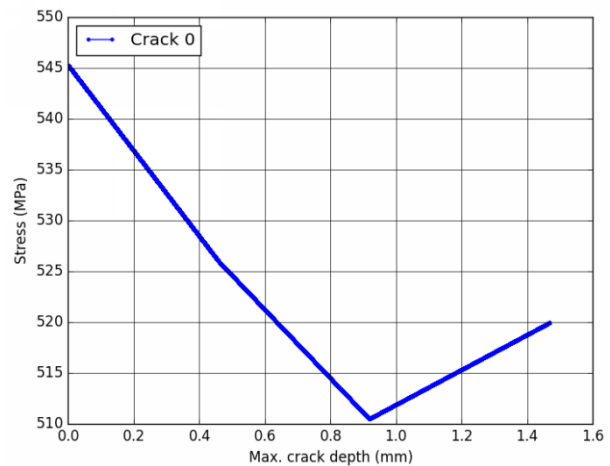


Figure 265 – Stress versus depth at the tip of the main crack predicted for specimen IN170, using the local model.

11.16. Simulations of the test on specimen IN171

11.16.1. Index initiation model with sigmoid CGR law

Parameters of the initiation model named 'index' (Code_Coriolis v2.1.5 intermediate version)

| init1 | init2 | init3 | init4 (j/mol) | init5 | init6 | Init_depth |
|-------|-------|-------|---------------|-------|------------------|------------|
| 1 | 6.8 | 1 | 185000 | 1 | 10 ⁻⁶ | 0.005 |

Parameters of the crack growth model named 'cgr_sigmoid_cw2_h' (Code_Coriolis v2.1.5 intermediate version)

| cgr1 | cgr2 | cgr3 | cgr4 | cgr5 | cgr6 | cgr7 | cgr8 | cgr9 | cgr10 | cgr11 | ecp1 | ecp2 |
|-------------------|------|------|------|------|------|------|-------|-------|-------|-------|--------------------|--------|
| 5×10 ⁴ | 0.5 | 0.66 | 12 | 15 | 0 | 0 | 3.604 | 11.33 | 43.36 | 65000 | 2×10 ⁻⁶ | 0.0256 |

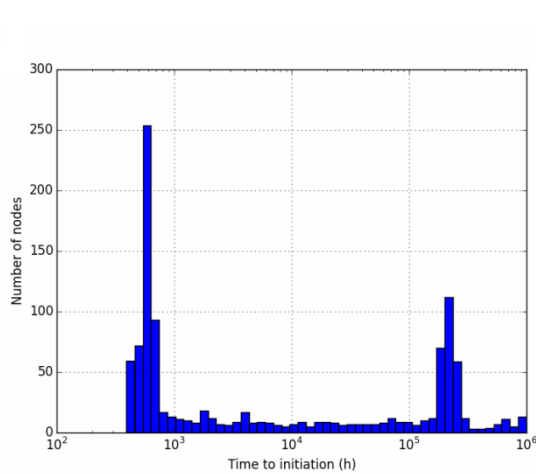


Figure 266 – Histogram of times to initiation predicted for specimen IN171, using the index model.

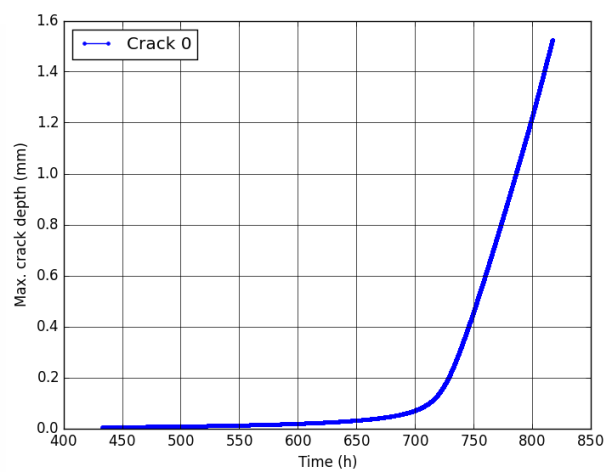


Figure 267 – Cracking kinetics predicted for specimen IN171, using the index model.

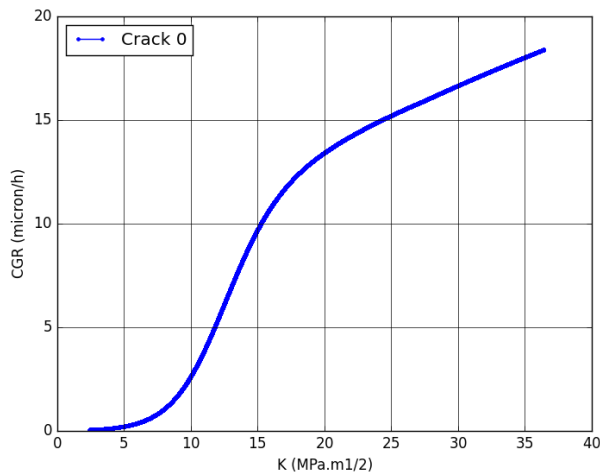


Figure 268 – Crack growth rate versus K at the tip of the main crack predicted for specimen IN171 using the index model.

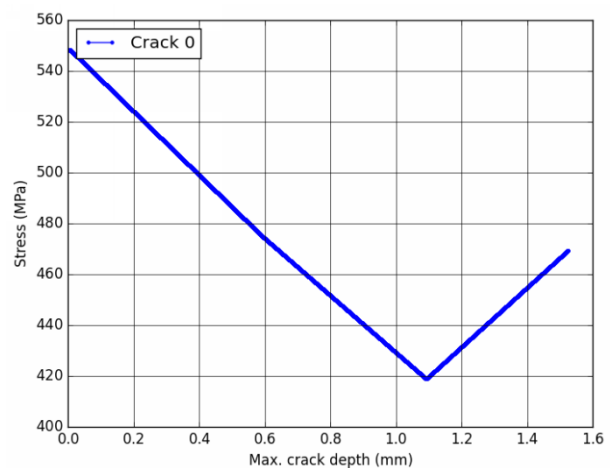


Figure 269 – Stress versus depth at the tip of the main crack predicted for specimen IN171, using the index model.

| | | |
|------------|---|--|
| MAI | Quantitative evaluation of the EDF local model and the EPRI-NRC xLPR models of crack initiation of the weld metals of Alloy 600 (Alloys 82 and 182) | 6125-4501-2018-00583-EN Version 2.0 |
|------------|---|--|

11.16.2. Local initiation model with sigmoid CGR law

Parameters of the initiation model named 'local_initiation_model' (Code_Coriolis v2.1.5 intermediate version)

| Grain boundaries | | | | | | | | | | | | |
|-------------------------------|--------------------------|----------------------|-------------|---------------------|--------------------------|-------------|---------------------|---------|-------------|------|------|------|
| Densite (mm/mm ²) | SfTot (mm ²) | SpaceResolution (nm) | | GBlength (nm) | GBResolution (joints/mm) | | GBC | rC (nm) | zCr (nm) | | | |
| 10 | 1 | 1 | | 200 | 10 | | 0.2 | 30 | 30 | | | |
| Intergranular oxidation | | | | | | | | | | | | |
| x0nom (nm) | bnom | cnom | x0depl (nm) | bdepl | Cdepl | x0carb (nm) | bcarb | Ccarb | oxQ (J/mol) | oxg1 | oxg2 | oxg3 |
| 0 | 1.86×10 ⁷ | 3 | 0 | 2.4×10 ⁷ | 3 | 0 | 2.6×10 ⁷ | 0.01 | 57000 | 0.1 | 0.3 | 0.04 |
| Cracking criterion | | | | | | | | | | | | |
| Poxc (nm) | | SigmaC (MPa) | | | StressLinearCoef | | | | | | | |
| 200 | | 790 | | | 0.25 | | | | | | | |

Parameters of the crack growth model named 'cgr_sigmoid_cw2_h' (Code_Coriolis v2.1.5 intermediate version)

| cgr1 | cgr2 | cgr3 | cgr4 | cgr5 | cgr6 | cgr7 | cgr8 | cgr9 | cgr10 | cgr11 | ecp1 | ecp2 |
|-------------------|------|------|------|------|------|------|-------|-------|-------|-------|--------------------|--------|
| 5×10 ⁴ | 0.5 | 0.66 | 12 | 0 | 0 | 0 | 3.604 | 11.33 | 43.36 | 65000 | 2×10 ⁻⁶ | 0.0256 |

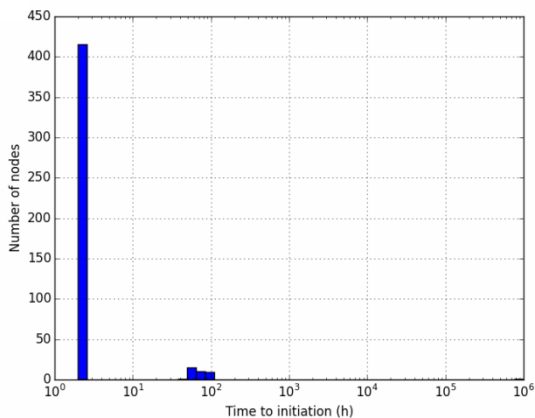


Figure 270 – Histogram of times to initiation predicted for specimen IN171, using the local model.

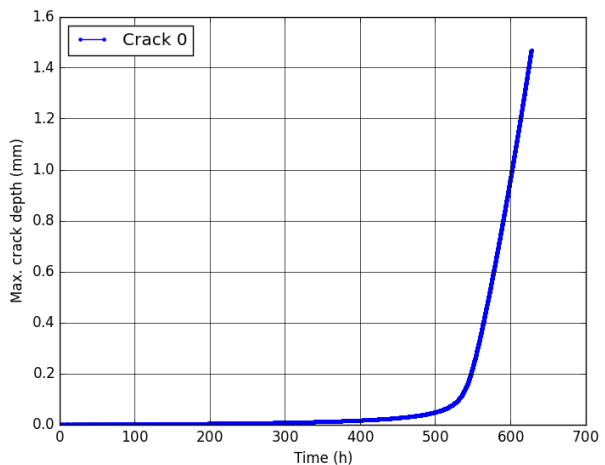


Figure 271 – Cracking kinetics predicted for specimen IN171, using the local model.

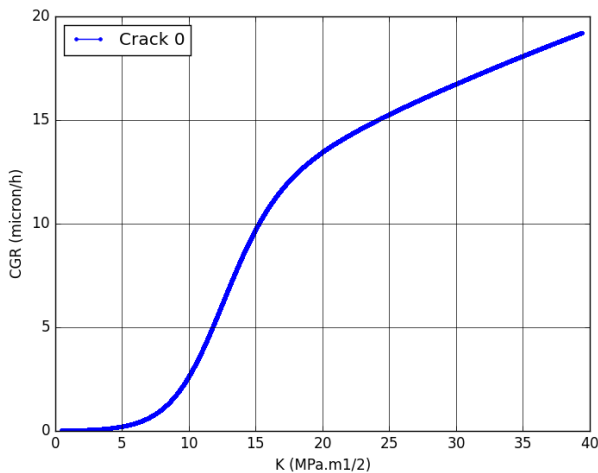


Figure 272 – Crack growth rate versus K at the tip of the main crack predicted for specimen IN171, using the local model.

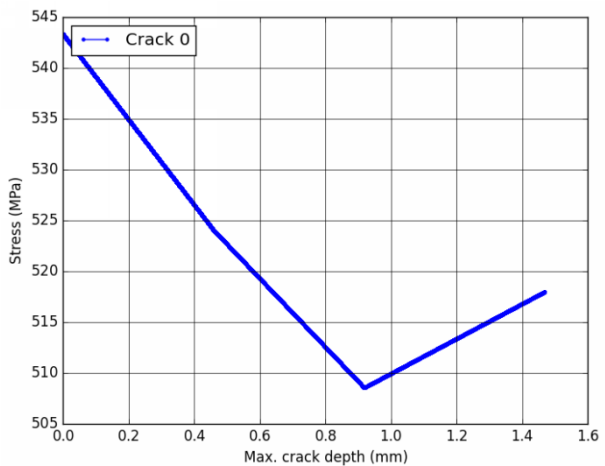


Figure 273 – Stress versus depth at the tip of the main crack predicted for specimen IN171, using the local model.

11.17. Simulations of the test on specimen IN191

11.17.1. Index initiation model with sigmoid CGR law

Parameters of the initiation model named 'index' (Code_Coriolis v2.1.5 intermediate version)

| init1 | init2 | init3 | init4 (J/mol) | init5 | init6 | Init_depth |
|-------|-------|-------|---------------|-------|------------------|------------|
| 1 | 6.8 | 1 | 185000 | 1 | 10 ⁻⁶ | 0.005 |

Parameters of the crack growth model named 'cgr_sigmoid_cw2_h' (Code_Coriolis v2.1.5 intermediate version)

| cgr1 | cgr2 | cgr3 | cgr4 | cgr5 | cgr6 | cgr7 | cgr8 | cgr9 | cgr10 | cgr11 | ecp1 | ecp2 |
|-------------------|------|------|------|------|------|------|-------|-------|-------|-------|--------------------|--------|
| 5×10 ⁴ | 0.5 | 0.66 | 12 | 15 | 0 | 0 | 3.604 | 11.33 | 43.36 | 65000 | 2×10 ⁻⁶ | 0.0256 |

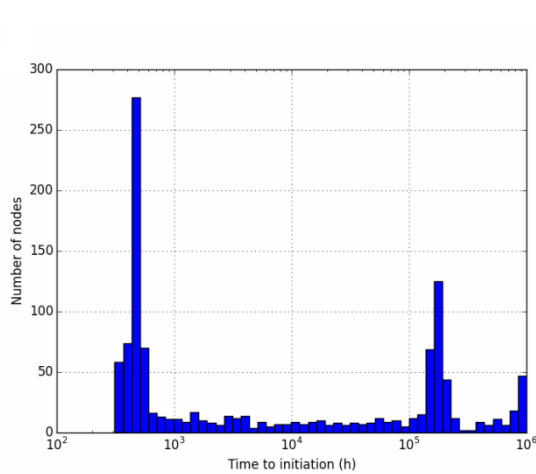


Figure 274 – Histogram of times to initiation predicted for specimen IN191, using the index model.

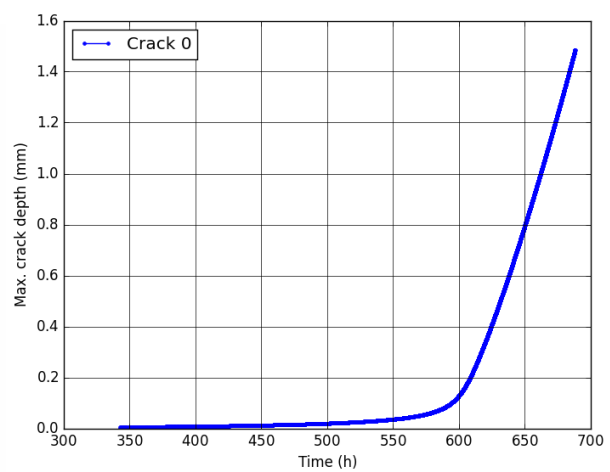


Figure 275 – Cracking kinetics predicted for specimen IN191, using the index model.

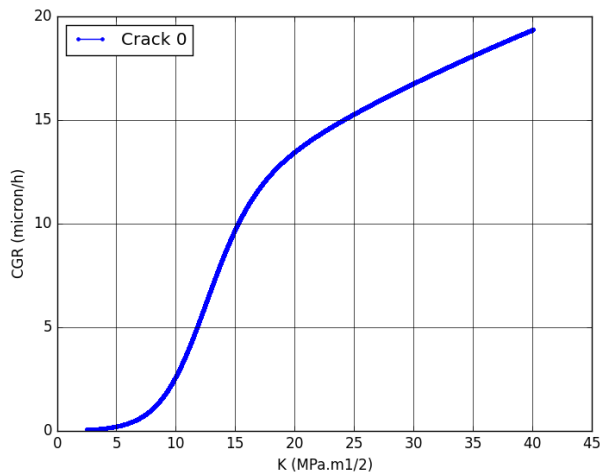


Figure 276 – Crack growth rate versus K at the tip of the main crack predicted for specimen IN191 using the index model.

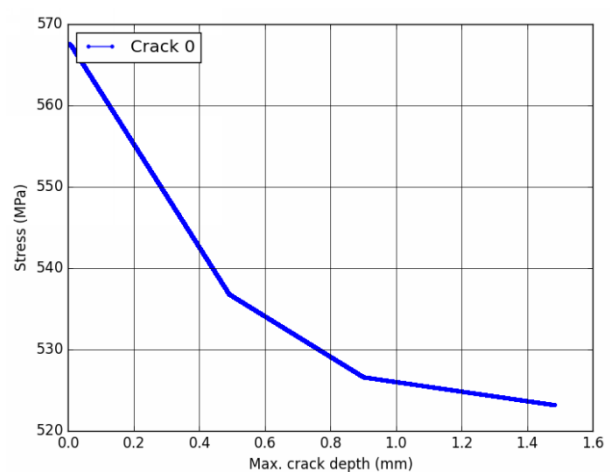


Figure 277 – Stress versus depth at the tip of the main crack predicted for specimen IN191, using the index model.

| | | |
|------------|---|--|
| MAI | Quantitative evaluation of the EDF local model and the EPRI-NRC xLPR models of crack initiation of the weld metals of Alloy 600 (Alloys 82 and 182) | 6125-4501-2018-00583-EN Version 2.0 |
|------------|---|--|

11.17.2. Local initiation model with sigmoid CGR law

Parameters of the initiation model named 'local_initiation_model' (Code_Coriolis v2.1.5 intermediate version)

| Grain boundaries | | | | | | | | | | | | |
|-------------------------------|--------------------------|----------------------|-------------|---------------------|--------------------------|-------------|---------------------|---------|-------------|------|------|------|
| Densite (mm/mm ²) | SfTot (mm ²) | SpaceResolution (nm) | | GBlength (nm) | GBResolution (joints/mm) | | GBC | rC (nm) | zCr (nm) | | | |
| 10 | 1 | 1 | | 200 | 10 | | 0.2 | 30 | 30 | | | |
| Intergranular oxidation | | | | | | | | | | | | |
| x0nom (nm) | bnom | cnom | x0depl (nm) | bdepl | Cdepl | x0carb (nm) | bcarb | Ccarb | oxQ (J/mol) | oxg1 | oxg2 | oxg3 |
| 0 | 1.86×10 ⁷ | 3 | 0 | 2.4×10 ⁷ | 3 | 0 | 2.6×10 ⁷ | 0.01 | 57000 | 0.1 | 0.3 | 0.04 |
| Cracking criterion | | | | | | | | | | | | |
| Poxc (nm) | | SigmaC (MPa) | | | StressLinearCoef | | | | | | | |
| 200 | | 790 | | | 0.25 | | | | | | | |

Parameters of the crack growth model named 'cgr_sigmoid_cw2_h' (Code_Coriolis v2.1.5 intermediate version)

| cgr1 | cgr2 | cgr3 | cgr4 | cgr5 | cgr6 | cgr7 | cgr8 | cgr9 | cgr10 | cgr11 | ecp1 | ecp2 |
|-------------------|------|------|------|------|------|------|-------|-------|-------|-------|--------------------|--------|
| 5×10 ⁴ | 0.5 | 0.66 | 12 | 0 | 0 | 0 | 3.604 | 11.33 | 43.36 | 65000 | 2×10 ⁻⁶ | 0.0256 |

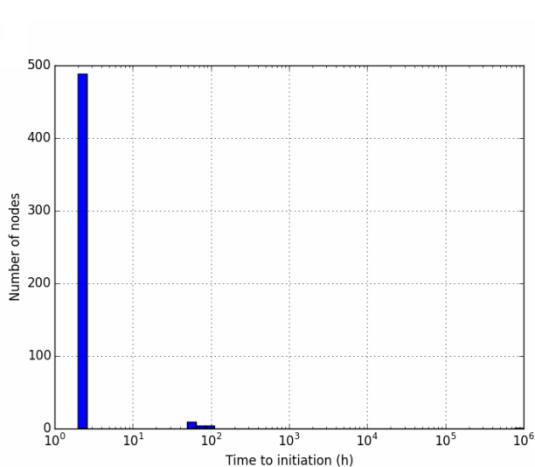


Figure 278 – Histogram of times to initiation predicted for specimen IN191, using the local model.

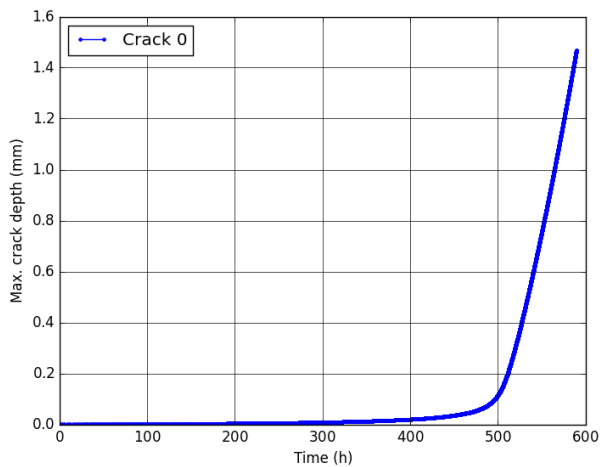


Figure 279 – Cracking kinetics predicted for specimen IN191, using the local model.

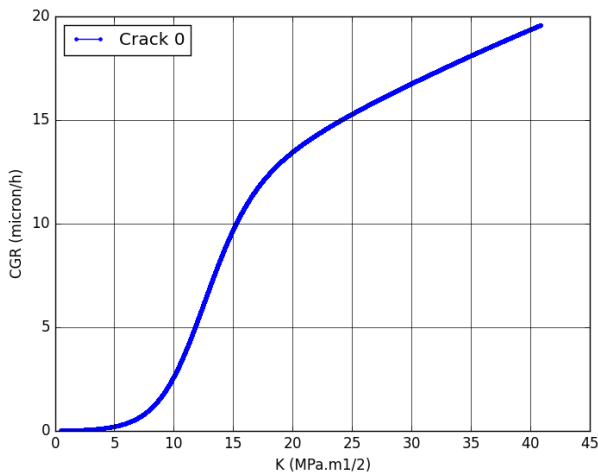


Figure 280 – Crack growth rate versus K at the tip of the main crack predicted for specimen IN191, using the local model.

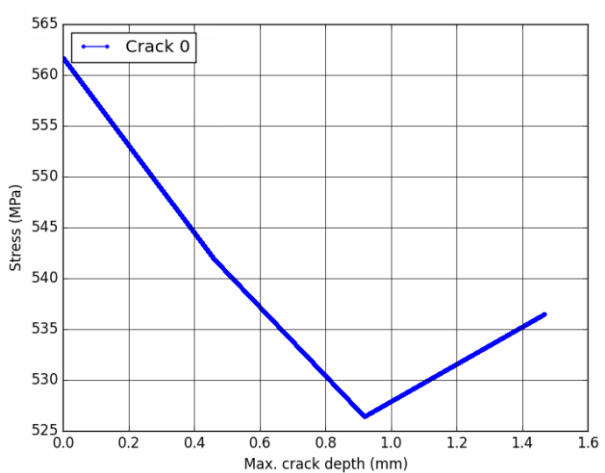


Figure 281 – Stress versus depth at the tip of the main crack predicted for specimen IN191, using the local model.

11.18. Simulations of the test on specimen IN192

11.18.1. Index initiation model with sigmoid CGR law

Parameters of the initiation model named 'index' (Code_Coriolis v2.1.5 intermediate version)

| init1 | init2 | init3 | init4 (j/mol) | init5 | init6 | Init_depth |
|-------|-------|-------|---------------|-------|------------------|------------|
| 1 | 6.8 | 1 | 185000 | 1 | 10 ⁻⁶ | 0.005 |

Parameters of the crack growth model named 'cgr_sigmoid_cw2_h' (Code_Coriolis v2.1.5 intermediate version)

| cgr1 | cgr2 | cgr3 | cgr4 | cgr5 | cgr6 | cgr7 | cgr8 | cgr9 | cgr10 | cgr11 | ecp1 | ecp2 |
|-------------------|------|------|------|------|------|------|-------|-------|-------|-------|--------------------|--------|
| 5×10 ⁴ | 0.5 | 0.66 | 12 | 15 | 0 | 0 | 3.604 | 11.33 | 43.36 | 65000 | 2×10 ⁻⁶ | 0.0256 |

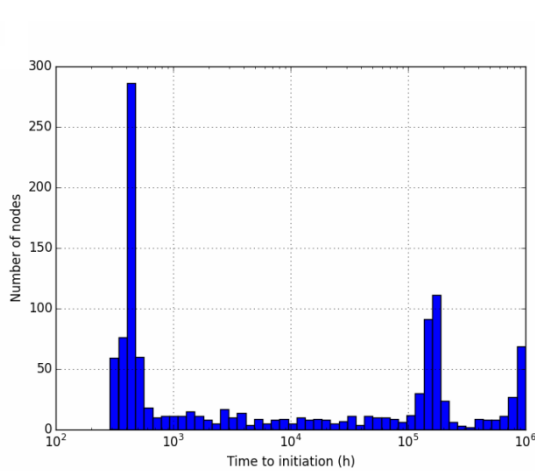


Figure 282 – Histogram of times to initiation predicted for specimen IN192, using the index model.

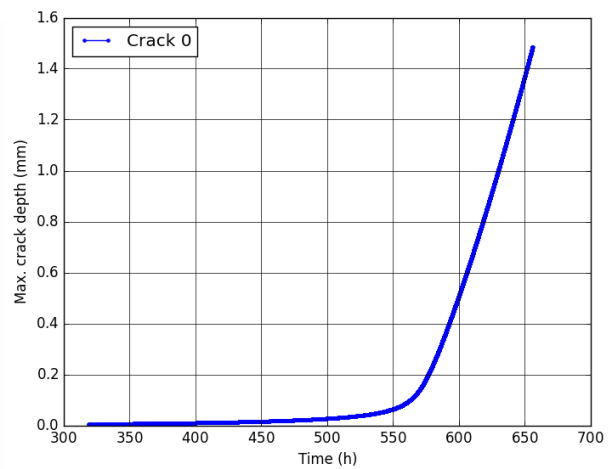


Figure 283 – Cracking kinetics predicted for specimen IN192, using the index model.

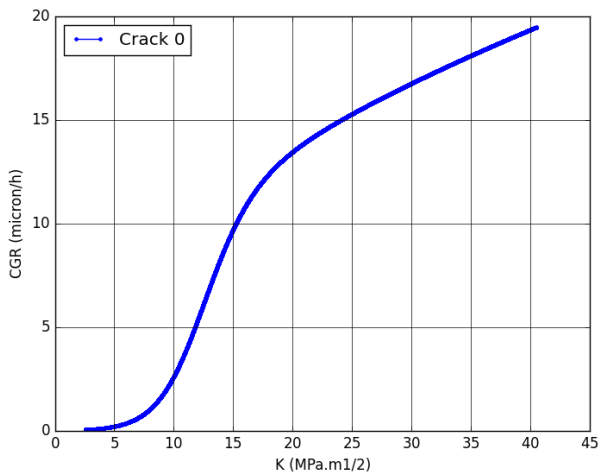


Figure 284 – Crack growth rate versus K at the tip of the main crack predicted for specimen IN192 using the index model.

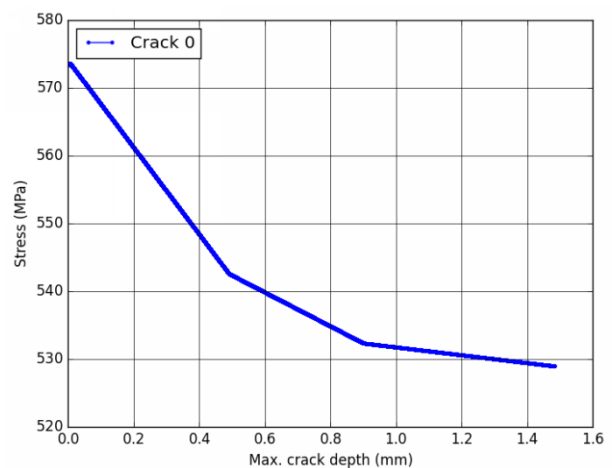


Figure 285 – Stress versus depth at the tip of the main crack predicted for specimen IN192, using the index model.

| | | |
|------------|---|--|
| MAI | Quantitative evaluation of the EDF local model and the EPRI-NRC xLPR models of crack initiation of the weld metals of Alloy 600 (Alloys 82 and 182) | 6125-4501-2018-00583-EN Version 2.0 |
|------------|---|--|

11.18.2. Local initiation model with sigmoid CGR law

Parameters of the initiation model named 'local_initiation_model' (Code_Coriolis v2.1.5 intermediate version)

| Grain boundaries | | | | | | | | | | | | |
|-------------------------------|--------------------------|----------------------|---------------|--------------------------|------------------|-------------|---------------------|-------|-------------|------|------|------|
| Densite (mm/mm ²) | SfTot (mm ²) | SpaceResolution (nm) | GBlength (nm) | GBResolution (joints/mm) | GBC | rC (nm) | zCr (nm) | | | | | |
| 10 | 1 | 1 | 200 | 10 | 0.2 | 30 | 30 | | | | | |
| Intergranular oxidation | | | | | | | | | | | | |
| x0nom (nm) | bnom | cnom | x0depl (nm) | bdepl | Cdepl | x0carb (nm) | bcarb | Ccarb | oxQ (J/mol) | oxg1 | oxg2 | oxg3 |
| 0 | 1.86×10 ⁷ | 3 | 0 | 2.4×10 ⁷ | 3 | 0 | 2.6×10 ⁷ | 0.01 | 57000 | 0.1 | 0.3 | 0.04 |
| Cracking criterion | | | | | | | | | | | | |
| Poxc (nm) | SigmaC (MPa) | | | | StressLinearCoef | | | | | | | |
| 200 | 790 | | | | 0.25 | | | | | | | |

Parameters of the crack growth model named 'cgr_sigmoid_cw2_h' (Code_Coriolis v2.1.5 intermediate version)

| cgr1 | cgr2 | cgr3 | cgr4 | cgr5 | cgr6 | cgr7 | cgr8 | cgr9 | cgr10 | cgr11 | ecp1 | ecp2 |
|-------------------|------|------|------|------|------|------|-------|-------|-------|-------|--------------------|--------|
| 5×10 ⁴ | 0.5 | 0.66 | 12 | 0 | 0 | 0 | 3.604 | 11.33 | 43.36 | 65000 | 2×10 ⁻⁶ | 0.0256 |

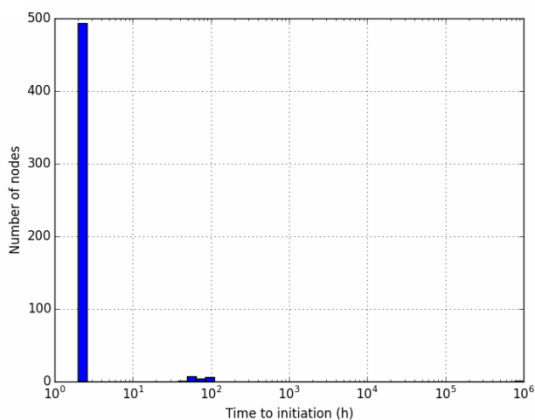


Figure 286 – Histogram of times to initiation predicted for specimen IN192, using the local model.

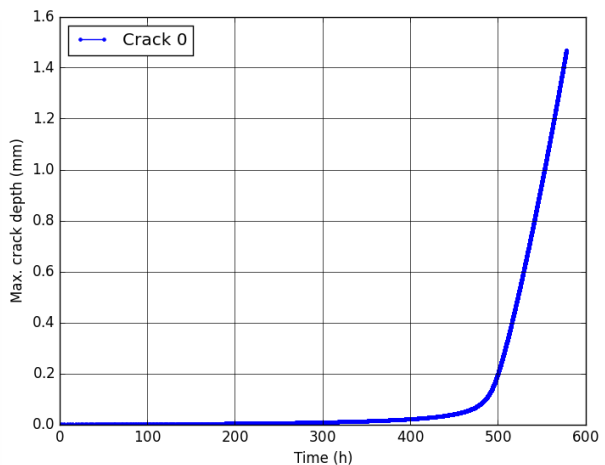


Figure 287 – Cracking kinetics predicted for specimen IN192, using the local model.

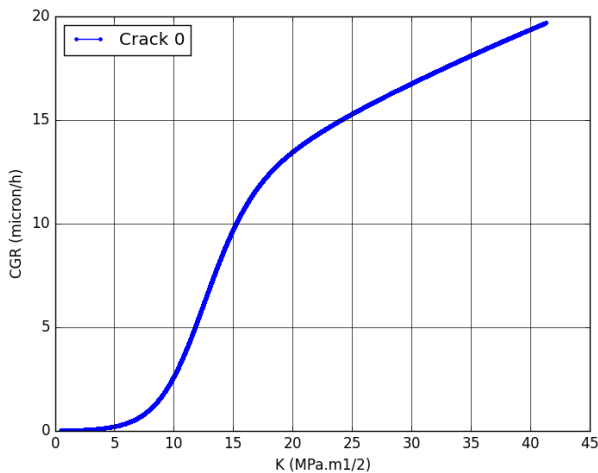


Figure 288 – Crack growth rate versus K at the tip of the main crack predicted for specimen IN192, using the local model.

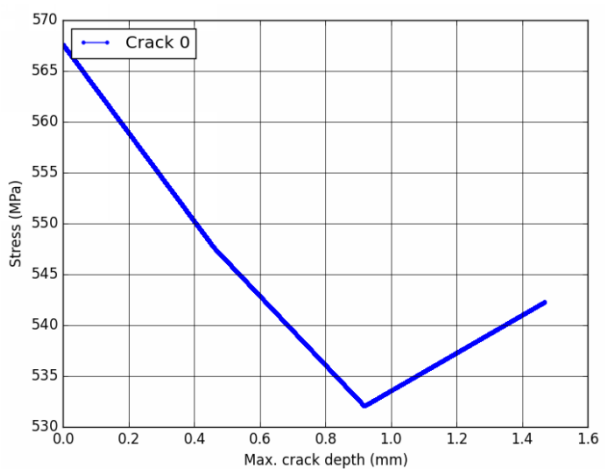


Figure 289 – Stress versus depth at the tip of the main crack predicted for specimen IN192, using the local model.

11.19. Simulations of the test on specimen IN193

11.19.1. Index initiation model with sigmoid CGR law

Parameters of the initiation model named 'index' (Code_Coriolis v2.1.5 intermediate version)

| init1 | init2 | init3 | init4 (j/mol) | init5 | init6 | Init_depth |
|-------|-------|-------|---------------|-------|------------------|------------|
| 1 | 6.8 | 1 | 185000 | 1 | 10 ⁻⁶ | 0.005 |

Parameters of the crack growth model named 'cgr_sigmoid_cw2_h' (Code_Coriolis v2.1.5 intermediate version)

| cgr1 | cgr2 | cgr3 | cgr4 | cgr5 | cgr6 | cgr7 | cgr8 | cgr9 | cgr10 | cgr11 | ecp1 | ecp2 |
|-------------------|------|------|------|------|------|------|-------|-------|-------|-------|--------------------|--------|
| 5×10 ⁴ | 0.5 | 0.66 | 12 | 15 | 0 | 0 | 3.604 | 11.33 | 43.36 | 65000 | 2×10 ⁻⁶ | 0.0256 |

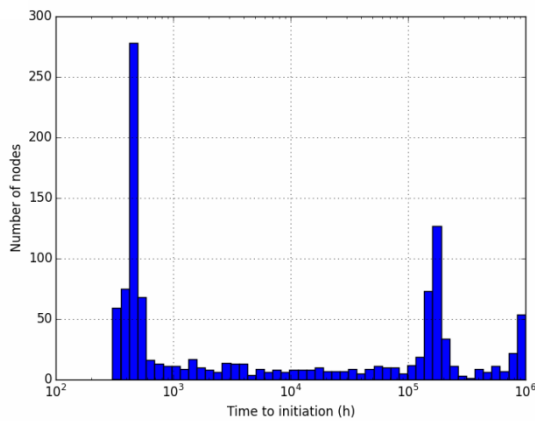


Figure 290 – Histogram of times to initiation predicted for specimen IN193, using the index model.

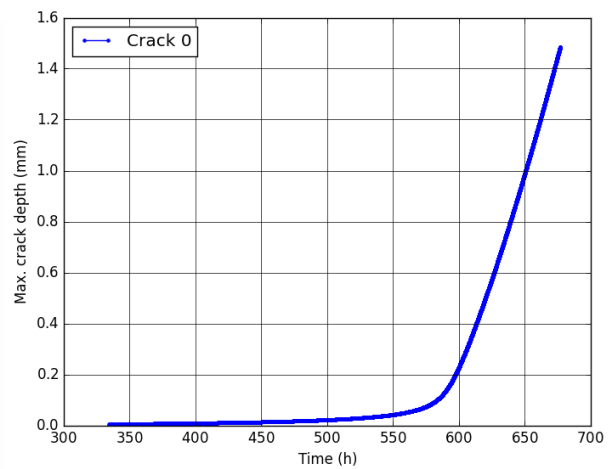


Figure 291 – Cracking kinetics predicted for specimen IN193, using the index model.

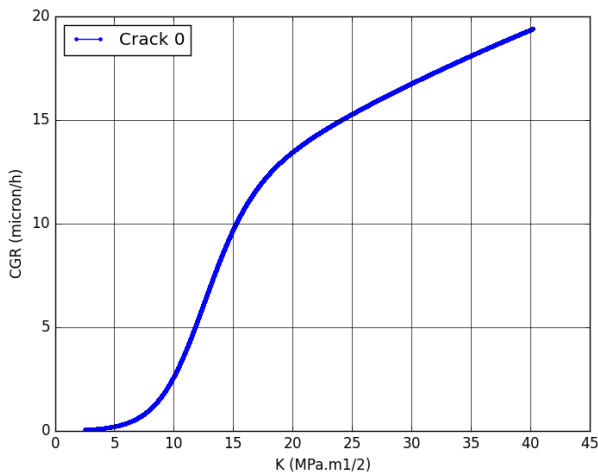


Figure 292 – Crack growth rate versus K at the tip of the main crack predicted for specimen IN193 using the index model.

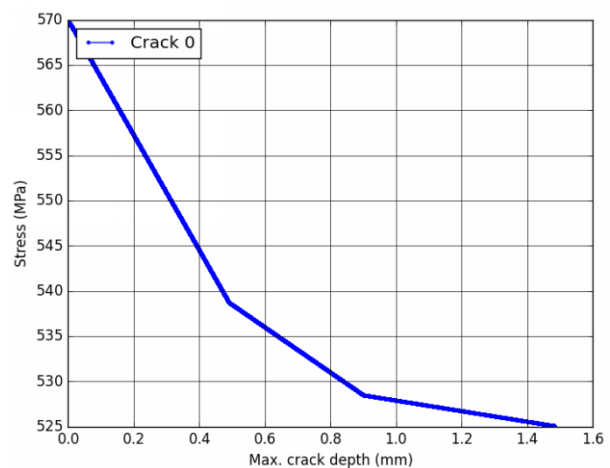


Figure 293 – Stress versus depth at the tip of the main crack predicted for specimen IN193, using the index model.

| | | |
|------------|---|--|
| MAI | Quantitative evaluation of the EDF local model and the EPRI-NRC xLPR models of crack initiation of the weld metals of Alloy 600 (Alloys 82 and 182) | 6125-4501-2018-00583-EN Version 2.0 |
|------------|---|--|

11.19.2. Local initiation model with sigmoid CGR law

Parameters of the initiation model named 'local_initiation_model' (Code_Coriolis v2.1.5 intermediate version)

| Grain boundaries | | | | | | | | | | | | |
|-------------------------------|--------------------------|----------------------|---------------|--------------------------|------------------|-------------|---------------------|-------|-------------|------|------|------|
| Densite (mm/mm ²) | SfTot (mm ²) | SpaceResolution (nm) | GBlength (nm) | GBResolution (joints/mm) | GBC | rC (nm) | zCr (nm) | | | | | |
| 10 | 1 | 1 | 200 | 10 | 0.2 | 30 | 30 | | | | | |
| Intergranular oxidation | | | | | | | | | | | | |
| x0nom (nm) | bnom | cnom | x0depl (nm) | bdepl | Cdepl | x0carb (nm) | bcarb | Ccarb | oxQ (J/mol) | oxg1 | oxg2 | oxg3 |
| 0 | 1.86×10 ⁷ | 3 | 0 | 2.4×10 ⁷ | 3 | 0 | 2.6×10 ⁷ | 0.01 | 57000 | 0.1 | 0.3 | 0.04 |
| Cracking criterion | | | | | | | | | | | | |
| Poxc (nm) | SigmaC (MPa) | | | | StressLinearCoef | | | | | | | |
| 200 | 790 | | | | 0.25 | | | | | | | |

Parameters of the crack growth model named 'cgr_sigmoid_cw2_h' (Code_Coriolis v2.1.5 intermediate version)

| cgr1 | cgr2 | cgr3 | cgr4 | cgr5 | cgr6 | cgr7 | cgr8 | cgr9 | cgr10 | cgr11 | ecp1 | ecp2 |
|-------------------|------|------|------|------|------|------|-------|-------|-------|-------|--------------------|--------|
| 5×10 ⁴ | 0.5 | 0.66 | 12 | 0 | 0 | 0 | 3.604 | 11.33 | 43.36 | 65000 | 2×10 ⁻⁶ | 0.0256 |

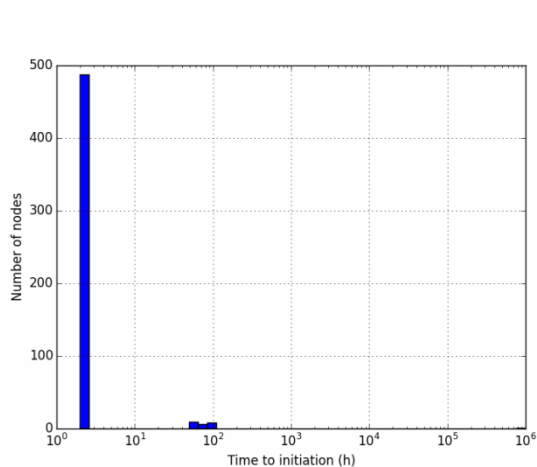


Figure 294 – Histogram of times to initiation predicted for specimen IN193, using the local model.

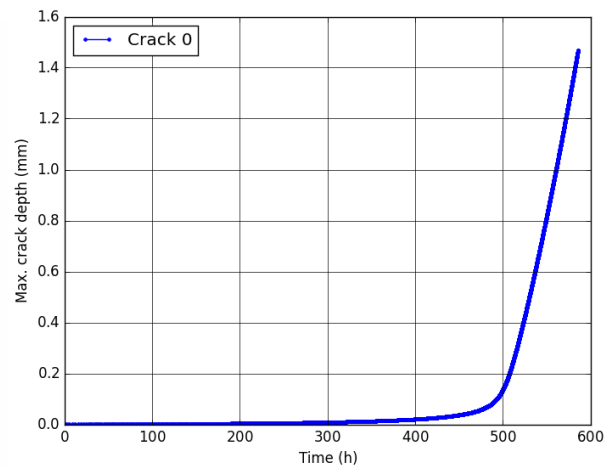


Figure 295 – Cracking kinetics predicted for specimen IN193, using the local model.

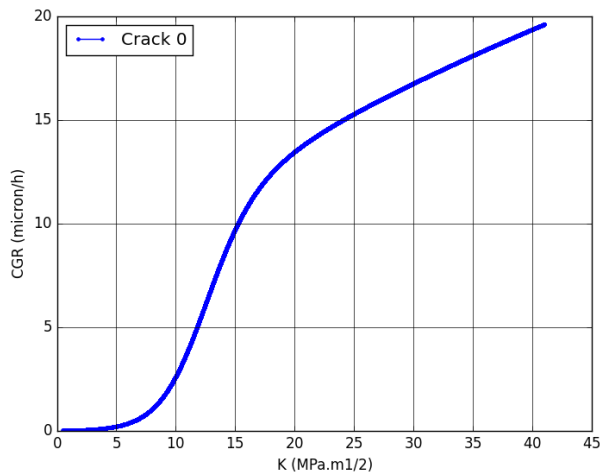


Figure 296 – Crack growth rate versus K at the tip of the main crack predicted for specimen IN193, using the local model.

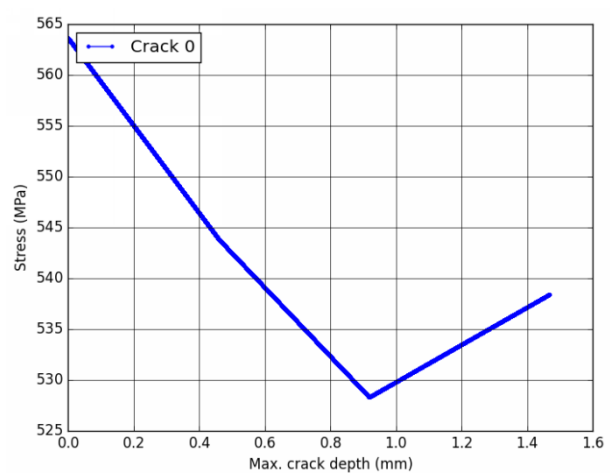


Figure 297 – Stress versus depth at the tip of the main crack predicted for specimen IN193, using the local model.

11.20. Simulations of the test on specimen IN233

11.20.1. Index initiation model with sigmoid CGR law

Parameters of the initiation model named 'index' (Code_Coriolis v2.1.5 intermediate version)

| init1 | init2 | init3 | init4 (j/mol) | init5 | init6 | Init_depth |
|-------|-------|-------|---------------|-------|------------------|------------|
| 1 | 6.8 | 1 | 185000 | 1 | 10 ⁻⁶ | 0.005 |

Parameters of the crack growth model named 'cgr_sigmoid_cw2_h' (Code_Coriolis v2.1.5 intermediate version)

| cgr1 | cgr2 | cgr3 | cgr4 | cgr5 | cgr6 | cgr7 | cgr8 | cgr9 | cgr10 | cgr11 | ecp1 | ecp2 |
|-------------------|------|------|------|------|------|------|-------|-------|-------|-------|--------------------|--------|
| 5×10 ⁴ | 0.5 | 0.66 | 12 | 15 | 0 | 0 | 3.604 | 11.33 | 43.36 | 65000 | 2×10 ⁻⁶ | 0.0256 |

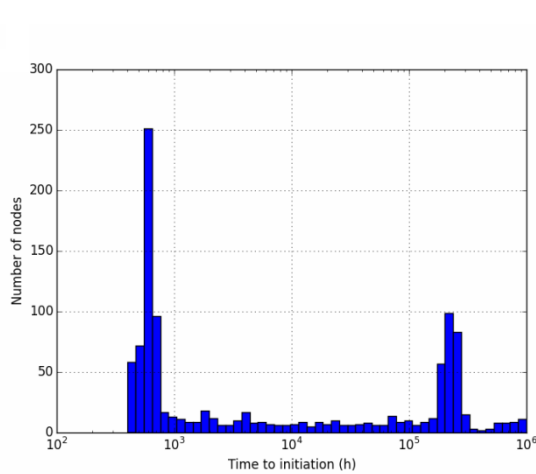


Figure 298 – Histogram of times to initiation predicted for specimen IN233, using the index model.

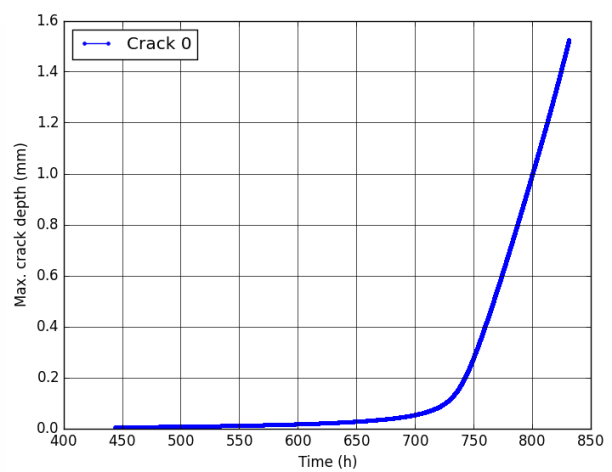


Figure 299 – Cracking kinetics predicted for specimen IN233, using the index model.

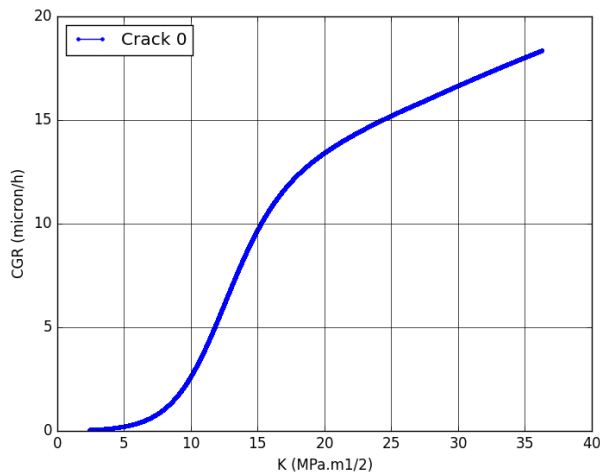


Figure 300 – Crack growth rate versus K at the tip of the main crack predicted for specimen IN233 using the index model.

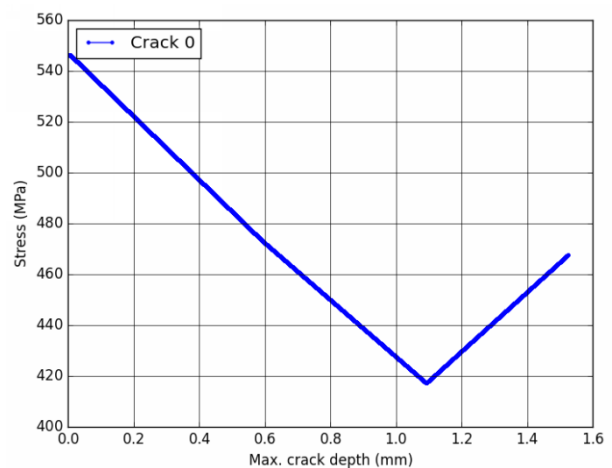


Figure 301 – Stress versus depth at the tip of the main crack predicted for specimen IN233, using the index model.

| | | |
|-----|---|--|
| MAI | Quantitative evaluation of the EDF local model and the EPRI-NRC xLPR models of crack initiation of the weld metals of Alloy 600 (Alloys 82 and 182) | 6125-4501-2018-00583-EN Version 2.0 |
|-----|---|--|

11.20.2. Local initiation model with sigmoid CGR law

Parameters of the initiation model named 'local_initiation_model' (Code_Coriolis v2.1.5 intermediate version)

| Grain boundaries | | | | | | | | | | | | |
|-------------------------------|--------------------------|----------------------|--------------|---------------------|--------------------------|------------------|---------------------|---------|-------------|------|------|------|
| Densite (mm/mm ²) | SfTot (mm ²) | SpaceResolution (nm) | | GBlength (nm) | GBResolution (joints/mm) | | GBC | rC (nm) | zCr (nm) | | | |
| 10 | 1 | 1 | | 200 | 10 | | 0.2 | 30 | 30 | | | |
| Intergranular oxidation | | | | | | | | | | | | |
| x0nom (nm) | bnom | cnom | x0depl (nm) | bdepl | Cdepl | x0carb (nm) | bcarb | Ccarb | oxQ (J/mol) | oxg1 | oxg2 | oxg3 |
| 0 | 1.86×10 ⁷ | 3 | 0 | 2.4×10 ⁷ | 3 | 0 | 2.6×10 ⁷ | 0.01 | 57000 | 0.1 | 0.3 | 0.04 |
| Cracking criterion | | | | | | | | | | | | |
| Poxc (nm) | | | SigmaC (MPa) | | | StressLinearCoef | | | | | | |
| 200 | | | 790 | | | 0.25 | | | | | | |

Parameters of the crack growth model named 'cgr_sigmoid_cw2_h' (Code_Coriolis v2.1.5 intermediate version)

| cgr1 | cgr2 | cgr3 | cgr4 | cgr5 | cgr6 | cgr7 | cgr8 | cgr9 | cgr10 | cgr11 | ecp1 | ecp2 |
|-------------------|------|------|------|------|------|------|-------|-------|-------|-------|--------------------|--------|
| 5×10 ⁴ | 0.5 | 0.66 | 12 | 0 | 0 | 0 | 3.604 | 11.33 | 43.36 | 65000 | 2×10 ⁻⁶ | 0.0256 |

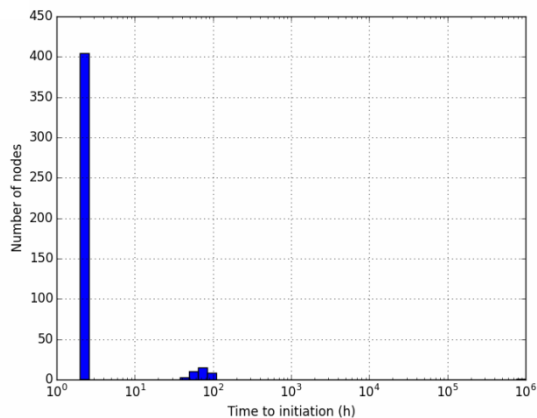


Figure 302 – Histogram of times to initiation predicted for specimen IN233, using the local model.

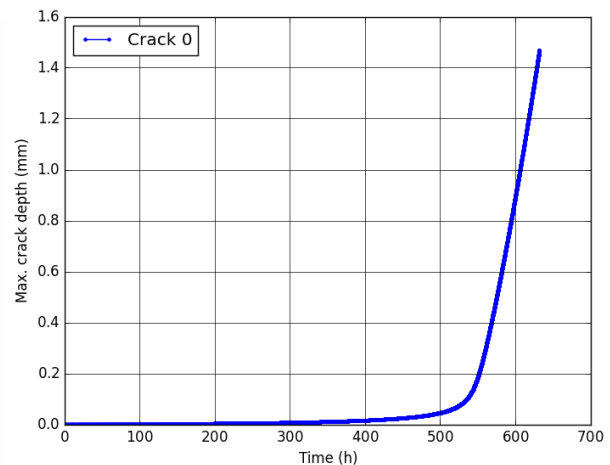


Figure 303 – Cracking kinetics predicted for specimen IN233, using the local model.

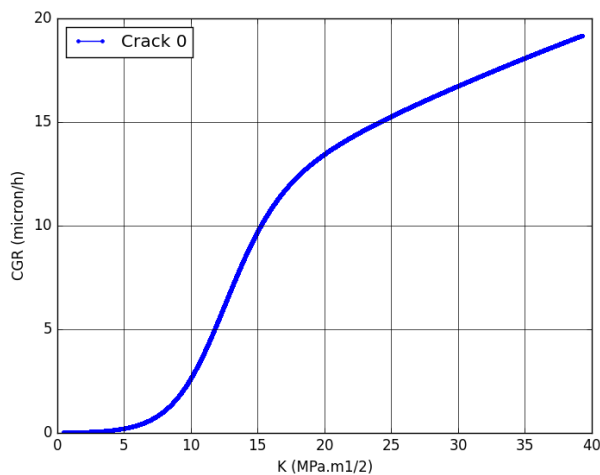


Figure 304 – Crack growth rate versus K at the tip of the main crack predicted for specimen IN233, using the local model.

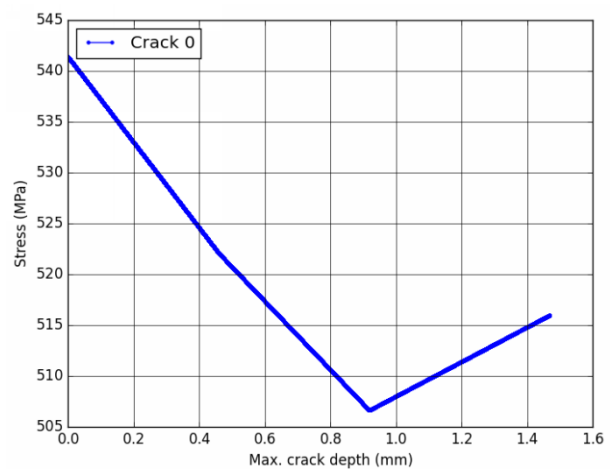


Figure 305 – Stress versus depth at the tip of the main crack predicted for specimen IN233, using the local model.

11.21. Simulations of the test on specimen IN234

11.21.1. Index initiation model with sigmoid CGR law

Parameters of the initiation model named 'index' (Code_Coriolis v2.1.5 intermediate version)

| init1 | init2 | init3 | init4 (j/mol) | init5 | init6 | Init_depth |
|-------|-------|-------|---------------|-------|------------------|------------|
| 1 | 6.8 | 1 | 185000 | 1 | 10 ⁻⁶ | 0.005 |

Parameters of the crack growth model named 'cgr_sigmoid_cw2_h' (Code_Coriolis v2.1.5 intermediate version)

| cgr1 | cgr2 | cgr3 | cgr4 | cgr5 | cgr6 | cgr7 | cgr8 | cgr9 | cgr10 | cgr11 | ecp1 | ecp2 |
|-------------------|------|------|------|------|------|------|-------|-------|-------|-------|--------------------|--------|
| 5×10 ⁴ | 0.5 | 0.66 | 12 | 15 | 0 | 0 | 3.604 | 11.33 | 43.36 | 65000 | 2×10 ⁻⁶ | 0.0256 |

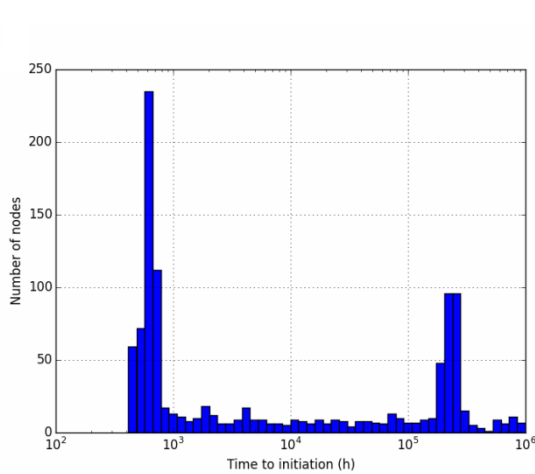


Figure 306 – Histogram of times to initiation predicted for specimen IN234, using the index model.

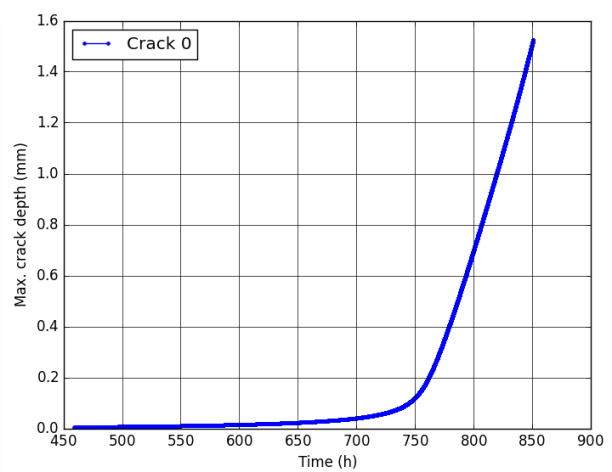


Figure 307 – Cracking kinetics predicted for specimen IN234, using the index model.

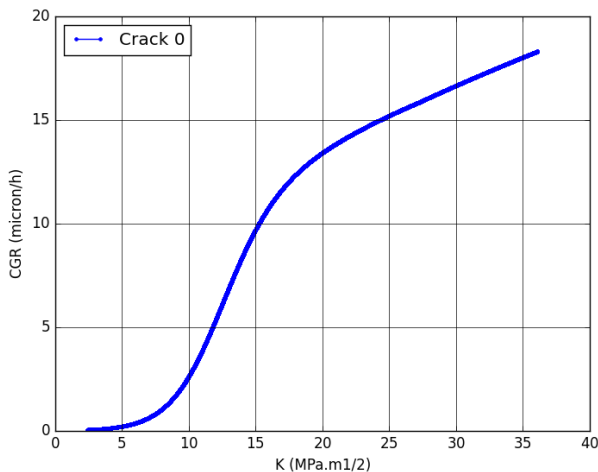


Figure 308 – Crack growth rate versus K at the tip of the main crack predicted for specimen IN234 using the index model.

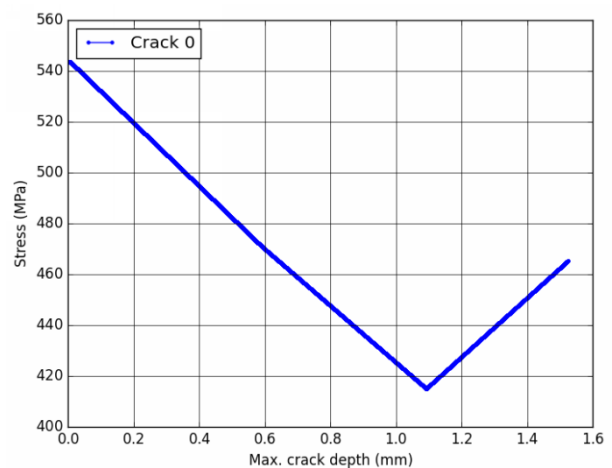


Figure 309 – Stress versus depth at the tip of the main crack predicted for specimen IN234, using the index model.

| | | |
|------------|---|--|
| MAI | Quantitative evaluation of the EDF local model and the EPRI-NRC xLPR models of crack initiation of the weld metals of Alloy 600 (Alloys 82 and 182) | 6125-4501-2018-00583-EN Version 2.0 |
|------------|---|--|

11.21.2. Local initiation model with sigmoid CGR law

Parameters of the initiation model named 'local_initiation_model' (Code_Coriolis v2.1.5 intermediate version)

| Grain boundaries | | | | | | | | | | | | |
|-------------------------------|--------------------------|----------------------|-------------|---------------------|--------------------------|-------------|---------------------|---------|-------------|------|------|------|
| Densite (mm/mm ²) | SfTot (mm ²) | SpaceResolution (nm) | | GBlength (nm) | GBResolution (joints/mm) | | GBC | rC (nm) | zCr (nm) | | | |
| 10 | 1 | 1 | | 200 | 10 | | 0.2 | 30 | 30 | | | |
| Intergranular oxidation | | | | | | | | | | | | |
| x0nom (nm) | bnom | cnom | x0depl (nm) | bdepl | Cdepl | x0carb (nm) | bcarb | Ccarb | oxQ (J/mol) | oxg1 | oxg2 | oxg3 |
| 0 | 1.86×10 ⁷ | 3 | 0 | 2.4×10 ⁷ | 3 | 0 | 2.6×10 ⁷ | 0.01 | 57000 | 0.1 | 0.3 | 0.04 |
| Cracking criterion | | | | | | | | | | | | |
| Poxc (nm) | | SigmaC (MPa) | | | StressLinearCoef | | | | | | | |
| 200 | | 790 | | | 0.25 | | | | | | | |

Parameters of the crack growth model named 'cgr_sigmoid_cw2_h' (Code_Coriolis v2.1.5 intermediate version)

| cgr1 | cgr2 | cgr3 | cgr4 | cgr5 | cgr6 | cgr7 | cgr8 | cgr9 | cgr10 | cgr11 | ecp1 | ecp2 |
|-------------------|------|------|------|------|------|------|-------|-------|-------|-------|--------------------|--------|
| 5×10 ⁴ | 0.5 | 0.66 | 12 | 0 | 0 | 0 | 3.604 | 11.33 | 43.36 | 65000 | 2×10 ⁻⁶ | 0.0256 |

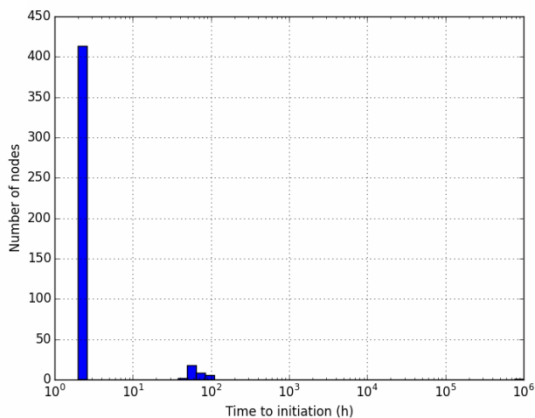


Figure 310 – Histogram of times to initiation predicted for specimen IN234, using the local model.

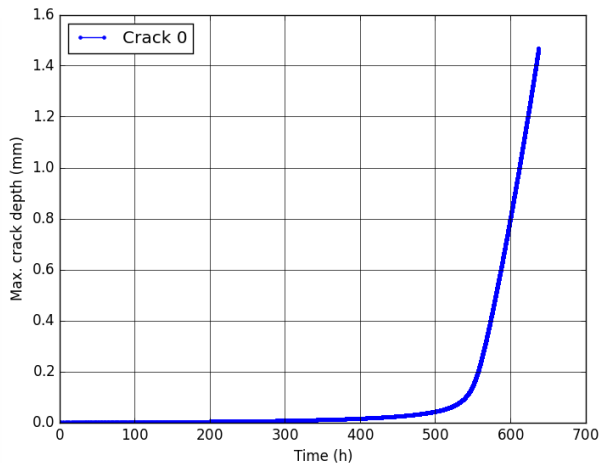


Figure 311 – Cracking kinetics predicted for specimen IN234, using the local model.

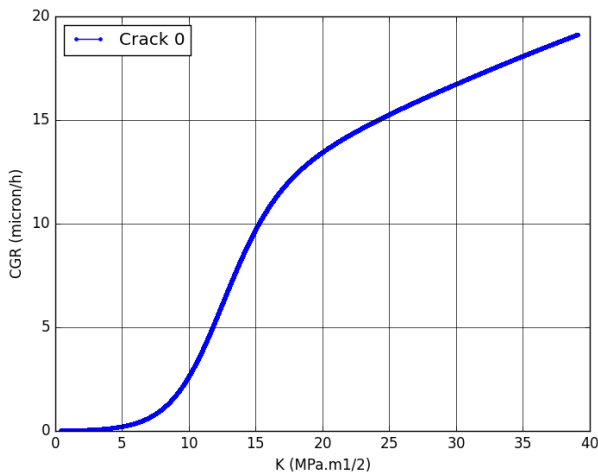


Figure 312 – Crack growth rate versus K at the tip of the main crack predicted for specimen IN234, using the local model.

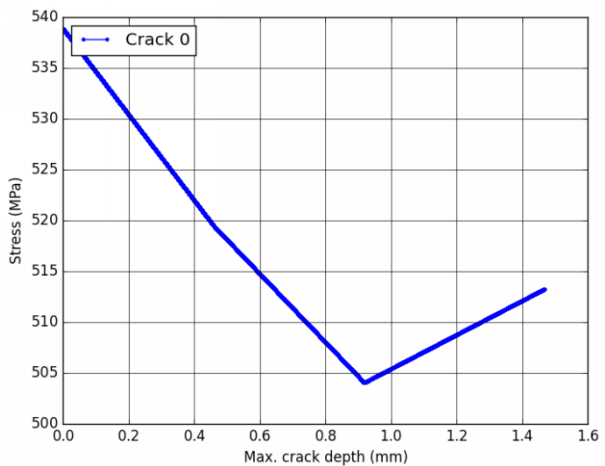


Figure 313 – Stress versus depth at the tip of the main crack predicted for specimen IN234, using the local model.

11.22. Simulations of the test on specimen IN235

11.22.1. Index initiation model with sigmoid CGR law

Parameters of the initiation model named 'index' (Code_Coriolis v2.1.5 intermediate version)

| init1 | init2 | init3 | init4 (j/mol) | init5 | init6 | Init_depth |
|-------|-------|-------|---------------|-------|------------------|------------|
| 1 | 6.8 | 1 | 185000 | 1 | 10 ⁻⁶ | 0.005 |

Parameters of the crack growth model named 'cgr_sigmoid_cw2_h' (Code_Coriolis v2.1.5 intermediate version)

| cgr1 | cgr2 | cgr3 | cgr4 | cgr5 | cgr6 | cgr7 | cgr8 | cgr9 | cgr10 | cgr11 | ecp1 | ecp2 |
|-------------------|------|------|------|------|------|------|-------|-------|-------|-------|--------------------|--------|
| 5×10 ⁴ | 0.5 | 0.66 | 12 | 15 | 0 | 0 | 3.604 | 11.33 | 43.36 | 65000 | 2×10 ⁻⁶ | 0.0256 |

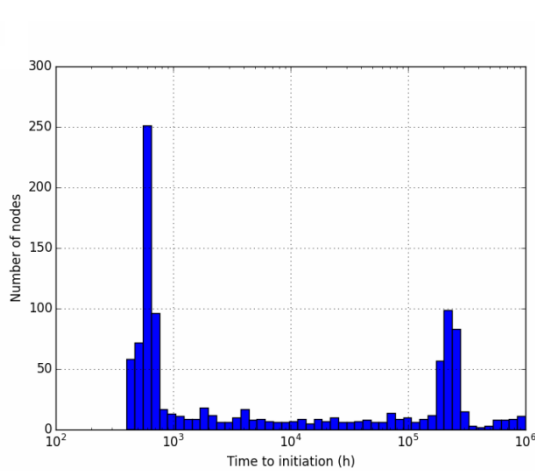


Figure 314 – Histogram of times to initiation predicted for specimen IN235, using the index model.

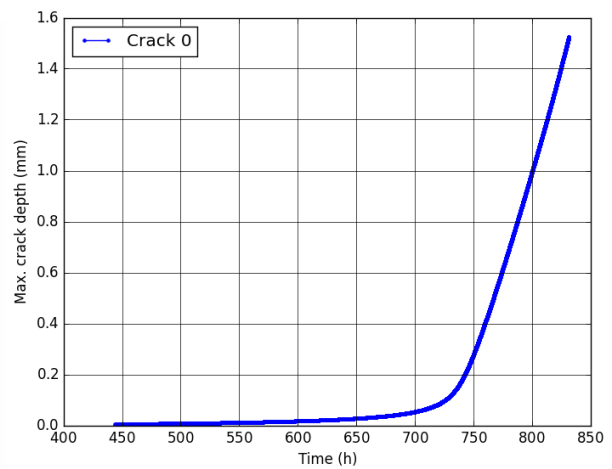


Figure 315 – Cracking kinetics predicted for specimen IN235, using the index model.

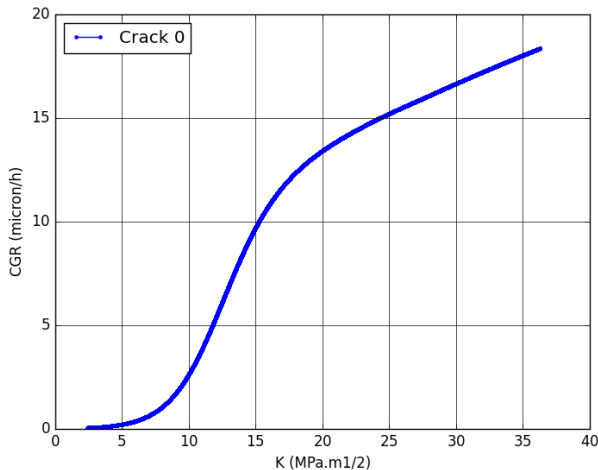


Figure 316 – Crack growth rate versus K at the tip of the main crack predicted for specimen IN235 using the index model.

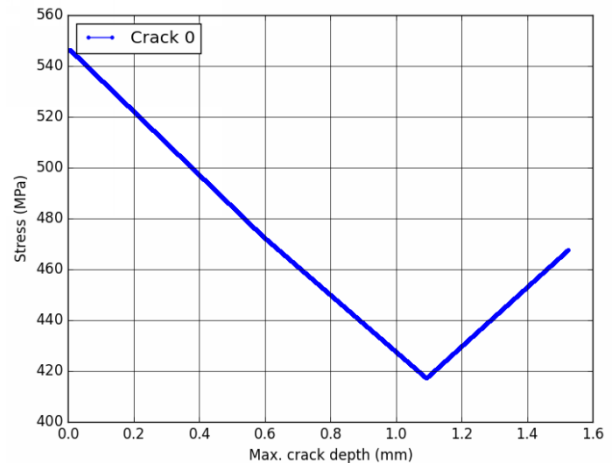


Figure 317 – Stress versus depth at the tip of the main crack predicted for specimen IN235, using the index model.

| | | |
|------------|---|--|
| MAI | Quantitative evaluation of the EDF local model and the EPRI-NRC xLPR models of crack initiation of the weld metals of Alloy 600 (Alloys 82 and 182) | 6125-4501-2018-00583-EN Version 2.0 |
|------------|---|--|

11.22.2. Local initiation model with sigmoid CGR law

Parameters of the initiation model named 'local_initiation_model' (Code_Coriolis v2.1.5 intermediate version)

| Grain boundaries | | | | | | | | | | | | |
|-------------------------------|--------------------------|----------------------|---------------|--------------------------|------------------|-------------|---------------------|-------|-------------|------|------|------|
| Densite (mm/mm ²) | SfTot (mm ²) | SpaceResolution (nm) | GBlength (nm) | GBResolution (joints/mm) | GBC | rC (nm) | zCr (nm) | | | | | |
| 10 | 1 | 1 | 200 | 10 | 0.2 | 30 | 30 | | | | | |
| Intergranular oxidation | | | | | | | | | | | | |
| x0nom (nm) | bnom | cnom | x0depl (nm) | bdepl | Cdepl | x0carb (nm) | bcarb | Ccarb | oxQ (J/mol) | oxg1 | oxg2 | oxg3 |
| 0 | 1.86×10 ⁷ | 3 | 0 | 2.4×10 ⁷ | 3 | 0 | 2.6×10 ⁷ | 0.01 | 57000 | 0.1 | 0.3 | 0.04 |
| Cracking criterion | | | | | | | | | | | | |
| Poxc (nm) | SigmaC (MPa) | | | | StressLinearCoef | | | | | | | |
| 200 | 790 | | | | 0.25 | | | | | | | |

Parameters of the crack growth model named 'cgr_sigmoid_cw2_h' (Code_Coriolis v2.1.5 intermediate version)

| cgr1 | cgr2 | cgr3 | cgr4 | cgr5 | cgr6 | cgr7 | cgr8 | cgr9 | cgr10 | cgr11 | ecp1 | ecp2 |
|-------------------|------|------|------|------|------|------|-------|-------|-------|-------|--------------------|--------|
| 5×10 ⁴ | 0.5 | 0.66 | 12 | 0 | 0 | 0 | 3.604 | 11.33 | 43.36 | 65000 | 2×10 ⁻⁶ | 0.0256 |

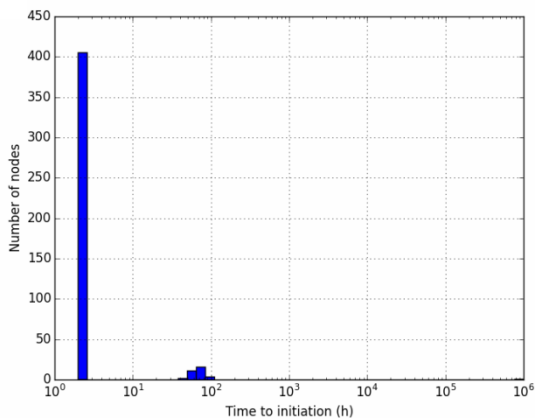


Figure 318 – Histogram of times to initiation predicted for specimen IN235, using the local model.

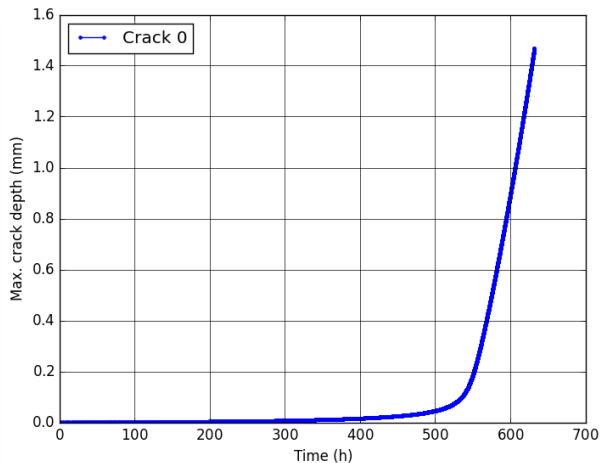


Figure 319 – Cracking kinetics predicted for specimen IN235, using the local model.

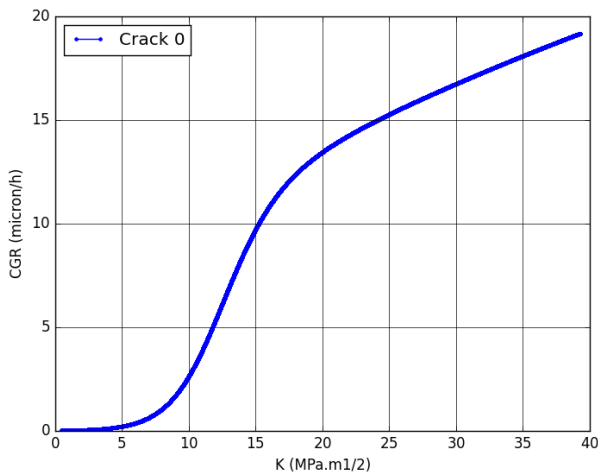


Figure 320 – Crack growth rate versus K at the tip of the main crack predicted for specimen IN235, using the local model.

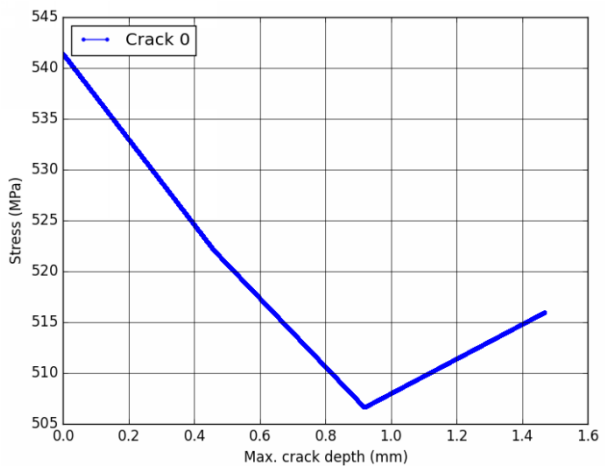


Figure 321 – Stress versus depth at the tip of the main crack predicted for specimen IN235, using the local model.

11.23. Simulations of the test on specimen IN166

11.23.1. Index initiation model with sigmoid CGR law

Parameters of the initiation model named 'index' (Code_Coriolis v2.1.5 intermediate version)

| init1 | init2 | init3 | init4 (j/mol) | init5 | init6 | Init_depth |
|-------|-------|-------|---------------|-------|------------------|------------|
| 1 | 6.8 | 1 | 185000 | 1 | 10 ⁻⁶ | 0.005 |

Parameters of the crack growth model named 'cgr_sigmoid_cw2_h' (Code_Coriolis v2.1.5 intermediate version)

| cgr1 | cgr2 | cgr3 | cgr4 | cgr5 | cgr6 | cgr7 | cgr8 | cgr9 | cgr10 | cgr11 | ecp1 | ecp2 |
|-------------------|------|------|------|------|------|------|-------|-------|-------|-------|--------------------|--------|
| 5×10 ⁴ | 0.5 | 0.66 | 12 | 15 | 0 | 0 | 3.604 | 11.33 | 43.36 | 65000 | 2×10 ⁻⁶ | 0.0256 |

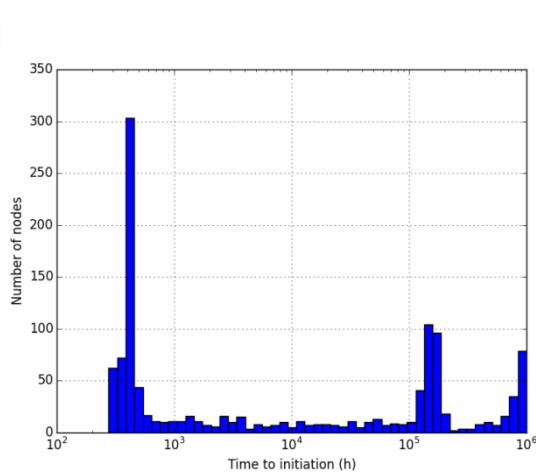


Figure 322 – Histogram of times to initiation predicted for specimen IN166, using the index model.

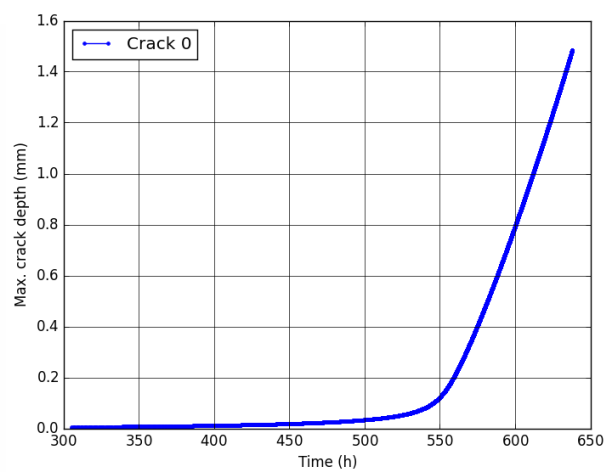


Figure 323 – Cracking kinetics predicted for specimen IN166, using the index model.

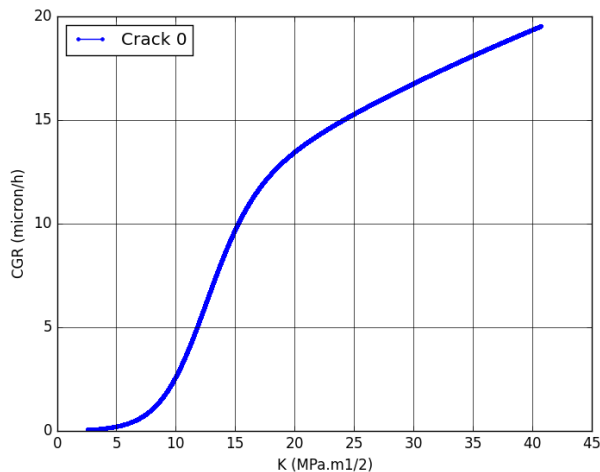


Figure 324 – Crack growth rate versus K at the tip of the main crack predicted for specimen IN166 using the index model.

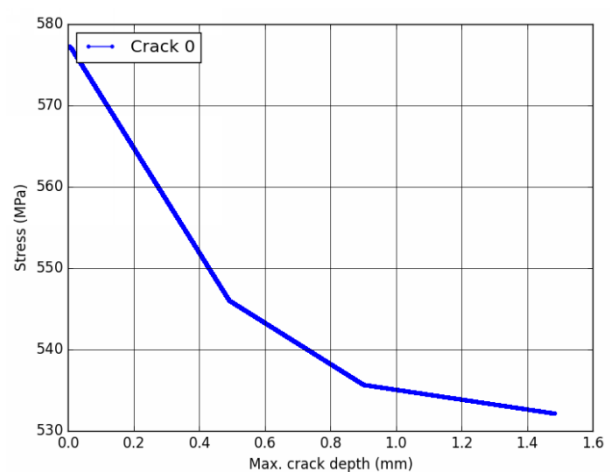


Figure 325 – Stress versus depth at the tip of the main crack predicted for specimen IN166, using the index model.

| | | |
|------------|---|--|
| MAI | Quantitative evaluation of the EDF local model and the EPRI-NRC xLPR models of crack initiation of the weld metals of Alloy 600 (Alloys 82 and 182) | 6125-4501-2018-00583-EN Version 2.0 |
|------------|---|--|

11.23.2. Local initiation model with sigmoid CGR law

Parameters of the initiation model named 'local_initiation_model' (Code_Coriolis v2.1.5 intermediate version)

| Grain boundaries | | | | | | | | | | | | |
|-------------------------------|--------------------------|----------------------|-------------|---------------------|--------------------------|-------------|---------------------|---------|-------------|------|------|------|
| Densite (mm/mm ²) | SfTot (mm ²) | SpaceResolution (nm) | | GBlength (nm) | GBResolution (joints/mm) | | GBC | rC (nm) | zCr (nm) | | | |
| 10 | 1 | 1 | | 200 | 10 | | 0.05 | 30 | 30 | | | |
| Intergranular oxidation | | | | | | | | | | | | |
| x0nom (nm) | bnom | cnom | x0depl (nm) | bdepl | Cdepl | x0carb (nm) | bcarb | Ccarb | oxQ (J/mol) | oxg1 | oxg2 | oxg3 |
| 0 | 1.86×10 ⁷ | 3 | 0 | 2.4×10 ⁷ | 3 | 0 | 2.6×10 ⁷ | 0.01 | 57000 | 0.1 | 0.3 | 0.04 |
| Cracking criterion | | | | | | | | | | | | |
| Poxc (nm) | | SigmaC (MPa) | | | StressLinearCoef | | | | | | | |
| 200 | | 790 | | | 0.25 | | | | | | | |

Parameters of the crack growth model named 'cgr_sigmoid_cw2_h' (Code_Coriolis v2.1.5 intermediate version)

| | | | | | | | | | | | | |
|-------------------|------|------|------|------|------|------|-------|-------|-------|-------|--------------------|--------|
| cgr1 | cgr2 | cgr3 | cgr4 | cgr5 | cgr6 | cgr7 | cgr8 | cgr9 | cgr10 | cgr11 | ecp1 | ecp2 |
| 5×10 ⁴ | 0.5 | 0.66 | 12 | 0 | 0 | 0 | 3.604 | 11.33 | 43.36 | 65000 | 2×10 ⁻⁶ | 0.0256 |

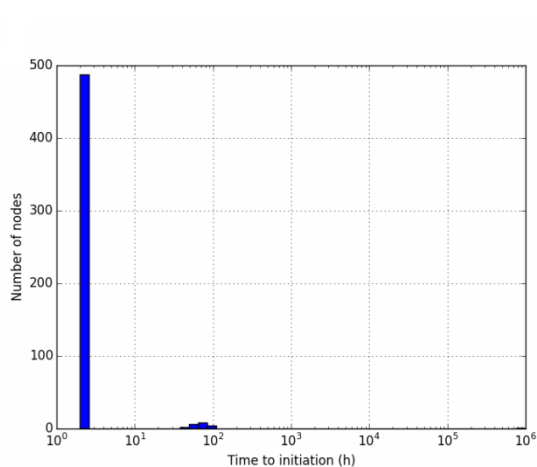


Figure 326 – Histogram of times to initiation predicted for specimen IN166, using the local model.

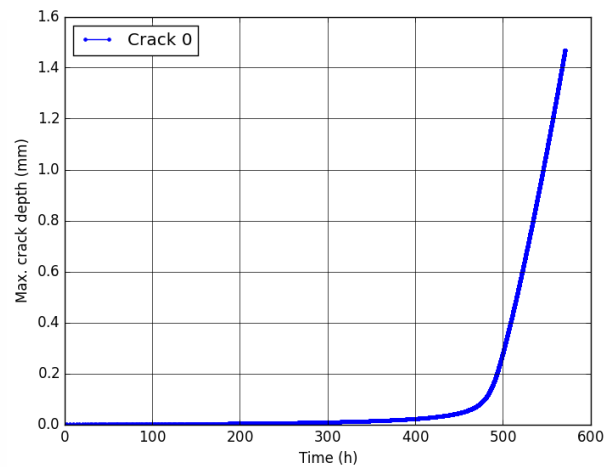


Figure 327 – Cracking kinetics predicted for specimen IN166, using the local model.

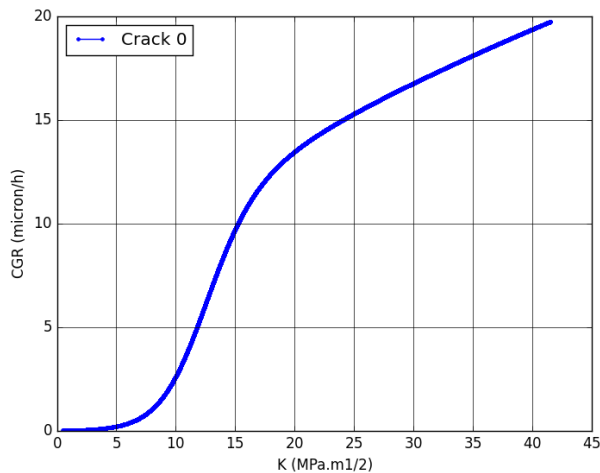


Figure 328 – Crack growth rate versus K at the tip of the main crack predicted for specimen IN166, using the local model.

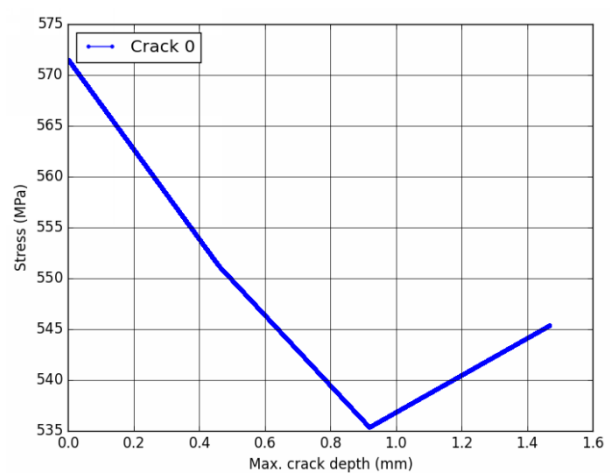


Figure 329 – Stress versus depth at the tip of the main crack predicted for specimen IN166, using the local model.

11.24. Simulations of the test on specimen IN167

11.24.1. Index initiation model with sigmoid CGR law

Parameters of the initiation model named 'index' (Code_Coriolis v2.1.5 intermediate version)

| init1 | init2 | init3 | init4 (j/mol) | init5 | init6 | Init_depth |
|-------|-------|-------|---------------|-------|------------------|------------|
| 1 | 6.8 | 1 | 185000 | 1 | 10 ⁻⁶ | 0.005 |

Parameters of the crack growth model named 'cgr_sigmoid_cw2_h' (Code_Coriolis v2.1.5 intermediate version)

| cgr1 | cgr2 | cgr3 | cgr4 | cgr5 | cgr6 | cgr7 | cgr8 | cgr9 | cgr10 | cgr11 | ecp1 | ecp2 |
|-------------------|------|------|------|------|------|------|-------|-------|-------|-------|--------------------|--------|
| 5×10 ⁴ | 0.5 | 0.66 | 12 | 15 | 0 | 0 | 3.604 | 11.33 | 43.36 | 65000 | 2×10 ⁻⁶ | 0.0256 |

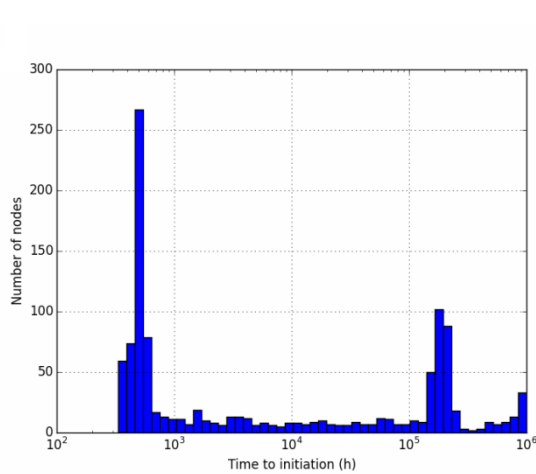


Figure 330 – Histogram of times to initiation predicted for specimen IN167, using the index model.

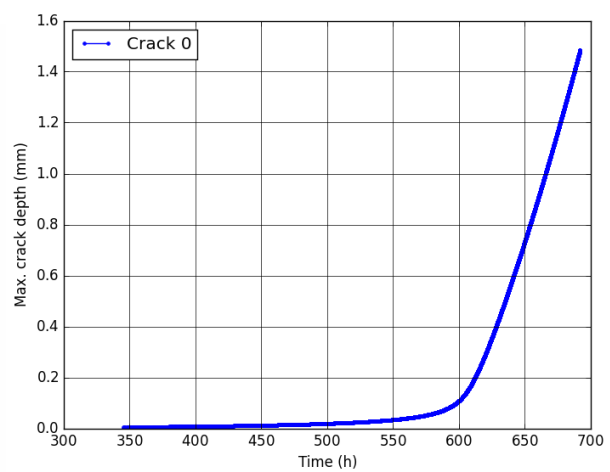


Figure 331 – Cracking kinetics predicted for specimen IN167, using the index model.

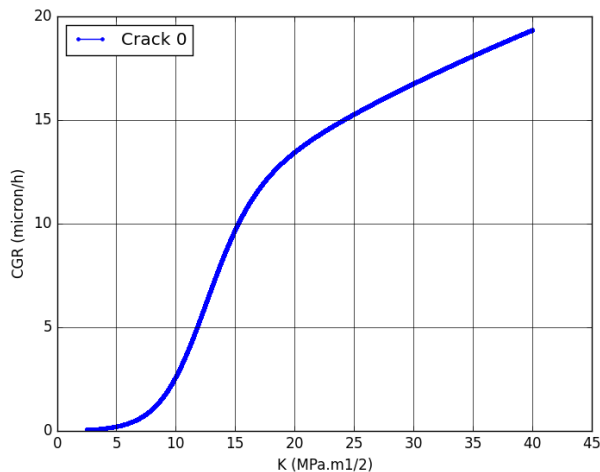


Figure 332 – Crack growth rate versus K at the tip of the main crack predicted for specimen IN167 using the index model.

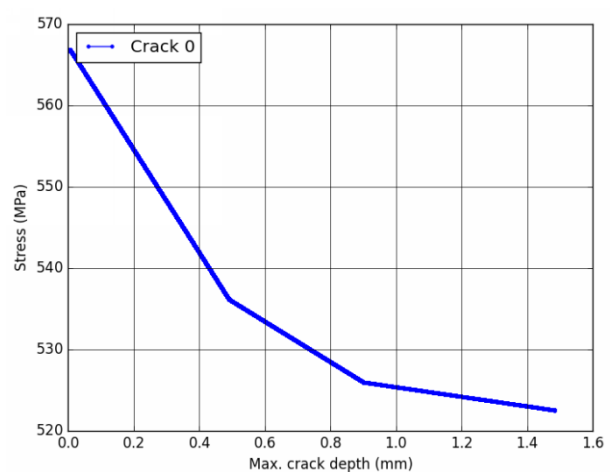


Figure 333 – Stress versus depth at the tip of the main crack predicted for specimen IN167, using the index model.

| | | |
|-----|---|--|
| MAI | Quantitative evaluation of the EDF local model and the EPRI-NRC xLPR models of crack initiation of the weld metals of Alloy 600 (Alloys 82 and 182) | 6125-4501-2018-00583-EN Version 2.0 |
|-----|---|--|

11.24.2. Local initiation model with sigmoid CGR law

Parameters of the initiation model named 'local_initiation_model' (Code_Coriolis v2.1.5 intermediate version)

| Grain boundaries | | | | | | | | | | | | |
|-------------------------------|--------------------------|----------------------|-------------|---------------------|--------------------------|-------------|---------------------|---------|-------------|------|------|------|
| Densite (mm/mm ²) | SfTot (mm ²) | SpaceResolution (nm) | | GBlength (nm) | GBResolution (joints/mm) | | GBC | rC (nm) | zCr (nm) | | | |
| 10 | 1 | 1 | | 200 | 10 | | 0.05 | 30 | 30 | | | |
| Intergranular oxidation | | | | | | | | | | | | |
| x0nom (nm) | bnom | cnom | x0depl (nm) | bdepl | Cdepl | x0carb (nm) | bcarb | Ccarb | oxQ (J/mol) | oxg1 | oxg2 | oxg3 |
| 0 | 1.86×10 ⁷ | 3 | 0 | 2.4×10 ⁷ | 3 | 0 | 2.6×10 ⁷ | 0.01 | 57000 | 0.1 | 0.3 | 0.04 |
| Cracking criterion | | | | | | | | | | | | |
| Poxc (nm) | | SigmaC (MPa) | | | StressLinearCoef | | | | | | | |
| 200 | | 790 | | | 0.25 | | | | | | | |

Parameters of the crack growth model named 'cgr_sigmoid_cw2_h' (Code_Coriolis v2.1.5 intermediate version)

| cgr1 | cgr2 | cgr3 | cgr4 | cgr5 | cgr6 | cgr7 | cgr8 | cgr9 | cgr10 | cgr11 | ecp1 | ecp2 |
|-------------------|------|------|------|------|------|------|-------|-------|-------|-------|--------------------|--------|
| 5×10 ⁴ | 0.5 | 0.66 | 12 | 0 | 0 | 0 | 3.604 | 11.33 | 43.36 | 65000 | 2×10 ⁻⁶ | 0.0256 |

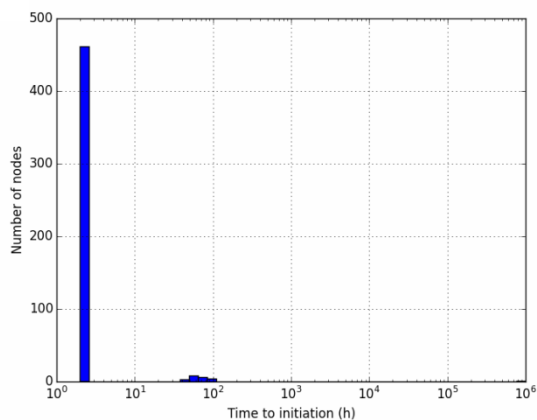


Figure 334 – Histogram of times to initiation predicted for specimen IN167, using the local model.

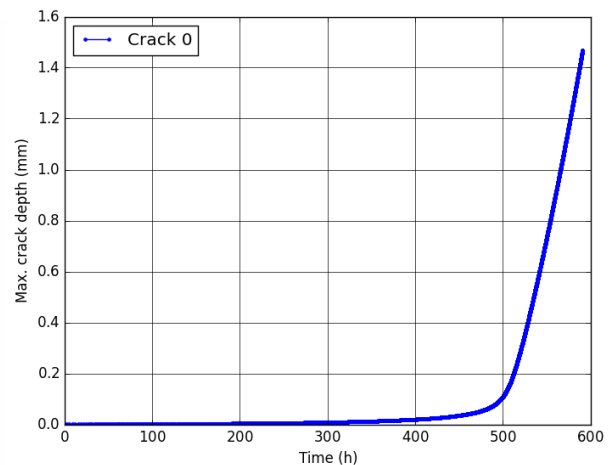


Figure 335 – Cracking kinetics predicted for specimen IN167, using the local model.

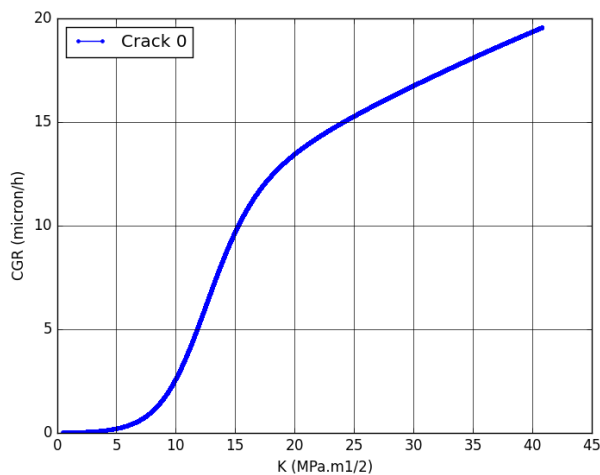


Figure 336 – Crack growth rate versus K at the tip of the main crack predicted for specimen IN167, using the local model.

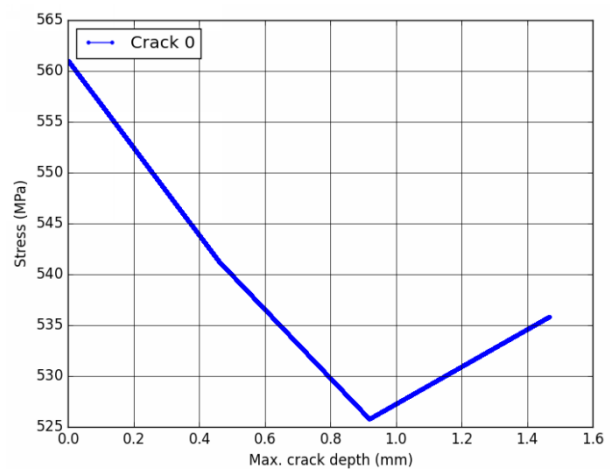


Figure 337 – Stress versus depth at the tip of the main crack predicted for specimen IN167, using the local model.

11.25. Simulations of the test on specimen IN168

11.25.1. Index initiation model with sigmoid CGR law

Parameters of the initiation model named 'index' (Code_Coriolis v2.1.5 intermediate version)

| init1 | init2 | init3 | init4 (j/mol) | init5 | init6 | Init_depth |
|-------|-------|-------|---------------|-------|------------------|------------|
| 1 | 6.8 | 1 | 185000 | 1 | 10 ⁻⁶ | 0.005 |

Parameters of the crack growth model named 'cgr_sigmoid_cw2_h' (Code_Coriolis v2.1.5 intermediate version)

| cgr1 | cgr2 | cgr3 | cgr4 | cgr5 | cgr6 | cgr7 | cgr8 | cgr9 | cgr10 | cgr11 | ecp1 | ecp2 |
|-------------------|------|------|------|------|------|------|-------|-------|-------|-------|--------------------|--------|
| 5×10 ⁴ | 0.5 | 0.66 | 12 | 15 | 0 | 0 | 3.604 | 11.33 | 43.36 | 65000 | 2×10 ⁻⁶ | 0.0256 |

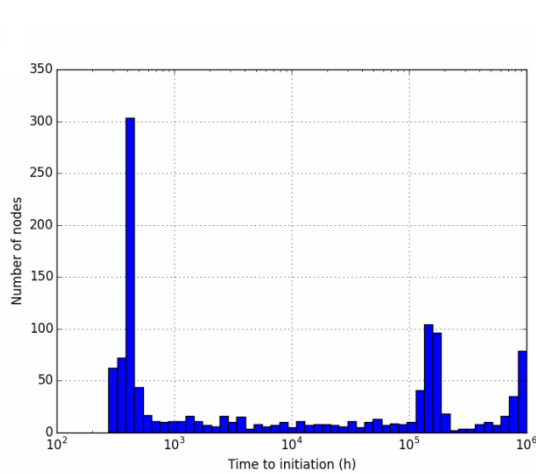


Figure 338 – Histogram of times to initiation predicted for specimen IN168, using the index model.

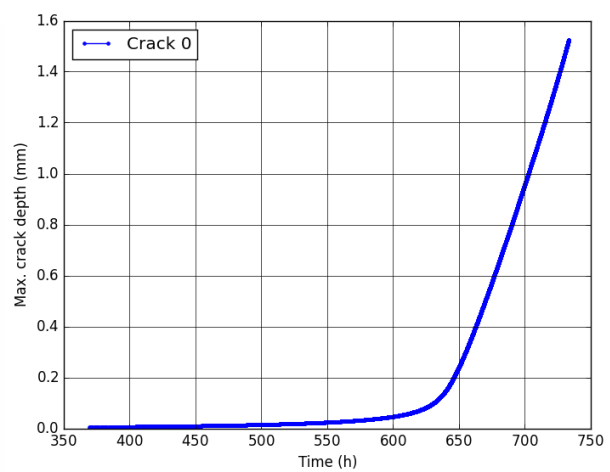


Figure 339 – Cracking kinetics predicted for specimen IN168, using the index model.

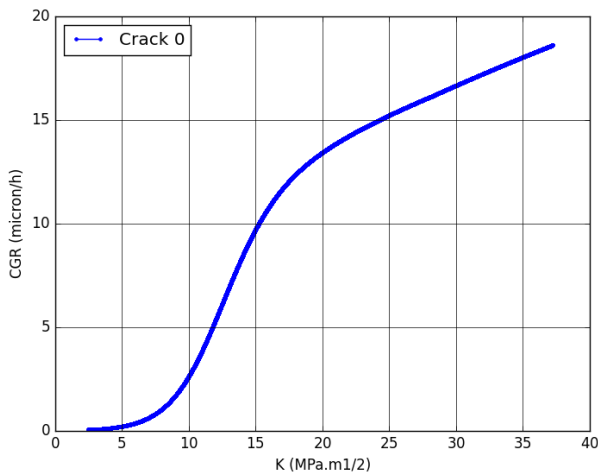


Figure 340 – Crack growth rate versus K at the tip of the main crack predicted for specimen IN168 using the index model.

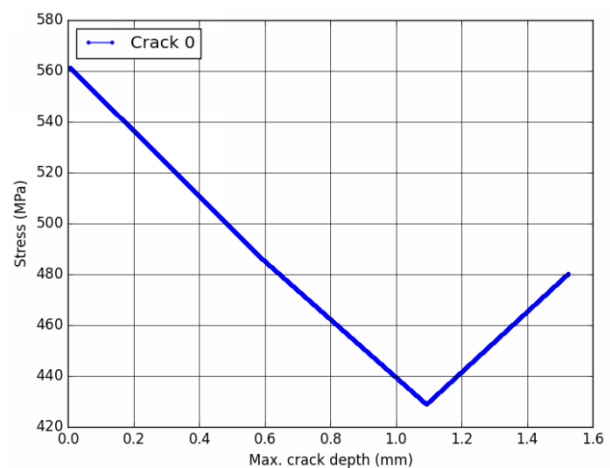


Figure 341 – Stress versus depth at the tip of the main crack predicted for specimen IN168, using the index model.

| | | |
|------------|---|--|
| MAI | Quantitative evaluation of the EDF local model and the EPRI-NRC xLPR models of crack initiation of the weld metals of Alloy 600 (Alloys 82 and 182) | 6125-4501-2018-00583-EN Version 2.0 |
|------------|---|--|

11.25.2. Local initiation model with sigmoid CGR law

Parameters of the initiation model named 'local_initiation_model' (Code_Coriolis v2.1.5 intermediate version)

| Grain boundaries | | | | | | | | | | | | |
|-------------------------------|--------------------------|----------------------|-------------|---------------------|--------------------------|-------------|---------------------|---------|-------------|------|------|------|
| Densite (mm/mm ²) | SfTot (mm ²) | SpaceResolution (nm) | | GBlength (nm) | GBResolution (joints/mm) | | GBC | rC (nm) | zCr (nm) | | | |
| 10 | 1 | 1 | | 200 | 10 | | 0.05 | 30 | 30 | | | |
| Intergranular oxidation | | | | | | | | | | | | |
| x0nom (nm) | bnom | cnom | x0depl (nm) | bdepl | Cdepl | x0carb (nm) | bcarb | Ccarb | oxQ (J/mol) | oxg1 | oxg2 | oxg3 |
| 0 | 1.86×10 ⁷ | 3 | 0 | 2.4×10 ⁷ | 3 | 0 | 2.6×10 ⁷ | 0.01 | 57000 | 0.1 | 0.3 | 0.04 |
| Cracking criterion | | | | | | | | | | | | |
| Poxc (nm) | | SigmaC (MPa) | | | StressLinearCoef | | | | | | | |
| 200 | | 790 | | | 0.25 | | | | | | | |

Parameters of the crack growth model named 'cgr_sigmoid_cw2_h' (Code_Coriolis v2.1.5 intermediate version)

| | | | | | | | | | | | | |
|-------------------|------|------|------|------|------|------|-------|-------|-------|-------|--------------------|--------|
| cgr1 | cgr2 | cgr3 | cgr4 | cgr5 | cgr6 | cgr7 | cgr8 | cgr9 | cgr10 | cgr11 | ecp1 | ecp2 |
| 5×10 ⁴ | 0.5 | 0.66 | 12 | 0 | 0 | 0 | 3.604 | 11.33 | 43.36 | 65000 | 2×10 ⁻⁶ | 0.0256 |

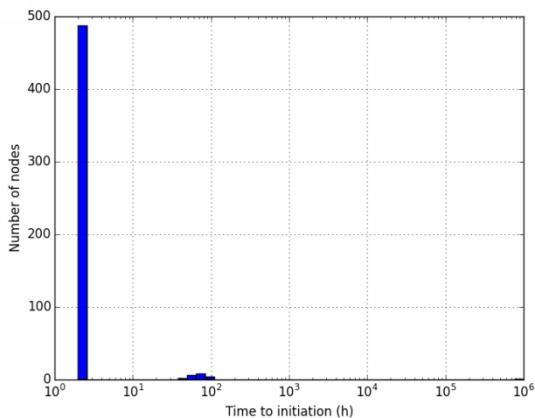


Figure 342 – Histogram of times to initiation predicted for specimen IN168, using the local model.

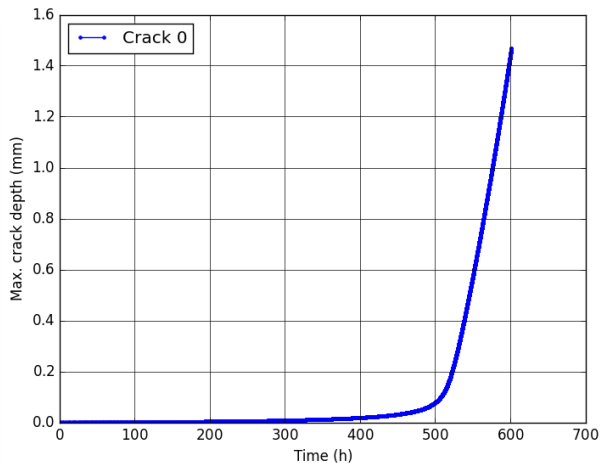


Figure 343 – Cracking kinetics predicted for specimen IN168, using the local model.

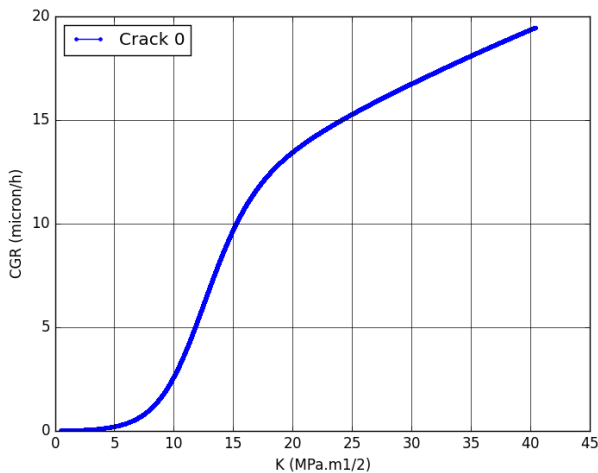


Figure 344 – Crack growth rate versus K at the tip of the main crack predicted for specimen IN168, using the local model.

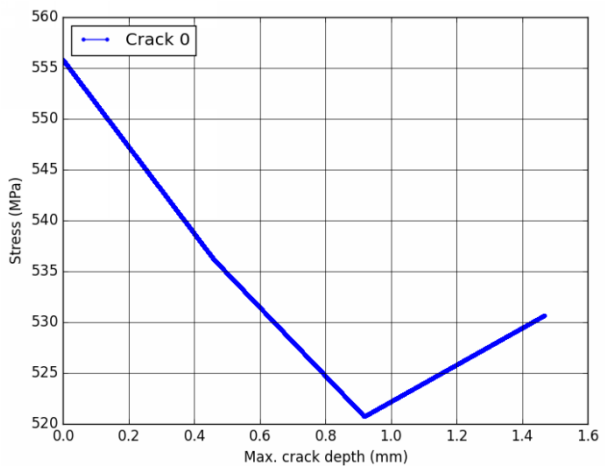


Figure 345 – Stress versus depth at the tip of the main crack predicted for specimen IN168, using the local model.

11.26. Simulations of the test on specimen IN194

11.26.1. Index initiation model with sigmoid CGR law

Parameters of the initiation model named 'index' (Code_Coriolis v2.1.5 intermediate version)

| init1 | init2 | init3 | init4 (j/mol) | init5 | init6 | Init_depth |
|-------|-------|-------|---------------|-------|------------------|------------|
| 1 | 6.8 | 1 | 185000 | 1 | 10 ⁻⁶ | 0.005 |

Parameters of the crack growth model named 'cgr_sigmoid_cw2_h' (Code_Coriolis v2.1.5 intermediate version)

| cgr1 | cgr2 | cgr3 | cgr4 | cgr5 | cgr6 | cgr7 | cgr8 | cgr9 | cgr10 | cgr11 | ecp1 | ecp2 |
|-------------------|------|------|------|------|------|------|-------|-------|-------|-------|--------------------|--------|
| 5×10 ⁴ | 0.5 | 0.66 | 12 | 15 | 0 | 0 | 3.604 | 11.33 | 43.36 | 65000 | 2×10 ⁻⁶ | 0.0256 |

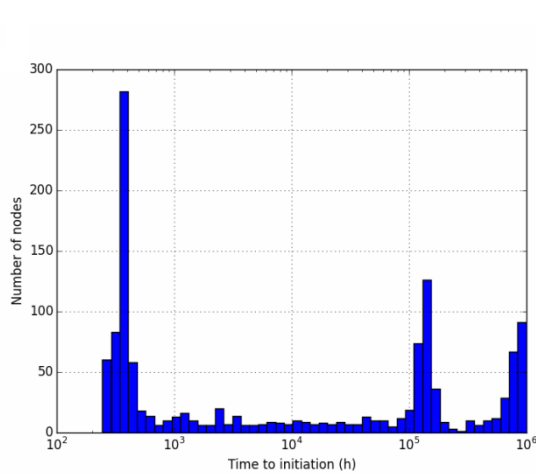


Figure 346 – Histogram of times to initiation predicted for specimen IN194, using the index model.

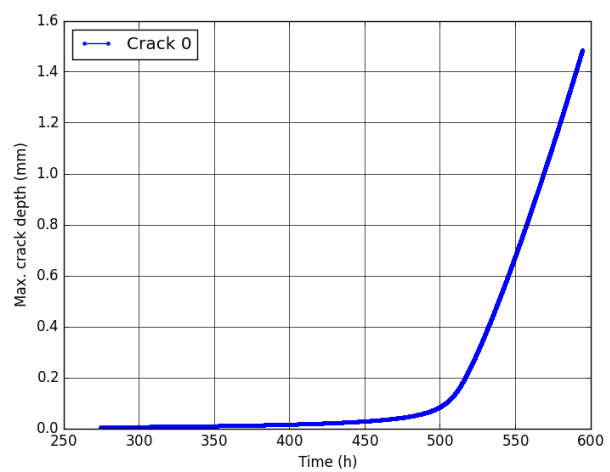


Figure 347 – Cracking kinetics predicted for specimen IN194, using the index model.

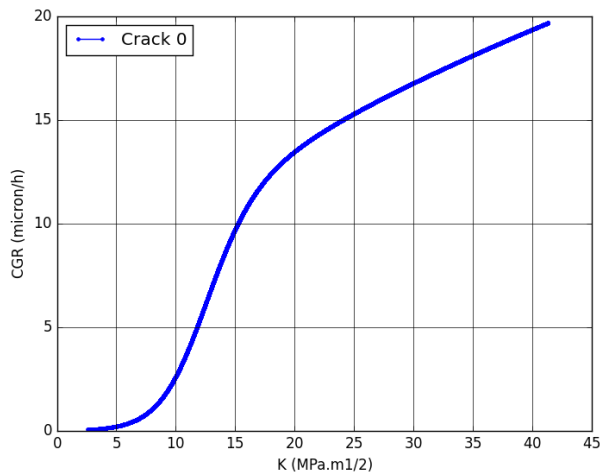


Figure 348 – Crack growth rate versus K at the tip of the main crack predicted for specimen IN194 using the index model.

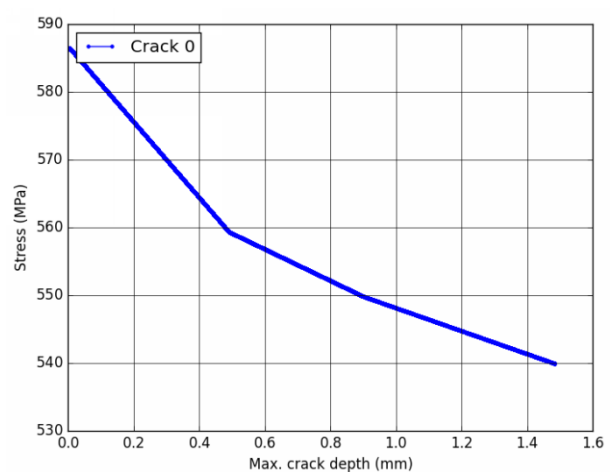


Figure 349 – Stress versus depth at the tip of the main crack predicted for specimen IN194, using the index model.

| | | |
|------------|---|--|
| MAI | Quantitative evaluation of the EDF local model and the EPRI-NRC xLPR models of crack initiation of the weld metals of Alloy 600 (Alloys 82 and 182) | 6125-4501-2018-00583-EN Version 2.0 |
|------------|---|--|

11.26.2. Local initiation model with sigmoid CGR law

Parameters of the initiation model named 'local_initiation_model' (Code_Coriolis v2.1.5 intermediate version)

| Grain boundaries | | | | | | | | | | | | |
|-------------------------------|--------------------------|----------------------|-------------|---------------------|--------------------------|-------------|---------------------|---------|-------------|------|------|------|
| Densite (mm/mm ²) | SfTot (mm ²) | SpaceResolution (nm) | | GBlength (nm) | GBResolution (joints/mm) | | GBC | rC (nm) | zCr (nm) | | | |
| 10 | 1 | 1 | | 200 | 10 | | 0.05 | 30 | 30 | | | |
| Intergranular oxidation | | | | | | | | | | | | |
| x0nom (nm) | bnom | cnom | x0depl (nm) | bdepl | Cdepl | x0carb (nm) | bcarb | Ccarb | oxQ (J/mol) | oxg1 | oxg2 | oxg3 |
| 0 | 1.86×10 ⁷ | 3 | 0 | 2.4×10 ⁷ | 3 | 0 | 2.6×10 ⁷ | 0.01 | 57000 | 0.1 | 0.3 | 0.04 |
| Cracking criterion | | | | | | | | | | | | |
| Poxc (nm) | | SigmaC (MPa) | | | StressLinearCoef | | | | | | | |
| 200 | | 790 | | | 0.25 | | | | | | | |

Parameters of the crack growth model named 'cgr_sigmoid_cw2_h' (Code_Coriolis v2.1.5 intermediate version)

| cgr1 | cgr2 | cgr3 | cgr4 | cgr5 | cgr6 | cgr7 | cgr8 | cgr9 | cgr10 | cgr11 | ecp1 | ecp2 |
|-------------------|------|------|------|------|------|------|-------|-------|-------|-------|--------------------|--------|
| 5×10 ⁴ | 0.5 | 0.66 | 12 | 0 | 0 | 0 | 3.604 | 11.33 | 43.36 | 65000 | 2×10 ⁻⁶ | 0.0256 |

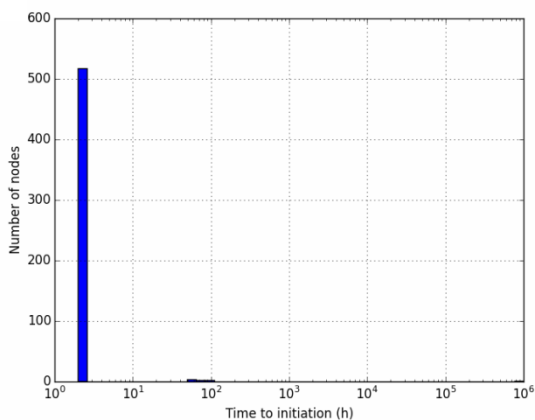


Figure 350 – Histogram of times to initiation predicted for specimen IN194, using the local model.

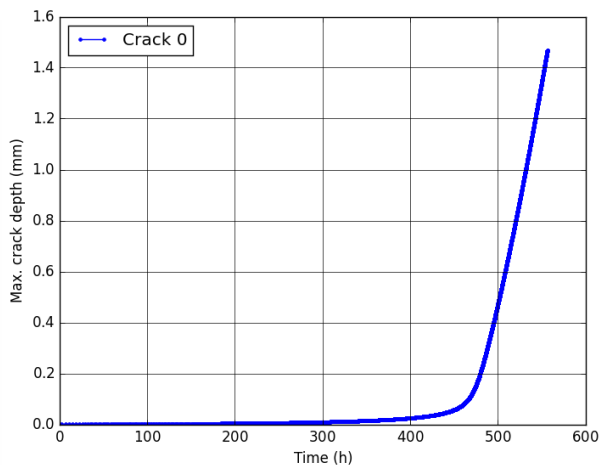


Figure 351 – Cracking kinetics predicted for specimen IN194, using the local model.

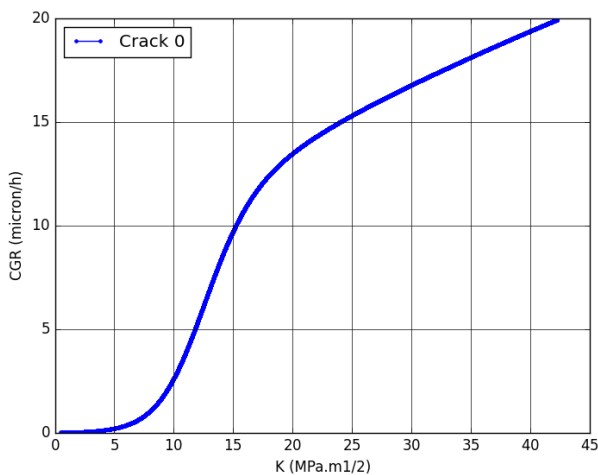


Figure 352 – Crack growth rate versus K at the tip of the main crack predicted for specimen IN194, using the local model.

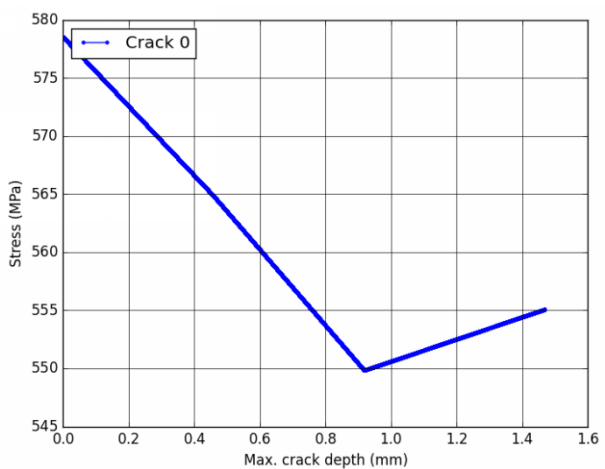


Figure 353 – Stress versus depth at the tip of the main crack predicted for specimen IN194, using the local model.

11.27. Simulations of the test on specimen IN195

11.27.1. Index initiation model with sigmoid CGR law

Parameters of the initiation model named 'index' (Code_Coriolis v2.1.5 intermediate version)

| init1 | init2 | init3 | init4 (j/mol) | init5 | init6 | Init_depth |
|-------|-------|-------|---------------|-------|------------------|------------|
| 1 | 6.8 | 1 | 185000 | 1 | 10 ⁻⁶ | 0.005 |

Parameters of the crack growth model named 'cgr_sigmoid_cw2_h' (Code_Coriolis v2.1.5 intermediate version)

| cgr1 | cgr2 | cgr3 | cgr4 | cgr5 | cgr6 | cgr7 | cgr8 | cgr9 | cgr10 | cgr11 | ecp1 | ecp2 |
|-------------------|------|------|------|------|------|------|-------|-------|-------|-------|--------------------|--------|
| 5×10 ⁴ | 0.5 | 0.66 | 12 | 15 | 0 | 0 | 3.604 | 11.33 | 43.36 | 65000 | 2×10 ⁻⁶ | 0.0256 |

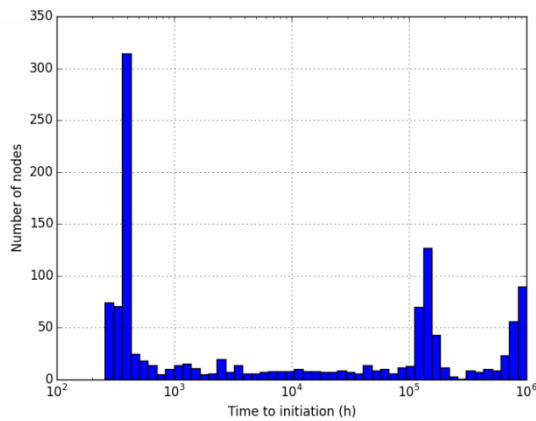


Figure 354 – Histogram of times to initiation predicted for specimen IN195, using the index model.

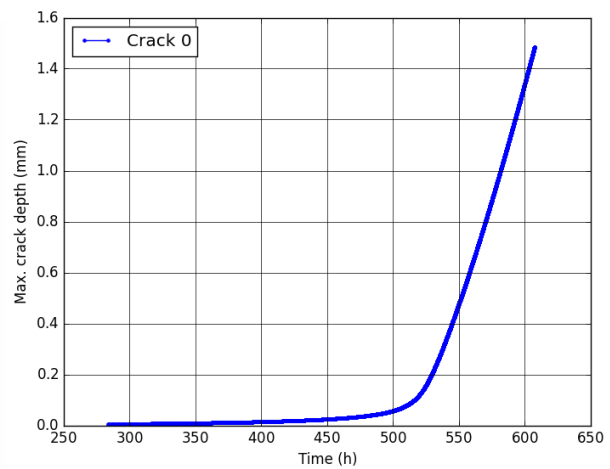


Figure 355 – Cracking kinetics predicted for specimen IN195, using the index model.

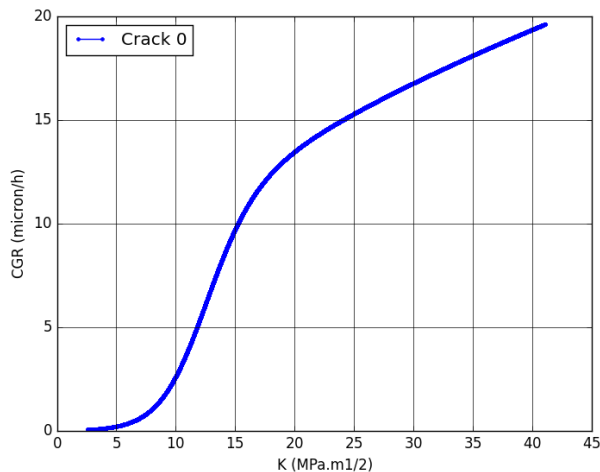


Figure 356 – Crack growth rate versus K at the tip of the main crack predicted for specimen IN195 using the index model.

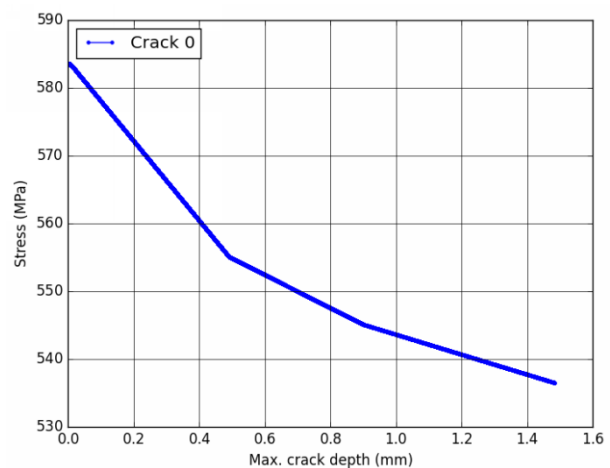


Figure 357 – Stress versus depth at the tip of the main crack predicted for specimen IN195, using the index model.

| | | |
|------------|---|--|
| MAI | Quantitative evaluation of the EDF local model and the EPRI-NRC xLPR models of crack initiation of the weld metals of Alloy 600 (Alloys 82 and 182) | 6125-4501-2018-00583-EN Version 2.0 |
|------------|---|--|

11.27.2. Local initiation model with sigmoid CGR law

Parameters of the initiation model named 'local_initiation_model' (Code_Coriolis v2.1.5 intermediate version)

| Grain boundaries | | | | | | | | | | | | |
|-------------------------------|--------------------------|----------------------|-------------|---------------------|--------------------------|-------------|---------------------|---------|-------------|------|------|------|
| Densite (mm/mm ²) | SfTot (mm ²) | SpaceResolution (nm) | | GBlength (nm) | GBResolution (joints/mm) | | GBC | rC (nm) | zCr (nm) | | | |
| 10 | 1 | 1 | | 200 | 10 | | 0.05 | 30 | 30 | | | |
| Intergranular oxidation | | | | | | | | | | | | |
| x0nom (nm) | bnom | cnom | x0depl (nm) | bdepl | Cdepl | x0carb (nm) | bcarb | Ccarb | oxQ (J/mol) | oxg1 | oxg2 | oxg3 |
| 0 | 1.86×10 ⁷ | 3 | 0 | 2.4×10 ⁷ | 3 | 0 | 2.6×10 ⁷ | 0.01 | 57000 | 0.1 | 0.3 | 0.04 |
| Cracking criterion | | | | | | | | | | | | |
| Poxc (nm) | | SigmaC (MPa) | | | StressLinearCoef | | | | | | | |
| 200 | | 790 | | | 0.25 | | | | | | | |

Parameters of the crack growth model named 'cgr_sigmoid_cw2_h' (Code_Coriolis v2.1.5 intermediate version)

| cgr1 | cgr2 | cgr3 | cgr4 | cgr5 | cgr6 | cgr7 | cgr8 | cgr9 | cgr10 | cgr11 | ecp1 | ecp2 |
|-------------------|------|------|------|------|------|------|-------|-------|-------|-------|--------------------|--------|
| 5×10 ⁴ | 0.5 | 0.66 | 12 | 0 | 0 | 0 | 3.604 | 11.33 | 43.36 | 65000 | 2×10 ⁻⁶ | 0.0256 |

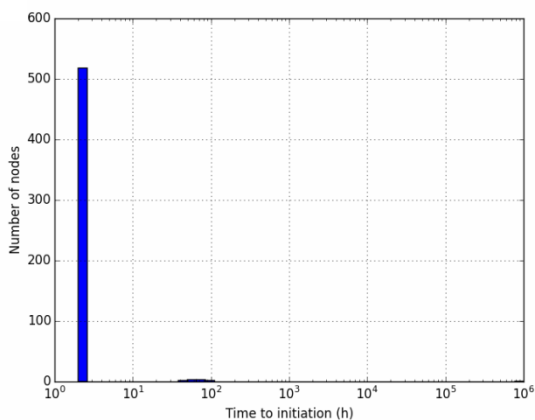


Figure 358 – Histogram of times to initiation predicted for specimen IN195, using the local model.

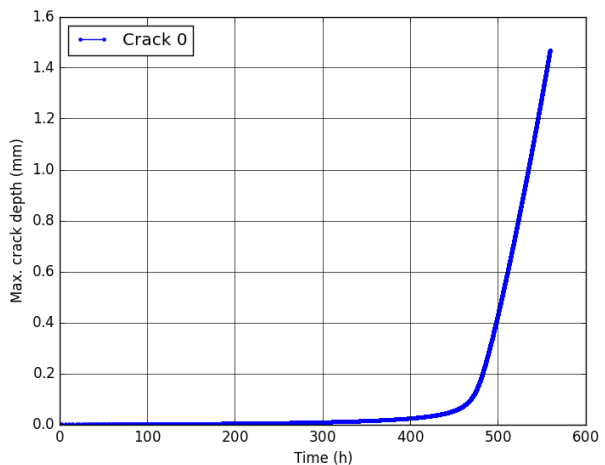


Figure 359 – Cracking kinetics predicted for specimen IN195, using the local model.

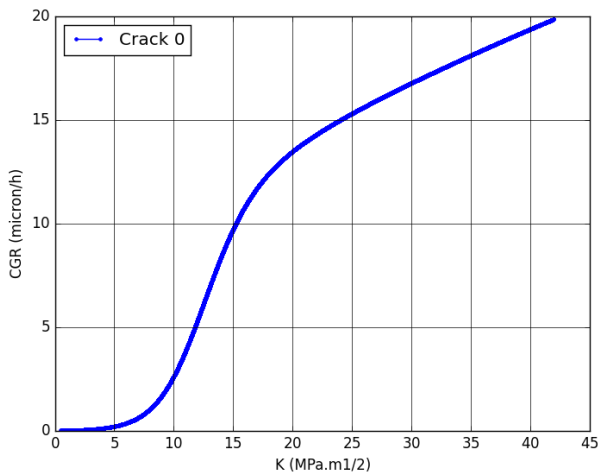


Figure 360 – Crack growth rate versus K at the tip of the main crack predicted for specimen IN195, using the local model.

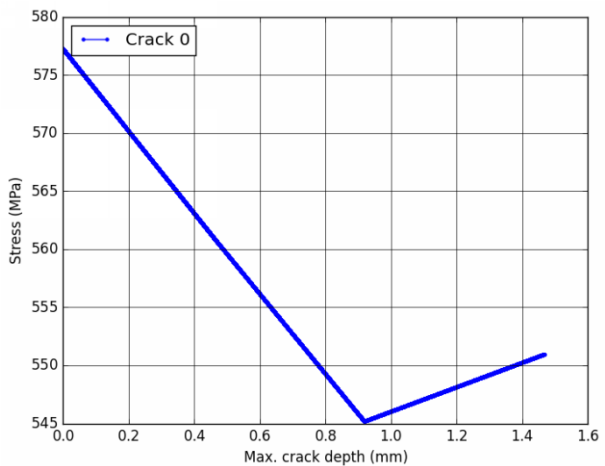


Figure 361 – Stress versus depth at the tip of the main crack predicted for specimen IN195, using the local model.

11.28. Simulations of the test on specimen IN196

11.28.1. Index initiation model with sigmoid CGR law

Parameters of the initiation model named 'index' (Code_Coriolis v2.1.5 intermediate version)

| init1 | init2 | init3 | init4 (j/mol) | init5 | init6 | Init_depth |
|-------|-------|-------|---------------|-------|------------------|------------|
| 1 | 6.8 | 1 | 185000 | 1 | 10 ⁻⁶ | 0.005 |

Parameters of the crack growth model named 'cgr_sigmoid_cw2_h' (Code_Coriolis v2.1.5 intermediate version)

| cgr1 | cgr2 | cgr3 | cgr4 | cgr5 | cgr6 | cgr7 | cgr8 | cgr9 | cgr10 | cgr11 | ecp1 | ecp2 |
|-------------------|------|------|------|------|------|------|-------|-------|-------|-------|--------------------|--------|
| 5×10 ⁴ | 0.5 | 0.66 | 12 | 15 | 0 | 0 | 3.604 | 11.33 | 43.36 | 65000 | 2×10 ⁻⁶ | 0.0256 |

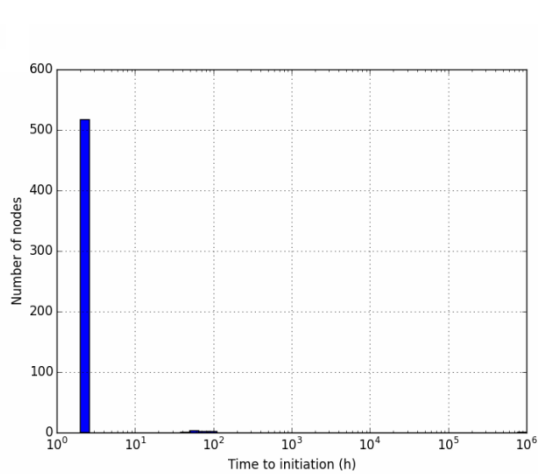


Figure 362 – Histogram of times to initiation predicted for specimen IN196, using the index model.

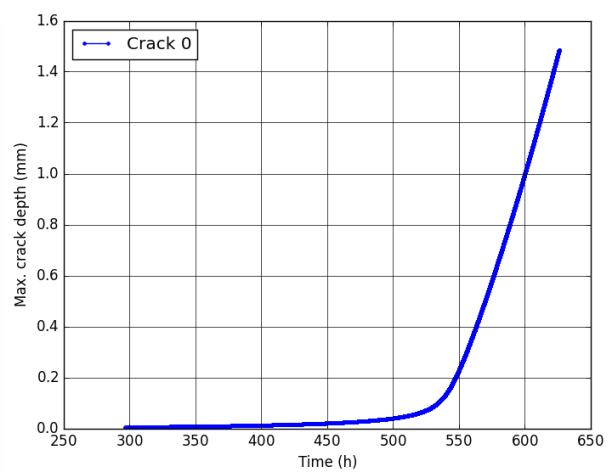


Figure 363 – Cracking kinetics predicted for specimen IN196, using the index model.

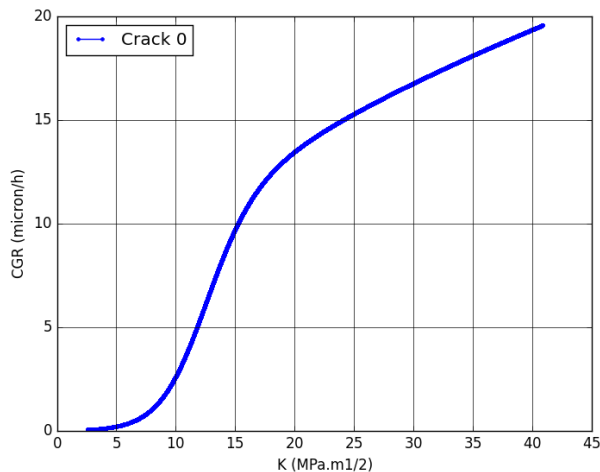


Figure 364 – Crack growth rate versus K at the tip of the main crack predicted for specimen IN196 using the index model.

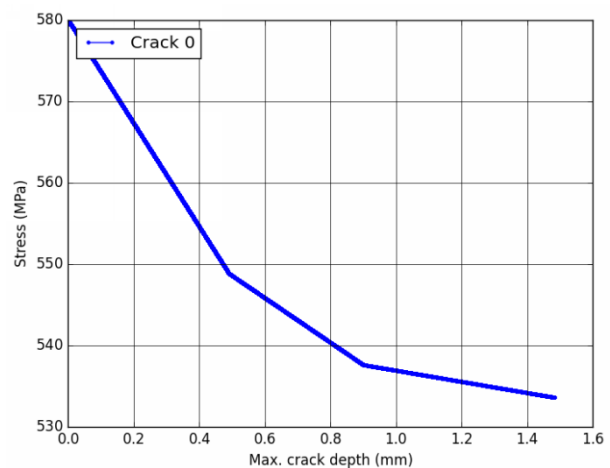


Figure 365 – Stress versus depth at the tip of the main crack predicted for specimen IN196, using the index model.

| | | |
|------------|---|--|
| MAI | Quantitative evaluation of the EDF local model and the EPRI-NRC xLPR models of crack initiation of the weld metals of Alloy 600 (Alloys 82 and 182) | 6125-4501-2018-00583-EN Version 2.0 |
|------------|---|--|

11.28.2. Local initiation model with sigmoid CGR law

Parameters of the initiation model named 'local_initiation_model' (Code_Coriolis v2.1.5 intermediate version)

| Grain boundaries | | | | | | | | | | | | |
|-------------------------------|--------------------------|----------------------|-------------|---------------------|--------------------------|-------------|---------------------|---------|-------------|------|------|------|
| Densite (mm/mm ²) | SfTot (mm ²) | SpaceResolution (nm) | | GBlength (nm) | GBResolution (joints/mm) | | GBC | rC (nm) | zCr (nm) | | | |
| 10 | 1 | 1 | | 200 | 10 | | 0.05 | 30 | 30 | | | |
| Intergranular oxidation | | | | | | | | | | | | |
| x0nom (nm) | bnom | cnom | x0depl (nm) | bdepl | Cdepl | x0carb (nm) | bcarb | Ccarb | oxQ (J/mol) | oxg1 | oxg2 | oxg3 |
| 0 | 1.86×10 ⁷ | 3 | 0 | 2.4×10 ⁷ | 3 | 0 | 2.6×10 ⁷ | 0.01 | 57000 | 0.1 | 0.3 | 0.04 |
| Cracking criterion | | | | | | | | | | | | |
| Poxc (nm) | | SigmaC (MPa) | | | StressLinearCoef | | | | | | | |
| 200 | | 790 | | | 0.25 | | | | | | | |

Parameters of the crack growth model named 'cgr_sigmoid_cw2_h' (Code_Coriolis v2.1.5 intermediate version)

| cgr1 | cgr2 | cgr3 | cgr4 | cgr5 | cgr6 | cgr7 | cgr8 | cgr9 | cgr10 | cgr11 | ecp1 | ecp2 |
|-------------------|------|------|------|------|------|------|-------|-------|-------|-------|--------------------|--------|
| 5×10 ⁴ | 0.5 | 0.66 | 12 | 0 | 0 | 0 | 3.604 | 11.33 | 43.36 | 65000 | 2×10 ⁻⁶ | 0.0256 |

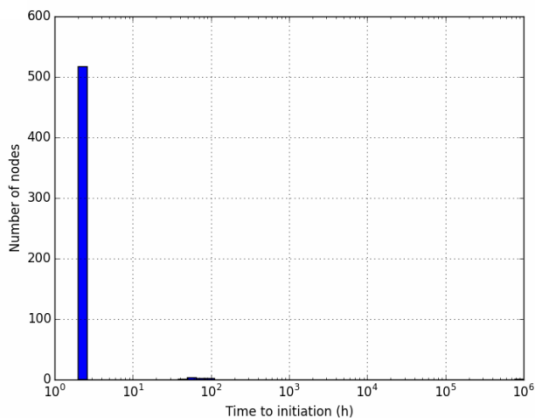


Figure 366 – Histogram of times to initiation predicted for specimen IN196, using the local model.

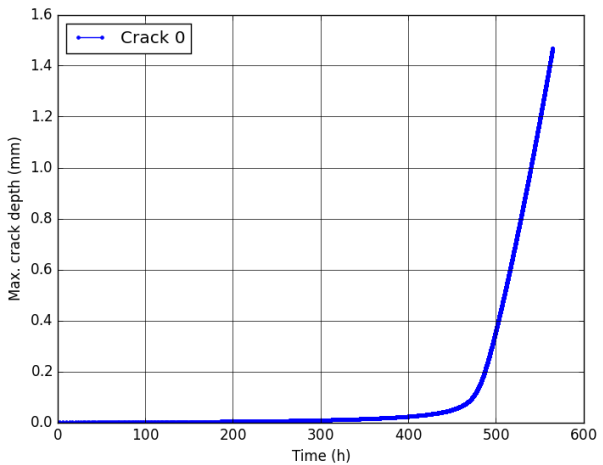


Figure 367 – Cracking kinetics predicted for specimen IN196, using the local model.

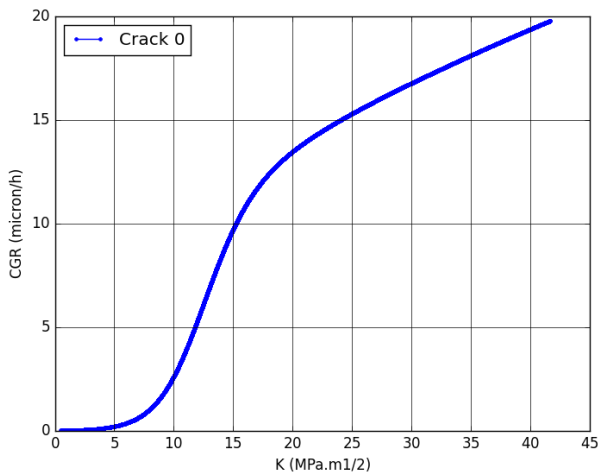


Figure 368 – Crack growth rate versus K at the tip of the main crack predicted for specimen IN196, using the local model.

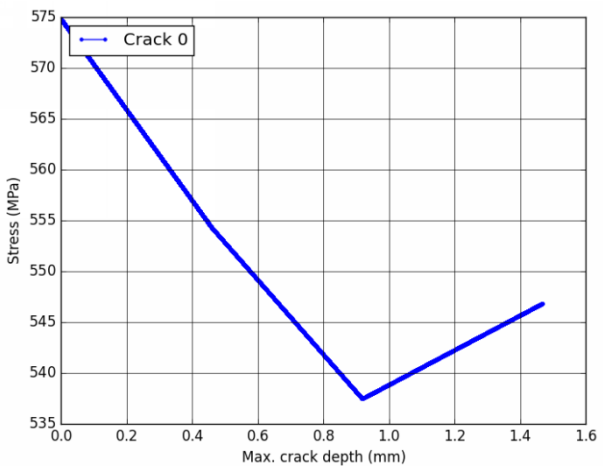


Figure 369 – Stress versus depth at the tip of the main crack predicted for specimen IN196, using the local model.

| | | |
|------------|---|--|
| MAI | Quantitative evaluation of the EDF local model and the EPRI-NRC xLPR models of crack initiation of the weld metals of Alloy 600 (Alloys 82 and 182) | 6125-4501-2018-00583-EN Version 2.0 |
|------------|---|--|



Materials Ageing Institute, EDF Lab Les Renardières - Ecuelles - 77818 Moret-sur-Loing cedex
Telephone +33 (0)1 60 73 60 73 - Fax +33 (0)1 60 73 72 22 contact@themai.org - <http://www.themai.org>
Members : EDF (F), EPRI (USA), KANSAI (J), CGNPC (CN), EDF Energy (UK), REA (RU), CRIEPI (J), MHI (J), TEPCO (J), CEA (F), AREVA (F)